

Dissertation

submitted to the
Combined Faculties for the Natural Sciences and Mathematics
of the Ruperto-Carola-University of Heidelberg, Germany
for the degree of
Doctor of Natural Sciences

Put forward by
Michael Schuricke, Dipl.-Phys.
born in: Neuenbürg, Germany

Date of oral examination: 31. October 2012

Two and Three Photon Double Ionization of Lithium

Referees: Priv.-Doz. Dr. Alexander Dorn
Prof. Dr. Andreas Wolf

Abstract

In this work the first differential studies on two- and three-photon double ionization (DI) of lithium, have been performed at two different VUV-photon energies. Through the unique combination of a magneto-optical trap (MOT), a Reaction Microscope (REMI) and the free-electron-laser in Hamburg (FLASH), the momentum vectors of the doubly charged ions created, were obtained. These contain information on the electrons' sum momentum, as well as their mutual emission angle and energy sharing and hence on the correlated motion of the two ejected electrons.

While at 50 eV photon energy a K-shell electron is ionized by non-resonant, simultaneous absorption of two photons, at 59.4 eV energy a one photon resonant transition ($1s \rightarrow 2p$) is followed by ionization through a second photon. In both cases it was observed that DI, i.e. the emission of the valence electron is either due to electron correlation or due to the uncorrelated, sequential absorption of a third photon. The comparison with results from non-perturbative close-coupling calculations is rather good at 50 eV, while poor agreement for the resonant process at 59.4 eV is found which most likely caused by an inaccurate description of the excited intermediate state.

Thus, new insight in non-linear few-photon few-electron quantum dynamics in the VUV-regime is provided which is of paramount scientific interest, as well as of practical importance for many experiments at free-electron lasers.

Zusammenfassung

Im Rahmen dieser Arbeit wurden die ersten differentiellen Untersuchungen zur zwei- und drei-Photonen Doppelionisation (DI) von Lithium bei zwei verschiedenen VUV-Photonenenergien durchgeführt. Durch die einzigartige Kombination einer magneto-optischen Falle mit einem Reaktionsmikroskop und dem freien-Elektronen Laser in Hamburg (FLASH) war es möglich, die Impulsvektoren der entstehenden doppelt geladenen Ionen zu ermitteln. Diese erlauben Rückschlüsse auf den Summenimpuls, den relativen Emissionswinkel und die Energieaufteilung der emittierten Elektronen und daher auch auf ihre korrelierte Bewegung.

Bei 50 eV Photonenenergie wird ein K-Schalenelektron durch simultane Absorption zweier Photonen ionisiert. Im Gegensatz dazu erfolgt bei 59,4 eV die Ionisation durch den resonanten Einphotonenübergang ($1s \rightarrow 2p$) und anschließende Absorption eines zweiten Photons. In beiden Fällen wurde beobachtet, dass die Emission des zweiten Elektrons entweder durch Elektronenkorrelation, oder durch die unkorrelierte, sequentielle Absorption eines dritten Photons geschieht. Der Vergleich mit Ergebnissen nichtperturbativer Close-Coupling Rechnungen zeigt gute Übereinstimmung bei 50 eV während beim resonanten Prozess bei 59.4 eV stärkere Abweichungen auftraten. Diese werden sehr wahrscheinlich durch eine ungenaue Beschreibung des angeregten Zwischenzustands verursacht.

Diese Ergebnisse erlauben neue Einblicke in die nichtlineare Quantendynamik der Wechselwirkung weniger Photonen mit wenigen Elektronen. Diese ist von großer wissenschaftlicher aber auch praktischer Bedeutung für viele zukünftige Experimente an freien-Elektronen Lasern.

Contents

1	Introduction	1
2	Photoionization by VUV Radiation	7
2.1	Single Photon Ionization	8
2.2	Photo-Double Ionization	11
2.2.1	Mechanisms of PDI	12
2.2.2	Manifestation of PDI Mechanisms	14
2.3	Multiple Ionization in Intense Fields	19
2.4	Many Electron Atoms	23
2.4.1	Convergent Close Coupling (CCC)	24
2.4.2	Time Dependent Close Coupling (TDCC)	26
2.5	Selection Rules for Double Electron Escape	27
3	Basic Concepts in Cooling and Trapping of Neutral Atoms	31
3.1	The Spontaneous Force	32
3.2	Doppler Cooling	35
3.3	Position Dependent Forces	37
3.3.1	Spatial confinement	39
4	Free Electron Lasers	43
4.1	Working principle	45
4.1.1	Undulator Radiation	46
4.1.2	Self-Amplified Spontaneous Emission	51
4.2	Properties of FEL radiation	53
4.2.1	Temporal and Spatial Coherence	54
4.2.2	Pulse Length and Intensity	57
4.2.3	Partial Coherence Model	58

5	A Reaction Microscope with an Ultra-Cold Target	59
5.1	Reaction Microscope	61
5.1.1	Spectroscopic System	64
5.1.2	Reconstruction of Momenta	68
5.1.3	Detector-System	72
5.1.4	Background suppression	76
5.1.5	Signal-to-Noise Ratio	80
5.2	Magneto-Optical Trap	82
5.2.1	Laser Setup	83
5.2.2	MOT-Coils	86
5.2.3	Zeeman slower	92
5.3	MOTREMI	95
6	Photo-Double Ionization of Doubly Excited and Aligned Lithium	99
6.1	Single Ionization	101
6.1.1	Results	102
6.2	Double Ionization	108
6.2.1	Two- and Three-Photon Double Ionization	110
6.3	Comparison with Theoretical Predictions	118
6.4	Discussion	124
7	Non-Sequential Two-Photon Double Ionization (NSDI) of Lithium	127
7.1	Experimental Framework	129
7.2	Multiphoton Single Ionization	132
7.3	Non-Sequential Two- and Three-Photon Double Ionization	136
7.3.1	Three-Photon Sequential Double Ionization (SDI)	140
7.3.2	Non-Sequential Two-Photon Double Ionization (NSDI)	143
7.4	Comparison with Theory	145
7.5	Discussion	150
8	Conclusion and Outlook	155
	Appendix A Atomic Units	159
	Appendix B Properties of Lithium	160
	Appendix C Filter transmissions	161
	Appendix D Dominant Decay Channels of singly excited ${}^7\text{Li}^+$	164

1 Introduction

Life is built upon the properties and interactions of its most basic elements, namely atoms and molecules. Taking into consideration, the merging of atoms to larger complexes, for example clusters and solids as well as their constituents, namely ions, electrons and bare nuclei, they even constitute the building blocks of the vast majority of all observable structures in the universe. Consequently, a profound knowledge of their structure and their dynamical behavior under the action of external forces, particle impact or photon absorption is of paramount scientific interest not only for physics but for practically all natural sciences.

To the best of our knowledge both the stationary state, as well as, the time-dependent progression of atomic and molecular systems is given by the solution of the Schrödinger equation¹. However, neither the stationary, i.e. time-independent, nor the time-dependent Schrödinger equation is solvable analytically for more than two interacting particles. For stationary states this very fundamental problem can be largely overcome by the use of iterative methods like MCDF (multi-configuration Dirac Fock) algorithms and the computational power available nowadays. Therefore, state-of-the-art structure calculations incorporating even quantum-electro dynamic (QED) effects can meet the precision of highly resolved measurements. This was demonstrated, for example, by the agreement of the experimental and the theoretical predicted $1s$ - $2s$ transition energy of atomic hydrogen [Fis04; Jen05] in the order of 10^{-14} .

In contrast, the prediction of the dynamical response of a quantum mechanical system to a perturber leading to changes in its internal structure or to its fragmentation still poses a tremendous challenge to the theoretical description. It was not before the onset of the new millennium that one of the most fundamental three-body Coulomb problems, the electron impact ionization of a hydrogen atom, was claimed to be "reduced to practical computation" [Res99]. Yet, even for the most simple three-body systems, numerical methods and computational approaches to solve the time-dependent Schrödinger equation (TDSE) still require the comparison with experimental data to validate or falsify them. Our insight and understanding of physical processes and the mechanisms inducing specific dynamic responses of an atom or molecule does, however, often not benefit from a pure numerical

¹In the non-relativistic case.

solution of the TDSE. Here, additional knowledge is frequently gained by applying approximative or perturbative theories. These allow to identify the most relevant interactions and the dominant pathways of the process under investigation and, therefore, develop simple, sometimes even mechanistic reaction models. (cp. Chap. 2).

Therefore, the processes leading to ionization and the influence of electron correlation in the initial state and during ionization offer a rich field of research. The special interest in studying these for the case of atoms, stems from their relative simplicity, which allows for the unambiguous determination of the driving mechanisms. In other words, if ionizing reactions are understood for very simple quantum mechanical systems, the methods developed here, can be employed to more complex systems, which are not only important in physics but for example in medicine, biology and chemistry. As electrons constitute the bonds between atoms to form molecules, ionizing reactions and electron correlation play a crucial role even in the break-up of large scale molecules. A very prominent example for this is embodied by DNA strand breaks induced by low energetic electrons in the scope of cancer treatment by heavy ion therapy (HIT) [Ngu11; BSS02; Bou00].

Many of the studies investigating the multiple ionization of atoms naturally choose helium as a target, as it comprises only two electrons it constitutes the simplest "many-electron" atom to study the dynamics of the removal of more than a single electron from the atomic potential. This holds for electron collisions [Dor02; Dür07], ion-atom collisions [Fis03], photo-double ionization (PDI) ([BKA04] and references therein) and non-sequential double-ionization in the infra-red (IR) [Wal94]. As a result, a range of theoretical models have been developed for this fundamental benchmark system and, in the meantime, have reached good agreement with the experimental findings. Apart from helium, the respective reactions have largely been investigated for the heavier rare gas atoms. As a result experimental data and theoretical cross sections for open-shell systems are rare even for photo-double ionization (PDI) [Ela09], which has been studied since the late 60's of the last century [Car67].

A new and spectacular development in this field constitutes the advent of free electron lasers. These facilities deliver partially coherent radiation in the VUV (cp. Chap. 4) and extreme ultra-violet XUV energy regime, with pulse lengths down to below 10 fs [Emm10]. Their brilliance, thereby exceeds the one observed in the most recent synchrotron radiation sources by up to nine orders of magnitude [Sch10a]. These unique properties of the radiation opened up new regimes of light-matter interaction, for experimental physics to explore. Among the many applications of these light sources the possibility to retrieve the structure of non-crystallized bio-molecules or even viruses in single-shot diffraction imaging [Cha11; Sei11] is perhaps the most exciting one. Another area of application is the investigation of reactions depending non-linear on the photon flux, e.g., multiphoton

processes, in the VUV and XUV. Thus, experiments on few-photon few-electron reactions in the VUV, as discussed in the present work, can be performed for the first time.

Multiphoton processes, i.e. the non-linear response of matter to the light fields' intensity, have first been proposed in 1931 [GM31]. Experimental evidence for their existence was already delivered in 1950 [HG50], through absorption spectroscopy in RbF-vapor. However, only the advent of pulsed laser sources, allowed for the generation of sufficiently high intensities to also observe multiphoton processes in the visible and infra-red regime [VD65]. Since then even single ionization by multiphoton absorption is an active field of research [DK99b; Rud04; Sch11]. With the progress of laser technology also double ionization through multiphoton absorption came into reach. It was found that there are basically two processes, contributing to the double ionization yield [Wal94]. In the sequential channel double ionization proceeds via the independent ejection of two electrons from the atom by multiphoton absorption. In contrast, the non-sequential channel was found to dominate in a regime, where the classical description of the light field is appropriate. Here, an electron which tunneled through the atomic potential modified by the electric field of the laser radiation is re-colliding with the parent ion, resulting in double ionization [BDM05]. This recollision is driven by the light field and not only leads to double ionization but also to the recombination, i.e., the recapture of the electron resulting in high harmonic radiation. Therefore, it constitutes an active field of research as it is the underlying mechanism for the generation of attosecond laser pulses [KI09].

In marked contrast to the non-linear response of matter to high intensity radiation fields in IR, the classical properties of the laser field are neglectable in the VUV (cp. Chap. 2). While in the IR, the unambiguous interpretation of the experimental data strongly depends on the knowledge of the exact shape and strength of the light field [Erg06], in multiphoton double ionization in the VUV the interaction with the light field and the atomic dynamics can be considered almost independent. Therefore, the VUV offers a uniquely "clean" environment to study the effects of multiphoton absorption on DI. The non-sequential double electron escape here is solely facilitated through electron correlation.

Among the first studies of two-photon - two-electron processes were these by the Heidelberg group [Rud08; Kur10] investigating helium double ionization induced by the simultaneous absorption of two photons (non-sequential double-ionization, NSDI). Interestingly, the results of various theoretical descriptions of the reaction differed by an order of magnitude even for the most basic property of the process the total cross section in dependence of the photon energy [Fei08]. By now, through combined experimental and theoretical efforts [Kur10], the huge discrepancies could be attributed to distinct numerical approximations made in the various calculations. Therefore, consensus has been reached on the magnitude of the cross section at least for photon energies below 50 eV [Pal10].

As a natural extension of these studies the present work deals with the correlated ejection of two electrons from the three-electron atom Li upon the absorption of two and three photons in the VUV. Therefore, it provides results, complementary to the before mentioned break-up of helium induced by simultaneous and sequential absorption of two photons [Rud10]. Given that lithium, provides the most fundamental open shell system, it can be viewed as a prototype system for all other open-shell atoms. Moreover, it evidently marks the next step in complexity compared to helium, comprising exactly one additional electron and is consequently on the brink of becoming the new benchmark system of atomic physics [Col01]. Nevertheless, due to the lack in experimental data, except for quantities like the total cross section, for PDI [WJL08] and a pioneering experiment on PDI of excited and aligned Li [Zhu09], before the present work this development had not taken place. Lithium contains a pair of tightly bound inner-shell electrons in the $1s$ -orbital, similar to helium, and a loosely bound electron in the valence orbital. Taking into consideration that the results presented here deal with the correlated ejection of either, one K-shell and the L-shell electron (Chap. 7), and PDI from a doubly excited and aligned state (Chap. 6) of lithium this work probes a very different regime of electron correlation, before, during and after double ionization compared to previous studies for helium.

The general lack of experimental studies and in particular differential cross section on the multiple ionization of lithium is caused by its chemical and physical properties. At room temperature lithium is in the solid state. Due to its low vapor pressure, dense atomic beams suitable for studies of the small DI cross section, are difficult to produce. Moreover, the thermal distribution of the atom's velocity in such a beam, smears out almost all the momentum information imprinted on the ion in an ionization reaction. In the present work an alternative approach is realized. The setup presented in Chap. 5 combines a magneto-optical trap (MOT), with a state-of-the-art momentum spectrometer, i.e., a Reaction Microscope (REMI) [Mos94], to form an apparatus dubbed MOTREMI [Ste07; Sch11; Fis12]. Here, lithium atoms are trapped in the center of the momentum spectrometer by means of the combined forces of light and magnetic fields. Prior to the measurement, these fields are switched off rapidly, in order to provide an unperturbed measurement (cp. Chap. 5).

All processes investigated in the scope of this work require the absorption of multiple VUV-photons by a single atom in a short interval of time. In the first reaction studied a K-shell electron in lithium is resonantly excited to the $2p$ -orbital by absorption of one

photon. In a second step absorption of one (or two) more photon(s) leads to ejection of both L-shell electrons. Thus, the data presented in Chap. 6 can be interpreted as two and three-photon double-ionization in the case of an intermediate resonance or as photo-double ionization (PDI) of excited and aligned lithium from the $\text{Li}^*(1s2s2p)_{m=0}$ initial state. Either way, the time-scale for the absorption of at least two photons is given by the lifetime of the intermediate state and amounts to approximately 100 fs.

In the second reaction studied a non-resonant photon energy was chosen well below the K-shell excitation threshold such that two-electron emission from the K- and L-shells requires the simultaneous absorption of two photons. We name this process non-sequential double-ionization (NSDI). Here, the relevant time-scale is given by the lifetime of the excited virtual state upon absorption of the first photon. Through the uncertainty relation of energy and time $\Delta E \Delta t < 1^2$, this can be estimated to be on the order of only several hundred attoseconds. Consequently, a huge photon flux in the VUV is essential for both measurements presented. As of now, there is only one source capable of providing laser-radiation with these properties, namely free electron lasers (FEL). Therefore, all experiments presented were performed at the Free-Electron Laser at Hamburg (FLASH).

This thesis is structured as follows. The subsequent chapter will introduce the theoretical background necessary for the interpretation of the experimental results presented. Thereby, two state-of-the-art theoretical approaches to solve the TDSE will be presented, namely the *time-dependent close-coupling* (TDCC) and the *convergent close-coupling* (CCC) method. The cross sections obtained with these calculations will be compared to the experimental data in Chaps. 6 and 7. In Chap. 4, the basic principles of light generation in free electron lasers are deduced and their impact on the properties of the light produced will be elucidated. The knowledge gained here will become important for the understanding of the data on non-sequential two-photon double-ionization. The concept of laser cooling, essential for the experimental methodology used, is briefly discussed in Chap. 3. Chapter 5 will give detailed insight on the experimental setup employed. In particular, an un-conventional mode-of-operation of the ion detector will be discussed, which allows to almost completely suppress the signal due to one-photon absorption. Furthermore, an overview on the efforts taken to facilitate coincident ion-electron detection in the future will be given. The next two chapters will present the results acquired at the free electron laser in Hamburg (FLASH) and their interpretation. In Chap. 6 differential experimental cross sections on PDI from doubly excited and aligned lithium will be presented and compared to the results

²In atomic units.

from the TDCC and CCC calculations. Despite the good mutual agreement between the two methods and with experimental data for helium, it will become apparent that this does not hold for lithium. Chapter 7 presents differential cross sections for the non-sequential two-photon double-ionization of lithium. In contrast, to the case of helium also a competing "sequential" three-photon reaction is observed. The obtained cross sections are found to be in excellent agreement with a theoretical investigation employing the TDCC method, despite an intensity two orders of magnitude higher and a pulse length two orders of magnitude shorter than the experimental one. The underlying reasons for this agreement will be elucidated. The final chapter summarizes the findings of this work and draws the resulting conclusions.

2 Photoionization by VUV Radiation

This work is dedicated to the multiple ionization of lithium upon photon impact of *vacuum-ultra-violet* (VUV) radiation. The term VUV, hereby, denotes the photon energy regime from ≈ 10 -125 eV, corresponding to wavelengths in the range of 10 – 120 nm. Due to the high energy of the incident photons a single photon absorption may already lead to double ionization, here. Indeed, the reaction studied in Chap. 6 deals with the simultaneous emission of two electrons from an excited state of lithium upon absorption of a single photon, dubbed photo-double ionization (PDI). This is solely possible if the outgoing electrons interact. In order to reach the excited state a primary VUV-photon has to be absorbed and hence a high photon flux is required to observe this reaction. Chapter 7 presents differential data on the non-sequential two-photon double ionization (NSDI) of lithium at a photon energy of 50 eV. Evidently, this implies the simultaneous absorption of both photons, as the removal of one of the electrons by a single photon would render the escape of the second electron upon single photon absorption impossible.

Therefore, the presented experimental results have been obtained at the *free electron laser in Hamburg* (FLASH) a fourth generation light source with a peak brilliance¹ on the order of 10^{29} (1/(smrad²mm²)) and thus a huge photon flux in a very short interval of time. This results in intensities of up to 10^{16} W/cm² [Sor07], implying electrical field strengths of the same magnitude as the intra-atomic ones. Still, field-assisted ionization channels, like tunneling ionization, are negligible here, as the oscillation frequency of the radiation is too high for the electrons to follow. In marked contrast, multiphoton processes, i.e. the "instantaneous" absorption of several photons leading to single or multiple ionization, are frequently observed [Kur09; Kur10; Rud10].

In this work both, PDI from an excited state and NSDI of ground-state lithium are investigated in the VUV. Therefore, this chapter aims at introducing various aspects of the photon-atom interaction encountered throughout this work.

This chapter is organized as follows. In the next section general properties of photoionization will be deduced from the example of single ionization of an one-electron atom. This includes the relations between the transition matrix element, the cross section and the

¹The peak brilliance is defined as photons per smrad²mm² in 0.1% of the bandwidth.

angular distributions shown in Chaps. 6 and 7. Subsequently, the process of PDI, i.e., multiple ionization induced by the absorption of a single photon, will be elucidated. Thereby, the intuitive mechanisms of *shake-off* and *two-step one* are introduced. In Sec. 2.3 the physics governing multiple ionization in an intense field are investigated. Furthermore, the problems arising in the theoretical treatment of many-electron atoms are briefly described, before the two theoretical models applied to reproduce the discussed results are introduced. In the final section, the selection rules for double electron escape will be discussed on the example of the reactions studied in Chaps. 6 and 7, respectively.

2.1 Single Photon Ionization

The term *single photon ionization* denotes the process where a single quantum of radiation is absorbed by an atom and thereby transfers sufficient energy to the atomic system to eject one of its electrons to the continuum. As a result, the electron is emitted with a kinetic energy E_e given by

$$E_e = E_\gamma - \text{IP} - E^* . \quad (2.1)$$

Here, $E_\gamma = \hbar\omega$ is the photon energy, IP is the ionization potential² and E^* marks a

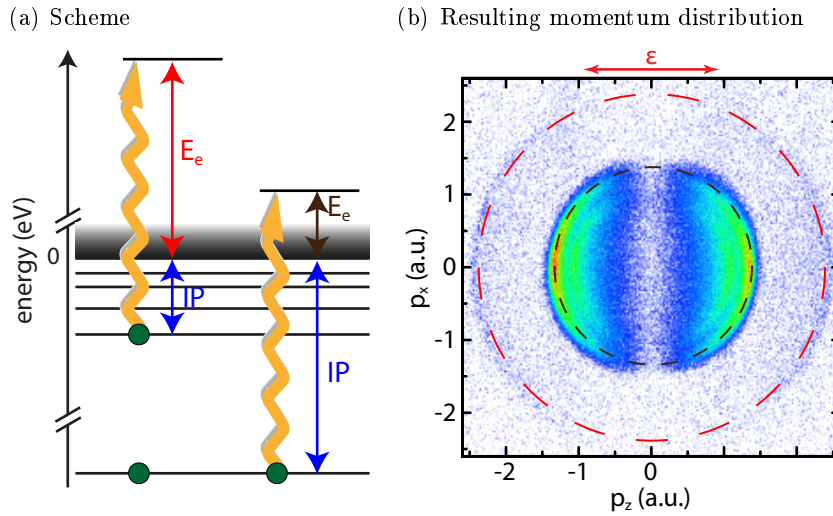


Figure 2.1: Schematic view of photon single ionization for lithium (a) and the resulting Li^+ recoil ion momentum distribution (b). The final-state electron energy calculates according to Eq. (2.1) as it is shown in (a) for ejection of a K- (brown) and a L-shell (red) electron. As the absorbed photon carries negligible momentum, the ejected electron and the recoiling ion are imprinted with the same final-state momentum of opposite sign. Evidently, a fixed final-state energy and hence momentum results in rings in the recoil ion momentum distributions shown in (b), for ground-state lithium upon impact of 91 eV photons.

possible excitation of the residual ion. If for example ground-state lithium, the first IP amounts to 5.39 eV, is irradiated by photons with an energy of $E_\gamma = 91$ eV, the kinetic energy of the outgoing electron is $E_e = 85.6$ eV. This corresponds to a momentum of $p_e = \sqrt{2m_e E_e} = 2.51$ a.u.³. Since photons hardly carry any momentum $\hbar k_{91 \text{ eV}} \approx 0.03$ a.u., momentum conservation dictates that the residual ion is imprinted with the same momentum of opposite sign. Therefore, the residual ion is usually referred to as *recoil ion*. Figure 2.1 illustrates this finding. On the right hand side of the figure the recoil and hence the electron momentum, is plotted as observed with a Reaction Microscope (see Chap. 5). Here the dashed red-line corresponds to the excess momentum for the given example. The Hamiltonian of a free electron in a radiation field will serve as starting point for the theoretical description of single photo-ionization (a thorough treatment is found for example in [HCP08]). In a general form it reads (in atomic units)

$$H = \frac{1}{2} \left(\vec{p} + \frac{\vec{A}}{c} \right)^2 - \phi, \quad (2.2)$$

where \vec{A} and ϕ constitute the vector and scalar potential defined by Maxwells equations, respectively. Here, $\vec{p} + \vec{A}/c$ describes the kinetic momentum of the electron in the radiation field, with $\vec{p} = -i\vec{\nabla}$ being its canonical momentum. If ϕ is chosen to be the potential perceived by an electron in an one-electron atom, i.e., $\phi = Z/r$, and the product is expanded, Eq. (2.2) is now given by

$$H = \underbrace{\frac{\vec{p}^2}{2} - \frac{Z}{r}}_{H_0} + \underbrace{\frac{\vec{p} \cdot \vec{A}}{c} + \frac{\vec{A}^2}{2c^2}}_{H_{\text{int}}}, \quad (2.3)$$

resembling the Hamiltonian of a one-electron atom in a radiation field, with the field-free part H_0 and the interaction term H_{int} . Considering a weakly perturbing electromagnetic field, i.e. $p \gg A$, the second term in H_{int} can be neglected. For the processes considered here this approximation even holds for intensities where multiphoton absorption becomes important (compare to Sec. 2.3). Postulating a plane electromagnetic wave the vector potential is given by

$$\vec{A}(\vec{r}, t) = \hat{e} A_0 \left(e^{i(\vec{k} \cdot \vec{r} - \omega t)} + c.c. \right), \quad (2.4)$$

where \vec{k} denotes the wavevector, ω the frequency and \hat{e} the polarization of the light field⁴. The time evolution of the system is naturally given by the time-dependent Schrödinger

²The first ionization potential corresponds to the binding energy of the outermost electron. The further IPs are calculated accordingly.

³The conversion factors for atomic units to SI units are found in App. A

⁴c.c.=complex conjugate

equation (TDSE). It reads

$$(H_0 + H_{\text{int}}) |\psi\rangle = i \frac{\partial}{\partial t} |\psi\rangle . \quad (2.5)$$

As the assumption of a weakly perturbing field was already made above, perturbation theory can now be applied to find the probability per unit time for a radiation induced transition W_{fi} of the system from its initial state $|\psi_i\rangle$ to a final state $|\psi_f\rangle$. For the time being both the initial and the final state will be assumed as bound states. The explicit execution of perturbation theory will be omitted here. It can be found for example in [HCP08]. Using first order perturbation theory, the transition rate W_{fi} after the absorption of a single photon from the light field is given by

$$W_{fi} = 2\pi \underbrace{|\langle \psi_f | H_{\text{int}} | \psi_i \rangle|^2}_{M_{fi}} \delta(E_f - E_i - E_\gamma), \quad (2.6)$$

where E_f , E_i are the energies of the final and initial state, respectively. Before the discussion continues the transition matrix element M_{fi} is evaluated. With the relation $\vec{E}(\vec{r}, t) = -1/c \left[\partial \vec{A}(\vec{r}, t) / \partial t \right]$, it is given by

$$M_{fi} = \hat{\epsilon} \cdot \frac{E_0}{\omega} \langle \psi_f | \exp(i\vec{k} \cdot \vec{r}) \nabla | \psi_i \rangle , \quad (2.7)$$

where E_0 and ω is the radiation field strength and frequency, respectively. Considering that the wavelength of the radiation is much larger than the spatial extension of the atom studied, i.e. $\vec{k} \cdot \vec{r} \ll 1$, the exponential function in Eq. (2.7) can be approximated according to

$$\exp(i\vec{k} \cdot \vec{r}) = 1 + i\vec{k} \cdot \vec{r} + \dots \approx 1 . \quad (2.8)$$

Equation (2.8) constitutes the so-called *dipole approximation*. In case of a hydrogen atom its validity ranges up to a photon energy of $E_\gamma \approx 10\text{keV}$. Hence, it holds for all wavelengths considered in this work. Through insertion of the relation $\langle \psi_f | \nabla | \psi_i \rangle = \omega \langle \psi_f | \vec{r} | \psi_i \rangle$ and assuming linear polarization in z direction, i.e. $\vec{r} = \hat{\epsilon}z$, the transition matrix element (Eq. (2.7)) reads

$$M_{fi} = E_0 \langle \psi_f | z | \psi_i \rangle . \quad (2.9)$$

Returning to the transition probability in Eq. (2.6), it is noted that its applicability is restricted to transitions between bound states. If it is evaluated for a transition from a bound to a continuum state and then divided by the photon flux, to obtain the transition probability per photon, the following relation for the angular dependence of the cross

section is derived

$$\frac{d\sigma}{d\Omega} = \frac{1}{N_\gamma} \frac{dw}{d\Omega} \propto \omega^3 |\langle \psi_f | z | \psi_i \rangle|^2. \quad (2.10)$$

Here N_γ denotes the photon flux. Assuming ionization from an initial s -state or ionization from a target with equally distributed m -sublevels the cross section given by Eq. (2.10) can be parametrized in terms of the second order Legendre-polynomial P_2 . It is the given by [DK99b]

$$\frac{d\sigma}{d\Omega}(\hbar\omega, \theta) = \frac{\sigma}{4\pi} [1 + \beta_2(\hbar\omega) P_2(\cos(\theta))], \quad (2.11)$$

for linear polarized light. The so-called anisotropy parameter β_2 , can take values in the interval $[-1;2]$ and does depend on the photon energy. If we consider for example ionization from a $2p$ target, the dipole selection rules (Eq 2.27) yield that the final state is a coherent superposition of s - and d -waves, and therefore does not only depend on their respective amplitudes but also on their relative phases. Since all of these quantities are energy dependent, also β_2 is. For higher order processes, for example multiphoton ionization, this simple parametrization for the angular distribution of the cross section does not hold. The corresponding relation can be found in Sec. 2.3.

2.2 Photo-Double Ionization

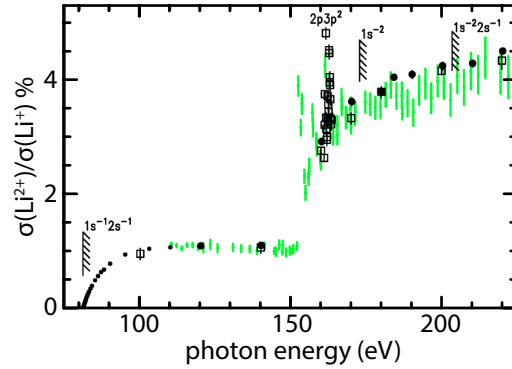


Figure 2.2: Ratio of the cross section of double to single ionization of lithium in dependence of the photon energy (changed from [Weh04]). The steep increase of the ratio around 160 eV originates from hollow lithium resonances and the onset of K-shell double ionization at 167 eV.

Given that the energy of a photon impinging on an atom is larger than the first double ionization threshold ($IP^{2+}(Li) = 81.03$ eV), not only single but also double ionization is observed. In Fig. 2.2 the ratio of the respective cross sections for double and single ionization as measured in [Weh04] is illustrated. It is found that for the photon energies (excess

energies) relevant in Chaps. 6 and 7, the double ionization yield is more or less constant at 1 % of the single ionization one. As it was seen in the previous section the photon-electron coupling is of single particle nature. Thus, double electron escape upon single photon absorption is facilitated solely by electron-electron correlations. Considering that this so-called process of *photon-double ionization* (PDI) is one of the most fundamental reactions including the correlated motion of electrons upon impact of a well defined projectile, it has been studied extensively over the past decades (see for example [AH05] and references therein). Naturally, the majority of the investigations approached this topic on the most simple "many"-electron system helium. Therefore, many of the examples given below will refer to He instead of Li, as the theoretical and experimental data on lithium and other open shell atoms is sparse.

On the theoretical side, the fact that both initial- and final-state correlation render PDI possible implies that independent particle models are not able to describe the photon induced ionization reaction. In particular, the long range Coulomb interaction among the three continuum particles (the two electrons and the ion)⁵, poses a tremendous challenge to *ab initio* investigations of PDI and defies any perturbative approach to the problem. As a result, accurate theoretical approaches, allowing for the "exact" treatment of the outgoing electrons in PDI have only recently been developed. In general they solve the Schrödinger equation for the given problem numerically on a grid (see also Sec. 2.4) to retrieve the final-state properties of the system. While excellent agreement with the experimental results has been reached for helium, the case of lithium offers additional challenges for theory, due to its more complex structure (see, in particular, Chap. 6).

2.2.1 Mechanisms of PDI

Despite the excellent agreement reached between numerical solutions of the Schrödinger equation and experimental results studying PDI of helium and other rare gases, the underlying mechanisms of PDI can usually not be retrieved from these kind of results. In fact, the understanding of reaction pathways often originates from approximations made in calculations leading to characteristic features in the observables. Consequently, two intuitive model mechanisms of PDI, namely the *two-step one* (TS1) [PB01; SCR02] and the *shake-off* (SO) process [Blo35; Abe70], will be discussed in the following. Note, that in general it is not possible to separate the two mechanisms as they can in principle occupy the same final states in phase-space. Therefore, the amplitudes of the respective pathways interfere. Nevertheless, in many configurations they lead to considerably different final-state

⁵The interaction of ejected electrons in the continuum is also often dubbed post collision interaction (PCI).

momenta and angular distributions, thus minimizing the interference term [SR03].

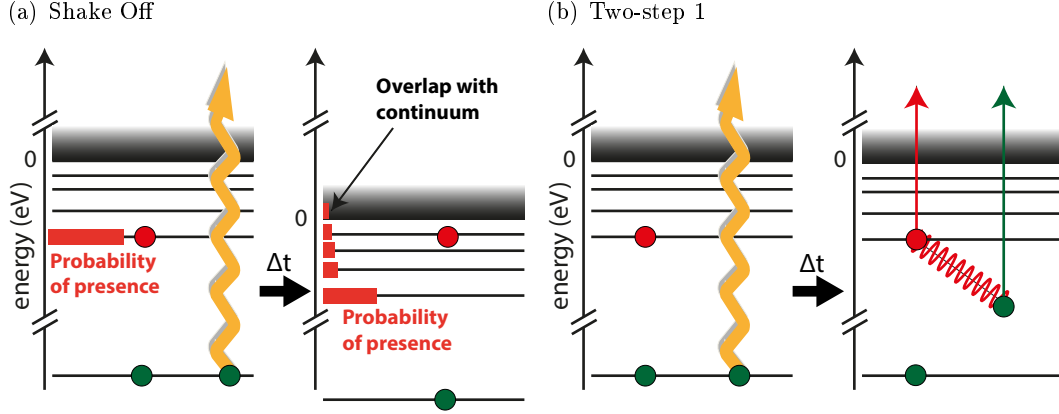


Figure 2.3: Scheme of the PDI mechanisms. In (a) the shake-off mechanism is illustrated. Upon photon impact the primary electron is ejected from the atom in a time interval smaller than the relaxation time of the secondary electron (sudden approximation). Consequently, the wavefunctions of the remaining electrons are projected on the eigenstates of the ionic Hamiltonian, which results in a certain overlap of the atomic wave-functions with the ionic continuum. In contrast, in the TS1 process the primary electron absorbs a photon and on its way out of the atom scatters on the secondary electron in an (e,2e) like collision.

Shake-off: The SO mechanism is illustrated in Fig. 2.3(a) for the case of lithium. After absorption of a single high-energetic photon ($\hbar\omega > 81$ eV) an inner-shell electron is ejected from the atom. If this ejection is fast in comparison with the relaxation time of the system (sudden approximation), the wavefunctions⁶ of the remaining electrons will not progress adiabatically to their respective ionic counter-parts. As a result, the atomic wave-functions are directly projected onto the eigenstates of the ionic Hamiltonian according to

$$\langle \psi_{\text{ion}} | \psi_{\text{atom}} \rangle . \quad (2.12)$$

Depending on the overlap of the atomic with the ionic wave-functions and continuum, a second electron, the valence electron in the figure, is eventually promoted either to the continuum (SO) or to different nl -shells of the system (shake-up).

Naturally, SO is a purely quantum mechanical double ionization channel, as there is no classical or semi-classical equivalent to it. It is caused by initial state correlations of the two liberated electrons. The fast removal of the primary electron, changes the effective charge of the nucleus for the secondary electron and thus interacts, in a way, indirectly

⁶Since the binding energies of the 1s and 2s electrons is vastly different we assume separable wavefunctions.

with it.

Two-Step One: In contrast to SO, the TS1 mechanism is mediated through electron correlation in the final state⁷. Its schematic progression is shown in Fig.2.3(b). After absorption of the photon by the atom the primary electron is energetically lifted to the continuum. On its way out of the atom it undergoes an (e,2e)-reaction with the secondary electron leading to its excitation (knock-up) or ejection TS1 (knock-out).

There are, however, differences in the collision geometries between the TS1 and an (e,2e)-collision. The energies of the electrons still bound in the system will differ from the analog process in an (e,2e) reaction of the singly charged ion, since the system hasn't relaxed yet. Furthermore, the impacting electron stems from inside the atom and thus lacks the influence of the approaching projectile on the ion and vice versa. As a consequence, the second step of the TS1 process is often referred to as *half-collision* [Sam90].

As TS1 resembles a “hard” collision of two electrons the interaction times and hence the amount of energy and angular momentum exchange can exceed the ones observed in SO considerably. Moreover, TS1 can be described semi-classically, as shown by *Schneider and Rost* [SR03], allowing for the distinction of the two-processes by calculating the TS1 and the full cross section individually.

In the case of lithium, PDI implies photon energies larger than 81 eV. Despite this large photon energies it was found in the considerations above that the photons carry only little linear⁸ momentum. Therefore, the momentum of the photoionized electron corresponding to the kinetic energy derived in Eq. (2.1) has to originate from the electrons wavefunction in the initial state. This rises the probability of photon absorption by inner-shell and *s*-electrons, since they show an increased probability of presence close to the nucleus.

2.2.2 Manifestation of PDI Mechanisms

The presented mechanisms of PDI manifest themselves in various ways in the energy distribution between the outgoing electrons and also in their mutual emission angles. Moreover, there are characteristic dependencies for the TS1 and SO process with respect to the excess energy available and the efficiency for distinct spin configurations of the two-electron wavefunctions. In the following these will be discussed qualitatively, mostly on examples for He. For the calculations the reader is referred to the references given.

⁷Note, that the final state is reached right after the photon absorption.

⁸In contrast to angular momentum.

Energy Dependence

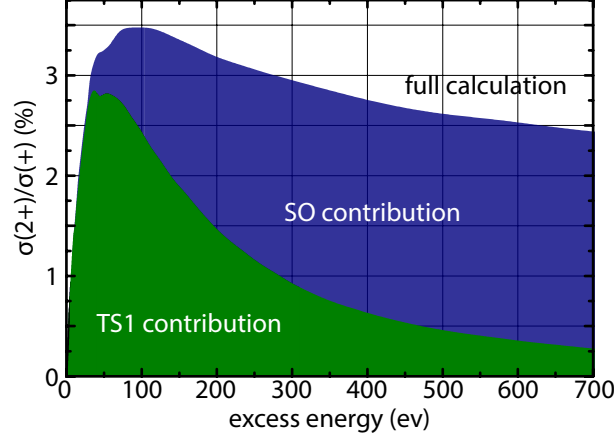


Figure 2.4: Individual contributions from SO and TS1 to the total ratio of the double-to-single ionization cross section of ground-state helium over the excess energy. Data taken from [Khe01]. The data was gained by performing a full calculation via the CCC method described in Sec. 2.4.1. Consequently, by calculating the Shake-off-only ionization probability, also the contribution of the TS1 mechanism is gained. Note that interferences of the two mechanisms are neglected here.

The distinct underlying physical mechanisms of TS1 and SO result in a different behavior of the processes with the energy available in the double electron continuum. This is illustrated in Fig. 2.4, where the results of a convergent-close coupling (CCC) and a SO only calculation from *Kheifets* [Khe01] are plotted. Their difference constitutes, therefore, the contribution of the TS1 mechanism to double ionization. It is found that close to threshold TS1 dominates the double ionization cross section, whereas for very high photon energies SO is the major origin for double ionization.

For energies close to the threshold of double ionization, i.e., starting from the Wannier-regime [Wan53], TS1 is dominant. This is also evidenced by the fact that the slope of the PDI cross section close to threshold is identical with the one for the (e,2e) reaction [Sam90]. From the perspective of the SO mechanism, it is clear that the slower the initial electron leaves the atom the more time the remaining electrons have to relax to their ionic counter-part. In the high energy limit, where the approximation of the sudden removal of the primary electron is well fulfilled, SO is dominant. As a general rule it can be stated: If the excess energy is high, the interaction of the electrons in the final state is weak and the primary electron is removed fast, favoring SO over TS1. If, on the other hand, the excess energy is small, electron correlation in the final state is strong and hence TS1 is favored. In the intermediate regime, which happens to cover the measurements discussed in Chaps. 6

and 7, the amplitudes of both processes will contribute to the cross section. Although, Figure 2.4 suggests that for excess energies of ≈ 20 and ≈ 40 eV TS1 is the major source of double ionization.

Energy Sharing and Angular Distributions

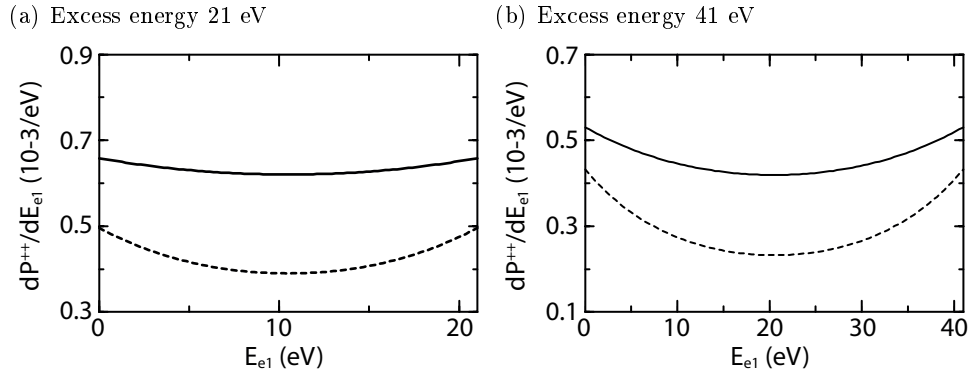


Figure 2.5: Singly differential probabilities for the TS1 (solid) and SO (dashed) mechanisms for excess energies of 41 and 21 eV from ground-state helium as a function of the energy of the primary electron e_1 [SCR02].

Figure 2.5 illustrates separate differential double escape probabilities for the TS1 (solid line) and SO (dashed-line) mechanisms over the energy of the primary electron e_1 ⁹. They are displayed for the PDI of ground state helium [SCR02] and 21 and 41 eV excess energy available. These probabilities are proportional to the respective cross sections. The figures demonstrate that for the available energies in the continuum, both TS1 and SO contribute to the cross section, although the TS1 contribution is stronger. Further, it is found that in both, Fig. 2.5(a) and (b), the SO contribution is more U-shaped compared to the TS1 one. Thus, indicating a higher likelihood for asymmetric energy sharing in case of SO. In the simple picture elucidated above this is understood considering the stronger interaction of the electrons in case of the TS1 mechanism, which allows for larger energy transfers between the outgoing electrons in the final state. In the case of shake-off, the energy transfer between the outgoing electrons is far less pronounced. Consequently, the energy sharing will be more asymmetric. For higher excess energies the interaction time in TS1 becomes shorter, hence less energy is transferred at a coinstantaneous rise of E_{e1} . Therefore, also TS1 exhibits a U-shape at higher excess energies.

⁹The energy of the second electron is always $E_{e2} = E_{\text{exc.}} - E_{e1}$.

Angular Distributions: As a result of the considerations above, distinct angular emission patterns are expected for SO and TS1. In both, PDI is considered as a two-step process, where the photon is absorbed by the atom and the primary electron is emitted to the continuum. Through direct (TS1) or indirect (SO) interaction the secondary electron is ejected.

As the primary photo-electron in SO does not directly interact with the second electron for an initial s -state an outgoing p -wave, with respect to the photon polarization axis is expected. In terms of Eq. (2.11) the anisotropy parameter would amount to $\beta_2 = 2$. The second electrons' angular emission pattern reflects the angular distribution of its wavefunction in the neutral atom. Consequently, it is isotropic for all s -states and in the ordinary case of equally occupied m -sublevels [Kna05]. Nevertheless, this is not the case for the data presented in Chap. 6, where PDI from the $\text{Li}^*(1s2s2p\ ^2P_{m=0})$ state is investigated. If PDI is mediated through shake-off here, a p -wave angular distribution is also expected for the secondary electron.

To give similar general predictions for the TS1 mechanism is more difficult. However, in [Kna05] a preferential mutual emission angle of 90° for electrons with energy sharings assigned to the TS1 mechanism was found and interpreted as a signature of TS1 at large photon energies (The total energy above the threshold was 450 eV). That this can not hold for all excess energies is clear considering that TS1 dominates in the Wannier regime, where back-to-back emission is dominant.

Spin-configuration

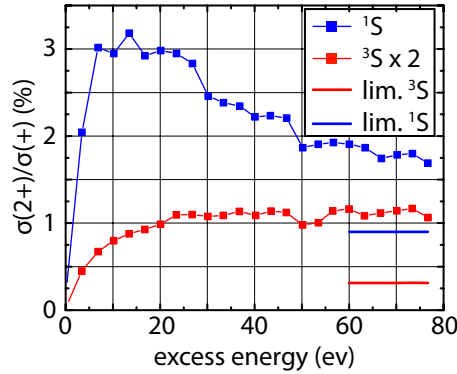


Figure 2.6: Ratio of the cross section of double to single ionization from $\text{He}(1s2s\ ^1S)$ and $\text{He}(1s2s\ ^3S)$. Data from [HMG98]. The data for the triplet case is scaled by a factor of two for better visibility. The lines between the data points are a guide to the eye.

In the introduction it was mentioned that lithium poses additional challenges to theoret-

ical models compared to helium. Apart from the simple fact that an additional electron is present, which is often frozen out in order to apply state-of-the-art numerical solutions of the TDSE, Li inherently allows for different spin-configurations (parallel or anti-parallel) of the outgoing electrons. This not only strongly modifies the ratio of double to single ionization of the cross section, as illustrated in Fig. 2.6, but also the energy sharing (Fig. 2.7) and the angular distributions of the emitted electrons (compare to Sec. 2.5).

Figure 2.6 shows calculations of the ratio of the double-to-single ionization cross section¹⁰ for both spin configurations of the helium ($1s2s\ ^1,^3S$)-states. It is found that the efficiency of double ionization for the singlet spin-configuration exceeds the triplet one by a factor of 6 for low excess energies and that this difference is getting less for higher values of $E_{\text{exc.}}$. Although, the singlet-coupling still yields a higher double ionization ratio in the infinite photon energy limit. In terms of the TS1 mechanism this finding is given by the fact that if the electrons couple to a spin-singlet, they are not restricted by the Pauli exclusion principle. Therefore, the electrons are allowed to approach each other in both configuration and momentum space. Ultimately, this results in a higher probability of energy exchange in an (e,2e)-like reaction and thus a higher double ionization cross section. The difference in the infinite energy limit, where only SO contributes, stems from the stronger configuration interaction of the singlet-states [HMG98].

Apart from the total cross section the spin-couplings also modify the energy sharing of the

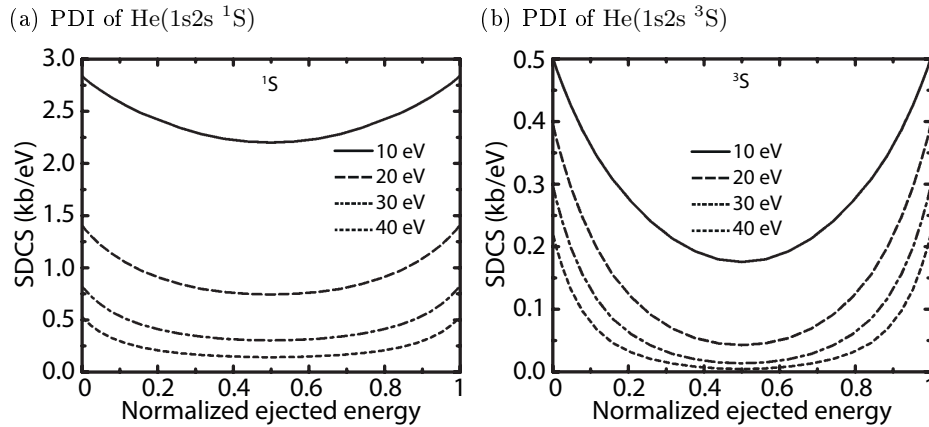


Figure 2.7: Singly differential cross section (SDCS) for the double ionization of He($1s2s\ ^1S$) (a) and He($1s2s\ ^3S$) (b) taken from [CP03]. Hence, a very similar configuration to ground-state lithium is displayed. The cross section for ionization of the singlet state exceeds the triplet one by a factor of 6 close to threshold. For higher excess energies, this difference decreases. Moreover, the SDCS of the triplet-state exhibits a stronger U-shape than the singlet one, thus indicating asymmetric energy sharing.

¹⁰The single-ionization cross section differs at most 1.5 % [HMG98].

outgoing electrons as shown in Fig. 2.7. In case of a triplet configuration in the final state the SDCS exhibits a much more pronounced U-shape than in the singlet-case. Evidently, this is caused by both the Pauli exclusion principle, rendering final states with equal energies impossible and the smaller relative contribution of TS1. The latter implies a higher contribution of SO. Moreover, the symmetry of the two-electron wavefunction which has to be anti-symmetric with respect to electron exchange dictates certain restrictions, even exceeding the pure Pauli exclusion principle, which will be discussed in Sec. 2.5.

2.3 Multiple Ionization in Intense Fields

To elucidate the effects of intense light fields on the process of photoionization the discussion will now turn to the infra-red (IR) regime first. Given that the photon energy is insufficient to cause ionization ($E_\gamma < \text{IP}$), a condition well fulfilled in the IR, ionization will not take place. If, however, the atom is placed in a very intense light field $I \gtrsim 10^{12} \text{ W/cm}^2$ and is therefore subjected to a tremendous photon flux it might absorb multiple quanta of light "instantaneously", leading to ionization. Considering that no real intermediate state is accessible this process is forbidden in a classical picture. This type of photoionization, dubbed multiphoton ionization (MPI) [DK00], is ultimately enabled by the "uncertainty" relation between energy and time $\Delta E \cdot \Delta t \geq 1$ ¹¹, where ΔE corresponds to the energy difference of the virtual state to the closest real state. The interpretation is that the transition from the initial state E_i to the virtual intermediate state $E_{\text{virt}} = E_i + E_\gamma$ is allowed, however, it is only populated for the time Δt . If, during that time another photon is absorbed, this enables the transition into a real or another virtual state. In this manner, MPI occurs through multiple virtual intermediate states as illustrated in Fig. 2.8(a) for the valence electron of lithium. The resulting recoil ion momentum distribution is shown in (b). A thorough treatment of intense field ionization in the IR goes beyond the scope of this thesis. It can be found for example in [Sch08]. Here, the Keldysh parameter γ_K [Kel65], will be introduced, which is commonly used to distinguish the regimes where ionization is mediated by the absorption of photons $\gamma_K \gg 1$ (multiphoton ionization) or by the electric field of the laser $\gamma_K \ll 1$ (tunneling ionization). It is calculated according to

$$\gamma_K = \frac{\omega_{\text{laser}}}{\omega_{\text{tunnel}}} = \sqrt{\frac{IP}{2U_p}}, \quad (2.13)$$

¹¹Note, that the term uncertainty relation is strictly not valid in this case, as it does not follow from the commutator, but is a property of Fourier transformation.

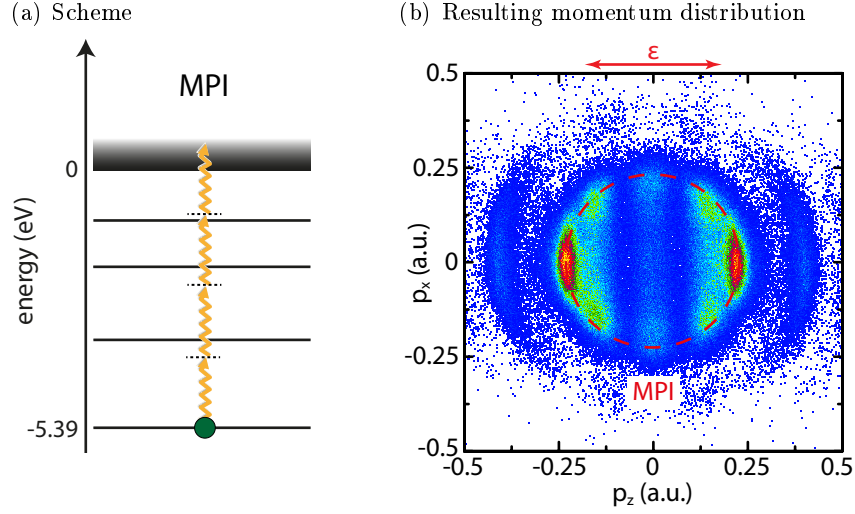


Figure 2.8: Schematic view of multiphoton (MPI) ionization of lithium in an intense infrared ($E_\gamma = 1.5$ eV) light field (a) and the corresponding recoil ion momentum distribution (b) (from [Sch11]). The angular distribution of the photo lines clearly shows two distinct minima per hemisphere indicating a dominant d -wave contribution to the cross section.

where ω_{laser} and ω_{tunnel} denote the light field and the tunneling frequency and the ponderomotive potential U_p has been introduced. It corresponds to the energy of the quivering motion of a free electron in the laser field and amounts to $U_p(\text{eV}) = 9.33 \cdot 10^{14} \cdot I (\text{W}/\text{cm}^2) \cdot \lambda_{\text{las}}^2 (\mu\text{m}^2)$. In the IR it can amount to several eV, for intensities of $10^{14} \text{W}/\text{cm}^2$.

For the calculation of the transition probability from a bound state to the continuum in MPI, lowest order perturbation theory (LOPT) can be employed [Fai86; Lam76]. Here, the n -photon transition is modeled by taking into account n interactions of the light field with the atom. The transition probability, in an extension of Eq. (2.6), reads

$$W_{fi}^{(n)} = 2\pi (2\pi\alpha)^n I^n \left| T_{fi}^{(n)} \right|^2 \rho(E_e) . \quad (2.14)$$

Here, α denotes the fine structure constant, $\left| T_{fi}^{(n)} \right|^2$ the LOPT transition matrix element for the absorption of n -photons and $\rho(E_e)$ the density of final states reachable in the continuum. $\left| T_{fi}^{(n)} \right|^2$ is given by [Fai86]

$$T_{fi}^{(n)} = \sum_{\kappa_1} \sum_{\kappa_2} \dots \sum_{\kappa_{n-1}} \frac{\langle \psi_f | \hat{\mathbf{e}} \cdot \mathbf{R} | \psi_{\kappa_{n-1}} \rangle \dots \langle \psi_{\kappa_2} | \hat{\mathbf{e}} \cdot \mathbf{R} | \psi_{\kappa_1} \rangle \langle \psi_{\kappa_1} | \hat{\mathbf{e}} \cdot \mathbf{R} | \psi_i \rangle}{(E_f + (n-1)\omega - E_{\kappa_{n-1}}) \dots (E_f + 2\omega - E_{\kappa_2})(E_f + \omega - E_{\kappa_1})} \quad (2.15)$$

in the dipole approximation. The sums run over the virtual intermediate states. Note, that this relation holds for all wavelengths. An important point here is that the *ionization rate of an n -photon transition scales with the intensity of the incident light field to the power of n* . As a result, the simple parametrization for the angular dependence of the cross section derived in Eq. (2.11) has to be modified to

$$\frac{d\sigma}{d\Omega}(\hbar\omega, \theta) = \frac{\sigma}{4\pi} \sum_{m=0,2,\dots,2n} [1 + \beta_m(\hbar\omega)P_m(\cos(\theta))] , \quad (2.16)$$

where the summation is over all even Legendre-polynomials up to the order of $2n$. The reason for the change from Eq. (2.11) to Eq. (2.16) is given by the selection rule $\Delta m = 0$, which implies that the intermediate states do not exhibit equally occupied m -sublevels. Hence, starting from an s initial state only the $m = 0$ sublevels of the virtual states are populated. As a consequence, these states are not spherically symmetric and the angular distribution will not only depend on the angular momentum of the ionizing photon, but also of the initial state¹².

So far single ionization through multiphoton absorption has been considered and indeed multiphoton single ionization in the IR and VUV proceed along the same principles. The major difference is the almost complete absence of "light-field" induced effects like tunneling ionization in the VUV, as the frequency of the light-field is large compared to typical tunneling frequencies and thus $\gamma_K \gg 1$. In a simple picture, the electrons are too heavy to follow the oscillations of the light field.

The analogies of MPI in the IR and VUV come to an end when non-sequential double ionization is considered. In the infra-red NSDI is mediated through the electric field of the laser radiation. An electron liberated to the continuum is driven by the electric field and recollides with the parent ion, where it knocks out a secondary electron in a "field-assisted" collision.

In contrast, for typical studies dealing with DI through non-linear absorption of two or more photons in the VUV, a single photon is usually sufficient to remove one of the electrons. Depending on the exact photon energy E_γ in comparison to the first and second ionization potential, even the sequential removal (SDI) of the electrons will be possible. Figure 2.9 illustrates different domains, defined by the photon energy of two and three-photon DI of lithium in the VUV. The regime shown in panel (a) includes the photon energy employed in Chap. 7. Here, both NSDI and SDI, require the simultaneous absorption of two photons. Therefore, NSDI is expected to dominate unless target depletion occurs¹³. In Fig. 2.9(b)

¹²This can be both a real or virtual intermediate state.

¹³If the number of singly ionized target atoms is on the same order of magnitude as the neutral ones, SDI might be more likely.

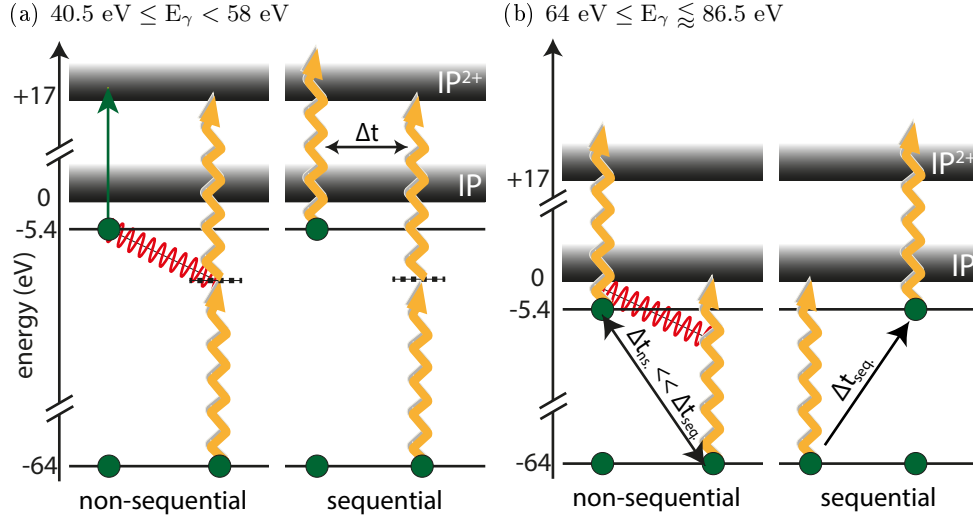


Figure 2.9: Illustration of the pathways of NSDI and sequential double ionization (SDI) in the VUV in two different photon energy domains. While, in (a) NSDI is expected to dominate the DI cross section the reversed situation is anticipated in (b). As a general rule, NSDI is only expected to constitute a major contribution to the cross section provided that sufficiently high intensities are reached and SDI requires the absorption of more photons. The gap between the two domains is due to intermediate resonances.

the two channels are shown above the first sequential threshold. Here, SDI will dominate. Given that for the sequential channel both, the absorption of photons and the emission of the electrons proceeds independently, sufficient time will pass between the two events such that the continuum electrons hardly influence each other¹⁴. In the direct, i.e., non-sequential, case the absorption of photons and the emission of electrons happens "instantaneously". Therefore, cross sections governed by electron correlation are expected here. In order to calculate which of the channels dominates for a given light field intensity and photon energy coupled rate equations for the respective pathways have to be calculated. If a photon energy of 50 eV is chosen (Fig. 2.9(a)) SDI can either proceed via initial ejection of the valence or the K-shell electron. Therefore, neglecting the coupling through the

¹⁴For very short light-pulses (< 2 fs) this does not hold [Fei09], as the respective single ionizations can solely occur in a short interval of time.

decrease in population of the neutral atoms, the yield for SDI reads

$$\begin{aligned} \frac{dN_2^{\text{seq.}}}{dt} = & \left[\int_{-\infty}^t N_0(t') \sigma_{01} \left(\frac{I}{\hbar\omega} \right) dt' \right] \times \sigma_{12}^{(2)} \left(\frac{I}{\hbar\omega} \right)^2 \\ & + \underbrace{\left[\int_{-\infty}^t N_0(t') \sigma_{01}^{(2)} \left(\frac{I}{\hbar\omega} \right)^2 dt' \right]}_{N_1(t)} \times \sigma_{12} \left(\frac{I}{\hbar\omega} \right), \end{aligned} \quad (2.17)$$

where the first term stands for initial L-shell emission and the second one for K-shell ejection in the primary step. N_k denotes the number of ions in charge state k , $\sigma_{if}^{(n)}$ the (generalized) cross section for the n -photon transition from the initial charge state i to the final charge state f and $\frac{I}{\hbar\omega}$ is the photon flux. The respective equation for the non-sequential reaction is given by

$$\frac{dN_2^{\text{ns.}}}{dt} = N_0(t) \sigma_{02}^2 \left(\frac{I}{\hbar\omega} \right)^2. \quad (2.18)$$

Evidently, not only the relative contributions of NSDI and SDI will depend critically on the shape, intensity, and duration of the laser pulse, but also the contributions of the individual sequential channels. Since the generalized cross sections for the non-linear parts in Eqs. (2.17) and (2.18) are not known and due to the complex pulse structure of FLASH (cp. Chap. 4) the prevalence of the specific channels is determined from the experimental momentum spectra in Chaps. 6 and 7.

2.4 Many Electron Atoms

In the above discussion of the cross sections arising from single and multiphoton absorption single electron wavefunctions were used in the transition matrix elements. For many electron atoms, like lithium, the calculation the transition probability in the perturbative approach does not change in principle. Nevertheless, since now an N-particle state is described the eigenstates of the system have to be approximated. For the case of lithium the Hamiltonian of the unperturbed atom reads

$$H_0 = \sum_{i=1}^3 \frac{\vec{p}_i^2}{2} - \frac{3}{r_i} + \sum_{i<j}^3 \frac{1}{|\vec{r}_i - \vec{r}_j|}, \quad (2.19)$$

where in comparison with the one-electron atom the Coulomb repulsion of the electrons was included. The N-particle states can, in the simplest case, be approximated by anti-

symmetrized products of single-particle-states¹⁵ or by the Hartree-Fock Method, where an effective potential is used to determine the individual single-particle states [Fri98]. These methods do, however, neglect the correlation between the electrons. A technique which allows for retrieving correlated N-particle states is for example the configuration interaction method [LMZ98], which was successfully applied to describe two-photon single ionization of helium [BL91].

In double ionization the problem to determine a set of correlated states reflecting the complexity of the system in the final state proofs difficult and highly elaborate [NL01]. The two-electron continuum is characterized by the long range Coulomb interaction which allows for both energy and angular momentum exchange and can no longer be considered a small perturbation to the system. Consequently, alternative approaches have been developed to investigate the problems of PDI and non-sequential two-photon double ionization¹⁶. Below two of these methods namely the *convergent close coupling* (CCC) and the *time-dependent close coupling* (TDCC) will be presented, as their results for the problems discussed in Chaps. 6 and 7 will be compared to the experimental findings. The discussion will focus on the basic ideas of the methods. The exact details of the calculation are found in [KFB09] for the CCC calculation performed by *Kheifets* and in [AC12] for the TDCC results from *Armstrong and Colgan*.

2.4.1 Convergent Close Coupling (CCC)

The convergent close coupling formalism was initially developed in the framework of inelastic electron collisions resulting in excitation and not ionization of the target atom. There, it was very successfully applied at low impact energies [BS92]. For these reactions, there is, however, only a single electron in the continuum, namely the incoming and scattered electron. Later, the method was also employed to ionizing electron collisions. An overview over the early development and application is given in the work of *Bray* [Bra02]. Its application to photon double ionization was put forward by *Kheifets and Bray* [KB96] for the case of helium. The extension of the CCC formalism beyond the helium iso-electronic sequence was achieved in 2009, where it was extended towards the lithium case [KFB09]. Hereafter, the CCC method will be elucidated on the example of an (e,2e)-reaction. As discussed above PDI is in a sense equivalent to an (e,2e) process of the photo-ionized electron and thus this approach is valid. The application of CCC to the PDI of lithium will be given in the next paragraph. The CCC approach constitutes a so-called *coupled channel* calculation, where the states of the target atom are expanded in a basis-set of eigenfunc-

¹⁵This is achieved by using Slater determinants.

¹⁶The case of sequential double ionization can be treated perturbatively given that the time difference Δt between the emission of the primary and secondary electron is long enough.

tions of the unperturbed system. For this basis-set L^2 integrable Laguerre functions are employed to construct the atomic eigenstates $|\psi_n\rangle$ such that

$$H_{\text{atom}} |\psi_n\rangle = E_n |\psi_n\rangle \quad (2.20)$$

holds. Thereby, these eigenstates do not only include bound-states of the system but also its free-states. As a result the eigenstates with negative energies correspond to bound-states, whereas the ones with positive energies embody states in the continuum. Naturally, the infinite number of states would render the calculation impossible. Thus, the calculation is restricted to an "arbitrary" finite number of states, dubbed pseudo-states, in the continuum, i.e., the continuum is discretized. Nevertheless, through inclusion of an increasing number of states the discretized continuum converges to the true continuum. With this states, the CCC approach seeks the solution of the T-matrix, whose elements are given by

$$T_{fi} = \langle \psi_f | H - E | \psi_i^{(+)} \rangle . \quad (2.21)$$

As before $|\psi_f\rangle$ stands for the asymptotic final states and $|\psi_i^{+}\rangle$ is the so-called scattering wave. Here, that is the scattered projectile electron. Apparently, the determination of the T-matrix (Eq. (2.21)) is equivalent to a solution of the time-independent Schrödinger equation. The matrix elements are found by expanding the scattered wave in terms of the eigenstates of the unperturbed Hamiltonian. The multichannel expansion reads

$$|\psi_i^{+}(N)\rangle = \sum_{n=1}^N c_n |\psi_n\rangle \quad (2.22)$$

where the expansion coefficients $c_n = \langle \psi_n | \psi_i^{(+)} \rangle$ are determined by solving the Lippmann-Schwinger equations. Since an (e,2e)-reaction is considered, the final states of two electrons, the scattered projectile and an ionized electron, are in the continuum. While the scattered projectile is described by either a plane or distorted wave, hence, as a free particle, the ejected electron is bound in one of the pseudo-states of the discretized continuum. Despite this asymmetric treatment of the continuum electrons, the CCC shows excellent agreement with electron impact ionization and PDI of helium [BF96; KB96]. This is even the case when equal energy sharing is considered [Ste05], where both final-state electrons are indistinguishable.

In case of PDI on lithium as discussed in Chap. 6 the application of the CCC method proceeds as follows. A complete treatment is given in [KFB09]. Single photon two-electron ejection is treated as a two-step process. In the first step the primary electron, this is most likely the 2s one for the excited $\text{Li}^*(1s2s2p)$ -state, absorbs the photon and is ejected to

the continuum. The wavefunctions of the remaining bound electrons are projected onto discrete states of the Li^+ -ion, which are found by the configuration interaction method. Consequently, in the second step PDI continues via the inelastic scattering of the "free" primary electron on the Li^+ -target and is calculated as described above.

2.4.2 Time Dependent Close Coupling (TDCC)

The time-dependent close-coupling (TDCC) approach is applied to both, PDI (Chap. 6) and NSDI (Chap. 7). Here, the TDSE is solved directly through time propagation of the discretized wavefunction on a three dimensional grid. In the cases examined in this work two electrons are actively participating in the reaction. Consequently, the third (1s) electron is treated in a frozen core approximation. A thorough treatment is found in [AC12] and references therein. There, also the slight differences in the treatment of single and two-photon double ionization are explained.

In order to solve the TDSE, given by

$$i \frac{\partial}{\partial t} \psi(\vec{r}_1, \vec{r}_2, t) = H \psi(\vec{r}_1, \vec{r}_2, t) , \quad (2.23)$$

the initial-state wavefunction is expanded in a basis set of coupled spherical harmonics $|l_1 l_2 L\rangle$. The indices denote the individual electrons. The wavefunction is found by solving Eq. (2.23) in imaginary time [AC12]. The expansion in the spherical harmonics reads

$$\psi^S(\vec{r}_1, \vec{r}_2, t) = \sum_{l_1 l_2 L} \frac{P_{l_1 l_2}^{LS}(r_1, r_2, t)}{r_1 r_2} |l_1 l_2 L\rangle . \quad (2.24)$$

The $P_{l_1 l_2}^{LS}(r_1, r_2, t)$ are the expansion coefficients constituting the radial wavefunctions and the indices L and S denote the total angular momentum and spin of the system, indicating that each LS-configuration yields a separate set of TDCC-equations. This implies that the cross sections for singlet- and triplet two-electron continuum wavefunctions are calculated separately and have to be added according to their statistical weight afterwards. Insertion of Eq. (2.24) into Eq. (2.23) yields the set of coupled channel equations

$$\begin{aligned} i \frac{\partial}{\partial t} P_{l_1 l_2}^{LS}(r_1, r_2, t) &= T_{l_1 l_2}(r_1, r_2) P_{l_1 l_2}^{LS}(r_1, r_2, t) \\ &+ \sum_{l'_1 l'_2} V_{l_1 l_2, l'_1 l'_2}^L(r_1, r_2) P_{l'_1 l'_2}^{LS}(r_1, r_2, t) \\ &+ \sum_{l'_1 l'_2 L'} W_{l_1 l_2, l'_1 l'_2}^{LL'}(r_1, r_2, t) P_{l'_1 l'_2}^{L'S}(r_1, r_2, t) , \end{aligned} \quad (2.25)$$

where $T_{l_1 l_2}(r_1, r_2)$ is the atomic Hamiltonian in the frozen core approximation, $V_{l_1 l_2, l'_1 l'_2}^L(r_1, r_2)$ contains the inter-electron repulsion and $W_{l_1 l_2, l'_1 l'_2}^{LL'}$ is the radiation field operator. The coupling between the individual channels thereby is mediated by both, the inter-electron repulsion and the radiation field. To solve Eq. (2.25) the partial-wave wavepacket is propagated in time on a two-dimensional grid¹⁷ according to

$$P_{l'_1 l'_2}^{L'S}(r_1, r_2, t + \Delta t) = \exp(-iH\Delta t) \sum_{l_1 l_2 L} P_{l_1 l_2}^{LS}(r_1, r_2, t) . \quad (2.26)$$

The asymptotic final state at time $t = T$ is obtained by projection of the final-state radial wavefunctions onto fully antisymmetric products of Li^{2+} continuum orbitals. From these the cross section is obtained. In contrast to the CCC method, the TDCC approach inherently includes all possible ionization pathways.

2.5 Selection Rules for Double Electron Escape

Selection Rules are guide-lines for estimating the probability or even possibility of a transition to occur. In general, they are derived by determining the condition for which the transition matrix element vanishes. The most simple example is given by the photon induced transition of an electron from one atomic state to another (see for example [Dem04]), where in the case of linear polarization the relations

$$\Delta l = \pm 1 \text{ and } \Delta m = 0 \quad (2.27)$$

hold. Here, l denotes the orbital angular momentum and m its projection on the quantization axis. Following the same principle as above *Maulbetsch and Briggs* [MB95] derived selection rules for transitions to two electron continuum states, which have successfully been applied to explain experimental results (see for example [Zhu09; Kna05; YMR10]). Owing to the complexity of the problem, the selection rules are no longer dependent on a single quantum number but rely on the emission angles $\theta_{1,2}$ with respect to the quantization axis, the corresponding wavevectors $\vec{k}_{1,2}$ of the two electrons and the quantum numbers L, M, S and π of the two-electron wavefunction in the continuum. These denote the total angular momentum, its projection on the quantization axis, the total spin and the parity of the state, respectively.

Hereafter, the discussion focuses on the selection rules applicable to the final states encountered for two-photon double ionization of ground-state lithium (see also Chaps. 6 and 7). Taking into account, the $^2S^e$ symmetry of the $\text{Li}(1s^2 2s)$ ground-state and that according to

¹⁷The grid is created by the discretization of the radial part of the wavefunction.

Eq. (2.8) the dipole approximation is valid, the absorption of each photon follows the rules set by Eq. (2.27). For this reason the reachable two-electron continuum wavefunctions are given by the following relations:

$$\text{Li}(1s^2 2s \ ^2S^e) + \gamma \longrightarrow \text{Li}^{2+}(1s \ ^2S^e) + 2e^- \ ^1S^e; \ ^1D^e \quad (\text{singlet}) \quad (2.28)$$

$$\text{Li}(1s^2 2s \ ^2S^e) + \gamma \longrightarrow \text{Li}^{2+}(1s \ ^2S^e) + 2e^- \ ^3S^e; \ ^3D^e \quad (\text{triplet}), \quad (2.29)$$

with the assumption that the remaining electron is a pure spectator, i.e. does not get promoted to higher shells and hence carries no angular momentum¹⁸. From Eq. (2.27) it is also found that the projection of the total angular momentum is zero $M = 0$, since $\Delta m = 0$. Inspection of Table 2.1 yields the absence of any restriction to the two-electron continuum wavefunctions in the singlet case (Eq. (2.28)). It shall be emphasized that this does not result in an isotropic emission pattern of the electrons, as the selection rules do neither account for the nature of the projectile-target interaction nor for eventual electron-electron interaction during ionization. They are purely derived from the properties of the asymptotic wavefunction.

final state	Selection rule						
	C	D	E	F	G	H	I
$^1S^e$							
$^3S^e$	×	×	×	×	×		×
$^1D^e$							
$^3D^e$	×	×		×	×	×	×

Table 2.1: Selection rules applicable to the encountered final states in Chaps. 6 and 7. The \times -sign marks the validity of the selection rule for the respective final state.

Intuitively, this is understood from symmetry considerations. Since the electrons are in a singlet state, i.e. the spin-part of the wavefunction is *anti-symmetric* for particle exchange, the configuration part of the wavefunction is *symmetric*. Hence, the *Pauli exclusion principle* has no impact on the emission pattern of the electrons. In addition the final state has even parity. Thus, regarding double ionization, the emission of the first electron does not yield any *avored* or *unavored* geometries for the second electron.

In contrast, regarding the triplet continuum wavefunctions, various selection rules apply. The designation of the selection rules will be guided by the one used in the work of *Maulbetsch and Briggs* [MB95] for a better visualization selection rule **E**, **F** and **G** are illustrated in Fig. 2.10.

¹⁸Regarding the processes discussed in this work this assumption is valid, as the excitation of the remaining electron is energetically forbidden.

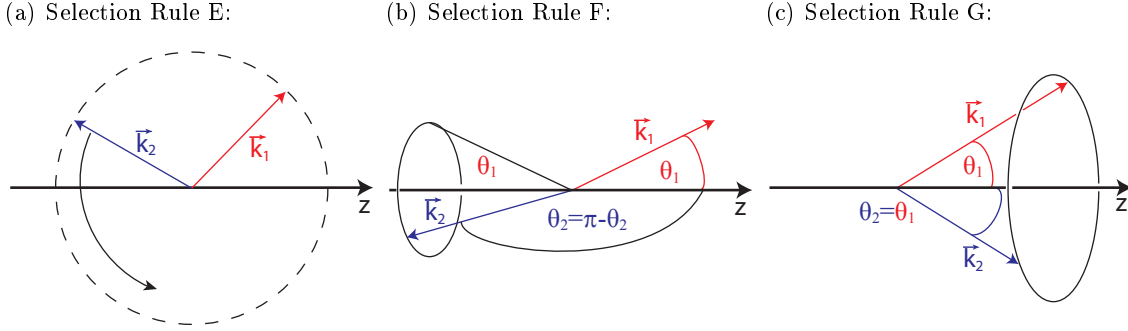


Figure 2.10: Illustration of the forbidden configurations according to selection rules E to G. In the experiment the quantization axis z is given by the laser polarization and the wavevectors $\vec{k}_{1,2}$ are replaced with the respective momenta. For selection rule E it is seen that emission of the first electron prevents the second electron to emerge with an equal energy and hence on a sphere around z . In (b) selection rule F is illustrated. Assuming again that the properties of electron 1 (e_1) are fixed, electron 2 (e_2) will not be emitted in the cone given by the condition $\theta_2 = \pi - \theta_1$. This includes the case where e_2 is emitted back-to-back to e_1 . Figure (c) is analogous to (b) for selection rule G.

- **Selection Rule C:** The cross section vanishes if the two electrons propagate back-to-back with equal energy. This applies in case $(\pi + S) = \text{odd}$. As an example for the $^3D^e$ -state this behavior is retrieved by the following line of argument. Given that, for a triplet state the spin-wave function is symmetric and the state has an even parity, the spatial wavefunction has to be anti-symmetric. In fact this is not possible for $\vec{k}_1 = -\vec{k}_2 \Rightarrow \vec{K} = 0$. Here, \vec{K} , denotes the total wavevector.
- **Selection Rule D:** For $\vec{k}_1 = \vec{k}_2$ the cross section vanishes in case of triplet states. Selection Rule D is a direct consequence of Pauli's exclusion principle. Put another way, back-to-back emission is forbidden for final triplet states.
- **Selection Rule E:** In case of the $^3S^e$ -state, the configuration is shown in Fig. 2.10(a), the cross section vanishes for equal energy sharing ($k_1 = k_2$).
- **Selection Rule F:** The two-electron wavefunction has a node for $k_1 = k_2$ and $\theta_1 = \theta_2 - \pi$ in case $(\pi + S = \text{odd})$ and $(\pi + L = \text{even})$. Assuming the properties of the first electron fixed, this results in a minimum of the cross section in a cone around the quantization axis with opening angle $\vartheta = \theta_1/2$ for the second electron as illustrated in Fig. 2.10(b). It includes the special case of back-to-back emission.
- **Selection Rule G:** Similar to rule F, triplet-states with $k_1 = k_2$, $\theta_1 = \theta_2$ and $M = 0$ do not contribute to the cross section. If again the properties of electron 1

are fixed then the second electron is not allowed to be emitted in a cone around the quantization axis containing \vec{k}_1 . The configuration suppressed by rule G is depicted in Fig. 2.10(c).

- **Selection Rule H and I:** These selection rules are included in selection rule F and G and cover configurations where $M \neq 0$. As these are not abundant in the experimental data they will not be discussed.

In conclusion the selection rules for transitions to two electron continuum states are far less restrictive than, e.g. the ones for single-photon single electron ejection from an atom. The wavefunction only vanishes for very specific configurations of \vec{k}_1 and \vec{k}_2 and only in case the final-state wavefunction fulfills certain conditions with respect to symmetry, i.e. its quantum numbers. Nevertheless, taking into account the continuous differentiability of the wavefunction it is inferred that the cross section, although being finite, is still small in the vicinity of the configurations defined in the selection rules. As a consequence the discussion in Chaps. 6 and 7 will not speak of allowed and forbidden configuration, but of favored and unfavored final-state geometries.

3 Basic Concepts in Cooling and Trapping of Neutral Atoms

The fact that photons carry momentum paves the way for the manipulation of atoms with tailored light fields. However, it was not until the advent of lasers, with their narrow bandwidths, in the 1960's, that cooling and trapping of atoms with light came into reach. The idea of cooling atomic gases by laser light was introduced by *Hänsch* and *Schawlow* in 1975 [HS75]. It took another ten years and several technical advances in the field of lasers before *Chu et al.* managed to confine slow atoms in a three-dimensional optical-molasses [Chu85], therefore trapping them in momentum space. Spatial confinement was achieved in 1986 by transferring the atoms from the molasses to an intense far red-detuned laser beam, where they are kept by the the force of the light field on the induced atomic dipole moment [Chu86]. One year later *Raab et al.* trapped neutral atoms by adding a magnetic gradient-field, which spatially modifies the light scattering-rate by the Zeeman effect [Raa87]. These techniques, now known under the terms far off resonance trap (FORT) and magneto-optical trap (MOT), have become work horses of atomic physics today. Their application ranges from precision spectroscopy, atomic clocks [Kas89], the preparation of ultra-cold atomic samples, namely BECs, first atomic [And95; Dav95] and later molecular [Don02; Joc03] to scattering experiments [Fle01; Bre03; Zhu09], where the temperatures in the order of μK allow for recoil-ion momentum spectroscopy with utmost resolution [Fle01; Sch11; WH00].

A MOT offers a relatively large number of atoms (typically 10^8) at very low temperatures. Depending on the species trapped the minimum temperature of the atoms range between $6\ \mu\text{K}$ and $150\ \mu\text{K}$. For the presented experimental setup temperatures on the order of $500\ \mu\text{K}$, corresponding to an initial momentum-spread well below the REMI recoil-ion momentum resolution of $\Delta p = 0.05\ \text{a.u.}$ [Sch11], are commonly achieved.

The following discussion will only consider a two-level atom in one dimension. Generalization, of the concepts introduced to three dimensions is feasible as the velocity of the atom (and the incident laser beams) can be separated into three orthogonal directions. Nevertheless, since lithium is not an ideal two-level atom adjustments to the cooling scheme derived below have to be made. These are considered in Sec. 5.2, where the actual exper-

imental setup is studied. For a textbook review on the topic the reader is revised to the work by *Metcalf and Van der Straten* [MS99] and *C.J. Foot* [Foo05], which provide the main reference for this chapter.

3.1 The Spontaneous Force

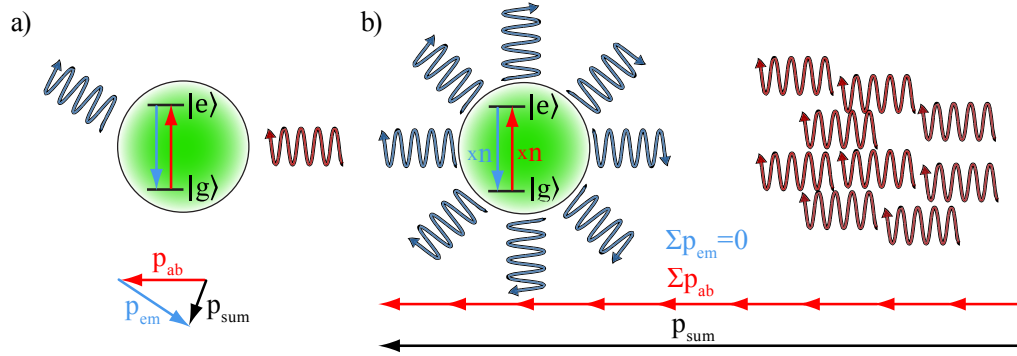


Figure 3.1: Principle of the manipulation of atomic trajectories with light. In (a) a single photon tuned to resonance between the ground $|g\rangle$ and excited state $|e\rangle$ is absorbed, transferring both, energy and momentum to the atomic system. Subsequently a photon of the same energy and momentum is emitted, leading to a momentum kick in arbitrary direction. In (b) this process is repeated over many optical cycles. Since spontaneous emission is isotropically distributed, the momenta of the emitted photons cancel while the momenta of the absorbed photons add up.

The discussion assumes a two-level system with ground-state $|g\rangle$ and excited-state $|e\rangle$ coupled by an optical dipole-transition of frequency ω_0 . If this is placed into a near-resonant light beam of frequency ω_l , with detuning $\delta = \omega_0 - \omega_l$, an atom in the ground state will eventually absorb a photon, acquiring an energy of $\hbar\omega_l$ and a momentum of $\hbar\vec{k}$ pointing in propagation direction of the light beam. In a subsequent step the excited state will decay emitting a photon of the same energy and momentum, but with a randomly distributed wavevector \vec{k}' . Averaged over many optical cycles the momenta of the emitted photons cancel, whereas the momentum transferred from the light field to the atom adds up. Ultimately, this leads to a force which depends solely on the number of absorbed photons per unit time, i.e. the scattering rate γ_{sc} and the photon momentum:

$$\vec{F}_{sp} = \hbar\vec{k} \cdot \gamma_{sc} . \quad (3.1)$$

In order to calculate its strength the scattering rate has to be determined. Considering a steady state situation the scattering rate will equal the rate of spontaneous emission γ .

Hence, it is given by

$$\gamma_{sc} = 1/\tau \cdot \rho_{ee} , \quad (3.2)$$

where the excited state population ρ_{ee} and the lifetime τ of the excited state have been introduced. While τ is defined by the natural linewidth Γ via the relation

$$\tau = \frac{1}{2\pi\Gamma} = \frac{1}{\gamma}, \quad (3.3)$$

here γ denotes the rate of spontaneous emission, the excited state population can be obtained in a semi-classical way. The derivation itself is not shown here. Solving the stationary optical Bloch equations yields [MS99]

$$\rho_{ee} = \frac{s}{2 \cdot (s + 1)} = \frac{s_0/2}{1 + s_0 + 2\delta/\gamma} , \quad (3.4)$$

with the saturation parameter s determined by

$$s = \frac{|\Omega|^2/2}{\delta^2 + \gamma^2/4} . \quad (3.5)$$

The *on-resonance saturation parameter* s_0 will be explained below. In Eq. (3.5) Ω refers to the *Rabi frequency*, i.e. the frequency with which the light field drives the atom between the ground and excited state. If the electric charge is denoted e and the field amplitude of the incident radiation E_0 , the Rabi frequency can be expressed as

$$\Omega = -\frac{e}{\hbar} E_0 \langle e | e \hat{r} | g \rangle . \quad (3.6)$$

Taking into account the relation $I = 1/2c\epsilon_0 E_0^2$ between the intensity and the amplitude of the light field, it is seen that Ω scales with \sqrt{I} . Thus, two regimes can be distinguished. First, if $\Omega \ll \gamma$ the system is governed by spontaneous emission. Second, when $\Omega \gg \gamma$ the population of the atomic states is coherently driven by the light field. Therefore the excited state population asymptotically approaches 50 % as the intensity rises. Higher populations are not possible in a steady state situation since absorption and stimulated emission are in equilibrium. To get an experimentally accessible quantity for the saturation of a transition, the so-called on-resonance saturation intensity I_{sat} is defined. It is given by

$$I_{sat} = \frac{\pi}{3} \frac{hc}{\lambda^3 \tau}, \quad (3.7)$$

with the wavelength of the transition λ . This corresponds to an excited state fraction of $\rho_{ee} = 0.25$ or likewise half of the maximum value of the spontaneous force $F_{sp} = \frac{1}{2} F_{sp}^{max}$.

Inserting these findings into Eq. (3.5) returns the on-resonance saturation parameter

$$s_0 = \frac{2|\Omega|^2}{\gamma^2} = \frac{I}{I_{sat}}. \quad (3.8)$$

The spontaneous force reads

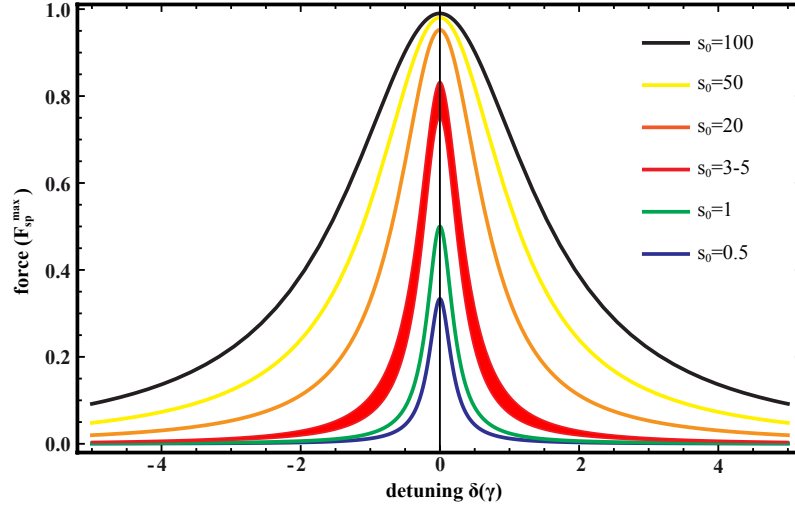


Figure 3.2: Spontaneous force in units of F_{sp}^{max} over detuning for several on-resonance saturation-parameters. The red-shaded area depicts the intensity regime the MOT laser beams and the Zeeman slower beam were usually operated. For high saturation parameters the linewidth begins to broaden since the transition is saturated on resonance.

$$\vec{F}_{sp} = \hbar \vec{k} \frac{\gamma s_0 / 2}{1 + s_0 + (2\delta/\gamma)^2}. \quad (3.9)$$

Figure 3.2 shows the spontaneous force in units of F_{sp}^{max} in dependence of the detuning for saturation parameters between 0.1 and 100. In the case of the D2-line of 7Li , with a natural linewidth of 5.87 MHz and a photon energy of 1.84 eV, the spontaneous force can amount to $F_{sp}^{max} = 1.8 \times 10^{-20}$ N, corresponding to an acceleration of 160,000 g.

With increasing saturation parameter the linewidth broadens due to saturation close to the resonance. As a result absorption in the wings of the absorption profiles becomes important. For the highest value depicted here ($s_0 = 100$), the force exerted on the atoms is still around half of its maximum for a detuning of already two linewidths. On the one hand this effect known under the term *powerbroadening* increases the minimum temperature achievable. On the other hand it is advantageous for applications such as the deceleration of an atomic beams, where it is crucial to keep the atom in resonance with a cooling laser for a considerably long time, as will be discussed in Sec. 3.3.

3.2 Doppler Cooling

So far only atoms at rest irradiated by a single laser beam have been considered. The 1D-model is now extended to the case where the atom is moving in the presence of identical, red-detuned and counter-propagating laser beams, i.e an one dimensional optical molasses. In the laboratory frame both laser beams are red-detuned by $\delta_0 = \omega_0 - \omega_l$ and the atom is moving towards one of them. Due to the Doppler-shift this changes in the rest frame of the atom. Here, the light moving anti-parallel to the atomic trajectory appears blue shifted by $\vec{k}\vec{v}$, while the parallel beam occurs to be further red-detuned by the same value. Thus, it is convenient to introduce an effective detuning

$$\delta_{\text{eff}} = \delta_0 - \vec{k}\vec{v} . \quad (3.10)$$

This results in an imbalance in the scattering rate of the incident light beams and thereby in a modulation of the force exerted on the atom. Insertion of the effective detuning in Eq. (3.9) yields

$$\vec{F}_{sp} = \hbar\vec{k} \frac{\gamma s_0/2}{1 + s_0 + (2(\delta_0 - \vec{k}\vec{v})\gamma)^2}, \quad (3.11)$$

for each of the laser beams. Given that the laser is red detuned the counter-propagating laser will be closer to resonance compared to the in-line one and the resultant force will oppose the direction of the atomic propagation. Hence, the atom is exposed to a frictional force, "cooling" it down until it drops out of resonance. Adding up the contributions of the individual beams, the force on the atom reads

$$\begin{aligned} F_{\text{Doppler}} &= F^+ + F^- \\ &= \sum_{\pm} \pm \hbar k \frac{\gamma s_0/2}{1 + s_0 + (2(\delta_0 \mp kv)\gamma)^2}, \end{aligned} \quad (3.12)$$

as illustrated in Fig. 3.3. There, the dashed lines show the contributions of the individual beams corresponding to F^+ and F^- , while the solid ones constitute their combined action. Evidently, the Doppler force (Eq. (3.12)) can be linearized in v for small velocities ($|v| \ll \gamma/k$). Neglecting I/I_{sat} in the denominator of the derivation leads to

$$\begin{aligned} F_{\text{Doppler}} &\approx \hbar k \frac{\partial F_{\text{Doppler}}}{\partial v} \cdot v \\ &= -\hbar k^2 \frac{8s_0\delta_0}{\gamma(1 + s_0 + 4(\delta_0/\gamma)^2)^2} \cdot v \\ &= -\alpha v , \end{aligned} \quad (3.13)$$

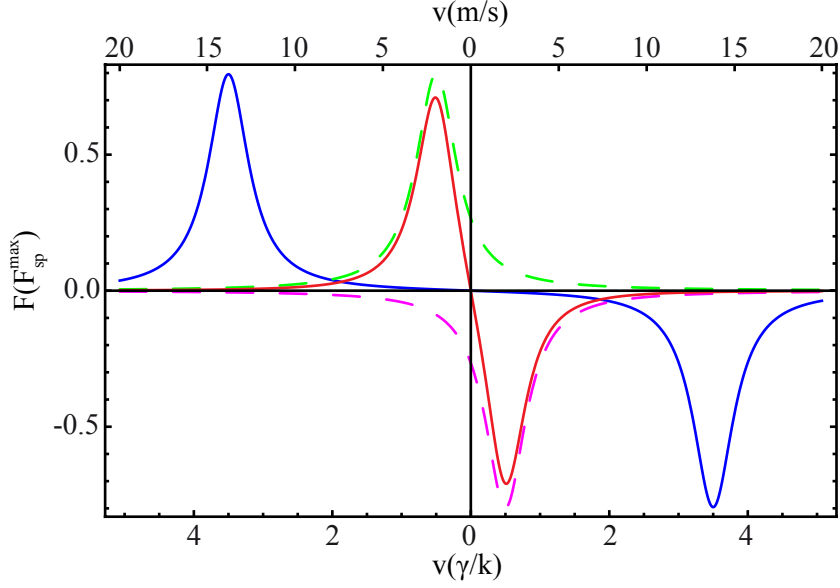


Figure 3.3: Force exerted on an atom in a red-detuned light field of counter-propagating beams in dependence of the atoms velocity. The detuning is chosen to be $\delta_{red} = \gamma/2$ for the red solid line and $\delta_{blue} = 3.5 \gamma$ for the solid blue line. The dashed lines represent the force created by the individual laser beams for δ_{red} . While the δ_{red} marks the detuning for minimal temperature, δ_{blue} is the commonly chosen value for our experimental setup. The upper x-axis converts the general units $[\gamma/k]$ to the actual values for atomic lithium.

revealing the frictional character of Doppler cooling. Apparently, atoms in an optical molasses move like a ball in a viscous liquid. Although they are confined in momentum space, there is no position dependent force trapping them configuration space.

It should be emphasized that this finding does not hold for very small velocities, i.e. when the scattering rates of the opposing beams are in equilibrium. Here, the stochastic and time-averaged nature of the *spontaneous force* manifests. As the fluctuations caused by the inherent randomness of spontaneous emission do not cancel on small time scales, the atom undergoes a random walk in momentum space with step size $\Delta p = \hbar k$ and rate γ . This limits the minimum temperature accessible in an optical molasses, to the so-called Doppler-limit, to [Foo05]

$$T_D = \frac{\hbar \Gamma}{2k_B} \quad (3.14)$$

for an optimum detuning of $\delta = \gamma/2$.

The discussion above is strictly only valid for intensities below saturation since I/I_{sat} has been neglected in the derivation of Eq. (3.13). For higher intensities saturation effects have to be taken into account, especially as the light fields of several laser beams add up

in a three-dimensional optical-molasses. In contrast to spontaneous emission, stimulated emission does not saturate for high intensities and thus, dominates the system for $I \gg I_{\text{sat}}$.

3.3 Position Dependent Forces

Up until now, the discussion was focused on velocity dependent forces slowing down the atomic motion. Spatial confinement and therefore trapping, can however only originate from potentials which depend on the actual position of the particle. A very common technique to introduce such potentials in laser cooling and trapping is the use of magnetic fields, modulating the scattering rate by variation of the transition frequency ω_0 through the Zeeman-effect [HCP08]. Hence, a condition precedent for this kind of scheme is that the Zeeman-shifts of ground $|g\rangle$ and excited state $|e\rangle$ evolve differently with magnetic field strength. Then the shifts in the transition frequencies imply a new effective detuning. The

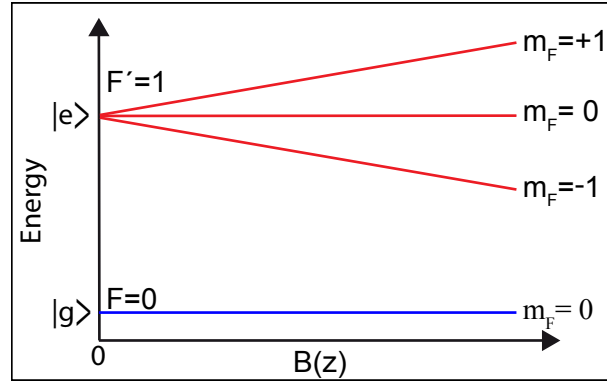


Figure 3.4: Zeeman-shift of a simplified two-level atom. The energy of the ground state with no angular momentum does not change with rising field strength, whereas the excited state sublevels, created by the precession of its total angular momentum around the magnetic field direction, split up. Hence, the frequency of the $|g\rangle - |e, m_{F'} = \pm 1\rangle$ transitions change with field strength.

expression in Eq. (3.10) changes to

$$\delta_{\text{eff}}^{\text{mag}} = \delta_0 - \vec{k}\vec{v} - \Delta\vec{\mu}\vec{B}/\hbar. \quad (3.15)$$

The term $\Delta\vec{\mu}\vec{B}$ stems from the position dependent energy shifts of ground and excited state of the transition under consideration. It reads

$$\Delta E = (\vec{\mu}^g - \vec{\mu}^e)\vec{B}/\hbar = \Delta\vec{\mu}\vec{B}/\hbar. \quad (3.16)$$

with the magnetic momenta $\vec{\mu}^g$ and $\vec{\mu}^e$ of the corresponding states. For weak magnetic fields, the magnetic momenta can be expressed as $\vec{\mu} = -mg\mu_B$, where m denotes the projection of the angular momentum on the quantization axis, g the Lande g-Factor and μ_B the Bohr magneton. Inserting these results into Eq. (3.16) yields

$$\Delta E = (m^e g^e - m^g g^g) \mu_B B. \quad (3.17)$$

Figure 3.4 shows the progression of the ground and excited state for a simplified two-level atom, assuming the ground state $|g\rangle$ has a total angular momentum of $F = 0$ and the angular momentum of the excited state $|e\rangle$ amounts to $F' = 1$. The respective projections of the magnetic sublevels on the quantization axis, $|e, m_F^e = 0, \pm 1\rangle$, degenerate in the absence of external fields, split up and evolve according to the energy shift derived in Eq. (3.17). Hence, the frequencies of the $|g\rangle - |e, m_F^e = \pm 1\rangle$ -transition varies with position and including the Doppler shift, velocity allowing for the manipulation of the atomic motion and position by the combined action of light and magnetic fields.

A very successful application of the above findings is the slowing of large fractions of thermal atomic beams to the same final velocity, dubbed Zeeman-slower and first experimentally realized by *Phillips* and *Metcalf* in 1982 [PM82]. In order to decelerate a single atom significantly its Doppler-shift has to be compensated by the Zeeman-effect over an extensive part of its trajectory. Thus, the condition

$$\delta_{\text{eff}}^{\text{mag}} = \delta_0 - \vec{k}\vec{v} - \Delta\vec{\mu}\vec{B}/\hbar \geq 0 \quad (3.18)$$

has to be fulfilled at all points of the slowing distance. Otherwise the transition drops out of resonance. As a result the atom progresses with constant velocity and is lost from the cooling process. From Eq. (3.9) the maximum acceleration an atom is exposed to is derived to

$$a_{\text{slower}} = \eta \frac{\hbar k}{m} \frac{\gamma}{2}, \quad (3.19)$$

where the safety factor η accounts for impurities in the magnetic field and intensities below saturation. In a good approximation the deceleration is constant over the slower distance and Eq. (3.19) is valid. Consequently, the velocity profile of an atom coming to a standstill at the end of the slower reads

$$v(z) = v_0 \sqrt{1 - \frac{z}{z_0}}, \quad (3.20)$$

where $z_0 = v_0^2/(2 \cdot a_{\text{slower}})$ denotes the stopping distance. Inserting this expression into the resonance condition Eq. (3.18) leads to the spatial profile of the magnetic field, required

for realizing a Zeeman-slower:

$$B(z) = B_0 \sqrt{1 - \frac{z}{z_0}} + B_{\text{bias}} \text{ with} \quad (3.21)$$

$$B_0 = \frac{\hbar}{\Delta\mu} kv_0,$$

displayed in Fig. 3.5. Considering a bias field on the order of $\mu_B B_{\text{bias}} \approx \hbar\omega_0 - \hbar\omega_l$ the atoms come to halt at the end of the slower. The reason B_{bias} is introduced originates from the necessity to extract the atoms out of the slower. Thus, it accounts for the desired final velocity of the atoms. Nevertheless, it should be noted that this is only an approximation.

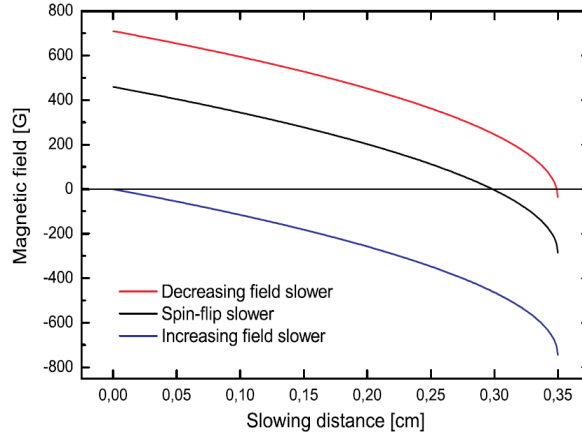


Figure 3.5: Possible magnetic field configurations for the realization of a Zeeman-slower. The field geometries for a decreasing-field (red), spin-flip (black) and increasing-field (blue) Zeeman-slower are displayed.

3.3.1 Spatial confinement

Combining the results above it is straightforward to deduce the working principle of a magneto-optical trap, illustrated in Fig. 3.6. The atom is now placed in a gradient magnetic field, given in first order approximation by $B(z) = B_0 z$, which switches polarity at $z = 0$. It is irradiated by a pair of counter-propagating and red-detuned laser beams with opposite helicity¹. Since the m_F sublevels of the excited state split up in the magnetic field the $\Delta m = -1$ transition energy is lowered for positive positions while the energy necessary to drive the $\Delta m = +1$ transition rises. Taking into account that σ^- light

¹The polarization of the light is actually the same.

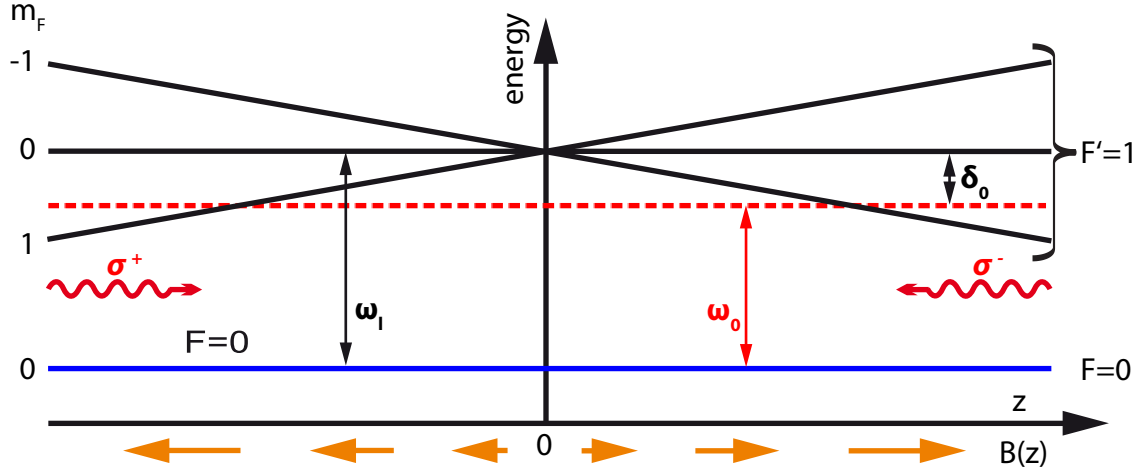


Figure 3.6: Schematic one-dimensional view of the working principle of a magneto-optical trap. A position dependent force is introduced by a magnetic gradient field with switching polarity in combination with a pair of counter-propagating, red-detuned laser beams of opposite helicity. If the direction of the magnetic field and the polarization of the incident light is chosen properly, the beam driving the atom back to $z = 0$ will always be more resonant compared to the counter-propagating one. Hence, an atom is pushed back to the zero crossing of the magnetic field, i.e. the trap center.

induces $\Delta m = -1$ transitions by definition, atoms propagating in or towards positive z -values will predominantly absorb σ^- light incident from the right hand side of Fig. 3.6. Hence, it is driven back towards the zero crossing of the magnetic field at $z = 0$. For negative values of z the considerations are analogous and the atoms are again pushed back to the trap center.

To gain a more quantitative understanding of the process, the effective detuning derived in Eq. (3.15) is substituted into the spontaneous force for a pair of counter-propagating laser-beams from Eq. (3.12). Inclusion of the position dependent part of scattering yields

$$F = \hbar k^2 \frac{8s_0\delta}{\gamma(1+s_0+4(\delta/\gamma)^2)^2} \cdot v + \hbar k \frac{\Delta\mu B'_z}{\hbar} \frac{8s_0\delta}{\gamma(1+s_0+4(\delta/\gamma)^2)^2} \cdot z \quad (3.22)$$

$$\begin{aligned} |(\Delta\mu B'_z/\hbar)z| &\ll \gamma \\ &\approx -\alpha v - \kappa z . \end{aligned} \quad (3.23)$$

Inspection of Eq. (3.23), showing the linearization of the force for small v and z , indicates a damped harmonic oscillator with frequency $\omega = \sqrt{\kappa/m}$ and damping rate $\beta = \alpha/(2m)$. Insertion of values typical for the operation of lithium MOTs, leads to the conclusion that the trapped atoms perform a strongly overdamped motion around the zero crossing of the magnetic field.

Generalization of the MOT concept to three dimensions is not as direct as it might appear. Indeed the force on the atoms is additive, i.e. can be understood in terms of a superposition of the forces from the individual laser beams. However, the dynamics of a 3D MOT are quite complicated, considering the interplay of six laser beams, a spatially varying magnetic field and effects arising from the density of atoms in the trap. Examining these effects goes beyond the scope of this work. In particular, since the concept of magneto-optical traps can already be understood in a good approximation with the ideas introduced so far. For a discussion of effects arising in a real, i.e. three-dimensional MOT, the reader is advised to the work of *Townsend et al.* [Tow95], which surveys the topic.

4 Free Electron Lasers

In free-electron laser sources light is generated by forcing electrons onto sinusoidal trajectories. Thus, Bremsstrahlung is emitted. The concept of *Stimulated Emission of Bremsstrahlung in a Periodic Magnetic Field* as a source of partially coherent radiation was introduced as early as 1971, in theory by *Madey* [Mad71] and only five years later also experimentally by him and coworkers [Eli76]. Although, the first free electron laser (FEL), was operated at a wavelength of $12.6\ \mu\text{m}$, Madey was already pointing out that this technique could, in principle, be used to generate coherent light in the VUV and XUV regime. However, FELs should play only a negligible role in many years to come,

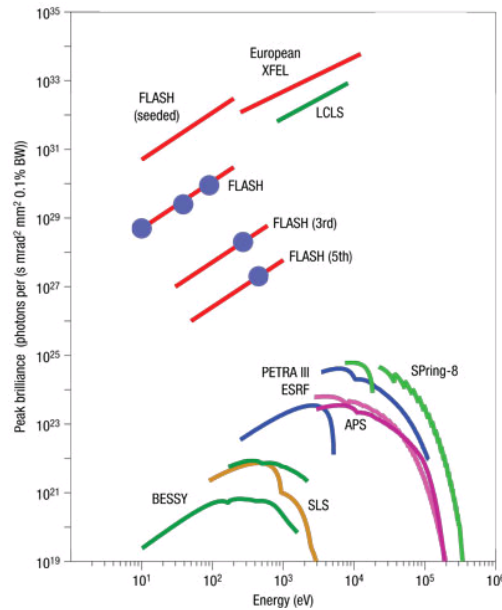


Figure 4.1: Peak brilliance achieved for several state-of-the-art third and fourth generation light sources, i.e., synchrotrons and FELs, respectively. (Source: [Ack07])

being employed mainly in the infrared and microwave regime, until their potential value as VUV/XUV lasers became technically accessible [Pel88; PS03]. Finally, the pioneering facility of FLASH (free-electron laser in Hamburg) [Sch10a; Fel10], delivering coherent

radiation pulses of unprecedented brilliance and intensity (see Fig. 4.1) down to a wavelength of about 4 nm, began to fully exploit the power of this concept. The successful user-operation of FLASH sparked tremendous interest, both experimental and theoretical, not only in atomic physics but also in other fields like chemistry and biology. As a result, several FELs have been build or are under construction worldwide, opening up ever new wavelength regimes for intense, coherent radiation. Among them are the *LINAC Coherent Light Source* (LCLS) in Stanford [Emm10], providing photon energies of up to 15 keV, the *Spring-8 compact SASE test facility* (SCSS) and *Spring-8 Angstrom Compact Free Electron Laser* (SACLA) in Japan [Shi08] and the so-called X-FEL in Hamburg (≈ 200 eV to 25 keV), which will become operational in 2015.

The advent of these light sources paved the way for a multitude of experiments. For once it allowed to study new regimes in interaction of intense light with matter [Rud10]. Here, one of the most prominent examples is the non-sequential two-photon double ionization of Helium [Kur10], which sparked overwhelming theoretical interest [BL91; NL01; Fei08; PBM06; Fou06] even before becoming accessible in experiment. The ever shorter pulse lengths achievable, down to 7 fs at LCLS, with the promising perspective of reaching the sub-fs¹ regime, will push time-resolved experiments to new limits with respect to temporal and spatial resolution. In contrast to setups, utilizing high harmonic generation (HHG) as source for coherent radiation, FELs offer higher photon fluxes and therefore allow XUV-pump XUV-probe experiments. Thus, the dream of imaging chemical reactions, i.e., observe the nuclear motion during the time a chemical bond is formed or broken, comes into reach [Jia10b]. In structural biology, the unprecedented peak brilliance of the radiation might eventually enable to image bio molecules with atomic scale resolution in their natural form. In particular, as methods like single-shot diffraction imaging [Lin05] and electron holography [Kra10] are developed. To illustrate this Fig. 4.2 shows a state-of-the-art example for the reconstruction of test structures from single-shot diffraction imaging [Cha06].

In the following this chapter will focus on the physics facilitating the laser-like emission of radiation from a FEL beginning with the interaction of the electron beam with the light field up to the SASE process (*Self Amplified Spontaneous Emission of Radiation*). A brief overview on one-dimensional FEL-theory will be given. Here, the main properties of the emitted radiation will be introduced and their potential impact on the experimental results in Chaps. 6 and 7 will be discussed. The considerations will largely follow the findings summarized in [SDR08].

¹In case of the HHG sources for VUV radiation even shorter pulses are commonly achieved

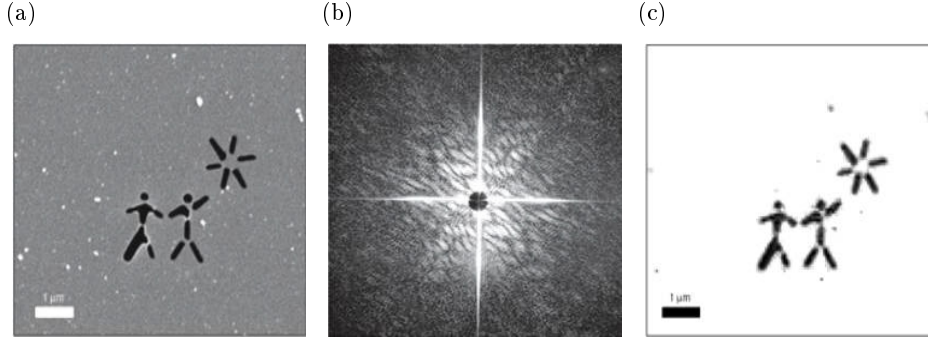


Figure 4.2: State-of-the-art imaging example demonstrating the feasibility of reconstructing structures illuminated with FLASH radiation from a single-shot diffraction image [Cha06]. In (a) a SEM, scanning electron microscope, picture of the test structure is shown. (b) displays the diffraction image obtained in a 25 fs FEL pulse, with an intensity of 4×10^{14} W/cm² and (c) the reconstruction of the test structure from (b).

4.1 Working principle

FLASH consists of three main components, a schematic is shown in Fig. 4.3. The first two being a pulsed electron source and an array of accelerators interlaced with bunch compressors. The former is realized by irradiating a photo cathode with a femtosecond laser source, producing an ultra-short electron bunch. To maintain the small phase-space volume achieved in this manner, the electrons, emerging from the source, are rapidly accelerated towards relativistic energies by a super-conducting LINAC. In the gaps between the accelerator modules, so-called bunch compressors are employed to shape the electron package. Both, the accelerators and the compressors are tuned such that the phase-space volume occupied by the electrons is minimized. This is crucial for the performance of an FEL as will be discussed below². In the last step the beam ejected from the accelerator array enters a linear array of dipole magnets (undulator). Their alternating polarity forces the electrons onto sinusoidal trajectories, leading to the emission of synchrotron radiation. Due to the electrons relativistic velocity the emitted radiation is almost entirely pointed in forward direction. The radiation emerging from relativistic charged particles in a magnetic field, is restricted to a cone with an apex angle of $\alpha = 1/\gamma$ with respect to the particles instantaneous velocity [Kin77]. Here, $\gamma = 1/\sqrt{1 - (v/c)^2}$ denotes the relativistic Lorentz factor. In fact the transverse velocity in an undulator is much smaller than the longitudinal one ($v_{tr} \ll v_{long}$). Therefore, the electronic motion can be assumed as purely longitudinal regarding the emission angle of photons.

²Note, that the indispensable demands on the electron-bunch properties, ultimately prevent third generation light sources, i.e., synchrotrons, from achieving the peak brilliance and coherence of FELs.

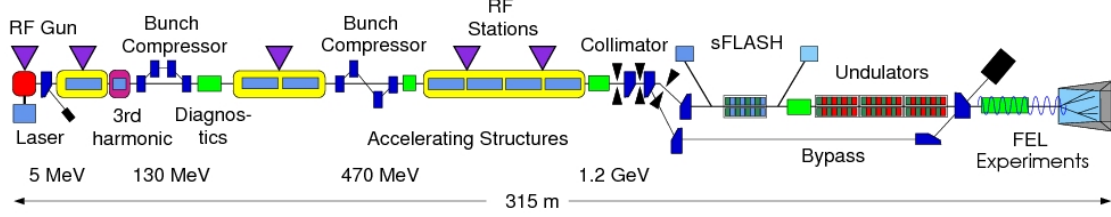


Figure 4.3: Schematic overview of the FLASH facility (taken from [Sch10b]). Starting from the left an electron-bunch is created in an rf-gun. After it has passed a series of bunch compressors and linear accelerators, the electron bunch is shaped in a collimator before it enters the undulators, thereby generating the VUV light.

While the demands on the electron beam quality, i.e., the phase-space volume occupied are crucial for FEL operation in the first place, most of the properties of FEL radiation originate from the interaction of the electron bunch with the magnetic and light field in the undulator. It is, hence, mandatory to closely investigate these.

4.1.1 Undulator Radiation

The *lasing* wavelength of free electron lasers or undulators is given by [Ack07]

$$\lambda_l = \frac{\lambda_u}{2\gamma^2} \left(1 + \frac{K^2}{2} \right). \quad (4.1)$$

Here, λ_u denotes the period of the undulator, i.e., the distance between the alternating dipole magnets (see Fig. 4.4), and K , the dimensionless undulator parameter. Given by

$$K = \frac{eB_0^u \lambda_u}{2\pi mc}, \quad (4.2)$$

it depends on the amplitude of the magnetic field in the undulator B_0^u . Assuming fixed values for the period λ_u and magnetic field B_0^u , the wavelength of the emitted radiation is solely defined by the energy of the incident electrons³. Thus, the photon energy is continuously tunable over a wide range⁴ of wavelengths, by changing the accelerator parameters, even though the undulator is fixed.

The considerations leading to Eq. (4.1) are easily conceived. If z defines the direction of propagation and the excursion, due to the magnetic field, points in x -direction the following

³Many VUV/XUV undulators are fixed. The LCLS undulator is an exception as it allows to shift the dipole magnets laterally [Sch10b]. FLASH II will be the first facility, which is able to change the period λ_u of the undulator.

⁴Currently FLASH is capable of providing photon energies between 26-300 eV (4.12-47 nm) [web13].

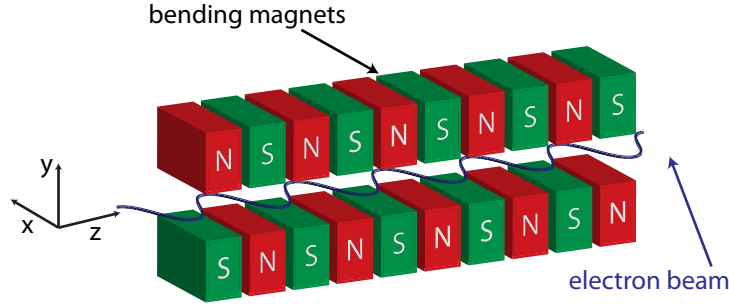


Figure 4.4: Schematic view on the electron trajectories inside the undulator with the coordinate system used throughout this chapter to describe the motion of the electrons.

statements can be made. To first-order approximation the electrons move with an average velocity $\overline{v_z} = \beta c$ in z -direction. Here, the longitudinal velocity oscillations caused by the sinusoidal excursion is neglected. Transforming into an inertial system moving alongside the electrons with $\overline{v_z}$, the electrons undergo harmonic oscillations in x with the Lorentz contracted undulator period $\lambda' = \lambda_u/\gamma$ and are radiating with the frequency $\nu' = c/\lambda'$. Through the relativistic Doppler shift the radiation frequency observed in the laboratory frame is boosted according to $\nu = \nu'/(\gamma\sqrt{1-\beta^2})$:

$$\nu = \frac{2\gamma^2 c}{\lambda_u} \Leftrightarrow \lambda = \frac{\lambda_u}{2\gamma^2} . \quad (4.3)$$

Taking into account the modulation of v_z caused by the harmonic oscillation in x an additional factor of $(1 + K^2/2)$ appears on the right-hand side of the wavelength relation in Eq. (4.3). For this reason, the emitted radiation will be red-shifted with respect to the first-order approximation derived above.

Interplay of the light field and the electron beam

Besides, the interaction of the electron beam with the undulators magnetic field, there is a second process which has to be taken into consideration in order to understand the properties of radiation emitted from an FEL. It is given by the interaction of the electrons with the light field. The emergence of photons in the first place will be neglected for now, as it is treated in Sec. 4.1.2. Lets assume a seeded FEL, i.e., light of the resonance wavelength according to Eq. (4.1) produced otherwise is brought to overlap with the electron beam. The condition for a more intense light beam originating from the undulator then injected is a net energy transfer from the electron bunch to the light field. Due to the small relative velocity of the electrons and the photons ($\beta \approx 1$), the electron bunch will interact with the

light field over the whole length of the undulator. For FLASH, for example, the undulator stretches to a length of 27 m with approximately 1000 bending magnets ($\lambda_u = 27\text{mm}$). Hence, achieving a reasonable gain requires the energy transfer to be continuous. All "out-of-phase mechanisms", where energy is transferred back and forth, would simply average out.

The light field is described in the form

$$E_x(z, t) = E_0 \cos(k_l z - \omega_l t + \psi_0) , \quad (4.4)$$

resembling a plain electromagnetic wave. The index l denotes the affiliation with the light field and ψ_0 is an arbitrary initial phase. Although in reality, both, the electron beam and laser light would be pulsed, this does not alter the resultant findings.

The energy of an electron in the undulator is $W = \gamma m_e c^2$. In order for the light field to gain energy, the electron has to loose it and hence the time derivative of W , i.e., the energy transfer, has to fulfill

$$\frac{dW}{dt} = \vec{v} \cdot \vec{F} = -ev_x(t)E_x(t) < 0 . \quad (4.5)$$

In other words the electric field of the laser and the velocity of the electron have to point *always* in the same direction to steadily increase the energy in the light field. Electrons, being massive particles and moreover traveling on a sinusoidal trajectory, are slower than light. Therefore, Eq. (4.5) can only be satisfied for certain wavelengths. Considering that the time delay between the light wave and the electron beam, for a half period of the electronic motion amounts to

$$\Delta t = t_e - t_l = \left[\frac{1}{\vec{v}_y} - \frac{1}{c} \right] \frac{\lambda_u}{2} , \quad (4.6)$$

the condition for sustained energy transfer is found to be a proper slippage of the light waves phase over the course of half an electron oscillation. The key is that the light wave has to spatially advance by half a wavelength period λ_l with respect to the phase of the electronic motion over a distance of λ_u . This relation expresses mathematically as follows

$$c\Delta t = (2m + 1)\lambda_l/2 \text{ with } m \in \mathbb{N}_0 \quad (4.7)$$

and is illustrated in Fig. 4.5. It displays the interaction of selected electrons with a Gaussian laser pulse for three points in time over a half period of the electrons transversal oscillation for the case that λ_l satisfies Eq. (4.7). At the time t_2 when the electron reaches its turning point the light pulse has traveled $\lambda_l/4$ further and thus changes its polarity at the same instant $v_x(t)$ reverses. For that reason the inequality $dW/dt < 0$ holds for all times and

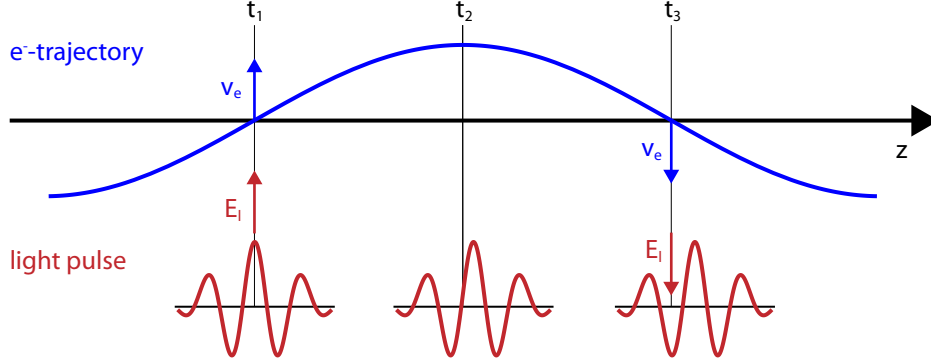


Figure 4.5: Illustration of the energy transfer from the electrons to the light-wave for electrons fulfilling the condition from Eq. (4.8). Since the lightwave and the electrons have the appropriate relative velocity, the phase of the lightwave slips such that its electric field is always pointing in the same direction as the transversal velocity of the electrons. For visualization of the phase slippage a light pulse is displayed instead of a continuous wave.

the energy in the light field rises continuously. Note, that Eq. (4.7) shows, that not only light of wavelength λ_l is amplified but also odd harmonics of this fundamental wavelength. However, the net amplification will be attenuated by the fact that even the third harmonic reverses its polarity thrice during a half period of the electronic motion. In general, the intensity of the harmonics will be in the per mille range for the third harmonic and fall off steeply for higher harmonics [Düs06].

Insertion of Eq. (4.7) in Eq. (4.6) yields the resonance condition [SDR08]

$$\lambda_l = \frac{\lambda_u}{2\gamma^2} \left(1 + \frac{K^2}{2} \right). \quad (4.8)$$

This is exactly the same relation as in Eq. (4.1) and thus constitutes a very important finding. The light spontaneously emitted by the electron beam in the undulator fulfills the condition for sustained energy transfer derived in Eq. (4.8). This paves the way for *self-seeded* FELs discussed in the next section.

Given the longitudinal extension of the electron bunch L_B (see Fig. 4.6), for which the relation $L_B \gg \lambda_l$ holds, only for a selected few of the electrons inside the bunch the initial phases of both light wave and electron trajectory will match. Sustained energy transfer, as described above, is achieved for an initial phase difference $\psi_0 = 0$ (see Eq. (4.4)). In order to gain insight on the effect of an arbitrary initial phase Eq. (4.4) and v_z are substituted

into Eq. (4.5) which leads to [SDR08]

$$\frac{dW}{dt} = -\frac{ecKE_0}{2\gamma} \cos \psi - \frac{ecKE_0}{2\gamma} \cos \chi, \quad \text{with} \quad (4.9)$$

$$\psi = (k_l + k_u)v_z \cdot t - \omega_l t + \psi_0 \quad \text{and} \quad (4.10)$$

$$\chi = (k_l - k_u)v_z \cdot t - \omega_l t + \psi_0 .$$

The second term in Eq. (4.9) does not contribute to the energy transfer as it averages out in half an undulator period. Equation 4.10 shows the so-called *ponderomotive phase*, where ψ_0 denotes the initial phase when the electron beam enters the undulator. For $(k_l + k_u)v_z = \omega_l t$, the ponderomotive phase is constant, i.e., Eq. (4.8) is valid and the effects of the initial phase can be investigated. The case of $\psi_0 = 0$ has already been discussed in Fig. 4.5. Figure 4.6 illustrates the two extreme cases of energy transfer for $|\psi_0| = \pi/2$ and $|\psi_0| = \pi$. Inspection of Eq. (4.9) yields, that for $|\psi_0| < \pi/2$ the electrons

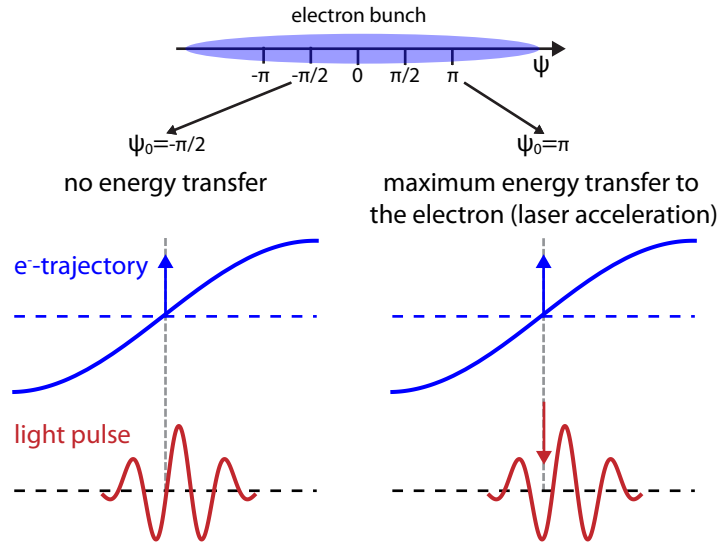


Figure 4.6: Illustration of the energy transfer between the electron bunch and the light field for $|\psi_0| = \pi/2$ and $|\psi_0| = \pi$, respectively. On top the bunch size relative to the initial phase ψ_0 is schematically shown. For $|\psi_0| = \pi/2$ there is no energy transfer at all, while for $|\psi_0| = \pi$ energy is constantly shifted from the light field to the electrons, as $dW/dt > 0$ at all points.

lose energy to the light field, while electrons with an initial phase of $\pi/2 < |\psi_0| < \pi$ gain energy from the light field. Taking into consideration that the particles deflection scales with $1/\gamma$, it can be deduced that the latter will be accelerated and the former will be slowed down. Ultimately, this results in a gathering of electrons at a phase of $\psi = 0$,

or likewise in a tremendous increase in the light fields amplitude.

4.1.2 Self-Amplified Spontaneous Emission

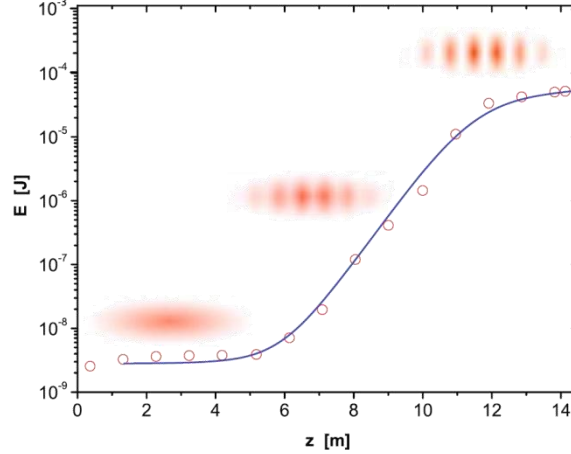


Figure 4.7: Intensity of the light emitted by FLASH plotted over undulator length, with an illustration of the density distribution in the electron bunch. In the beginning of the undulator the force exerted by the spontaneously emitted photons, on the electrons, is not strong enough to compress them at points where $\psi = 0$ holds. Starting from a distance of 6 m the electrons are pushed towards the resonant phase. Here, the energy in the light field increases exponentially with undulator length until the space charge repulsion of the electrons prevents any further compression and the energy saturates. Graph taken from [Ayv02].

Owed to the lack of suitable seed sources and optical resonators *Self-Amplified Spontaneous Emission* of radiation, or short SASE, is the underlying principle of almost all free-electron lasers in the deep VUV and XUV regime. Sparked by spontaneous emission in the beginning of the undulator, the interplay of the processes described above yields an enormous gain in just a single pass of the undulator ($\approx 10^6$). The light emitted by these machines is unsurpassed in its brilliance (see Fig. 4.1) and intensity. It constitutes the only possibility to produce partially coherent light in the XUV⁵.

Above, it was shown that the light-electron interaction leads to the gathering of electrons at fixed values of the ponderomotive phase where the energy transfer to the light wave is at its maximum. Hence, the intensity of the light field increases and the electron density at values of $\psi = 0$ rises, as shown in Fig. 4.7. Eventually, this cycle continues until the mutual

⁵Third-generation light sources, namely synchrotrons equipped with undulators, can also produce wavelengths in the same regimes as FELs but lack the high peak brilliance and the coherence of the radiation. HHG sources generate fully-coherent light, but are not able to reach the short wavelengths of FELs, like LCLS.

repulsion between the electrons circumvents any further compression. By then the initially flat, i.e., homogeneous, distribution of electrons over the bunch length is converted to a micro-bunched structure with density maxima at distances of λ_u . Ultimately, the longitudinal extension of the individual microbunches is significantly less than half of the lights wavelength, resulting in coherent radiation from the individual bunches. As the intensity of coherently radiating particles scales as

$$I_N^{\text{coh}} = N^2 I_1 \quad (4.11)$$

compared to $I_N^{\text{incoh}} = N I_1$ in the incoherent case, the intensity is boosted even more. In particular, taking into account that not only electrons inside a single microbunch are coherent emitters. In fact the radiation emerging from different microbunches is inherently coherent, as they are spaced by a distance of λ_u [Sch10b].

Figure 4.7 illustrates the progression of the energy in the light wave over the distance traveled in the undulator. Shortly after entering the undulator, where spontaneous emission of synchrotron radiation takes place, the light wave starts to affect the electrons in the bunch as described above. This so-called *linear regime* is characterized by exponential growth in intensity and energy output, as well as, high fluctuations in the pulse energy distributions. Once further microbunching is inhibited by space charge the saturated regime is reached, leading to a slower (not exponential) growth of the pulse energy with less fluctuations. Moreover, the statistical properties of the emitted radiation like temporal and spatial coherence change drastically and the pulse exhibits a Gaussian energy distribution (see Fig. 4.8).

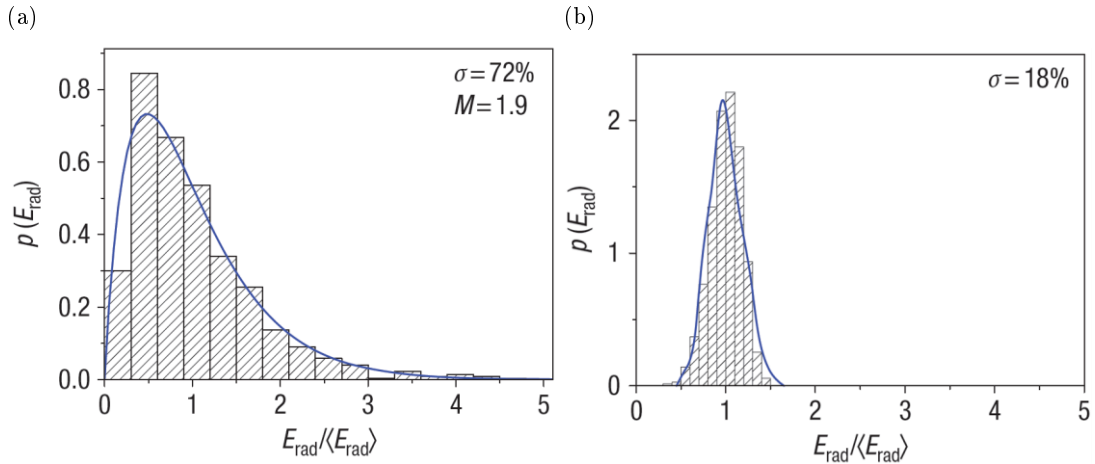


Figure 4.8: Energy distributions of the emitted radiation in the linear regime (a) and the saturated regime (b). Taken from [Ack07].

An important quantity to specify the transition from the linear to the saturated regime is the so-called *gain length* L_g , constituting the distance for which the intensity of the radiation increases by a factor of e . It depends on several FEL parameters, the most crucial one being the energy distribution inside the electron bunch, e.g. the energy spread. As a general rule, saturation of the electron density and thus the intensity of the radiation, takes place at a distance of around 20 times the gain length inside the undulator [HK07]. To summarize the discussion above it is stated, that FEL radiation, i.e., SASE, in the VUV and XUV domain is *always* initiated by random action. Embodied by either spontaneous emission of radiation from accelerated charged particles or inhomogeneities in the electron-bunch density distribution [BPN84], it is the stochastic nature of these processes which yields important consequences on the properties of the emitted radiation. Understanding these provides a valuable handle, when experimental findings are compared to theoretical models.

4.2 Properties of FEL radiation

The stochastic nature of SASE radiation gives rise to intrinsic fluctuations in its energy, wavelength and temporal distribution. Therefore it is often referred to as *chaotic light* [SDR08]. While this still allows for the determination of statistical averages, the single shot properties are broadly defined at best. Figure 4.9 illustrates the shot-averaged temporal distribution of FLASH-pulses modeled with the partial coherences method. Besides a number of individual sing-shot distributions (dashed-lines) the average temporal distribution (solid line) is plotted. Although the exact shape of a single-shot spectrum greatly

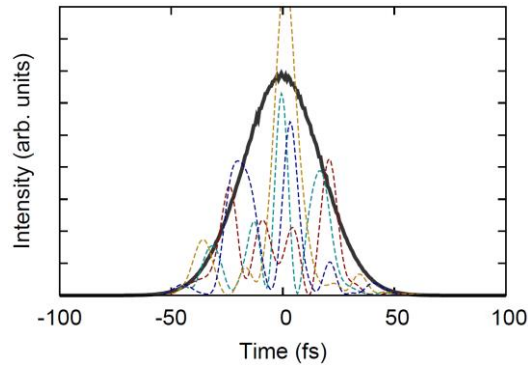


Figure 4.9: Temporal distribution averaged over many FEL shots (black solid line) and for single shots (dashed and dotted lines) obtained with the *Partial Coherence Model* from [Pfe10]. Taken from [Sen12].

varies, there are properties inherent to the radiation, which this section aims to explore.

4.2.1 Temporal and Spatial Coherence

Coherence of a light field is defined as a fixed phase relation of its different parts both in time and space. It is of utmost importance considering the investigation of non-linear processes, such as multiphoton ionization, and pump-probe experiments. Owed to its stochastic nature, light emerging from SASE FELs is emitted in short temporal spikes (modes) with random phase relationship between them [FAH05]. The spikes can be viewed as single wavepackets, which are individually excited by electrons from different positions in the bunch. Provided that the electron bunch is longer than the wavepackets duration several wavepackets can exist simultaneously, without mutual interaction. Thus, creating the multiply spiked temporal structure of the output pulses. Since the temporal and spectral domain are interrelated by Fourier transform, the temporal spikes also lead to spikes in frequency, i.e., wavelength within the bandwidth of the undulator⁶. For a homogeneous electron distribution of the bunch the number of spikes, also dubbed *longitudinal* modes M , can be estimated

$$M = \frac{T_{\text{bunch}}}{\tau_{\text{coh}}} . \quad (4.12)$$

Here, T_{bunch} denotes the duration of the electron bunch and τ_{coh} the coherence time (derivation see below). This can be understood by the subsequent considerations. Each of the modes is triggered by a single spontaneous emission. Although, a huge number of modes will be excited initially, only few of them will fulfill Eq. (4.7) and thus be amplified in the undulator. However, Eq. (4.12) does not hold for the creation of ultra-short light pulses, in the so-called *femtosecond mode*, where the electron density is being far from homogeneous [Ack07].

A common indicator for the degree of temporal coherence is the correlation function $G(\tau)$ of the electric field $E(t)$ at a fixed position \vec{r} for different times t and $t + \tau$. It reads [SSY06]

$$G(\tau) = \int_{-\infty}^{\infty} dt E^*(t) E(t + \tau) . \quad (4.13)$$

If τ is chosen to be zero it yields the time averaged intensity profile of the pulse under investigation. With this the temporal correlation function can be defined as

$$g(\tau) = \frac{G(\tau)}{G(0)} , \quad (4.14)$$

⁶Due to the finite length of the undulator the emitted radiation has a bandwidth of $\Delta\lambda_l/\lambda_l = 1/N_U$. Where N_U denotes the number of undulator periods.

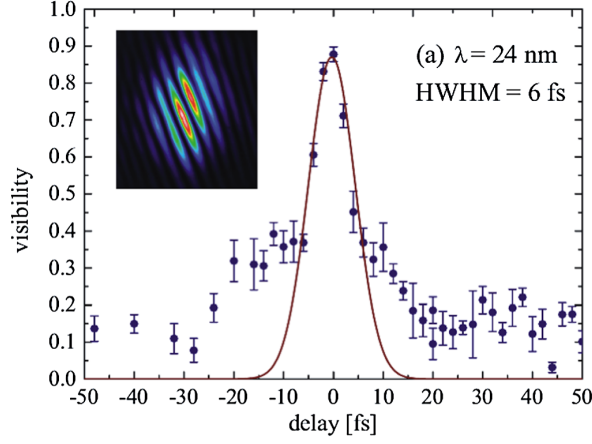


Figure 4.10: Coherence time measurement from [Rol11]. The inset is showing the interference fringes observed on the CCD.

with $0 \leq g \leq 1$. Here, $g = 0$ corresponds to a vanishing phase relation, while $g = 1$ is only observed for full coherence. Integration over Eq. (4.14) yields the coherence time

$$\tau_{\text{coh}} = \int_{-\infty}^{\infty} d\tau |g(\tau)|^2. \quad (4.15)$$

The coherence time can be determined experimentally by recording the autocorrelation of a non-linear process [Jia10a], performing a streaking measurement [Frü11] or directly interfering light waves on a CCD [Mit08]. The latter will serve as an example, as the results of [Rol11] will be summarized.

Figure 4.10 depicts their findings for a wavelength of 24 nm. The coherence time τ_{coh} of 6 ± 2 fs was obtained, by splitting up the individual FEL pulses into two sub pulses with a permanently installed autocorrelator [Mit08] capable of delaying one of the resulting sub pulses from -3 up to 20 ps, before overlapping them on a CCD. Scanning the relative delays, the visibility of the interference fringes was recorded from which τ_{coh} is deduced. Other measurements of the coherence time of FLASH yielded values of 6 ± 2 fs at 23.9 nm [Mit08], 4 ± 1 fs at 27.2 nm [Jia10a] and 2.9 ± 0.5 fs at 8 nm [Rol11]. In general τ_{coh} should scale like

$$\tau_{\text{coh}} \propto \sqrt{\lambda_l} \quad (4.16)$$

according to [Rol11], which is well fulfilled, as illustrated in Fig. 4.11.

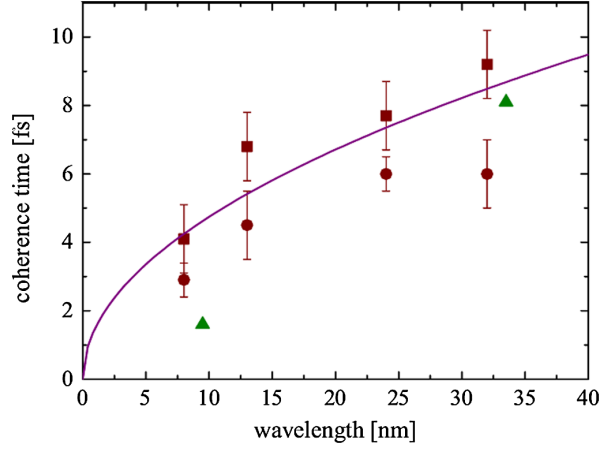


Figure 4.11: Coherence time in dependence of the emitted wavelength. All times are defined as HWHM. Graph taken from [Rol11]

Spatial Coherence

Concerning the spatial, more precisely, transversal coherence the line of argument is analogous to the case of temporal coherence. In the beginning of the undulator a vast amount of transversal modes are excited by spontaneous emission. Here, Eq. (4.7) does not constitute any exclusion criteria, as in principle all transversal modes can be produced with the resonance wavelength. However, only the fundamental TEM_{00} mode, defined like in conventional lasers, exhibits a maximum at zero, e.g. on the axis of propagation. Since it has the largest overlap with the electron bunch, it exhibits the highest gain factor of all modes. At the onset of the saturated regime of operation the fundamental transversal mode therefore dominates the spatial coherence properties of an FEL, leading to almost full spatial coherence of the beam [SDR08]. Deep in saturation this behavior is gradually altered, as the fundamental, being saturated already, will not gain energy anymore, while higher modes will.

In analogy to Eq. (4.13) the correlation function of the electric field at the same time for different radial positions is defined, yielding

$$G(r_{\perp,1}, r_{\perp,2}) = \int_{-\infty}^{\infty} dt E^*(r_{\perp,1}, t) E(r_{\perp,2}, t) . \quad (4.17)$$

This in turn allows for the definition of a spatial coherence function. It reads [ST07]

$$g(r_{\perp,1}, r_{\perp,2}) = \frac{G(r_{\perp,1}, r_{\perp,2})}{\sqrt{I(r_{\perp,1})I(r_{\perp,2})}} , \quad (4.18)$$

with $I(r_{\perp,i})$ being the time-averaged intensity at position r_{\perp} . Experimentally the spatial coherence is accessible through inspection of the interference fringes resultant from exposure of a double slit. Measurements in the linear regime yielded values for the transversal coherence between 500 and 600 μm [Sin08].

4.2.2 Pulse Length and Intensity

As discussed above the stochastic origin of SASE FEL radiation allows only for the determination of statistic averages of quantities like the pulse duration and intensity profile, both in wavelength and time. The spiked temporal structure of single FEL pulses, translates into a more or less smooth Gaussian distribution [SSY06] when averaged over several thousand FEL shots. Experimentally, the pulse length is typically defined as the FWHM of the intensity profile in time. The peak intensity is consequently deduced by the pulse energy ϵ , duration τ and focus size w_0^2 . Assuming a Gaussian shape the formula for the peak intensity reads

$$I_{\text{peak}} = 4\sqrt{\frac{\ln 2}{\pi^3}} \frac{\epsilon}{w_0^2 \tau} . \quad (4.19)$$

This approach is justified for linear processes such as single-photon absorption leading to single or multiple ionization.

For non-linear processes, we have to consider the individual pulses in more detail, since the yield Y depends non-linear on the intensity (compare Sec. 2.3). If $\sigma^{(n)}$ is the generalized cross section for n -photon absorption it reads

$$Y^{(n)} \propto \sigma^{(n)} I^n . \quad (4.20)$$

Hence, it is very sensitive to changes in intensity. Due to the spikes in the pulse profile the yield obtained at the same calculated peak intensity can be significantly larger for chaotic light compared to fully coherent light [Lec75]. The peak intensity in the spikes can thus exceed the one calculated in Eq. (4.19) by far, as can be seen in Fig. 4.9. Therefore, if non-linear processes like in Chap. 7 are investigated, substantial ionization might only take place during the intensity spikes. Thus, reducing the *effective* pulse duration to the coherence time in the ideal case.

If one aims at reproducing the actual pulse structure of single FEL pulses there are basically two different approaches. The first one is *bottom-up* employing three-dimensional FEL theory, with codes like GENESIS [Gen] . Naturally, this demands advanced knowledge on FEL theory and the machine parameters most often not available to FEL users. The second relatively new approaches are *top-down* methods like the *partial coherence model*, where the pulse structure is retrieved from the easily accessible spectra and quantities. It

will be briefly described in the next section.

For the results presented in this work, starting from Chap. 6, approximate intensities will be given calculated according to Eq. (4.19). While all other quantities of the radiation are easily accessible, the pulse length τ_{FEL} is not measured by the FLASH facility itself and therefore has to be inferred from either the experiment itself or settings of the FEL. In [Sen12], the dependency between the bunch charge of the electron bunch and the pulse length has been studied. The findings therein will provide the basis for the calculation of the intensities given in Chaps. 6 and 7.

4.2.3 Partial Coherence Model

The partial coherence model is a numerical method intending to provide sets of partially-coherent light fields with the same statistical properties as SASE FEL radiation. Thereby, it only relies on the average pulse properties, namely average spectral shape and pulse duration⁷. Briefly, if $\tilde{I}(\omega)$ is the average spectral intensity distribution, the electric field is described in the frequency domain as [Pfe10]

$$E_0(\omega) = \tilde{A}(\omega)e^{i\tilde{\phi}_0(\omega)} \quad (4.21)$$

where $\tilde{\phi}_0(\omega)$ denotes the spectral phase. Subsequently Eq. (4.21) is divided into sampling intervals satisfying $|\omega_i - \omega_{i+1}| \ll 2\pi/\tau_{\text{fel}}$. In each interval the amplitude is chosen as $\tilde{A}_0(\omega_i) = \sqrt{\tilde{I}(\omega_i)}$ and the spectral phase is assigned with a random value $\tilde{\phi}_0(\omega_i) \in [-\pi, \pi]$. The resulting random pulse is then transformed to the time domain, resulting in an infinitely long pulse (Nyquist limit) with electric field $E_0(t)$. By applying a temporal amplitude filter describing the average temporal shape of the pulse $F_0(t)$ a finite pulse $E_f(t) = F_0(t)E_0(t)$ is retrieved. Transforming back into the frequency domain yields spectral phases, no longer purely arbitrarily distributed, but partially related to each other. Put another way *partially coherent*.

In [Pfe10] it is shown that this method is able to reproduce the features characteristic of light generated by means of SASE (Figure 4.9 shows an example) from the averaged quantities down to properties of single FEL pulses. It thus provides a powerful tool in the attempt to model non-linear processes taking place in intense FEL radiation and has been applied to interpret experimental findings [Jia10a].

⁷For experiments not incorporating any of the methods described in Sec. 4.2.1 this still might constitute a problem.

5 A Reaction Microscope with an Ultra-Cold Target

The purpose of the presented setup is to gain knowledge on the ionization dynamics of lithium under the action of various ionization mechanisms induced by either photon or charged-particle impact. In the present work the focus is on light-matter interaction under extreme conditions, such as high intensities and short wavelengths in the VUV to XUV regime. Strongly associated with these *few-photon few-electron* quantum dynamical processes is the question on the significance of electron correlation, i.e. to what extent does it influence the dynamics in multiple ionization through photon impact. The special interest in studying these reactions on Li naturally arises from its relative simple structure, allowing for the extension and testing of theoretical models successfully applied for helium. In the following the experimental framework applied to accomplish this goal will be motivated and described.

To retrieve information on the dynamics of the processes studied, momentum spectroscopy is employed, demanding for a profound knowledge of the initial velocity, i.e., momentum of the target atoms prior to ionization. Consequently, cold targets are desired. In many cases, even for molecules, these are prepared in a supersonic jet, where the target-gas is released from a region of high pressure through a small nozzle ($\varnothing \approx \mu\text{m}$) into the vacuum chamber. Through the adiabatic expansion of the gas, temperatures in the mK regime are reached [Sco88]. The choice of lithium as a target to investigate ionizing reactions brings about new challenges and demands on the experimental methodology for target preparation. At room temperature Li is in the solid state. Hence, it can not directly be prepared in a supersonic gas jet. If it is seeded into a carrier jet, of helium for example, its high second ionization potential¹ would result in considerable background from the carrier. In particular, for studies on double ionization and coincident ion-electron detection this is unwanted. Consequently, taking advantage of the fact that lithium, like the other alkalis, is an appropriate target for laser cooling, a *magneto-optical trap* (MOT), as a cold and dense target, was set up [Ste07].

The methods applied today for tracing ionization dynamics cover a wide range of ex-

¹It is the highest of all atomic species.

perimental setups. From “simple” time-of-flight spectrometers [Ric09] through velocity map imaging (VMI) [EP97] up to highly sophisticated systems like CAMP [Str10], which combine the state-of-the-art technologies of Reaction Microscopes (REMI) [Mos96; Ull03], VMIs and large area, energy resolving X-ray CCDs. The line of argument will neglect all but REMIs in the following, as a detailed discussion would go beyond the scope of this introduction.

Reaction Microscopes are essentially enhanced versions of COLTRIMS (COLd Target Recoil Ion Momentum Spectroscopy) setups [Mer95], brought forward by *Moshammer*, *Dörner* and *Ullrich* in the mid 90’s [Mos96; Ull97]. REMIs, in comparison to COLTRIMS apparatuses, incorporate an additional electron spectrometer and a constant magnetic field, allowing for the coincident detection of the 3D momenta of *all* charged particles emerging from an ionization event. Thus, the data recorded with a REMI corresponds to a full mapping of the final-state wavefunction in momentum space or put another way, fully-differential cross sections (FDCS). In order to completely exploit the capabilities of REMIs the count rate has to be kept low (see Sec. 5.1). Therefore, the need for statistics results in long experimental runs. In particular if compared to non-coincidence techniques such as VMIs.

In the presented experimental setup the target preparation in a MOT is combined with the capabilities of REMIs. Due to the inherently incompatible magnetic field geometries of MOTs (gradient field) and REMIs (constant field) new challenges arise. They are constituted by switching-off the magnetic field of the MOT fast enough to allow for coincident ion-electron detection, while preserving the target density [Sch08]. Although, coincident measurements were not feasible for the presented data² (cp. Chaps. 6 and 7), it will be shown below that the requirements for full REMI operation are met by now, and coincident measurements will be possible in the future.

This chapter is organized as follows. The next section introduces the basic principles of REMIs, before the specific setup employed throughout this work is described. In particular, the detectors are discussed in detail, as only their unconventional mode-of-operation allowed for the detection of double ionization. Thereafter, the discussion focuses on the technical realization and characteristics of the MOT, before elucidating the challenges, benefits and possible future developments arising when a MOT is combined with a REMI to form a so-called MOTREMI. In the last section the experimental details for the measurements presented in the subsequent chapters are described.

²The reason for this are not only the field geometries but also the huge count-rate.

5.1 Reaction Microscope

Initially designed for studies on ion-atom collisions in the middle of the 1990's [Mos96], Reaction Microscopes have become one of the “work horses” of atomic physics today. Their scope of application covers all kinds of collisional physics, where charged fragments emerge from an ionization event (see [Ull03; Dör00] and references therein). Recently, the concept has been extended by merging a large area X-ray CCD detector with the measurement capabilities of a REMI to form the CAMP apparatus [Str10]. The great success of REMIs as a tool to study reactive processes stems from their capability to measure the full three-dimensional momentum vector of all charged particles emerging from an ionization reaction on an *event-by-event basis* and hence in *coincidence*. Thus, allowing for the determination of fully-differential cross sections.

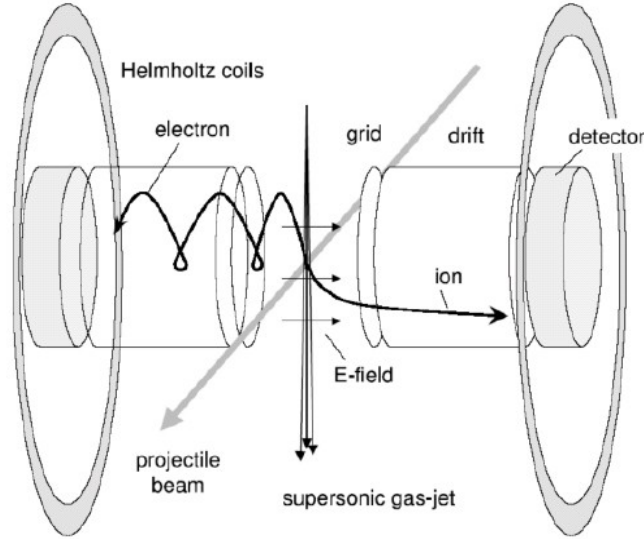


Figure 5.1: Schematic overview of the generic design of a Reaction Microscopes

Figure 5.1 illustrates the working principle of a Reaction Microscope. Charged fragments created by particle impact, like photons, ions and electrons, are guided onto two opposing time- and position-sensitive detectors by means of a constant electric field. The trajectories of light particles, i.e. electrons, is confined to the size of the detectors, through an additional constant magnetic field, boosting the solid angle covered for electron detection from typically 10^{-3} to 4π . Despite the strong impact of the magnetic field on the electrons motion the full information on the momentum is preserved (see Sec. 5.1.2). When the charged fragments hit the detector their momentum vector corresponds to the asymptotic final state of the reaction under investigation, as their Coulomb repulsion is neglectable at

the length scale of REMIs. Hence, given sufficient statistics, the data taken with Reaction Microscopes resembles the final-state wavefunction of the ionization process.

To exploit the full kinematics of a reaction at least $N - 1$ of N fragments created in a collision have to be recorded. Applying the principle of momentum conservation the momentum in the final state f has to balance the initial one i . It reads

$$\vec{p}_p^i + \vec{p}_r^i = \vec{p}_p^f + \vec{p}_r^f + \sum_j (\vec{p}_e^f)_j + \sum_l (\vec{p}_\gamma^f)_l . \quad (5.1)$$

The indices p, r, e and γ denote the projectile, target atom (recoil ion), liberated electrons and emitted radiation (photons), respectively. The beauty of this relation lies in the possibility to reconstruct even tiny relative shifts in the projectiles momentum vector, inaccessible otherwise, by recording all other final state particles. If ionization by photon impact is studied Eq. (5.1) simplifies to

$$\vec{p}_r^i = \vec{p}_r^f + \sum_j (\vec{p}_e^f)_j , \quad (5.2)$$

since the linear momentum of photons $\vec{p}_\gamma = \hbar \vec{k}$ is negligible, as long as no high resolution experiment is conducted deep in the VUV-regime. Here, the photon momentum can be on the same order of magnitude as the momentum resolution of REMIs. If a photon energy of 100 eV is assumed, its momentum amounts already to $p_\gamma \approx 0.03$ a.u. . As a matter of fact this is just little below the best momentum resolutions reported so far with REMIs [Sch11; WH00].

In conclusion, the concept of Reaction Microscopes embodies several advantages when compared to other state-of-the-art imaging techniques. The most crucial being the large acceptance of the spectrometer. It can be tuned by appropriate settings for the electric and magnetic field to spread over the full solid angle, given that no high-energetic fragments are created. Taking into account that conventional electron spectrometers, typically covering solid angles of $\frac{\Omega}{4\pi} \approx 10^{-3}$ and that for multiple-ionization events more than one detector is needed to record the full kinematics, REMIs yield an increase in detected phase space of at least 10^6 . This becomes decisive if processes with low cross sections are studied. Moreover the time-of-flight spectrometers in REMIs allow for the inherent separation of the ionic species created by their charge-to-mass ratio, e.g. the charge state and the mass of ions impinging on the detector can be determined. While this would render multiple events at a single projectile-shot possible, the coincident detection of electrons, all with the same charge-to-mass ratio, demands that at most *one* target atom or molecule is ionized

per shot³. Otherwise, the assignment of the individual electrons to their parent ions is hampered if not impossible.

Influence of Target Temperature

Equation (5.1) implies that the resolution of the spectroscopic system will depend on the capability to precisely determine the momenta of all fragments, the projectiles and the target atoms or molecules. The latter is largely given by the thermal momentum spread and it is thus of utmost importance when high-resolution momentum spectra are desired. For a better understanding of the significance of the momentum spread due to thermal motion in the initial state a few examples with the typical temperatures for atomic beams, room temperature, supersonic jets and magneto-optical traps are given in Table 5.1. The

Species	$\Delta p(600 \text{ K})$ (a.u.)	$\Delta p(300 \text{ K})$ (a.u.)	$\Delta p(1 \text{ K})$ (a.u.)	$\Delta p(0.5 \text{ K})$ (a.u.)
^4He	3.88	2.64	0.15	0.003
^7Li	5.14	3.49	0.20	0.005
^{20}Ne	8.69	5.90	0.34	0.008
e_{He}^-	0.001	$\approx 10^{-4}$	$\approx 10^{-5}$	$\approx 10^{-7}$

Table 5.1: Thermal momentum spread for several atomic species and electrons emerging from an helium atom for a number of temperatures. The momentum spread is given in atomic units.

values are calculated assuming a one-dimensional motion. Hence, the absolute value of the thermal momentum is given by

$$\Delta p = |p_{\text{thermal}}| = \sqrt{m_{\text{Ion}} k_B T}, \quad (5.3)$$

where k_B denotes the Boltzmann constant and T the temperature given in Kelvin. As the electrons are bound to the parent atom they do acquire the same additional velocity as the atom. Therefore, the ion mass in Eq. (5.3) has to be replaced by the mass of the electron. Given that Δp scales with the square root of m it is generally easier to achieve high resolution with light atomic species. Furthermore, Table 5.1 shows that for plain supersonic jets, where no further cooling is applied, the recoil-ion momentum resolution will be limited by the target temperature (see also Sec. 5.3). In contrast, the resolution of the electron momentum distributions will hardly be influenced by thermal effects at all. For that reason highly resolved measurements of electron momenta are still feasible with hot atomic beams, as for example shown in [Sch11].

³In reality the count rate is set to a value corresponding to less than one event per shot of the projectile.

5.1.1 Spectroscopic System

The centerpiece of every Reaction Microscope is the spectroscopic system, consisting of the spectrometer generating the electric field and magnetic field coils required to produce the magnetic extraction field and potentially compensate the earth's magnetic field. In the following, the technical realization of these components in the setup employed will be described.

Electric Extraction Field

Recoil-ion momentum spectrometers are high precision devices capable of distinguishing meV kinetic energies with μeV accuracy. These values demand not only a careful design and profound knowledge of the geometrical properties of the spectrometer, but also a stable power supply, i.e. low to no fluctuations in its output voltage. Figure 5.2 shows a

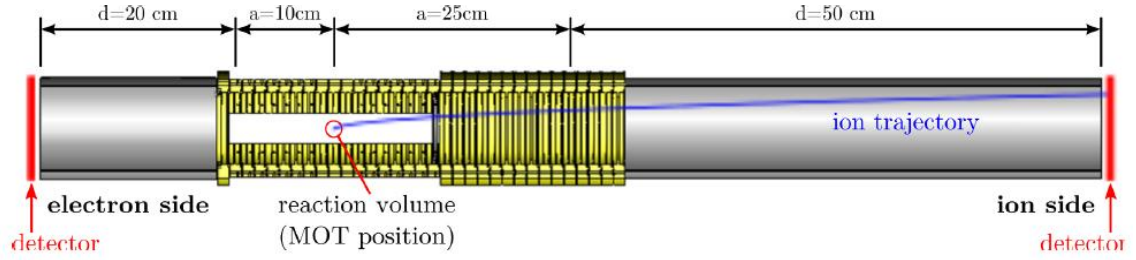


Figure 5.2: Cut through the spectrometer, with the respective acceleration and drift lengths for ions and electrons.

cut through the spectrometer. It is divided into an accelerating part $a_{e,r}$ in the central region and field-free drift regions $d_{e,r}$ at the outer parts on both the electron and the ion side. The ratio of the drift to acceleration distance is chosen to fulfill the so-called time-focusing or Wiley-McLaren configuration [WM55], given by the relation $d = 2a$. For this special geometry particles starting at different positions along the spectrometer axis but with the same longitudinal momentum will arrive simultaneously at the detector. Thus, compensating for the target spread along the spectrometer axis. The Wiley-McLaren configuration is easily derived by the following considerations. Let z be the spectrometer axis and E_z the kinetic energy of a charged particle along z . The time-of-flight t is then, according to Newtonian mechanics, given by

$$t_{\pm}(E_z) = f \cdot \sqrt{M} \left(\frac{2a}{\sqrt{E_z + qU} \pm \sqrt{E_z}} + \frac{d}{\sqrt{E_z + qU}} \right), \quad (5.4)$$

with the accelerating potential U , the charge state of the fragment q and the pre-factor f , which depends on the units chosen. Most commonly it is given in units corresponding to the ones used in experiment and amounts to

$$f = 719.9 \cdot \frac{\text{ns}}{\text{cm}} \sqrt{\frac{\text{eV}}{\text{amu}}} . \quad (5.5)$$

The “+” applies for particles moving towards the detector, whereas the “-”-sign is valid for momenta pointing away from the detector. A Taylor expansion of Eq. (5.4) for small deviations in the starting position Δz shows that the particles TOF is not depending on z as long as $\Delta z \ll a$ holds [Sch08]. In order to prevent the strong electric fields applied to the detectors from penetrating into the spectrometer both ends are terminated with copper meshes.

As illustrated in Fig. 5.2 and 5.3 the inner electrodes of the spectrometer are gold coated, to prevent surface potentials, i.e. inhomogeneities in the electric field, which might interfere with measurements of low-energetic recoil ions. Adjacent electrodes are connected via 18 k Ω thin film resistors, baked and tested on deviations of less than 0.1 % prior to installation. The free aperture of the spectrometer is 83 mm in z -direction allowing to exploit the full active area of the detectors (\varnothing 80 mm). The central electrodes enclose an opening at the sides with an extension of 30×200 mm and a round opening at the top and bottom of 30 mm diameter. While this gives easy access for the MOT-lasers and all kind of projectiles, it also embodies a problem regarding stray fields from the chamber walls and components build into the chamber. All electrodes and drift tubes are cut at least once to reduce the effect of eddy currents in case the MOT coils are switched (see Sec. 5.3 for details).

Figure 5.3 shows the electrical connections composing the voltage divider formed by the spectrometer. While in the inner part the resistors are directly mounted onto the electrodes, the “closed” rings on the ion side are externally attached to the voltage divider. Therefore, the configuration of the spectrometer can be changed, with relative ease, from the time-focusing configuration (employed for the measurements in Chaps. 6 and 7) discussed above to the so-called 3D-focusing geometry.

The term 3D focusing signifies an arrangement where not only distinct starting positions along the spectrometer axis are compensated, but also radial offsets. This is achieved by incorporating an electrostatic einzel lens (here one of the electrodes) in order to correct for the radial offsets while maintaining the TOF focus as good as possible [Dör98]. To prevent the potential of the lens penetrating into the source volume additional meshes or in the presented case apertures are build into the experiment. The *spatial-focusing* geometry has been successfully operated in the presented setup [Dor11].

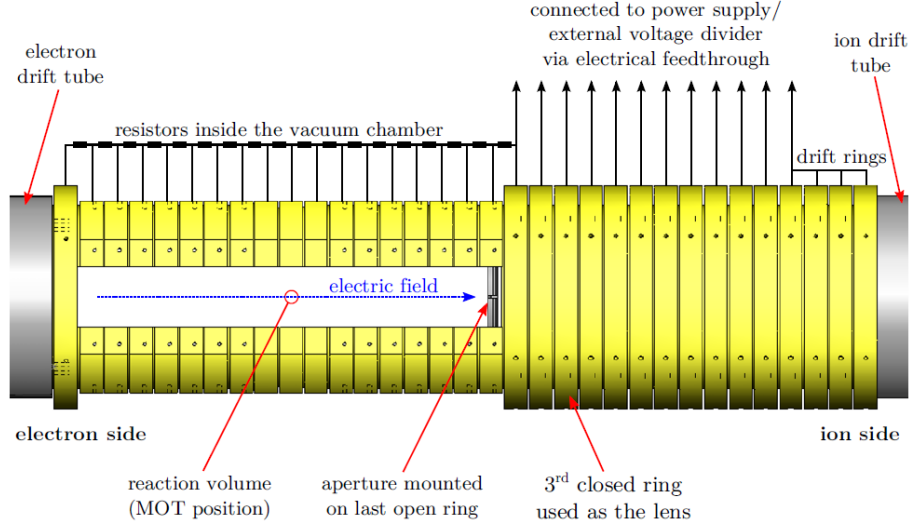


Figure 5.3: Close-up of the inner part of the spectrometer with the connection scheme applied. Attaching part of the resistors outside the vacuum chamber not only yields the possibility of changing of the spectrometer geometry, but also enhances the vacuum conditions.

Magnetic Field Configuration

Generated by a pair of coaxial coils in Helmholtz-configuration (radius equals distance), the magnetic extraction field confines the motion of the electrons emerging from a collision to their cyclotron or likewise Larmor radius

$$r_e = \frac{m_e v_{e,\perp}}{eB} = \frac{p_{e,\perp}}{eB} . \quad (5.6)$$

Here, $v_{e,\perp}$ and $p_{e,\perp}$ denote the velocity and momentum perpendicular to the coil axis. To ensure the fields homogeneity over all possible electron trajectories inside the spectrometer the coils have to be designed rather large. Electrons ejected in direction of the ion detector can, depending on the extraction field, penetrate deep into the ion part of the spectrometer. Consequently, the magnetic field has to be constant over a distance of 55 cm (from the electron detector to the end of the accelerating field⁴). Figure 5.4 illustrates the axial magnetic field of the Helmholtz-coils employed in the setup. The two coils are made of 24 windings of plastic-insulated copper tubing and feature a mean radius of 80 cm. Therefore, they allow for additional water-cooling if strong magnetic fields are required. The field produced by the coils is parallel to the spectrometer axis and thus also to the

⁴Electrons, penetrating deeper in the ion spectrometer are usually lost, as they propagate in the field-free drift region until they eventually hit the spectrometer walls.

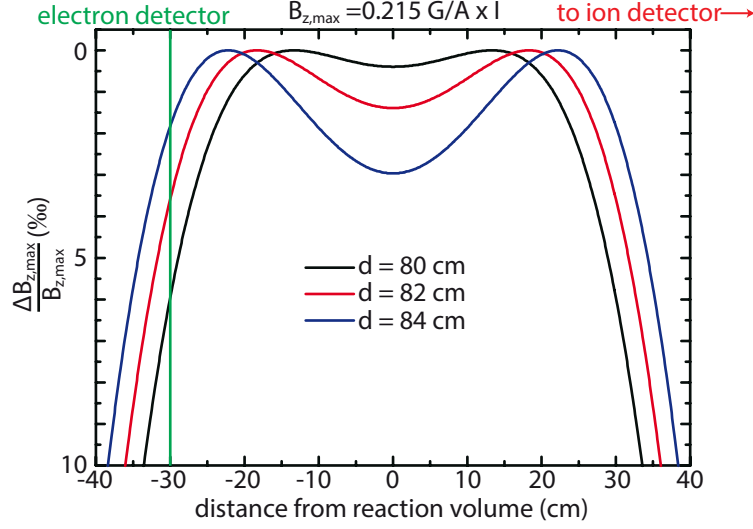


Figure 5.4: Magnetic extraction field generated by the Helmholtz-coils as a function of distance from the interaction volume. The homogeneity of the field is best for an inter-coil distance slightly larger than suggested by the Helmholtz condition (red-line).

electric field. It amounts to

$$B_{\max,z} = 0.215 \times I \text{ [G/A]}. \quad (5.7)$$

Figure 5.4 demonstrates that the field deviates less than 3 ‰ from the values calculated with Eq. (5.7) and that the homogeneity of the field critically depends on the distance of the coils.

Taking into account the high accuracy of the field, the earths' magnetic field has a significant influence, demanding for additional coils canceling it. The spatial restraints in the lab and in particular on beamtimes, as well as the requirements on accuracy leave only a small window of free parameters in the construction. The final design then consists of two pairs of additional square coils of edge length 1.72 m, spaced by 0.95 m, which create an approximately constant magnetic field in x -direction, and respectively of edge length 1.90 m, spaced by 1.05 m, for the y -direction. The magnetic fields generated are retrieved via

$$B_{\max,x} = 0.188 \times I \text{ [G/A]} \text{ and} \\ B_{\max,y} = 0.170 \times I \text{ [G/A]}. \quad (5.8)$$

Figure 5.5 shows the relative deviations of the real fields from the ones approximated with

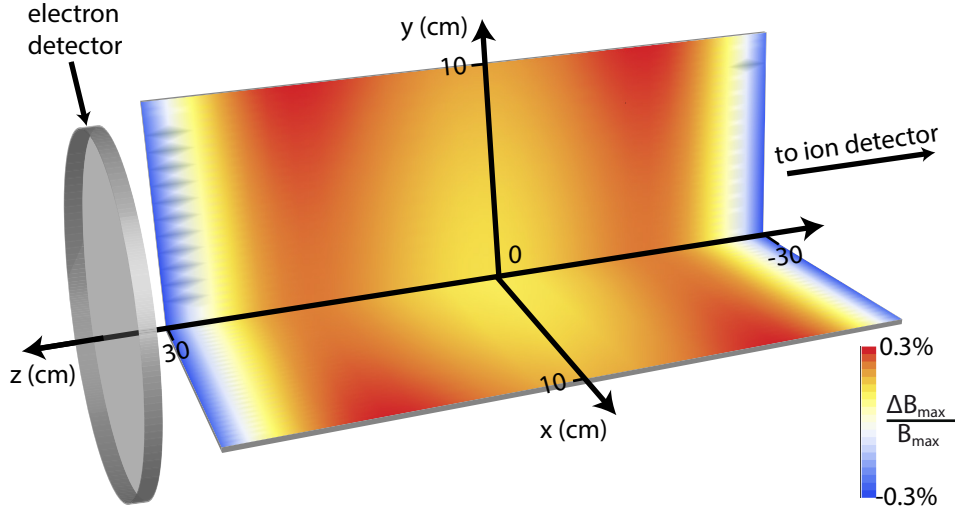


Figure 5.5: Homogeneity of the field generated by the compensation coils displayed for one fourth of the spectrometer volume. The field is generated by two pairs of square coils and exhibits deviations from the desired field strength of less than 3 ‰ over the whole electron spectrometer.

Eq. (5.8). It is found that in analogy to the Helmholtz coils, the field departs less than 3 ‰ from the calculated values.

5.1.2 Reconstruction of Momenta

This section aims at giving an overview on the calculation of the three dimensional momentum vector from the measured time-of-flight (TOF) and impact position on the detector. The symmetry of the spectrometer naturally suggests the application of cylindrical coordinates to recalculate the momentum vector. Consequently, they will be used throughout this section. Thereby, the time-of-flight, or likewise longitudinal axis shall be denoted, as before, with z , while the radial direction is addressed as r .

Ion Momentum: The TOF of charged particles in dependence of their initial kinetic energy along the spectrometer axis (E_z) has been introduced in Eq. (5.4). The reconstruction of E_z and thus the determination of the longitudinal momentum $p_z = \sqrt{2mE_z}$ through Eq. (5.4) requires the knowledge of its inverse function in an analytical form and the exact time-of-birth (TOB) of the measured ion. Nevertheless, in case of “heavy” particles such as ions, i.e. when the initial kinetic energy E_z is small compared to the energy gained in the extraction field, a Taylor expansion of Eq. (5.4) for small energies is justified. The difference in time for a particle with initial kinetic energy (momentum) to one without is

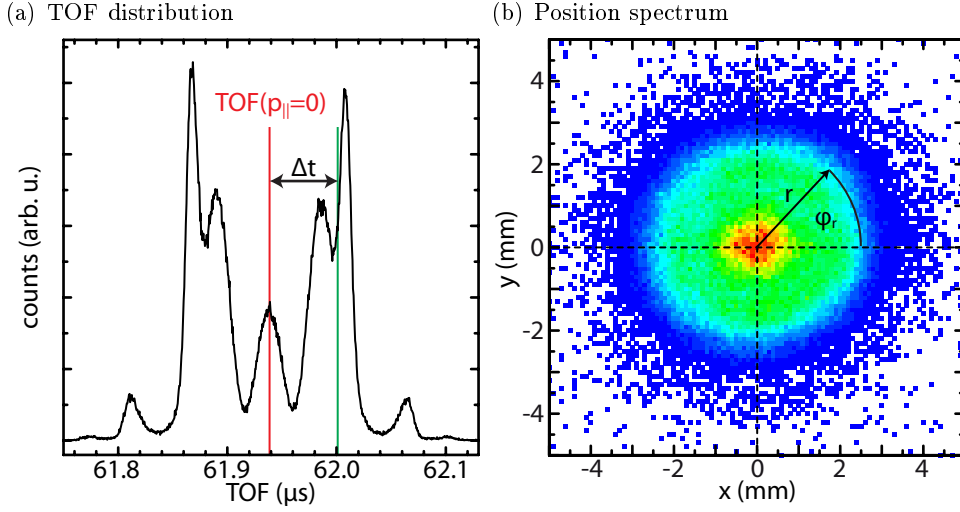


Figure 5.6: Illustration of the calculation of the longitudinal (a) and transversal momentum (b) from the time-of-flight and position spectrum of recoil ions.

then given by

$$\Delta t = t(E_z) - t(E_z = 0) \approx \left[\frac{dt(E_z)}{dE_z} \frac{dE_z}{dp_z} \right]_{p_z=0} \Delta p_z . \quad (5.9)$$

Insertion of Eq. (5.4) yields

$$p_z(\Delta t) = 8.042 \frac{qU}{a} \Delta t \times 10^{-3} \frac{\text{cm a.u.}}{\text{eV ns}} , \quad (5.10)$$

with the same units as in Eq. (5.4). As Eq. (5.10) shows, this demands for the determination of $t(E_z = 0)$, i.e. the TOF of a particle without initial kinetic energy. The absolute TOF is actually not required. There are different methods to acquire $t(E_z = 0)$. Figure 5.6(a) illustrates the method applicable for processes which exhibit momentum distributions symmetric with respect to TOF axis, i.e. emission towards and away from the detector. Here, the symmetry point of the distribution defines $t(E_z = 0)$. One example, for such a process is photoionization, where the linear polarization is parallel to the TOF and thus the spectrometer axis. Other methods to retrieve $t(E_z = 0)$ incorporate either very precise trigger signals, hence the absolute TOF is determined, or deduce $t(E_z = 0)$ through momentum conservation.

The radial momentum, perpendicular to the TOF-axis, is inferred from the impact position on the detector. Like above this demands for the determination of the arrival position (x_0, y_0) of particles with vanishing transversal momentum. In case of the photoioniza-

tion process illustrated in Fig. 5.6(b) and any other axial symmetric reaction, this can be achieved by determination of the rotational symmetry center of the distribution. The radius $r = \sqrt{(x - x_0)^2 + (y - y_0)^2}$ of the ions clearly depends on their TOF as initial transversal momenta will result in larger spatial offsets on the detector the longer the particles need to reach it. However, as typical TOFs are on the order of tens of μs , whereas the width of TOF distributions amounts only to a few hundred ns, the use of Eq. (5.4) for $E_z = 0$ provides a good approximation. Therefore, the calculation of the transversal momentum follows from

$$p_r = 11.6 \sqrt{qU m} \frac{r}{2a + d} \frac{\text{a.u.}}{\sqrt{\text{amu eV}}}. \quad (5.11)$$

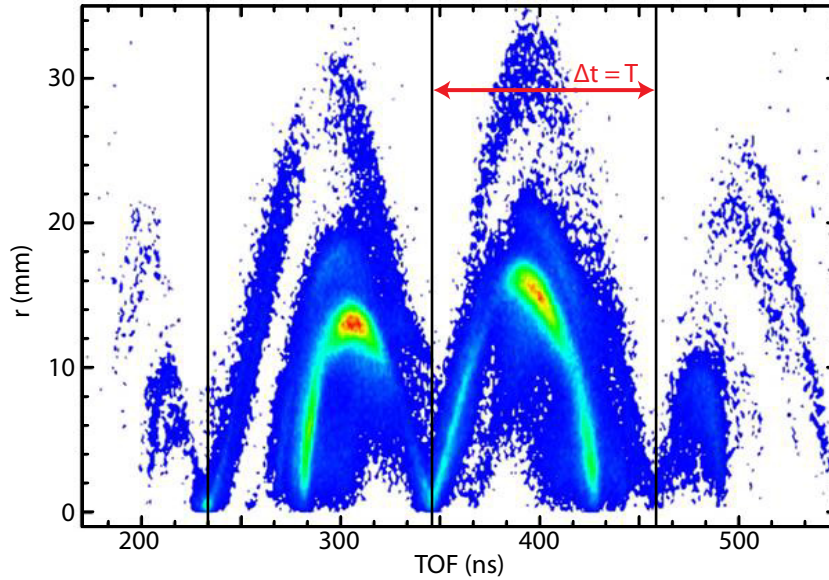


Figure 5.7: Radius over TOF spectrum for electrons. The transversal motion of the electrons is strongly affected by the magnetic extraction field resulting in the so-called *Wiggle* structure.

Electron Momentum: As elucidated in Sec. 5.1.1 the transversal motion of electrons is strongly affected by the magnetic extraction field. This is illustrated in Fig. 5.7, where the impact radius on the detector is plotted over the TOF. Confined by the Lorentz-force, the electrons propagate on helical trajectories through the spectrometer. While the helix radius is given by Eq. (5.6) and depends on the electrons energy, the frequency of the motion is given by the cyclotron frequency

$$\omega_c = \frac{eB}{m_e} \quad (5.12)$$

which is independent of the particles energy. Thus, electrons emerging from the source volume will be confined to a volume the same size as the source volume after each full period of the cyclotron motion and being spread out the most at odd half multiples of it. Ultimately, this yields the so-called wobble structure displayed in Fig. 5.7. Although, being an artifact of the experimental method, the wiggles contain valuable information on the experiment. First, they allow for an exact calibration of the magnetic field strength (time-difference between two nodes) and give an upper limit to the extension of the source volume (size of the distribution in the nodes). The most important quantity retrieved is, however, the TOB of the electrons.

Indeed, the TOB has to be coincident with a node, as an electron with infinite momentum towards the detector would not undergo any helical motion and instantly reach the detector. Therefore, the TOB can be inferred by comparison of the wobble structure, with an externally acquired trigger signal. As will be shown below this is essential for the determination of the longitudinal electron momentum.

Due to the mass ratio of at least $\frac{m_{\text{ion}}}{m_e} \geq 1836$, electrons, although exhibiting momenta on the same order as the recoil ions, gain much higher initial kinetic energies. As a result, (Eq. (5.9)) loses its validity for electrons as their initial kinetic energy can not be neglected. Nevertheless, since Eq. (5.4) still holds⁵ the TOF can be calculated by either the iterative Newton method [Bro01] or employing an approximation to the inverse function of Eq. (5.4) [Sch98]. For both methods the time-of-birth (TOB) of the electrons is required.

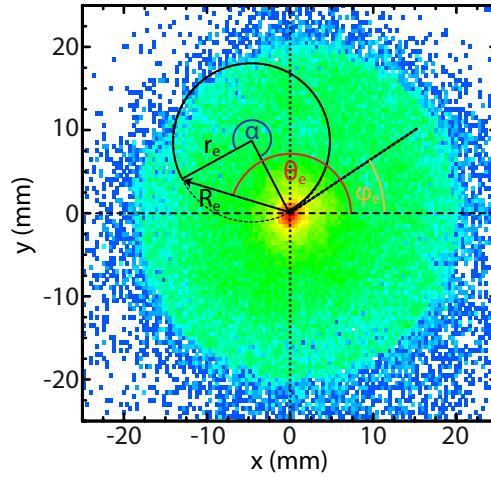


Figure 5.8: Position spectrum of electrons with the quantities essential for the retrieval of the transversal momentum and emission angle.

⁵The motion of the electrons parallel to the TOF-flight axis is not influenced by the magnetic field as it is co-linear with the magnetic field lines. Thus, the Lorentz force vanishes.

Figure 5.8 shows the essential quantities for retrieving the transversal momentum p_r imprinted on electrons emerging from an ionization event. For the ease of discussion the dependence of the cyclotron radius on the transversal momentum is repeated here:

$$r_e = \frac{p_{e,\perp}}{eB} . \quad (5.13)$$

Given that r_e is not directly accessible in the experiment, since only the impact position is recorded the transversal momentum calculates as follows. After assigning the absolute zero position $R_e(0) = (x_{0,e}, y_{0,e})$ to the symmetry center of the position distribution⁶, the radius R_e of the impact position is correlated to the cyclotron radius according to

$$r_e = \frac{R_e}{2 \left| \sin(\frac{\alpha}{2}) \right|} = \frac{R_e}{\left| \sin(\frac{\omega t_e}{2}) \right|} , \quad (5.14)$$

resulting from geometrical relations. Substitution of r_e by Eq. (5.13) thus yields

$$p_{e,\perp} = 8.04 \left[\frac{1}{\text{mm G}} \right] \frac{BR_e}{2 \left| \sin(\frac{\omega t_e}{2}) \right|} \text{ a.u.} . \quad (5.15)$$

Finally, the emission angle in the detector plane is determined, taking into account the TOF and therefore multiple revolutions on the helical trajectory. It reads

$$\varphi_e = \vartheta - \text{mod}(\omega_c t_e / 2, 2\pi) , \quad (5.16)$$

where ϑ denotes the angle enclosed with the arbitrarily chosen X-axis.

While the nodal structure characteristic for the radius over TOF spectra does not alter the longitudinal momentum resolution of the data, inspection of Fig. 5.7 yields that for all other momentum components the resolution, recorded with a REMI, is a function of time $\left(\frac{\Delta p_{\text{rad}}}{p_{\text{rad}}}(t) \right)$. In the nodes the position resolution approaches 0 and thus also all other properties related, like azimuthal or polar angle, are smeared out. There is solely one solution to this inherent technical difficulty. Either the magnetic or the electric extraction field is varied and several experimental runs are conducted.

5.1.3 Detector-System

The detection system, illustrated in Fig. 5.9, consists of a pair of stacked microchannel plates (MCP) and a delay-line anode, which allow for the recording of the time and position signal, respectively. Apart from the MCPs and the delay-line anodes, two grids in front

⁶For electrons this procedure is always valid as the nature of the helical motion demands symmetry in the position data.

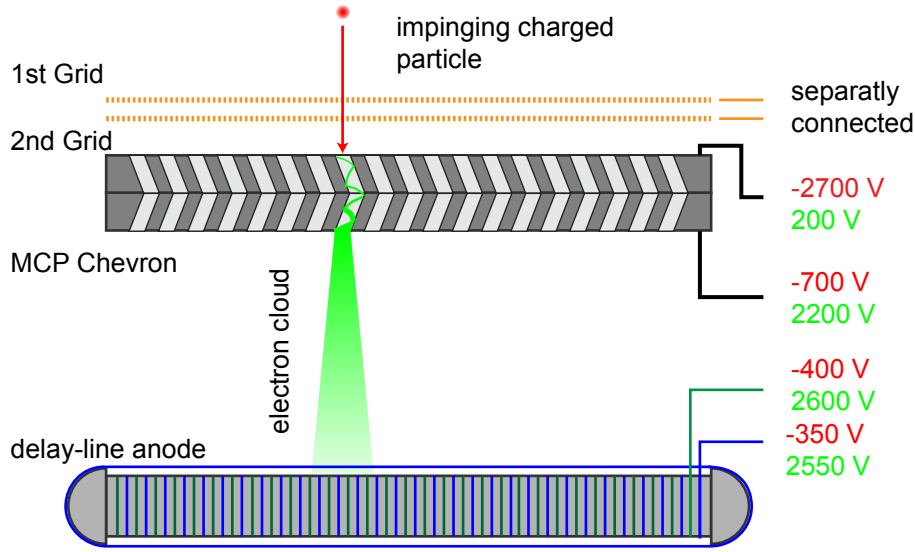


Figure 5.9: Schematic overview on the detector assembly. Particles impacting on the MCP front face eventually trigger an electron avalanche which is then detected by the delay-line anodes. While the impact on the MCP serves as time signal, the delay-line data contains the information on the impact position. On the right hand side the typically applied voltages for ion (red) and electron (green) detection are given.

of the channel plates, and operating voltages for both, ion (red) and electron (green) detection, are displayed. Although, the same potential difference is applied to the MCP in chevron configuration for both settings, the bias voltage on the front face of the MCP is considerably higher in the latter case. The underlying reason is the higher ion mass which demands for a stronger acceleration of the particles (cp. Sec. 5.1.4).

Upon impact a particle may trigger an electron avalanche in one or several channels of the MCP. If this is the case a cloud of electrons (typically around 10^7) emerges from the backside of the channel plates and imprints a charge on the wires of the delay-line anode. Both, the voltage drop on the MCP, when an electron avalanche is triggered and the voltage spike arriving at the respective ends of the wires are read out capacitatively. They serve as time and position signals, respectively. Details of the post-detector information processing are not discussed here. A description of the electronics employed to process the signals from the detector are found in [Sch08] for systems employing time-to-digital-converters (TDC) and in [Kur11; Fou08] for so-called FLASH-ADCs, which record the trace of the voltage spikes.

The two grids in front of the MCP stack are essential to shield the spectrometer from the high potentials on the MCP front faces (1st grid) and for suppression of charged particles

created amidst the interaction volume and the detector (2nd grid). Furthermore, the 2nd grid can also be used to prevent feedback between the ion and electron detector, caused by electrons emerging from the MCPs (see for example [Ste07]).

The probability of detecting a charged particle created in the interaction volume depends on the absolute detection efficiency $P_{\text{abs}}^{\text{MCP}}$ of the MCPs, the acceptance of the spectrometer and the transmission T of the grids in front of the detector. Assuming an acceptance covering the full solid angle and all kinetic energies and additionally $P_{\text{abs}}^{\text{MCP}} = 58\%$ [Kre05] only the transmission of the grids has to be determined. From the geometrical properties of the grids (mesh size: $224 \mu\text{m}$; wire diameter: $30 \mu\text{m}$) a throughput of $T_{\text{grid}} \approx 78\%$ for a single grid is anticipated. Therefore, the maximal detection efficiency is

$$P_{\text{max}}^{\text{Det}} = P_{\text{abs}}^{\text{MCP}} \cdot T_{\text{grid}}^2 = 35\% . \quad (5.17)$$

Microchannel Plates

MCPs originated from an idea first suggested by *Farnsworth* in the 1930s, the so-called *continuous dynode electron multiplier* [Far30]. However, technical realization was first achieved 30 years later by two independent groups [Osc60; GW62]. Due to the fact that the majority of the performance characteristics of electron multipliers does neither depend on channel length l nor channel diameter d but only on their ratio $\alpha = l/d$ [Wiz79], they can be reduced almost arbitrarily in size. Ultimately, this lead to the development of MCPs.

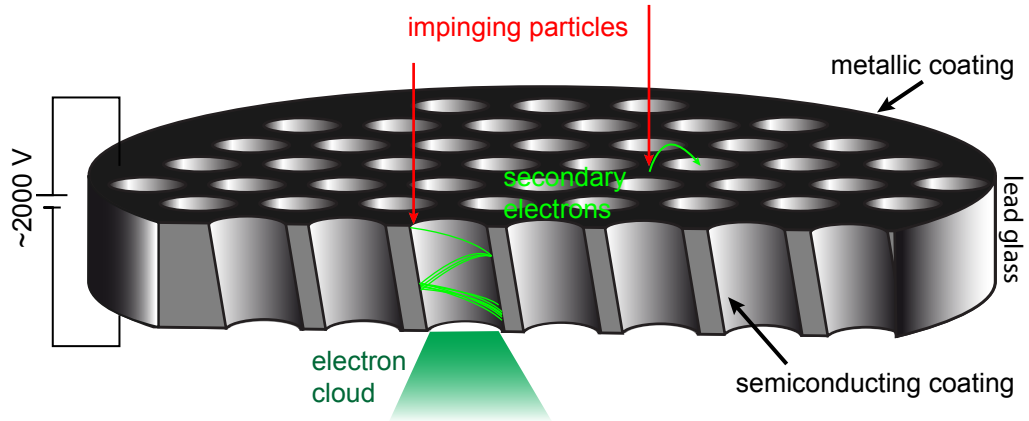


Figure 5.10: Illustration of a MCP and its working principle. Charged and neutral particles can trigger secondary electron emission upon impact on the MCP. Due to the large potential difference between its front and back side each of the channels acts as continuous dynode electron multiplier, leading to an electron avalanche at its back side.

Figure 5.10 shows a schematic of a MCP, with an illustration of the electron amplification

process. A MCP is a thin (typically 1-1.5 mm), highly resistive lead-silicate glass-plate, coated with metallic layers on its front and back side in order to grant a homogeneous supply voltage over all channels. The resistance from front-to-back is on the order of $10^8 - 10^9 \Omega$, allowing for the usually applied voltage drop over a single MCP of 1000 V. The high electric gradient field created facilitates the build-up of an electron avalanche inside the individual channels. Thereby, each of the channels acts as an individual electron multiplier with an amplification factor on the order of 10^4 , given that secondary electrons are produced in the first place. Although, the dead time of a single channel ranges in the ms regime⁷ the huge amount of channels reduces the effective dead time to $10^{-6} - 10^{-7} s$, for moderate count rates.

Additionally, MCPs exhibit a high time (< 100 ps) and position resolution, which is only limited by the channel dimensions and spacing. Today MCP setups consist most commonly of stacks of either two or three plates, the so-called chevron or Z-stack configuration. In combination with slightly tilted channels this allows not only for higher amplification factors of approximately 10^7 , but also minimizes the effect of ion feedback [Leo94]. This originates from ionization of rest gas atoms, in and especially at the end of the channels, in electron-atom collisions and sparks post-pulses leading to the degradation of both, the time resolution and the dead time of one or several channels.

Delay-line Anodes

There are several methods available to obtain the position information of the electron cloud emerging from the back side of the MCP, including direct imaging on a CCD, indirect imaging on a phosphor screen and two methods employing resistive anodes, namely *wedge-and-strip* and *delay-line* anodes. While the first two methods take only a single picture per event and detector and thus do not allow for coincidence measurements, the latter techniques do. In the presented setup delay-line anodes are employed as they offer a good trade-off between dead time and resolution.

A delay-line anode consists of either two or three wire pairs each of which forms a so-called Lecher-line (see [Dem04]), with defined impedance. The wire-pairs are wound onto ceramic insulators mounted on a solid-steel plate, with mutual angles of 90° and 60° for quad (two wire pairs) and hex (three wire pairs) anodes, respectively. The operating principle of delay-line anodes is illustrated in Fig. 5.11. The electron cloud emerging from the back side of the MCP imprints a charge on the wires. The charge distribution travels to both ends of the wire, where it produces a voltage spike, which is read out capacitatively. Taking into account that the signal travels with constant speed in both directions, the

⁷This time is given by the time it takes to replenish the channel with electrons.

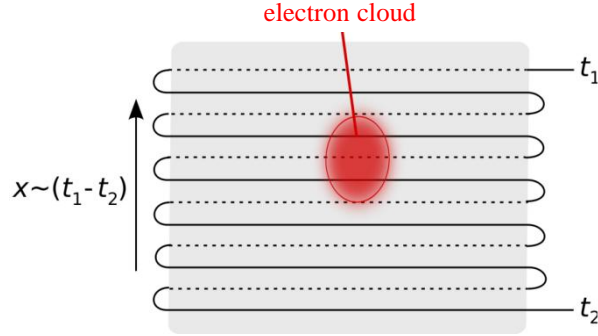


Figure 5.11: Determination of the impact position via delay line anodes (from [Sen09]). The charge cloud emerging from the MCPs back side imposes charge on the delay line wire, which will propagate to both ends of the wire. From the arrival time on both ends the position perpendicular to the delay line windings is calculated. The resolution reached exceeds the wire spacing.

impact position on the wire can be retrieved from the arrival time on the respective wire ends, e.g. t_1 and t_2 . Thus the position X is a function of the time difference

$$X \propto (t_1 - t_2). \quad (5.18)$$

In the presented setup, a quadanode is employed for ion detection and a hexanode for the detection of electrons. Although, the quadanode is sufficient to obtain the full position information it lacks the multihit capabilities of a hexanode, often essential for the detection of electrons. Details on hexanodes can be found in [Sch08] and [Jag02], respectively.

Despite the very small signals created by the electron cloud (< 5 mV), the signal-to-noise ratio is kept high by applying a slightly higher voltage to one of the wires of each pair. Therefore, this signal wire will gather the majority of the electrons, while both wires pick up the same ambient noise and subtraction of the two wire-signals leads to an almost noise free measurement. The accuracy of the acquired position exceeds the pitch between the wires, as the center-of-mass of the charge distribution can be determined with higher precision.

5.1.4 Background suppression

If reactions with low cross sections, like sequential and non-sequential two-photon double ionization, are studied (cp. Chaps. 6 and 7), strong competing processes not only in the target atoms, but also in the rest gas remnant in the vacuum chamber constitute a major obstacle. In the worst case scenario these do not only hinder the unambiguous determination of the observables, but even render the reaction under investigation “invincible”.

In the scope of this work multiphoton absorption of lithium has been studied with photon energies from 50 to 60 eV. For this high photon energies the most prominent process to occur is single ionization of both rest gas and target atoms. Here, the count-rate, in particular for one-photon single ionization (PSI), can even modify the recorded momentum spectra, due to the dead time of the MCP and overlapping signals on the delay-line. The latter, is usually more critical. PSI in the target is inevitable and does not alter the measurement of double ionization, since singly and doubly charged ions can easily be distinguished by their TOF. However, the multitude of different atomic species and therefore TOFs in the rest gas in combination with the pulse structure of FLASH, i.e. a micro-bunch distance much shorter than the TOF, prevents a complete distinction of the atomic species by their TOFs (see [Kur11]). Thus, the signal of DI might be superimposed with the one of other ionic species, emerging from different micro-bunches.

Indeed, the Li^{2+} signal overlapped with the very diffuse proton signal emerging from Coulomb explosion of H_2 . Small changes in the extraction field could not change this. Therefore, the solution to this problem would either be an increased micro-bunch distance or likewise a substantially higher extraction field for the ions. While the former comes at the expense of count rate⁸, the latter implies less resolution. Due to the limited beamtime and the demand for highly resolved data neither of them was chosen.

Instead, the possibility to suppress background events by appropriate detector settings was explored. Before, the resultant improvement in the signal-to-noise ratio (SNR) and the number of background events is presented, the underlying mechanisms for secondary electron emission from the MCP surface are reviewed, as the question whether a particle is detected upon impact on the MCP, is given by the question whether it yields secondary electrons.

Kinetic Emission: The detection efficiency of MCPs has been studied for decades, for an overview the reader is revised to the theoretical work by *Fraser* [Fra02] and references therein. In short, early studies showed that for high ion-impact energies around 3-5 keV the efficiency saturates, almost regardless of the ionic species studied, while for low-impact energies different ionic species exhibited distinct threshold behavior [PK61]. It remained unclear whether the crucial property for kinetic emission of secondary electrons is given by the impact velocity or energy. Only recently *Krems et al.* succeeded in providing an “universal” scaling law for the absolute detection probability [Kre05] of positive ions⁹. The main result of this study is illustrated in Fig. 5.12. It is found that the detection probability for all ionic species is compressed to a single curve if the efficiency is plotted over

⁸The bunch train is limited to a total duration of approximately 400 μs

⁹Note, that [BLZ67] arrived at a similar result a few decades earlier for channel electron multipliers.

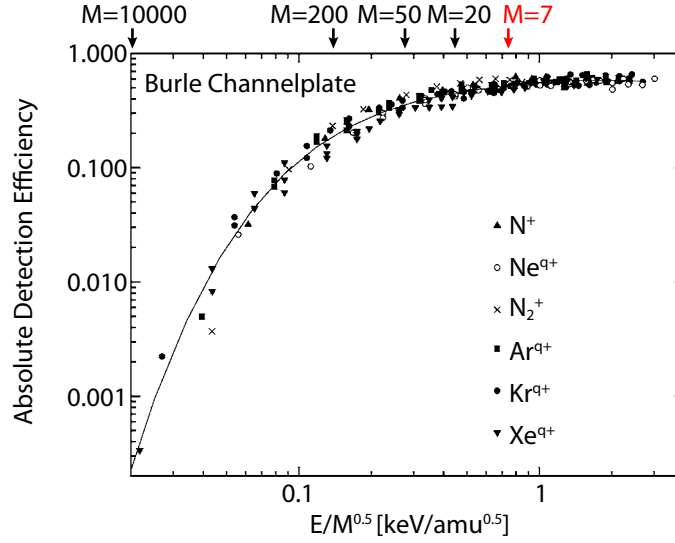


Figure 5.12: Absolute detection efficiency of an MCP (from [Kre05]). The efficiency is plotted as a function of impact energy over the square root of the particles mass. The efficiencies of various ionic species are described by a single curve (solid line). The arrows on the top axis indicate the efficiency for a number of masses at a bias voltage of -2 kV at the front face of the MCP.

$E_{\text{ION}}/\sqrt{M_{\text{ION}}}$. These results imply that for a defined potential drop and biasing voltage at the front side of a MCP, therefore in practically all measurements, the probability for detecting different ionic species can show considerable variations. The above dependence of the detection probability on the impact energy is due to kinetic emission (KE). Yet, there is another process responsible for the liberation of secondary electrons, which does not depend on the kinetic but rather on the internal energy of an impinging ion.

Potential Emission: Figure 5.13 illustrates the reactions taking place when a multiply charged ion (MCI) approaches the surface of solid metal. Once the MCI is close enough, i.e. its wavefunctions overlap with the one from the solid, a multitude of processes can lead to potential electron emission (PE). Only a selected number of them, will be discussed. A complete picture can be gained in [AW]. In *resonant neutralization* (RN) one or more surface electrons are transferred from the valence band of the surface into unoccupied states of the approaching ion¹⁰. In a subsequent step the atom can *autoionize*¹¹. If the excitation energy of the atom is still larger than the work function ϕ of the solid (for lead silicate glass

¹⁰A necessary condition for this process is the overlap of the wavefunction of the ionic state and the surface electron. Therefore, inner-shell RN only takes place at the late stages of the impact.

¹¹In fact this constitutes an Auger decay.

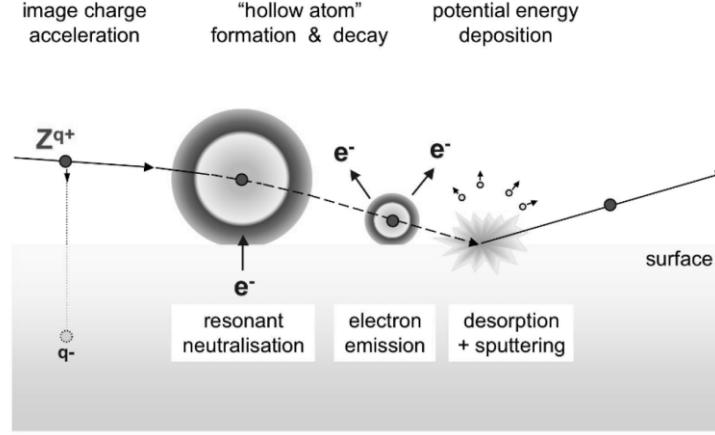


Figure 5.13: Scheme of potential electron emission for a multiply charged ion upon impact on a metal surface. Taken from [AW]. For details see text.

ϕ amounts to ≈ 8 eV), it might also undergo a so-called *Auger de-excitation*. In Auger de-excitation an electron in the atom is demoted, while an electron from the surface is emitted. Finally, in *Auger capture* one surface electron is captured by the ion and liberates a second surface electron. For this reaction to happen the ions' internal energy has to exceed twice the work function of the surface.

Either way the impact of an ion or excited atom on a surface creates free electrons in the continuum. Considering the surface of MCPs, these free electrons trigger electron avalanches, leading to the detection of the ion independent of its kinetic energy. It is found that an indispensable condition for detecting a charged particle via potential emission is given by

$$E_{\text{int}}^{\text{ion}} > 2\phi \quad (5.19)$$

where E_{int} is the internal, e.g. ground state neutralization energy of the ion. In the case of Li, this implies that Li^+ has to be in an excited state and Li^{2+} is always detected via PE. The principle of potential emission of secondary electrons can even result in the detection of slow neutral atoms in excited metastable states [KM96]. However, to the authors knowledge, there is no analytical expression or rule of thumb to estimate the probability for the creation of secondary electrons upon impact of an ion or atom in a specific state. The only existing quantitative relation is an empirical formula. Given that γ_p denotes the electron yield, it reads [Bar79]

$$\gamma_p = 0.032 (0.78E_{\text{int}} - 2\phi) \quad (5.20)$$

for values of E_{int} and ϕ in eV. Strictly, this relation only holds for noble gas ions hitting a polycrystalline metal surface. From the discussion above the following rules for PE are

deduced:

- (i) In contrast to kinetic emission PE depends on the ground-state neutralization energy.
- (ii) If $E_{\text{int}} < 2\phi$ potential emission does not occur.
- (iii) The potential emission rate γ_p is independent from the kinetic energy. Thus, it will dominate over kinetic emission for small ion velocities, i.e. low bias voltage.

As a direct consequence of (iii) PE can be utilized to suppress background events, if the ionic species of interest is either metastable, in an excited ionic state or multiply charged and Eq. (5.19) holds. Therefore, the scheme of a reduced bias voltage to increase the SNR for the detection of Li^{2+} is possible. This will be shown in the following.

5.1.5 Signal-to-Noise Ratio

For the reasons elucidated above, the bias voltage U_{bias} of the MCP has been reduced significantly for the measurements presented in this work. While, standard settings of the detector would imply $U_{\text{bias}} \approx -2700$ V, the actual experimental runs have been conducted at $U_{\text{bias}} = -100$ V. The resultant TOF distributions for the singly and doubly charged Li-ions are illustrated in Fig. 5.14. Here, the TOF is plotted for two values of the bias voltage, both of which are far below the standard settings. The respective distribution for standard settings is not shown, as no trace of DI is visible there.

Inspection of the respective TOF-spectra in Fig. 5.14 reveals an improvement in the SNR for double ionization by a factor of 10 in reducing U_{bias} from -200 to -100 V. This is understood, by taking into account the detection efficiencies listed in Table 5.2 for several bias voltages. In particular, the ones for Li^{2+} and H^+ . As mentioned before, the cardinal difficulty for the determination of the Li^{2+} momentum, was given by the superimposed, diffuse H^+ distribution. For $U_{\text{bias}} = -200$ V, kinetic emission is still effective for the relatively light protons. In contrast for all other species listed in Table 5.2, except Li^{2+} this is not the case. The situation changes for a potential of -100 V at the MCP front surface. Here, only every tenth proton hitting the detector triggers an electron avalanche. While this is even worse for the case of doubly charged lithium, the high internal energy $E_{\text{int}}^{\text{Li}^{2+}} \geq 81$ eV $\gg 2\phi$ enables the detection through potential emission described above, and hence the SNR increases. In case of H^+ , the neutralization energy (13.6 eV) is too small to trigger PE.

Apparently, single ionization of Li is still the dominant contribution to the TOF spectrum shown in Fig. 5.14 even for the smallest bias voltage. This is due to the creation of core excited and metastable Li^+ ions (cp. Secs. 6.1 and 7.2), which exhibit lifetimes longer than

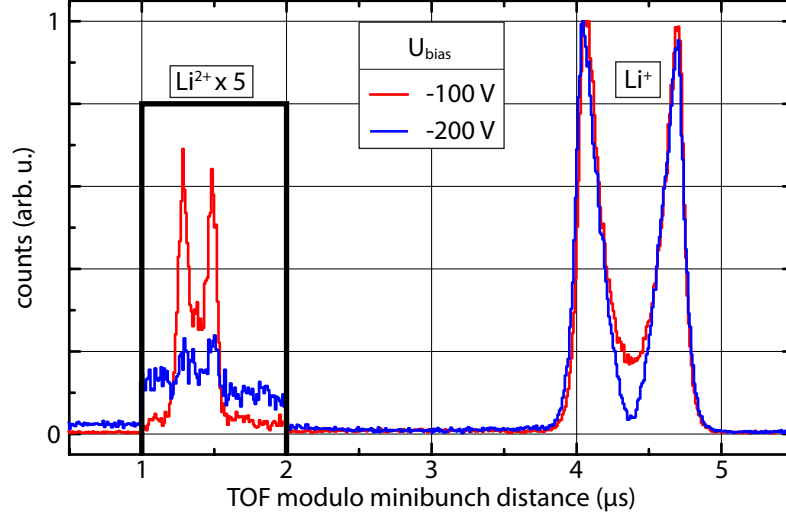


Figure 5.14: Raw TOF spectrum of Li^+ and Li^{2+} after absorption of two photons for different bias voltages on the front side of the MCP. The data-sets are peak normalized to the single-ionization yield of Li^+ to make them comparable. Evidently, the SNR increases for decreasing bias voltage at the MCP.

the TOF. As the cross sections for these reactions are larger than for DI and the Li^{+*} ground-state neutralization energy amounts at least to 58 eV this is expected. The change in the detected Li^+ final states is also evidenced by the change in the shape of the Li^+ TOF distribution. Appendix D gives an overview on the detected final states of singly charged lithium for the detector settings used.

Ionic species	$P_{\text{det}}(-2.7 \text{ keV})$	$P_{\text{det}}(-0.2 \text{ keV})$	$P_{\text{det}}(-0.1 \text{ keV})$
H^+	58 %	27 %	11 %
Li^+	55 %	6.2 %	0.7 %
Li^{2+}	58 %	20 %	6.2 %
N^+	53 %	2.5 %	0.1 %
N^{2+}	58 %	12.6 %	2.5 %
H_2O^+	50 %	1.6 %	$< 10^{-3}$
N_2^+	46 %	0.7 %	$< 10^{-3}$
Ar^+	43 %	0.3 %	off scale

Table 5.2: Detection efficiencies of selected ionic species for the detector settings used in Chaps. 6 and 7 and also displayed in Fig. 6.7. The values are extracted from [Kre05].

5.2 Magneto-Optical Trap

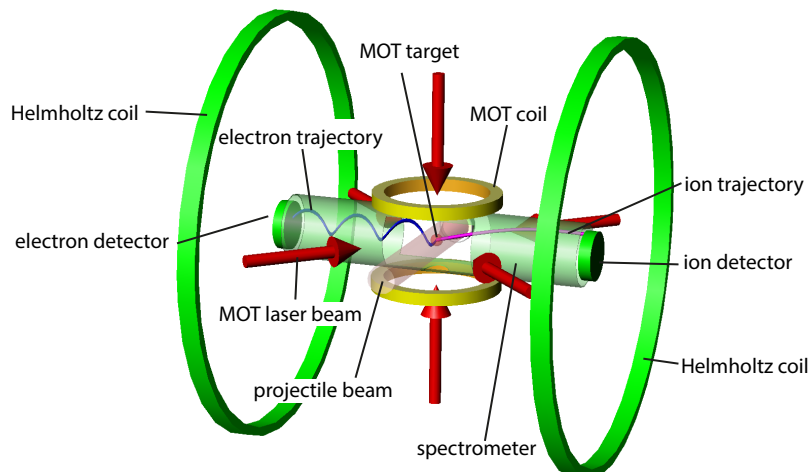


Figure 5.15: Schematic view of the complete setup incorporating the most important components of the magneto-optical trap and the Reaction Microscope.

For the reasons given in the introduction to this chapter a magneto-optical trap is employed to study DI of lithium. On the one hand this provides a uniquely cold and well defined target for momentum spectroscopy. Target temperatures on the order of $500\ \mu\text{K}$ are routinely achieved and the lasers employed for the realization of the MOT can also be used to prepare the target in an excited or even aligned state [Zhu09]. As a result the ion momentum resolution obtained in experiments solely depends on the properties of the spectrometer (cp. Sec. 5.1.1). On the other hand, the operation of a MOT is inherently incompatible with the operation of a REMI. While the former requires a gradient magnetic field, the latter demands for a constant field. This poses great experimental difficulties, in particular, if coincident ion-electron detection is desired. Although, the proof-of-principle coincident measurement is still to be performed for this apparatus, it will be shown (in particular in sec. 5.3) that without major changes coincident detection of ions and electrons will be realized soon.

In Chap. 3 the basic principles of laser cooling and trapping of neutral atoms have been introduced and a very detailed overview is found in [Ste07]. Here, the focus is on the technical realization of a MOT, with the requirement of simultaneous REMI operation. Figure 5.15 shows the components of the MOT together with the REMI parts. The components discussed below are the loading system (not shown), the Anti-Helmholtz coils (yellow rings on top and bottom) and the laser system (indicated by the red arrows). The description will be emphasized on newly implemented parts.

5.2.1 Laser Setup

In the history of the presented experimental setup, several laser system have been used to cool and trap lithium. An overview over these “early” setups can be found in [Ste07]. However, it was not until the advent of external cavity diode-laser systems and tapered amplifiers for the lithium wavelength that the quest for a suitable laser source ended. Since then, also in the course of this work, distinct optical arrangements have been employed to meet the respective demands of the experiments at hand [Zhu10; Ste07]. Here, the actual layout of the laser system will be presented, as it embodies a reasonable trade-off between laser power and control.

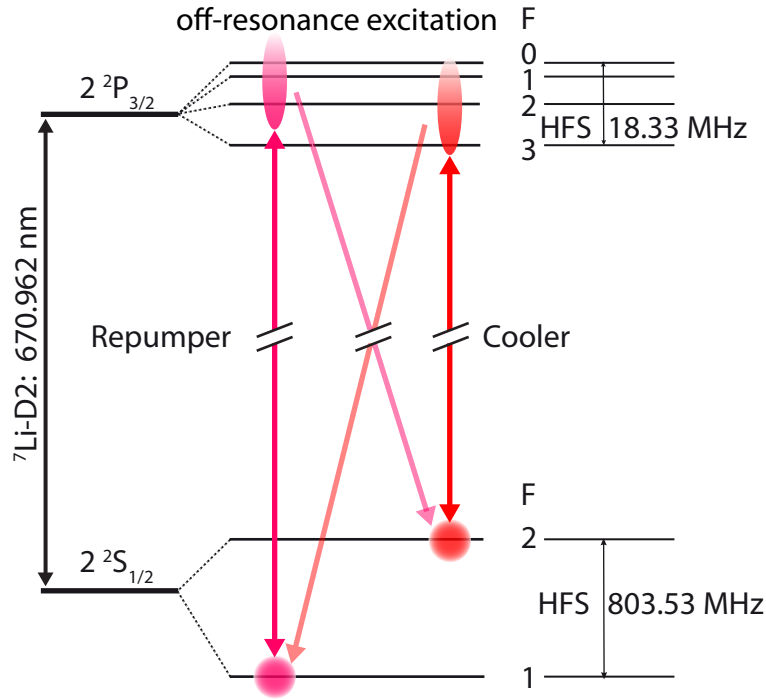


Figure 5.16: Level scheme of the ${}^7\text{Li}$ D2-line. Displayed are the hyperfine splitting of the ground and excited state due to the interaction of the nuclear magnetic moment with the electronic one. The “smeared” out transitions to the excited states indicate an inevitable off-resonant population of the states caused by the small hyperfine splitting of the $|2\,{}^2P_{3/2}\rangle$ state.

Figure 5.16, illustrates the level-structure of the ${}^7\text{Li}$ D2-line and the respective hyperfine splittings of the $|2\,{}^2S_{1/2}\rangle$ -ground and the $|2\,{}^2P_{3/2}\rangle$ excited-state. It shows that the hyperfine splitting (HFS) of the excited state is not resolved by the laser. The small splitting of only 18.33 MHz, or likewise 3Γ , where Γ denotes the natural linewidth, renders

the exclusive population of the $|2\ ^2P_{3/2}, F = 3\rangle$ -state impossible. Thus, driving solely the “closed” $|2\ ^2S_{1/2}, F = 2\rangle - |2\ ^2P_{3/2}, F = 3\rangle$ cooling transition, results in the accumulation of all atoms in the $|F = 1\rangle$ ground state in a period of only a few hundred scattering cycles. Introducing a second laser, dubbed *repumper*, on or slightly below resonance with the $|2\ ^2S_{1/2}, F = 1\rangle - |2\ ^2P_{3/2}, F = 2\rangle$ -transition solves this issue. The extraordinary small HFS of the lithium $2P$ -state marks an exception considering other alkalis. All of which have larger HFS than lithium. Hence, a single and weak laser beam with the repumping frequency is usually sufficient to keep the atoms in the cooling transition. In contrast in lithium almost equal intensities in the *cooler* and *repumper* are required, as it constitutes an effective λ -type 3-level system. Note, that the small HFS is responsible for the inaccessibility of lithium to *Sisyphus cooling* techniques.

The scheme for preparing the two laser beams required is the following. First, shown in Fig. 5.17, the master laser (Toptica DL100) has to be stabilized to a well defined frequency. Therefore a small portion (≈ 1 mW) of the total output power is diverted into a setup for Doppler-free absorption spectroscopy in a ^7Li vapor cell. The cross-over frequency¹² is chosen for stabilization, as it not only provides the strongest signal but also leaves only a gap of ≈ 400 Mhz to the transition frequencies. The majority of the output power of the master laser is subsequently used to seed a tapered amplifier (Toptica TA 500) after which a total laser power of around 400-500 mW is available, depending on the current settings and material degradation.

The whole setup is build on a 1.5×0.9 m movable laser table, specially constructed to allow for the transportation to beam times with relative ease. The cooling and repumping frequency are prepared, by two separate 200 MHz accusto-optical modulators (AOM) in double-pass configuration. Apart from shifting the frequency to the appropriate transitions a small red-detuning is introduced. The double-pass configuration provides several advantages here. State-of-the-art 400 MHz AOMs only yield around 50-60 % efficiency and critically depend on the beam shape. In contrast the efficiency of the employed AOMs is at about 75 % for a single pass and was boosted to over 80 % by replacing the factory delivered voltage controlled oscillators (VCO), amplifiers (AMP) and attenuators (ATT) through a custom-built system of mini-circuits components. In this manner approximately 64 % of the input power is preserved at the output of the double pass. The double-pass configuration yields the advantage that it allows for large frequency shifts, with virtually no displacement in the outgoing beam.

Subsequently the two frequencies get overlapped and approximately three quarters of the

¹²The cross-over frequency is right in the middle between the cooling and repumping transitions. The spectroscopy signal exhibits a dip for that frequency, since the laser light gets absorbed by atoms in both possible hyperfine ground-states.

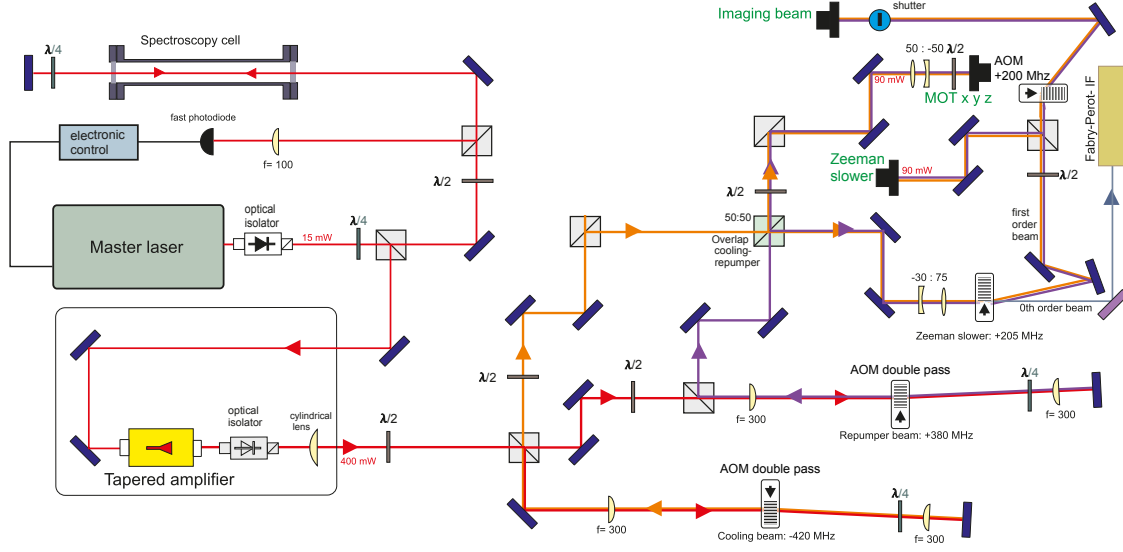


Figure 5.17: Optical arrangement to prepare the laser beams required for MOT operation, imaging and target preparation. For details see text.

available power is coupled into fibers for transport to the vacuum chamber. The remaining part passes another 200 MHz AOM preparing the *slowing* frequency (see also Sec. 5.2.3), which is 210 MHz red-detuned of the resonance frequencies. Finally, a last AOM, also with 200 MHz central frequency is employed to provide either an imaging or likewise a beam for optical pumping. There are two schemes how the imaging, i.e. near resonant, beam is produced. One is to just shift the light frequency back to resonance by imprinting a blue shift to the beam. This requires the use of the mechanical shutters (rise time $\approx 1 - 2$ ms) if the MOT lasers are to be off during imaging/pumping. Another possibility (not shown in the figure) is to red detune the cooler and repumper AOM so far that the light in the MOT beams hardly interacts with the lithium atoms any more. This requires a detuning of $\delta \approx 14\Gamma$ (determined in experiment) of the cooler and repumper AOM. Therefore, a frequency blue-shift in the imaging AOM of nearly 270 MHz has to be achieved. Despite, being far off the specifications of the AOM, still a efficiency of 60 % could be reached, providing sufficient laser power for both imaging and target preparation. In addition, the switching is on the order of several 10 ns.

The efficiency of the fiber coupling is around 50 % for all fibers employed. On the REMI side the beams constitute a 3-Beam MOT, and are retroreflected into themselves. Provided no major disturbances occur, the laser setup proofed to be stable, as it was running continuously, i.e. without re-locking of the laser, up to days.

5.2.2 MOT-Coils

The quadrupole magnetic field generated by the MOT coils is essential to provide an ultra-cold target in the center of the spectrometer. However, in an experiment aiming at high resolution momentum spectroscopy there are considerable restraints to the design of the Anti-Helmholtz coils. The strong fields not required for MOT operation but naturally occurring for larger distances from the trap center, have a big impact on the momentum distributions. Even more so if particles as light as electrons are to be studied. For this reason the MOT coils are usually operated in a switched mode, i.e. they are switched off during data acquisition (DAQ), in all MOTRIMS (magneto-optical trap recoil ion momentum spectroscopy) experiments [Fle01; Ngu04; WH00; Bre03]. Data containing information on electron momenta or time-of-flights could, however, not be obtained. Induced eddy currents, in the chamber walls and other parts of the vacuum chambers rendered the retrieval of these impossible. It was not before 2008 that [HM08] claimed a solution to the problem, the AC magneto-optical trap. Finally, in 2012 the first successful ion-electron coincidence measurement was reported [Fis12], although not in an AC-MOT but in a MOTREMI.

In [Sch08] it was shown, that the problem of eddy currents also persists in the presented setup. Naturally, for the switching behavior, i.e. for the magnitude and decay time of eddy currents, the actual parameters of the MOT coils play a crucial role. As will be shown in the following it was necessary to build new coils in order to allow for coincident ion-electron detection in the future. In [Ste07] the criteria for building fast-switching MOT coils with the restrictive condition of electron spectroscopy are formulated. Including the findings of [Sch08], the coil assembly needs to satisfy the subsequent demands:

- (i) Field gradients should be as high as possible. A high field gradient enables strong compression of the atomic cloud. Moreover, loading of the trap is enhanced, due to the increased capture velocity of the MOT.
- (ii) The coils have to be switched on the shortest time scales feasible. Considering the dependence of the time constant for switching of magnetic fields:

$$\tau_{\text{on/off}} = L/R , \tag{5.21}$$

where L denotes the inductivity and R the ohmic resistance of the circuit, this implies low conductivity. Thus small coils are advantageous.

- (iii) The magnetic field has to be contained to a preferably small volume to minimize the effects arising from eddy currents. Like (ii) this favors small coils. In fact it

demands for an intra-vacuum setup of the coils. Otherwise the magnetic flux has to pass through the chamber walls.

- (iv) Power dissipation has to be taken into account, as the coils are mounted inside the vacuum chamber.
- (v) The rim and mounting of the coils has to be both stable and insensitive to eddy currents.

The initial MOT coils fulfilled most of these demands. They were mounted inside the vacuum chamber with an inner distance of 10.4 cm given by the extension of the spectrometer in direction of the coil axes. Power dissipation was taken care of by manufacturing them from a hollow copper tube, thus allowing for water cooling. The rim and mountings were cut at least once to prevent closed-loop conductors in the vicinity of the magnetic field and the magnetic field was switched by an insulated-gate bipolar transistor (IGBT) on a time scale of 400 μ s.

Despite these efforts, a measurement of electron momentum spectra with coinstantaneous simulation of switched MOT operation (see [Sch11] for the experimental details) yielded a minimum field-off time¹³ of nearly 3 ms before electron spectra become accessible. This rendered coincident detection of electrons and ions impossible (see Sec. 5.2.2). For this reason, new MOT coils have been build and implemented into the setup with the goal to further confine the magnetic field and, if technically feasible, to reduce the energy stored in it. Additionally, the rim of the coil should be less susceptible for eddy currents.

Design and Simulation

Spatial confinement of the magnetic field is most easily obtained by reducing the size of coils. Since the minimal distance of the coils is restricted by the size of the spectrometer to be at least 10.4 cm, that implies coils far off the (Anti-)Helmholtz condition of $r = D$, where r denotes the radius of the coils, and D their mutual distance. It can be shown, that for this configuration, the power dissipation is minimal at a given gradient in the center of the coils [Ste07].

In order to achieve spatial confinement of the field while maintaining a geometry as close as possible to the Helmholtz condition the new coils are designed as a two coil setup (see Fig. 5.18(a)). The inner MOT-coil pair generates the MOT gradient field, and an outer slightly larger pair, dubbed compensation coils from here on, with opposing current dampens the field of the MOT coils for large distances from the trap center. Moreover and despite the fixed inner distance of the coils, the mean distance of the coils was reduced, by

¹³The field-off time denotes the time the MOT-coils are off before the DAQ starts.

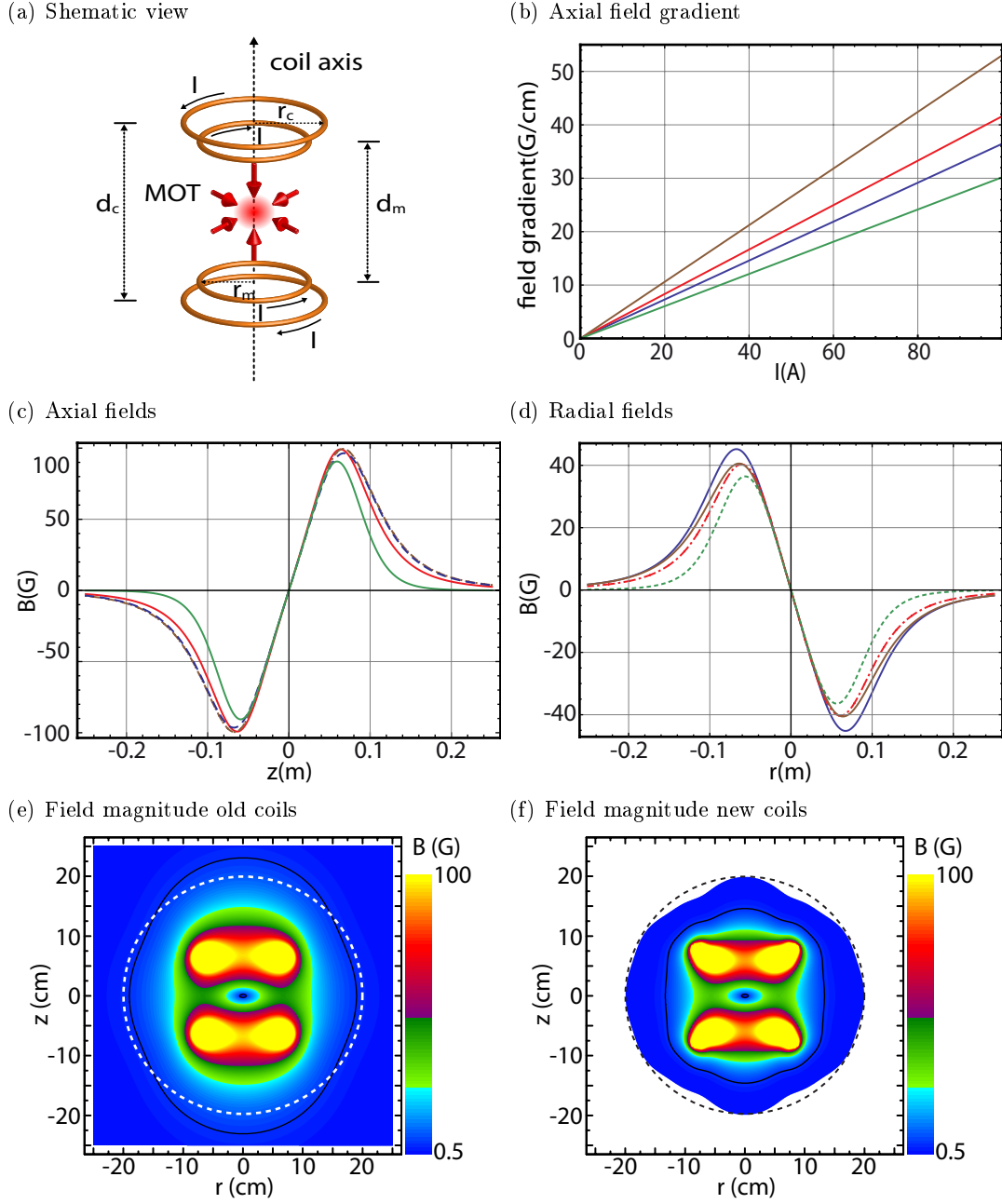


Figure 5.18: Steady-state properties of the new coil assembly in comparison with the old one. In (a) a schematic of the new coil geometry is displayed. Panel (b)-(d) show various properties of the old setup (blue), the MOT-coil pair alone (red) and MOT and compensation coils with opposing (green) and parallel (brown) currents. In (e) and (f) the absolute value of the magnetic field of the old setup and the spatial confinement (opposing currents) configuration are shown. The solid line marks a field of 5 G and the dashed ring indicates the chamber walls.

employing a thinner copper tube (Sf-cu 4/0.5), less insulating material (2 layers 0.025 mm Kapton tape) and tighter wrapping of the coils (see Table 5.3).

According to the law of Biot-Savart, the magnetic flux of co-axial coils at any point in space is given by [Gre02]

$$\vec{B}(\vec{r}) = \frac{\mu_0}{4\pi} \left(I_1 \oint d\vec{s}_1 \otimes \frac{\vec{r} - \vec{r}_1}{|\vec{r} - \vec{r}_1|^3} + I_2 \oint d\vec{s}_2 \otimes \frac{\vec{r} - \vec{r}_2}{|\vec{r} - \vec{r}_2|^3} \right), \quad (5.22)$$

where $I_{1,2}$ denotes the currents in either coil, $r_{1,2}$ the respective coordinates of the coils and the integral runs over the closed-loop conductors. The new coil assembly was simulated employing a *Mathematica* script originally written by M. Gehm [Geh03], which was extended and adjusted to the task at hand. The results are illustrated in Fig. 5.18, together with the respective values for the former coil setup. Briefly, Eq. (5.22) is solved by the use of elliptic integrals in cylindrical coordinates in order to gain an expression for the transversal and axial field component. For plotting the absolute values of the magnetic flux the derived values are added according to vector analysis. To minimize the error of the calculation the coils have been described by single wire loops.

Figure 5.18 illustrates the resultant magnetic fields and the coil setup. The MOT and compensation coils are connected individually allowing for various possibilities of magnetic field configuration. In spatial-confinement configuration the two coils are operated with opposing currents (green line). If a higher field gradient is desired only the MOT coils can be used (red line) or even both coil pairs, now with parallel currents (brown line). All except the spatial-confinement configuration yield higher field gradients, both axial and radial, compared to the prior setup (blue line), as illustrated in Fig. 5.18(b). Figure 5.18(c) and (d) show the axial and radial magnetic fields of all coil setups, for the same field gradients in the trap center. Evidently, the field for the spatial-confinement configuration drops off for smaller distances from the trap center. A more detailed view of this is given in (e) and (f), where the absolute value of the magnetic field inside and outside of the vacuum chamber is displayed.

To summarize the results illustrated in Fig. 5.18, the new coil assembly offers a magnetic field reduced by a factor of 10 to 20 at the chamber walls compared to the old ones, when using the spatial-confinement configuration. This comes at the expense of an increased power consumption on the order of 20 %. Still, no heating up of the coils in steady state operation has been observed. Moreover, if electron momentum spectroscopy is not feasible¹⁴, they allow for higher field gradients by employing the compensation coils to enhance the MOT field. Thus, facilitating shorter loading times or likewise higher target densities

¹⁴Measurements of electron momentum distributions are for example hindered by high count rates, as it is the case for the data presented in the next chapters.

of the MOT.

Mechanical Assembly: In principle the mounting of the new MOT-coil setup follows the same ideas as the old one (see [Ste07]). There are, however, subtle but decisive differences. As mentioned before, the rims are not closed in order to not build closed loop conductors susceptible for eddy currents. For the same reason, at most one of the rim holders electrically connects the chamber walls to the coil rim, while the others are insulated. In the new assembly, the direct connection to the chamber was completely relinquished. Instead, the rim itself is connected via a feedthrough to an external power supply allowing for an independent choice of its potential¹⁵. The afore mentioned use of copper tubes with smaller diameter (4 mm instead of 5 mm), brought about a reduction of the mean distance of the coils and also helped in reducing their mean diameter. Evidently this results in a larger distance to the chamber walls and yields the additional advantage of a smaller rim. The rims of the new setup are substantially smaller than the previous one, despite the fact that it is the base for both the MOT coils and the compensation coils. The most striking contrast are the side walls of the rims. While these were solid before, they have now been reduced to single flaps which are removable if desired. From this two main advantages arise. First, it allows for a better gas removal from the coils, i.e. a very evident reduction of virtual leaks, and second it considerably reduces the amount of surface traversed by the magnetic flux. In Table 5.3 important design parameters of the old and new MOT-coil setup are summarized.

Coil assembly	Old MOT coils	New MOT coils
Type	intra-vacuum	intra-vacuum
Material	5/1 Sf-cu hollow copper tube	4/0.5 Sf-cu hollow copper tube
Insulation	125 μm Kapton tape	25 μm Kapton tape
Mean radius r_m	7.8 cm	6 cm
Mean Distance d_m	13 cm	12.3 cm
Mean radius r_c	–	8.1 cm
Mean Distance d_c	–	15.8 cm

Table 5.3: Comparison of the old with the new MOT-coil assembly.

Switching behavior So far only the static properties of the coils have been discussed. However, the crucial quality of MOT coils in a momentum spectrometer is the switching

¹⁵This is particularly advantageous if the center of the spectrometer is held at a high potential, since it allows to adapt the rims potential. In this manner there are no stray electric fields from the rims into the spectrometer.

behavior. For that reason not only new MOT coils have been build but also the switching devices have been improved. As mentioned before, the MOT coils are switched on and off by an IGBT switch (for details of the circuit see [Ste07]). This switch now features a switch-off time of $80 \mu\text{s}$, instead of $400 \mu\text{s}$ before, which was achieved by applying a more elaborate cooling scheme, named "shower-power" to the IGBT itself. The coils are thus definitely not producing any magnetic field already $80 \mu\text{s}$ after applying the trigger signal for switching off. Nevertheless, the time scale for switching is not solely defined the current in the MOT-coils but also by the decay of eddy currents, induced by switching off the coils. Therefore the decay of the magnetic fields was measured inside the vacuum chamber and hence on realistic conditions by using a pick-up coil for detecting changes in the magnetic field. The results are presented in Fig. 5.19, where not only the switching properties of the new setup (blue) is presented but also the the one of the old coil assembly (red).

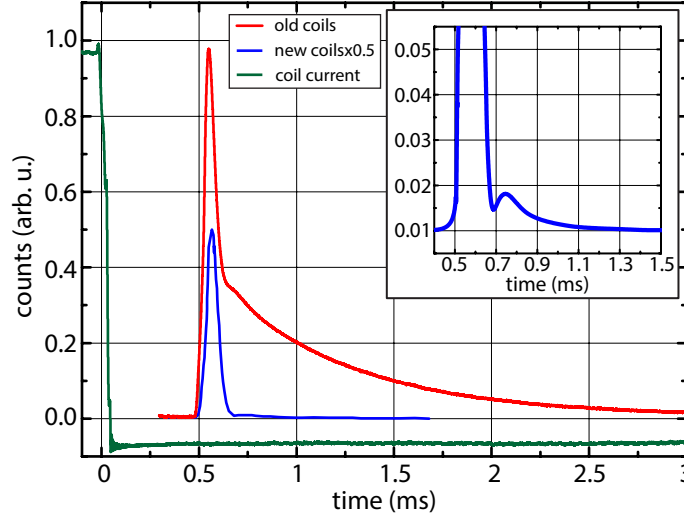


Figure 5.19: Decay of the magnetic field for the previous MOT-coil assembly (red) and the new MOT-coils in spatial-confinement configuration (blue) as measured with a pick-up coil. The green line shows the switching off of the coils. The data for the decay was shifted by 0.5 ms, such that it does not overlap with the current switching curve (green).

The properties of the home-build pick-up were tested with a single air-coil. Figure 5.19 demonstrates that switching, i.e. the decay of the magnetic field generated by eddy currents, proceeds at least a factor of three faster for the new coil setup compared to the old one. The inset on the right hand side of the figure shows a magnification of the blue curve for small induced currents in the pick-up coil. It is found that the improved coil setup guarantees field free conditions¹⁶ in below **1 ms**. Moreover the new coils were tested

¹⁶This means free of the field or any induced fields generated by the switching of the MOT coils.

inside the vacuum chamber, i.e. in the fully operational experiment, whereas for the prior MOT-coils a test-setup was build, comprising solely the flanges with the coils in the right distance and no vacuum chamber. Therefore, it is found that the major factor for the decay of the magnetic field after switching is not only the flux through the chamber walls, but also the mounting of the coils themselves. It is worth mentioning that this is no effect of the improved switching¹⁷. Consequently, coincident ion-electron detection is feasible in future measurements. Taking into account that the data presented in Chaps. 6 and 7 have been acquired 2 ms after switching off the magnetic field, it is clearly seen that with the new coils coincident ion-electron detection would have been possible.

5.2.3 Zeeman slower

In order to load a MOT, it is essential to provide a source of relatively cool atoms. Typical capture velocities for MOTs are below 100 m/s [LSW92; Mun01], depending on the atomic species, the wavelength of the cooling laser, the laser intensity and the field gradient in the trap center. Commonly applied sources range from simple filaments via Zeeman slowers and 2D magneto-optical traps to very brilliant beam sources combining the last two techniques. All techniques share the concept that a certain fraction of atoms, emerging from evaporation and therefore Maxwell-Boltzmann distributed, up to a maximum velocity are cooled below the capture velocity of the MOT. In case of filaments and two-dimensional MOTs this maximum velocity is given by the capture velocity of the 3D and 2D MOT respectively. In contrast, the last two techniques, both employing Zeeman slowers, allow for a high degree of freedom in the choice of the maximum velocity which is cooled. In this section the motivation for the design and construction of a new Zeeman slower will be given. Furthermore, its most important features will be discussed. Details on the old setup and the principle of Zeeman slowing are found in [Ste07; Spi05].

The concept of Zeeman slowers was introduced in Sec. 3.3 and a number of possible field configurations are shown in Fig. 3.5. There are different concepts on the technical realization of such a field geometry. Either permanent magnets, continuous solenoids or arrays of solenoids are commonly employed. The latter concept was chosen for both the former and the new Zeeman slower, as it offers a large flexibility in the magnetic fields applied and allows for convenient chilling of the coils compared to a continuous solenoid. Figure 5.20 shows technical drawings of the new Zeeman-slower beamline. The setup has a total length of approximately 70 cm, 30 cm shorter than the old one, and consists of an oven part on the left hand side and the Zeeman slower on the right hand side. A mechanical shutter is implemented in order to allow for switching off the atomic beam in release-recapture

¹⁷Both coils were tested with the improved IGBT switch.

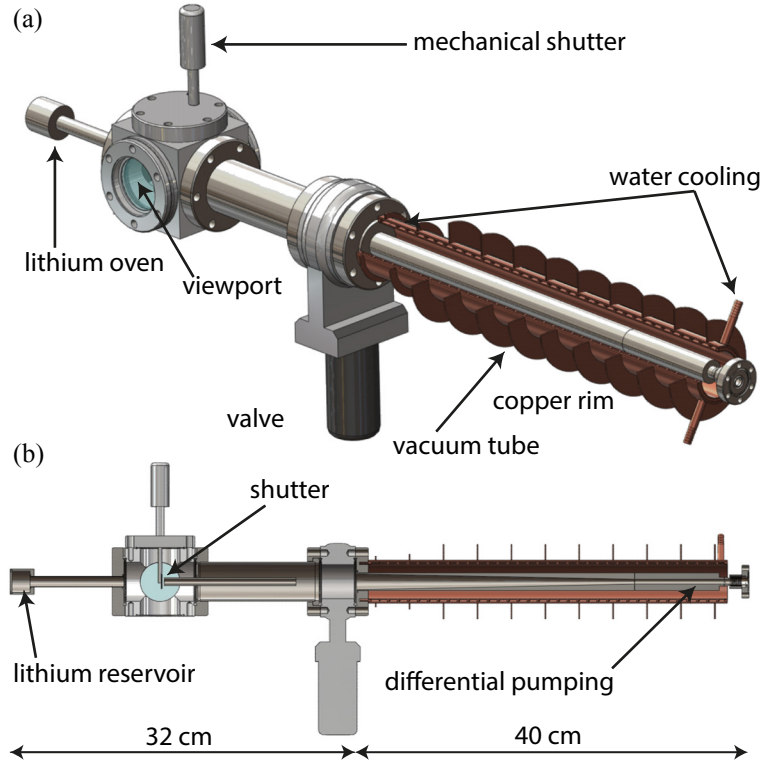


Figure 5.20: CAD drawing of the newly designed Zeeman-slower beamline. For details see text.

cycles (cp. Sec. 5.3). Differential pumping is achieved by the vacuum tube of the Zeeman slower which is conically shaped on the inside and ends in a tube of 9 cm length with a diameter of 0.7 cm. Therefore the excellent vacuum conditions in the main chamber 10^{-10} - 10^{-11} mbar are not influenced by the Zeeman slower. The rim of the coils allows for internal water cooling through a double-helix structure in its inside. Water enters the rim, flows through one of the strands and flows back through the other, providing efficient and equally distributed cooling.

An extensive discussion on the original Zeeman slower designed for the presented setup is found in [Spi05]. Due to ambiguous labeling of radius and diameter in the simulations during the course of that work, the final design exhibited “bumps” in the magnetic field configuration (see Fig. 5.21 (a) and (b)). This still enabled the cooling of atoms below the capture velocity of the MOT for high intensities of the slowing laser as shown in Fig. 5.21(a), due to power broadening (see Sec. 3.3) of the transition. However, the implementation of optical fibers to transport the laser beams from the optical table to the experimental chamber brought about a drop in laser intensity and thus rendered Zeeman slowing ineffective

(Fig. 5.21(b)). In an interim solution, simulations have been conducted, accounting for the

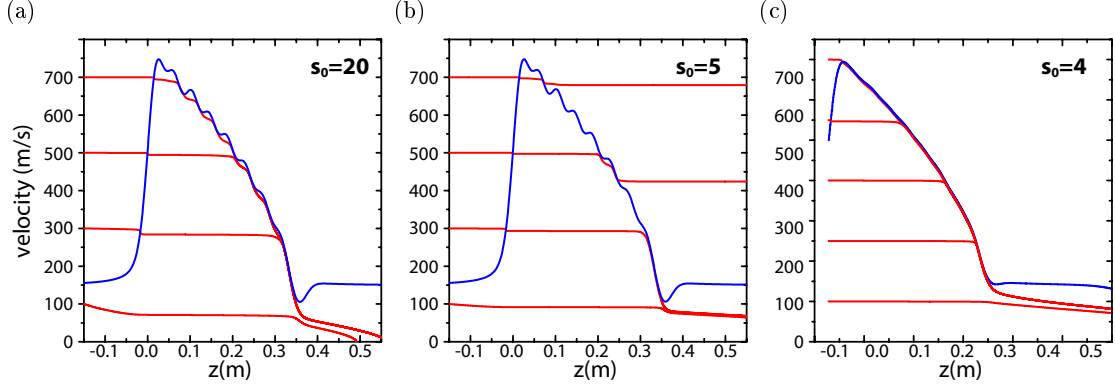


Figure 5.21: Simulated velocity profiles for the different Zeeman-slower setups. The blue line indicates the resonance velocity, i.e. the velocity for which the Doppler shift is compensated by the laser detuning and the Zeeman shift (cp. Sec. 3.3) and the red lines display the velocity profile for atoms entering the slower with different velocities. In (a) and (b) profiles for the previous slower setup for saturation parameters of 20 and 5 are illustrated. In contrast (c) shows the same for the newly-built Zeeman slower.

reduced saturation intensity for the $(2^2S_{1/2}; F = 2; m_F = 2) - (2^2P_{3/2}; F' = 3; m_F = +3)$ transition. The results are not shown here. The main difference to Fig. 5.21(a) is a reduced maximum capture velocity¹⁸. This was accounted for by an increased oven temperature, as the exponential increase in the vapor pressure with temperature over compensates for the higher mean velocity of the atoms.

With regard to the reduced laser intensity (from $s_0 = 20$ to $s_0 = 4$) the safety parameter η introduced in Eq. (3.19), was conservatively chosen to be 0.5 for both the simulations with the new and old Zeeman slower. The magnetic field produced by the individual coils was subsequently fitted to the ideal field, by variation of the individual coil currents, in a *least-square fit*, minimizing the value of

$$\left(\int_{z=0}^L dz (B_{\text{ideal}}(z) - \sum_{k=1}^n (I_k B_k(z))) \right)^2 \quad (5.23)$$

for 80 points along the Zeeman-slower extension. Hence, closely resembling the desired field calculated with Eq. (3.22). The result was used to calculate the corresponding Zeeman shift and the resonance velocity, i.e. the velocity for which the combined Zeeman and Doppler-shift compensate the red-detuning of the laser beam, of atoms in the states investigated in dependence of the actual position inside the Zeeman slower (blue lines in Fig. 5.21). In

¹⁸Here, capture velocity denotes the maximum velocity parallel to the Zeeman-slower axis.

a second script, this time utilizing MATLAB, the trajectories of the atoms entering the Zeeman slower with given velocities are simulated (red lines). The script was originally designed by [Geh03]. It solves the equation of motion along the atomic beam path

$$m\ddot{z} = F(B(z), \dot{z}) , \quad (5.24)$$

with the Euler-forward method. Here, F denotes the scattering force with the effective detuning derived in Eq. (3.15) and hence depending on the instantaneous magnetic field $B(z)$ and the velocity of the atom \dot{z} . Given that the time interval chosen for integration of Eq. (5.24) is chosen sufficiently small, the results obtained by using the Euler-forward method are accurate. For the simulations presented here it amounts to $\Delta t = 500$ ns. To get an estimate of the capture velocity of the magneto-optical trap also the MOT laser beams have been incorporated in the simulation. In Fig. 5.21(c) the result for the newly-built Zeeman slower is illustrated. Evidently, the new design matches the performance of the old-slower with a four times higher saturation intensity and does not exhibit the bumps in the magnetic field as the smooth progression of the resonance velocity shows. Together with the new MOT-coil assembly loading times of less than 2 s for oven temperatures of 650 K have been achieved with the new Zeeman-slower beamline.

5.3 MOTREMI

While in the previous sections the individual components of the experimental setup have been described in detail, this section aims at giving a brief overview on the peculiarities when a magneto-optically trapped target is used to perform momentum spectroscopy. In particular, if the momentum of particles as sensitive to stray magnetic fields as electrons are to be detected. As already mentioned in the course of this work the combination of a magneto-optical trap and a Reaction Microscope implicates modifications on the design and mode-of-operation of both the MOT and the REMI, respectively.

The major obstacle in a MOTREMI setup is constituted by the inherently incompatible magnetic field geometries of MOTs (gradient field in all directions) and REMIs (constant magnetic field). It is this simple fact, which renders the coincident detection of ions and electrons and thus kinematically complete experiments on multiple ionization problematic. Although, the operation of a MOT does not require large magnetic fields, the creation of reasonable field gradient in the center of the trap is achieved at the expense of large fields for larger distances from the trap center. In the presented setup they reach almost 100 G for the new coils in the spatial confinement configuration (cp. Fig.5.18(c)). Therefore, even in the case of pure recoil-ion detection, i.e., in MOTRIMS setups, the MOT-coils

are switched off rapidly (see for example [Kno05]). The currents in the coils creating the anti-Helmholtz field of the MOT can, although with some effort, be switched-off on very short time-scales (here $80 \mu s$). However, eddy currents arising from the rapid change in the magnetic flux prevented coincidence measurements until very recently [Fis12]. As the discussion of the switching behavior of the new coil setup showed, this is now also possible for the setup presented here (see Fig. 5.19).

Mode-of-Operation: For the MOTREMI setup there are, in principle, two modes-of-operation commonly employed in experimental runs with the presented apparatus. They are illustrated in Fig. 5.22(a) and (b). In (a) the apparatus is operated in so-called release-recapture cycles. Here, first a large number of atoms is accumulated in the magneto-optical trap in the loading-phase. If the desired number of atoms is reached the Zeeman slower is switched off and a mechanical shutter (cp. Fig. 5.20) blocks the atomic beam emerging from the Li-oven. In the following release-recapture cycles, the MOT, i.e. the MOT magnetic field, is switched-off to guarantee "field free"¹⁹ measurement conditions and after a certain data acquisition time (DAQ), the gradient field is switched-on again to recapture a large fraction of the released atoms into the MOT. Depending on the settings of the lasers, i.e. if molasses cooling is applied during the "field-off" time, and other experimental conditions as for example the background pressure and field-off time itself, these cycles can be performed up to 2000 times before reloading becomes necessary.

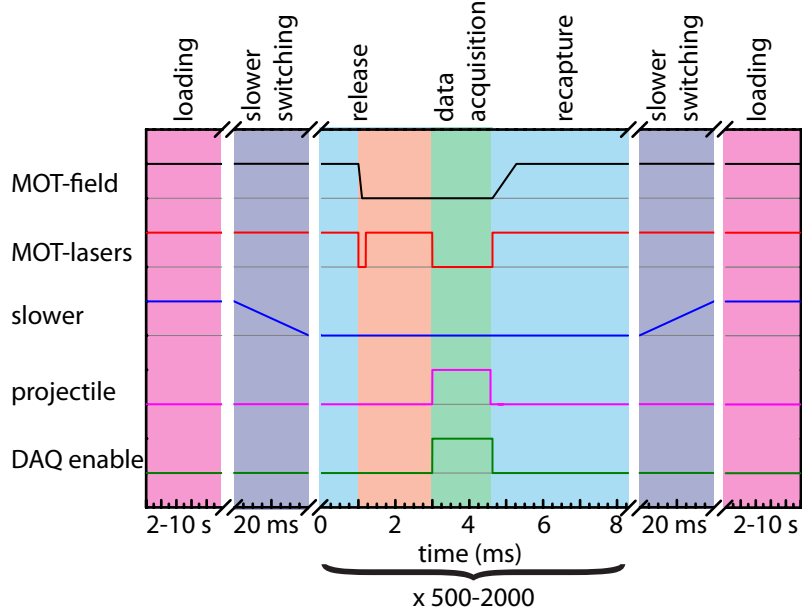
Mode-of-Operation and Experimental Setup at FLASH: If the small cross sections of reactions like double ionization are studied at FLASH, i.e. within a very short amount of time it is disadvantageous to "loose" FLASH laser pulses due to the reloading of the MOT. Therefore a different operation mode, was chosen here. It is illustrated in Fig. 5.22(b). Taking advantage of the low principle repetition rate of FLASH the MOT is reloaded inbetween the individual laser pulse trains of FLASH. That leaves a timeframe of approximately 95 ms for the loading of the MOT. Therefore, the switching time of the Zeeman slower was reduced from 80 to 20 ms which left an effective loading time of around 50 ms ²⁰. In the experiments presented below the MOT was loaded once at the beginning of each experimental run and then continuously operated in the cycle shown in Fig. 5.22(b) for the remainder of the measurement. In this way a duty cycle of virtually 100 % was reached during FLASH beamtimes.

Typical field-off times during the FLASH measurements ranged between 2 and 2.5 ms.

¹⁹If electrons are detected as well field free signifies the absence of the MOT gradient field not the fields of the REMI.

²⁰The switching of the MOT-gradient field is uncritical here.

(a) Release-recapture



(b) Constant reloading

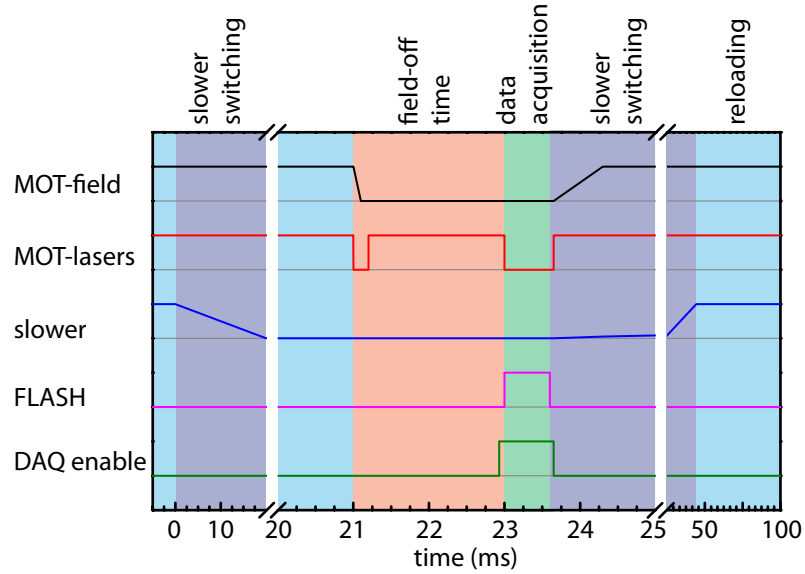


Figure 5.22: Different operation modes. In (a) the most efficient mode-of-operation for projectile beams with low repetition rate, as for example FLASH is displayed. In contrast (b) illustrates the mode-of-operation for high repetition rates of the projectile beam. Note the different scalings on the X-axis.

This rendered the coincident detection of ions and electrons impossible due to the induced eddy currents by the switching-off of the MOT-coils. However, the FLASH beamtimes were still performed with the old MOT coils, which only allow for coincident ion-electron detection for field-off times longer than 3 ms.

Figure 5.23 shows a schematic of the MOTREMI setup connected to the FLASH beamline. In particular, the differential pumping stages the orientation of the FLASH-polarization, as well as the electric field of the spectrometer are illustrated. It is seen that the TOF-direction coincides with both, the laser polarization ϵ and the z -direction. In the center of the MOT around 10^8 lithium atoms are stored at a target temperature of approximately $500 \mu\text{K}$. The whole setup is movable in the z and y -direction for finding the overlap of the MOT and the focus of the VUV-radiation.

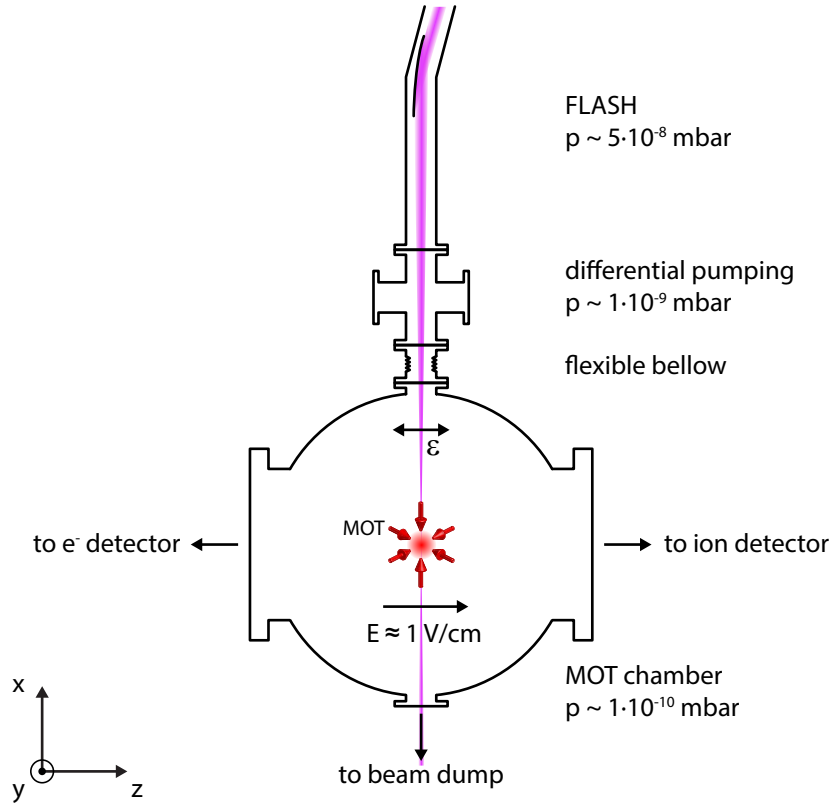


Figure 5.23: Schematic view of the experimental setup connected to the FLASH beamline.

6 Photo-Double Ionization of Doubly Excited and Aligned Lithium

The understanding of the correlated motion of two or more electrons in an atom, molecule or solid, is of high interest not only in physics but also in other fields such as chemistry and biology. Correlated electron-pairs constitute the bonds between atoms in molecules, which in turn constitute the building blocks of life. A profound knowledge on the influence of electron correlation on, for example, the ionization or the break-up of a molecule upon photon impact, could pave the way to control these processes.

The most fundamental reaction to study the influence of electron correlation on ionization is the photo-double ionization of atoms, in particular helium. The absorption of a single energetic photon can either lead to single ionization (SI), single ionization and excitation (IE), double excitation or double ionization (DI). Here, the last three reactions are solely mediated by correlation between the involved electrons as the light-matter interaction is of single-particle nature. In studying electron correlation the use of photons instead of particles yields the advantage of a projectile, which transfers a well defined angular momentum and energy. In addition the polarization of the light field inherently introduces a natural quantization axis. As a consequence, the DI final state will exhibit symmetry constraints on the ejection angles and energy sharings of the emitted electrons [MB95]. Moreover, the final state of PDI on helium, an alpha-particle and two free electrons, constitutes the pure three-body coulomb continuum. Therefore, the methods developed to accurately describe the evolution of this final state in the continuum are of utmost importance in virtually all fields of the physical science.

Consequently, PDI of helium has been studied extensively since the pioneering experiments of *Carlson* [Car67] over the last decades (see [AH05; BKA04; Weh10] and references therein) and remarkable agreement between experimental and theoretical results has been achieved [BKA04]. Besides the overwhelming interest in the fundamental case of helium a lot of studies focused on the PDI of other closed shell atoms, such as Neon [Kra96] and Xenon [Way93]. Here, the many electron nature of the atomic species creates processes competing with DI, such as Auger-decay of the excited singly charged ion. On one hand this enables the investigation of different facets of electronic correlations and light-matter

interaction such as interferences between the direct process and the indirect one, proceeding via the intermediate excited state of the singly charged ion [Ela09]. On the other hand it hampers the unambiguous assignment of the observed structures. Owed to the complex structure of these many electron systems, theoretical description and experimental results still lack the excellent agreement achieved for helium.

In contrast to the well studied two-electron systems He, H₂ and D₂, rare gases and other closed-shell systems, differential data on the PDI of open-shell and excited atoms is rare on both the experimental [Ela09] and the theoretical side [CP03]. Only recently, pioneering experiments at FLASH were performed, investigating the dependence of PDI on the alignment of the excited 2p-orbital of Li*(1s²2p) close to threshold [Zhu09]. This work sparked further theoretical interest to investigate PDI for the case of open-shell atoms both, in the ground and excited state [Col09; Khe10a; Khe10b; Khe11; YMR10].

Atomic lithium embodies the next step in complexity compared to helium and is thus an ideal testing ground for the extension of theories successfully employed there, towards the theoretical *ab initio* description of more complex atoms and molecules. Naturally, this requires the availability of differential experimental data. Nevertheless, apart from cross section ratios [WJL08; Weh04] the only differential data so far is the PDI measurement of *Zhu* [Zhu09]. The investigation of the multiple ionization of lithium is thus of high importance for a deeper understanding of the impact of electron correlations on the multiple ionization of complex atoms.

Therefore, in continuation of earlier work [Zhu09], PDI from doubly excited and aligned lithium is investigated in this chapter. For a photon energy of approximately 60 eV, DI of lithium proceeds via a resonant intermediate state and the absorption of two-photons. It can thus either be viewed as two-photon double ionization (TPDI) with an intermediate resonance or as PDI of the excited state, where the first photon excites the atom to the Li*(1s2s2p)-state and in the second step DI ionization occurs due to the absorption of a single photon.

The most stringent test of theories describing PDI are fully-differential cross sections (FDCS). In case of PDI that means differential with respect to the electrons energy sharing and relative emission angle. In the performed experiment however, the momentum of the recoil ion was measured, corresponding to the sum momentum of the emitted electrons. Although the recoil momentum distribution alone does not allow for a direct determination of the underlying dynamics of PDI, comparison with differential theoretical data yields not only conclusive evidence on the applicability of the theoretical models employed, but also on the mechanisms driving the correlated motion of the two outgoing electrons.

6.1 Single Ionization

The goal of this chapter is to investigate the PDI of lithium at a photon energy of $E_\gamma = 59.4$ eV, however, it is instructive to study SI first. In SI, the excess energies of the electrons are well known (given by Eq. (2.1)) and since only a single electron is ejected the recording of the recoiling ion is indeed a kinematically complete experiment. The data acquired for the singly ionized atom can therefore be used to extract valuable information for the interpretation of PDI, such as the achieved resolution. This is particularly important if recoil-ion momenta of the doubly-charged ion are studied and compared to theoretical predictions. There, the width of observed peaks does not necessarily have to originate from the experimental resolution but can also stem from electron correlation.

Experimental Framework

The experimental data presented has been acquired at the focused beamline 2 (BL2) of the free electron laser in Hamburg (FLASH). FLASH was operated with an effective repetition rate of 270 Hz, distributed on 10 pulse trains, consisting of 27, so-called *micro-bunches* with an intermutual delay of 10 μ s. The VUV-light was focused by a toroidal mirror to a spot size of around 25 μ m. The pulse energies measured with a permanently installed gas monitor detector was determined to be 70 μ J, this corresponds to a mean peak intensity of 4×10^{13} W/cm², assuming a pulse length of 150 fs. The FLASH spectrum was chosen to be centered at a wavelength of 20.9 nm ($E_\gamma = 59.4$ eV) in order to allow for the resonant excitation of the Li(1s2s2p)²P-term. Note, that the first step can actually excite two different states. As this is not important for the SI results, it will be discussed in the scope of DI.

The MOTREMI setup was connected to the FLASH beamline as depicted in Fig. 5.23. It was operated in switched mode (cp. Fig. 5.22), with a field-off time¹ of at least 2 ms, prior to the arrival of FLASH laser pulses. The low principle repetition rate of FLASH in combination with the faster switching of the Zeeman-slower (cp. Sec. 5.3) allowed for constant reloading of the MOT, between the individual bunch trains. Therefore, all FLASH pulses could be used without interruptions for reloading the MOT, i.e., a duty-cycle of 100% has been reached.

Ion Yield: From the pulse energy a total number of photons per pulse of 8×10^{12} (1/pulse) is derived. As each of these photons can cause single ionization either in the target or the

¹The field-off time is the time which passes between switching of the MOT gradient field and the start of the data-acquisition.

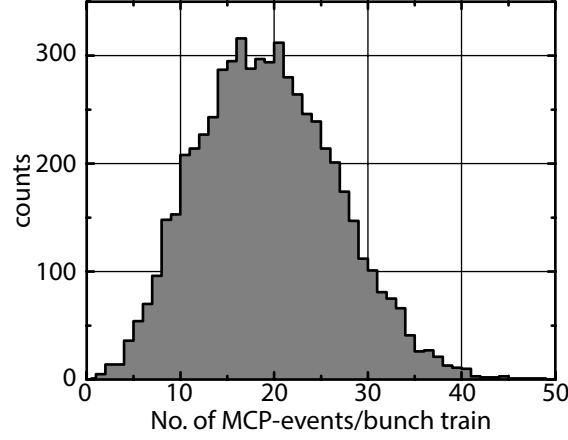


Figure 6.1: Number of detected ions per bunch-train (27 microbunches) for a bias voltage of -200 V at the front face of the MCP.

rest gas remnant in the chamber, a large number of ions are created per laser shot. Therefore, the background suppression scheme described in Sec. 5.1.4 was applied. Figure 6.1 shows the total number of detected ions for a detector bias voltage $U_{\text{bias}} = -200$ V, for which an absolute detection probability of 6.2 % is found for Li^+ in the ground-state (see Table 5.2). Despite, this small probability for detection, it is assumed that this is the major contribution to the overall ion yield, which can also be seen in Fig. 5.14, where the ion TOF is plotted for different detector settings. In average a total number of 19.36 ions per bunch train are detected. With 27 micro-bunches that leads to a total number 0.72 ions per shot of the FEL. As a result taking into account the transmission of the grids T_{grid}^2 (cp. Sec. 5.1.3) the total number of ions created per pulse is estimated to be

$$N_{\text{Li}(1s^2)^+} = \frac{N_{\text{detected}}}{P_{\text{MCP}}^{\text{Det}}(-200V) \cdot T_{\text{grid}}^2} \approx 21 \frac{1}{\text{pulse}}. \quad (6.1)$$

6.1.1 Results

Studying SI it has to be considered that not all final states are detected (cp. Sec. 5.1.4). In fact, for the detector settings used ($U_{\text{bias}} = -100$ eV), ions in the ground-state ($\text{Li}^+(1s^2)$) are not observed and so are all final states, which decay to this state prior to impact on the detector. Figure 6.2 shows a selected number of reaction pathways that lead to two-photon SI. Here, (a) illustrates the channel, where in the second step the $2s$ -electron is ejected from the $\text{Li}^*(1s2s2p)$ excited-state. As the $2p$ -electron originates from the K-shell it has to form a singlet configuration with the remaining $1s$ -electron. Consequently, the $\text{Li}^+(1s2p)$ -state will quickly decay to the ionic ground state (cp. App. D). Figure 6.2 (b)

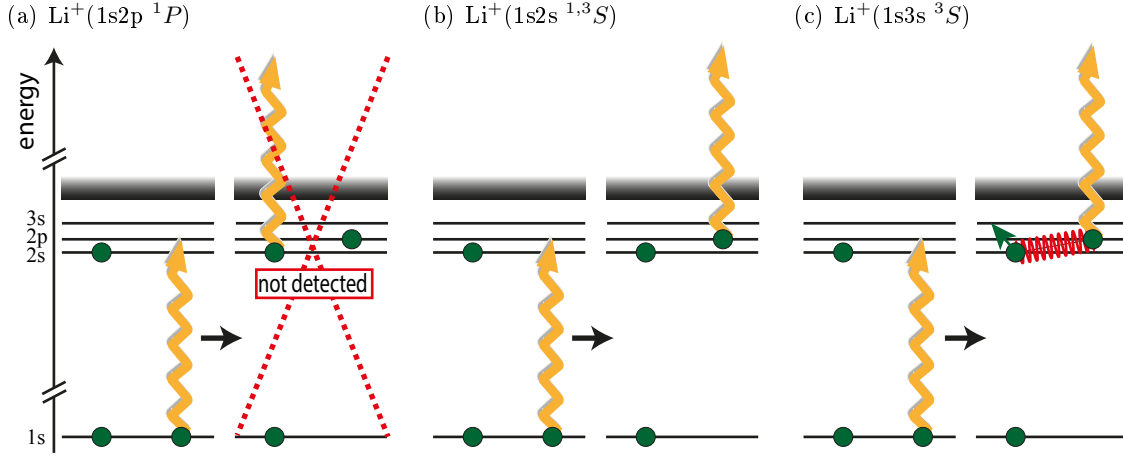


Figure 6.2: Selected reaction channels of TPDI. In (a) ionization of the $2s$ -electron after excitation to the $\text{Li}^*(1s2s2p)$ excited state is shown. As the $1s$ and $2p$ electron couple to a spin-singlet, the Li^+ ion will decay to the ionic ground-state and is thus not detected (cp. App. D). If, the $2p$ -electron is ejected in the second step (b) and (c), both ionization (b) and IE (c), are detected. Although, for IE only the triplet-configuration of the $1s3s$ electron pair is detected. The jagged red line indicates electron correlation.

and (c) illustrates reactions, where the $2p$ -electron is removed. For pure $2p$ removal all final states are detected due to their long lifetime. In case of the triplet-configuration this is due to the Pauli exclusion principle and for singlet-spins only a two-photon transition allows for the decay to the ionic ground-state. If the $2s$ -electron is excited to another state during $2p$ -ejection only triplet states are observed as all singlet states decay to the ionic ground-state. In summary, all excited triplet-states and the $\text{Li}^+(1s2s)$ singlet state are detected.

Measurement	Filter	Thickness (nm)	Intensity (W/cm^2)	Ratio ($I_{\text{fund.}}/I_{\text{harm.}}$)
Low intensity	Zr	294	2×10^{11}	2
High Intensity	Al	100-300	$(2 - 4) \times 10^{13}$	$10^3 - 10^5$

Table 6.1: Ratio R between fundamental ($E_\gamma = 59.4$ eV) and 3rd harmonic radiation ($E_\gamma = 178$ eV) and intensity of the measurements for low and high intensity.

In order to study space charge effects due to the large number of ions created in the laser focus together with the impact of 3rd harmonic on the Li^+ , as well as, the Li^{2+} momentum distributions, experiments for low and high intensity of the FLASH laser radiation have been conducted. The results for SI are illustrated in Fig. 6.3. The high intensity measurements have been performed employing different Al-filters of thickness (100-300 nm),

thereby reducing the relative contribution of harmonic radiation. As neither qualitative nor quantitative differences between the individual datasets were observed, they were summed up and are displayed together. In contrast, a Zr-filter was used for the low intensity experiments, thus reducing the contribution of the fundamental wavelength considerably (cp. App. C). Table 6.1 give an overview on the exact experimental conditions for the respective measurements.

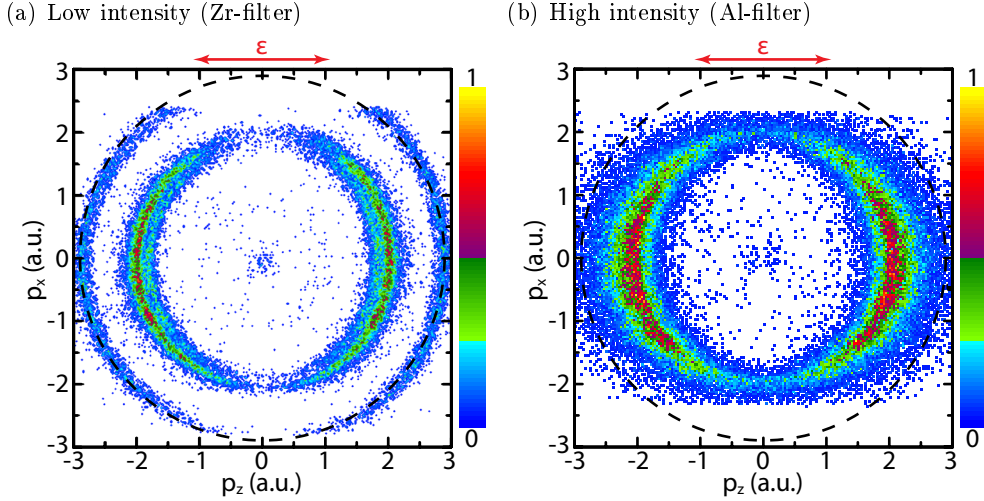


Figure 6.3: Li^+ recoil ion momentum distributions for low (a) and high (b) intensities of the fundamental wavelength. In both graphs the momentum out-of-plane, i.e., in p_y -direction is restricted to values below 0.25 a.u.. The dashed ring marks the final-state momentum associated with ionization through third harmonic radiation and ϵ shows the orientation of the laser polarization.

Comparison of Fig. 6.3(a) and (b) shows great differences between the measurements for high and low intensity. The Li^+ recoil-ion momentum distributions, i.e., cross sections, for low intensity are evidently better resolved than the ones obtained at high intensity. This might partly be attributed to the lower number of ions created in the laser focus (see discussion below) in case the Zr-filter is used. Moreover, it is found that Fig. 6.3(a) shows an increased number of lines² in contrast to panel (b), where essentially a single broad line is visible around 2 a.u. of momentum. In both panels the dashed ring marks the final-state photo-electron momentum and hence energy associated with ionization of a 1s electron through 3rd harmonic radiation. Clearly, there is a strong contribution of this channel to the final-state cross section in (a). Furthermore, very weak lines appear

²The rings or circles in the momentum distribution correspond to fixed energies and can therefore be associated with certain reaction channels. For this reason they will also be referred to as photo-lines in the following.

for vanishing final-state momenta and at $p_{\text{tot}} \approx 1$ a.u.. It is also found that the line for photo-electron momenta of 2 a.u. splits up into two. The reason for this is that the line at higher momenta corresponds to SI by two-photon absorption while the one at smaller momenta is due to IE to the $\text{Li}^+(1s3s)$ -state (cp. Table 6.2).

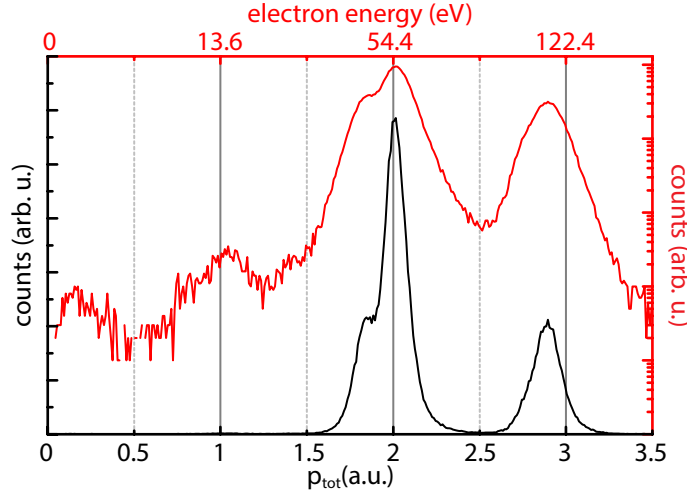


Figure 6.4: Momentum distribution of the absolute value of the 3D-momentum vector as observed in the low-intensity measurement. The data is displayed both, on a linear (black) and logarithmic scale (red). In the logarithmic scaling the low energy lines at $p_{\text{tot}} \approx 1$ a.u. and $p_{\text{tot}} \approx 0$ a.u. are visible.

The mapping of the observed structures to the respective reaction channels is achieved through inspection of Fig. 6.4 where the cross section for the low intensity measurement is shown in dependence of the total final-state momentum. Taking into consideration energy and momentum conservation, i.e., Eqs. (2.1) and (5.2), as well as, the energy of the intermediate state populated, the reaction channels listed in Table 6.2 are identified.

Regarding the obtained cross section for high intensities, only the two lines for two-photon SI with the intermediate resonance are observed. Additionally, single counts in the center of the distribution, assigned to the hollow ionic lithium states (Fig. 6.3(b)) appear, however, no traces of K-shell single ionization at $p_{\text{tot}} \approx 2.9$ a.u. is visible. Thus, indicating the negligibility of 3rd harmonic radiation for the high intensity measurements. An upper limit for the contribution of 3rd harmonic radiation to the cross section for high intensities is found by integration over the momenta associated with the two-photon and 3rd harmonic reactions, respectively. This yields a value of 0.5 % of the total cross section, when applying the Al-filters.

Figure 6.5 shows the photo-electron angular distribution (PAD) as observed in two-photon SI without excitation. The red line shows a fit to the data, with the parametrization given

p_{tot} (a.u.)	E_e (eV)	E_γ (eV)	Int.-state	Final-state
≈ 0	≈ 0	$1 \cdot 178.2$		$\text{Li}^+(3\text{snl})_{n>4}$
≈ 1.0	≈ 13.6	$1 \cdot 178.2$		$\text{Li}^+(2\text{snl})_{n>4}$
1.79	43.6	$2 \cdot 59.4$	$\text{Li}(1s2s2p)$	$\text{Li}^+(1s3l)$
2.02	55.5	$2 \cdot 59.4$	$\text{Li}(1s2s2p)$	$\text{Li}^+(1s2s)$
2.75	102.9	$1 \cdot 178.2$		$\text{Li}^+(1s3l)$
2.88	112.8	$1 \cdot 178.2$		$\text{Li}^+(1s2s)$

Table 6.2: Overview on the observed photo-lines, with the respective final-state electron energies, the number of absorbed photons and the ionic final state. The energies of the hollow Li^+ -states have been retrieved from [Scu06].

in Eq. (2.16). Taking into account that two photons are absorbed they include β_2 and β_4 . It is found that the angular distribution is dominated by β_2 , whereas the value of β_4 is almost negligible. In addition a strong s-wave contribution is apparent, as the peak normalized PAD exhibits a considerable probability for emission perpendicular to the laser polarization axis. The extraction of the respective PAD for the IE reaction showed almost the same partial-wave composition.

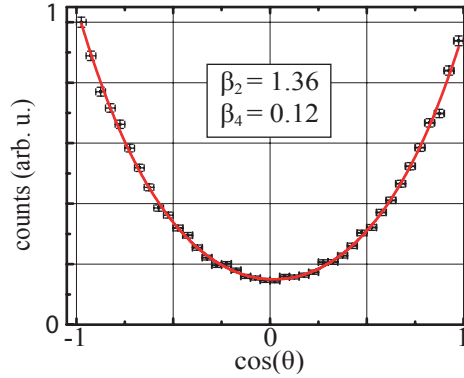


Figure 6.5: Angular distribution as observed in the high intensity measurement of two-photon SI. The red line is a fit to the data according to Eq. (2.16) and the retrieved β -parameters, which yield excellent agreement with the experimental data.

Space Charge and Resolution: In the comparison of Fig. 6.3(a) and (b) it was found that the cross sections obtained with high intensities were smeared out, in particular in p_z -direction. The respective longitudinal momentum distributions, parallel to p_z and ϵ are illustrated in Fig. 6.6. Clearly, the peaks originating from two-photon absorption at ($|p_z| = 2$ a.u.) dominate the high-intensity spectra (red line) and are considerably wider as

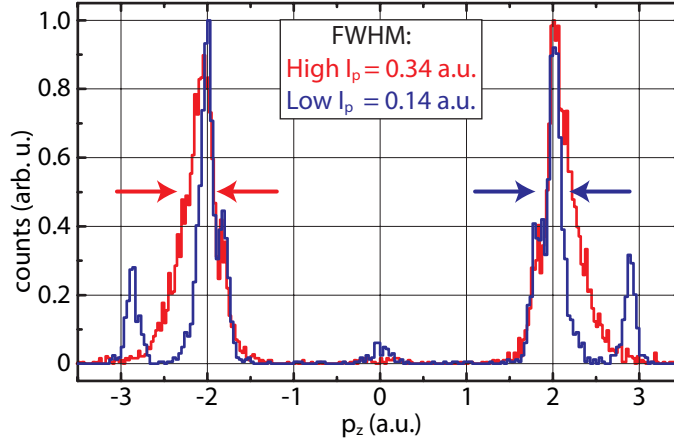


Figure 6.6: Longitudinal Li^+ momentum distributions as obtained with low (blue) and high (red) peak intensity I_p . The transverse momentum components (p_x and p_z) are restricted to absolute values below 0.2 a.u.. Evidently, the peaks emerging from 3rd harmonic radiation are not apparent for high I_p . Moreover, for high I_p the center-of-mass is shifted towards higher values, although the "rising edge of the peaks is not.

in the low intensity (blue line) case. Furthermore, there are no traces of ionization by 3rd harmonic radiation ($|p_z| = 2.9$ a.u.) in the high-intensity distribution. Comparison of the two-photon peaks yields that the center-of-mass (cms) is shifted towards higher momenta, while the position of the maxima stays constant for high intensities. The shift in the cms is due to a "smeared out" falling edge³ of the peaks and resulting in a modified shape.

These findings can not be assigned to any physical process originating from two- or three-photon absorption. For two-photon absorption, the maximum final-state momentum is approximately 2 a.u. and in the three-photon reaction higher momenta are expected. In [Kur10] it was found that space charge originating from the creation of many ions (≈ 80) at the same instant of time, led to a shift and a broadening of the observed final-state momenta in single ionization. This is understood by taking into account the small kinetic energy of the recoil ions for photo-ionization, which amounts to approximately 4.23 meV for the studied case. Therefore, they are highly sensible on changes in the local electric potential.

However, the total number of ions here is considerably less compared to [Kur10]. In addition space-charge is expected to broaden momentum structures in both directions towards higher, as well as, lower momenta. A particle might be slowed down overcoming the potential created by space-charge but might also be accelerated sliding down the potential. It is thus expected, that the impact of space-charge on the final-state momentum crucially

³The falling edge, here means the edge towards large absolute values of p_z -momenta.

depends on the relative time-scales of the "explosion" of the charge cloud in comparison with the velocity of the ions due to ionization and their extraction through the spectrometer field.

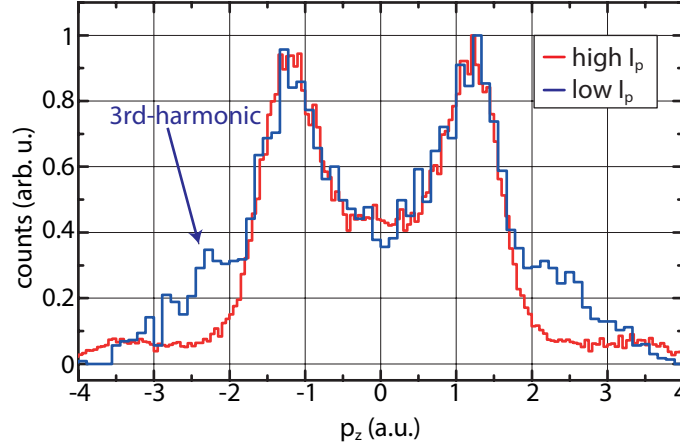


Figure 6.7: Projection of the Li^{2+} recoil ion momentum on the longitudinal momentum axis, for low peak intensity I_p (blue) and high peak intensity (red).

This finding is confirmed by studying the effect of the high and low intensity on the longitudinal momentum distributions of doubly charged lithium. These are shown in Fig. 6.7⁴. The major difference between the two distributions in Fig. 6.7 is constituted by an additional peak for low intensities, which reaches its maximum at ≈ 2.4 a.u. and extends up to 2.7 a.u.. Taking into account, the ionization potential for DI of 81 eV and the high relative contribution of 3rd-harmonic radiation for that measurement, this peak is assigned to K-shell ionization by the 3rd-harmonic. There is, however, no shift or broadening of the peaks apparent in both distributions observed. This indicates that no broadening due to space charge is present for the Li^{2+} momentum distribution and hence $\Delta p_{\text{FWHM}}(2+) = \sqrt{2} \cdot \Delta p_{\text{FWHM}}(1+) \approx 0.2$ a.u..

6.2 Double Ionization

In the following two-photon double ionization (TPDI) will be studied for the case of an intermediate resonance. The reaction investigated below is sequential concerning the absorption of photons and simultaneous regarding the emission of the two electrons. Its

⁴Note, that the data presented here is from the same experimental runs as the single ionization discussed above.

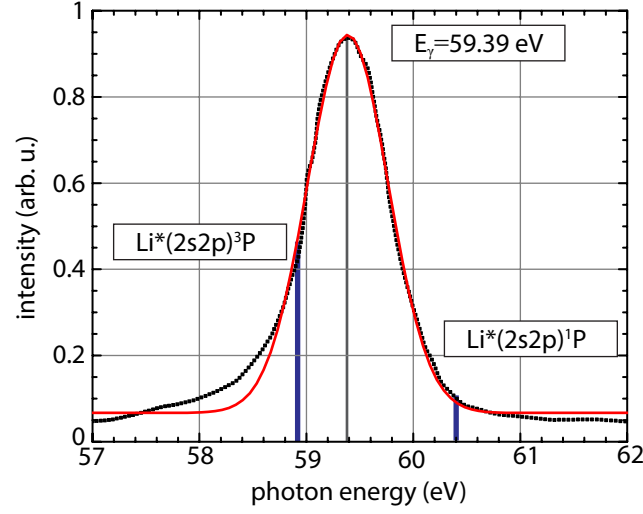
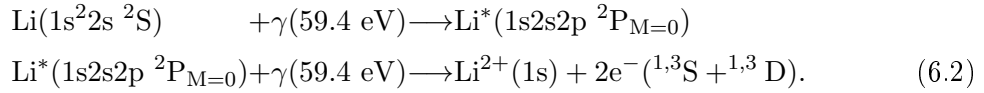


Figure 6.8: Energy distribution of the emitted FLASH radiation for the measurements discussed. The central photon energy amounts to $E_\gamma = (59.4 \pm 0.5)$ eV corresponding to a wavelength of 20.9 nm. The energies of the two possible spin configurations for the electrons in the L-shell, 58.9 eV for the triplet and 60.4 eV for the singlet configuration are indicated by the blue lines. The distribution features an almost Gaussian shape, which leads to the conclusion that FLASH was operated in or at the onset of the saturated regime.

reaction equation reads:



In the first step the doubly excited and aligned $\text{Li}^*(1s 2s 2p^2 P_{M=0})$ -state is excited by the absorption of a single photon. Subsequently, in the second step an additional photon ejects both electrons in the valence shell simultaneously. As the interaction of photons is of single-particle nature⁵, DI is solely mediated through electron correlation.

In Sec. 2.5 selection rules for the double electron ejection have been presented. It was found that in particular triplet final-states exhibit a number of constraints regarding the energy sharing and mutual emission angles of the outgoing electrons. As Eq. (6.2) demonstrates, both triplet and singlet continuum electron wavefunctions are reached. It is therefore instructive to not only focus on the second photon absorption but also inspect the excitation process.

Figure 6.8 shows the wavelength distribution of the FLASH radiation, together with the respective energies of the $\text{Li}^*(1s(2s 2p^1 P)^2 P)$ and $\text{Li}^*(1s(2s 2p^3 P)^2 P)$ states according to

⁵At least for the wavelengths considered.

[Chu97]. Clearly, the wavelength distribution favors excitation of the triplet excited state. Moreover, the excitation cross sections for these states are vastly different. As found in [Chu97] the ratio between them is given by

$$R_{3/1} = \frac{\sigma(1s^2 2s^2 S \rightarrow (1s(2s2p^3 P)^2 P))}{\sigma(1s^2 2s^2 S \rightarrow (1s(2s2p^1 P)^2 P))} \approx 20. \quad (6.3)$$

Taking into account the ratio in photon flux of $R_{3/1}(\hbar\omega) = 7$ a total ratio of the triplet compared to the singlet excited states of $R_{3/1}^{\text{total}} \approx 140$ is derived for the experiments presented below. Given that photon absorption in the second step of Eq. (6.2) does not induce spin-flips the DI cross section is expected to be dominated by triplet final-states of the two-electron continuum wavefunction.

In order to ensure this finding a Hartree-Fock calculation was performed to determine the mixing ratio of the two states, which is not given in literature. It was found that the states are 96 % pure, meaning that the state denoted by $\text{Li}^*(1s(2s2p^3 P)^2 P)$, features a contribution of 4 % of $\text{Li}^*(1s(2s2p^1 P)^2 P)$ and vice versa. As a consistency check the same calculation was performed for states where the $(1s2s)$ electron pair was coupled first, which yielded mixing ratios of roughly 50% in agreement with literature [VH01]. In summary, the initial state for the photo-double ionization reaction (second line in Eq. (6.2)) consists of roughly 95.3 % $(2s2p^3 P)$ and 4.7 % $(2s2p^1 P)$.

6.2.1 Two- and Three-Photon Double Ionization

Figure 6.9 shows the obtained recoil-ion momentum distribution for two and three-photon absorption from ground-state lithium. It directly maps the sum momentum of the emitted electrons and thus contains information on the mutual emission angle and energy sharing of the two emitted electrons. The two inner rings in Fig. 6.9(a) mark the maximum achievable momentum for the two extreme cases of energy sharing for the two-photon process. The black dashed circle corresponds to the case where one electron, the one interacting with the light field (compare Sec. 2.1), takes all the excess energy and therefore the second electron is just liberated to the continuum with little to no kinetic energy. The solid ring maps the achievable momenta if both electrons are emitted into the same direction with equal energy. This corresponds to the maximum momentum, which can be imprinted on the doubly-charged ion for double electron escape in the investigated case. Ions recorded with no momentum at all originate from events where the electrons are emitted back-to-back with equal energy sharing. from Fig. 6.9(b) it is found that over 90 % of the integrated counts lie within the boundary conditions set by the kinematics of the two-photon reaction (see also Table 6.3). Here, the respective reachable momenta are marked with the black

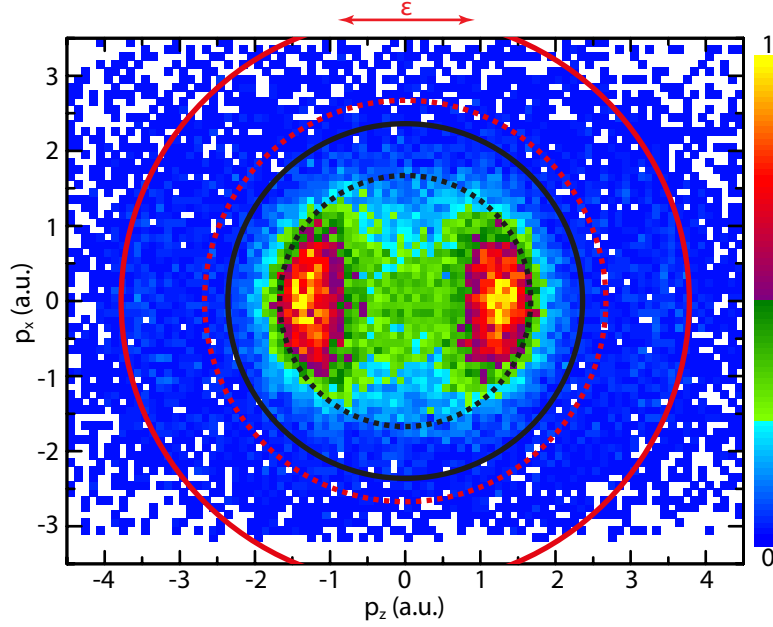
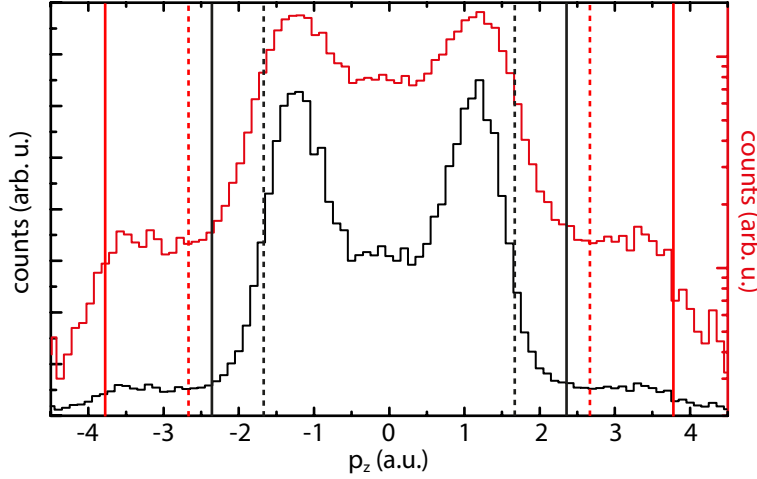
(a) Li^{2+} momentum distribution(b) Projection of (a) on the p_z -axis

Figure 6.9: Recoil-ion momentum distribution of doubly charged lithium ions (a) and its projection on the p_z , i.e, laser polarization axis (b). The dashed and solid rings (lines) correspond to the maximum reachable momentum for extreme asymmetric energy sharing and equal energy sharing, respectively. Hereby, the black rings mark two-photon absorption the red ones three-photon absorption. The data in (a) is integrated over p_y .

dashed and solid lines.

Absorbed photons	$E_{\text{exc.}}^{\text{total}}$ (eV)	$p_{\text{max}}^{\text{lon}}(E_{e1} \approx E_{\text{exc.}})$ (a.u.)	$p_{\text{max}}^{\text{lon}}(E_{e1} = E_{e2})$ (a.u.)
2	37.8	1.67	2.36
3	97.2	2.67	3.78

Table 6.3: Final-state momenta expected for certain energy sharings between the outgoing electrons for two- and three-photon absorption from ground-state lithium at a photon energy of 59.4 eV.

Clearly, there are also structures outside the kinematics set by two-photon absorption from the ground-state, as the Li^{2+} cross section shows peaks close to the maximum achievable momentum associated with three-photon absorption (see Fig. 6.9(b)). The peaks are strongly oriented along the laser polarization axis and appear at momenta of $p_z \approx 3.5$ a.u.. Their magnitude is on a 5 % level compared to the peaks originating from the two-photon reaction. The special electron-emission configurations, i.e., asymmetric and symmetric energy sharing, for the three-photon process are marked by the dashed and solid red rings and lines, respectively. Their absolute values are found in Table 6.3.

In contrast to single ionization studied before not only events in which the p -electron absorbs the second photon are recorded (see Fig. 6.2), but also those where the s -electron interacts with the light field. In fact, comparing the radial wave-function of s and p states it is noted that while s -states have a finite probability of presence close to the nucleus, p radial wavefunctions exhibit a node at the nucleus resulting in larger mean distance from the atomic core. As discussed in Sec. 2.1 the final-state momentum, in photo-ionization, has to originate from nucleus-electron interaction as photons carry hardly any momentum. Therefore, the photo-absorption cross section for the $2s$ -electron exceeds the one of the $2p$ electron. For an excess energy of approximately 54 eV, the ratio in the cross sections is $R_{\sigma(2s)}/\sigma(2p) \approx 5$. Therefore, interaction of the light field with the $2s$ -electron will be the major source of double ionization in the second step of Eq. (6.2).

Three-photon double ionization As discussed above there are structures in Fig. 6.9 beyond the maximal momentum of the two-photon reaction, arising from three-photon double ionization. To not confuse the processes of two- and three photon DI, the three-photon reaction will be abbreviated *3PDI* in the following. The relevant reaction equations

for 3PDI are

$$\begin{aligned} \text{Li}^*(1s2s2p \ ^2P_{M=0}) + \gamma &\rightarrow \text{Li}^+(1s2s \ ^1S) + e^- (52.5, 54.4 \text{ eV}) \\ \Rightarrow \text{Li}^+(1s2s \ ^1S) + \gamma &\rightarrow \text{Li}^{2+}(1s) + e^- (44.7, 42.8 \text{ eV}) \end{aligned} \quad (6.4)$$

$$\begin{aligned} \text{Li}^*(1s2s2p \ ^2P_{M=0}) + \gamma &\rightarrow \text{Li}^+(1s2p \ ^1P) + e^- (51.2 \text{ eV}) \\ \Rightarrow \text{Li}^+(1s2p \ ^1P_{M=0}) + \gamma &\rightarrow \text{Li}^{2+}(1s) + e^- (46.0 \text{ eV}), \end{aligned} \quad (6.5)$$

where the continuum wavefunctions of the electrons and the absorption of the first photon have been omitted. There is no triplet configuration in Eq. (6.5), as the $2p$ -electron stems from the K-shell. For this reason it must couple to a singlet state with the $1s$ electron. The two values for the electron energies in Eq. (6.4) denote the energies for the singlet and triplet spin-configuration, respectively. In Fig. 6.9(a) 3PDI manifests as a faint line close to $p_{\max}(3\text{PDI})$ and in (b) especially on the logarithmic scale (red line) it is observed that it peaks around $p_z \approx 3.5$.

Ionization through the 3rd harmonic is excluded as the origin of the observed intensity for large momenta. As it was shown in Fig. 6.7 the removal of a $1s$ -electron through 3rd harmonic radiation would result in a peak close to 2.5 a.u. in longitudinal direction, which is not observed here. Another reaction which can be omitted is constituted by:

$$\begin{aligned} \text{Li}(1s^2 2s \ ^2S) + \gamma &\rightarrow \text{Li}^+(1s^2 \ ^1S) + e^- \\ \text{Li}(1s^2) + 2 \cdot \gamma &\rightarrow \text{Li}^{2+}(1s) + e^-. \end{aligned} \quad (6.6)$$

Here, the second ionization step requires the non-sequential absorption of two photons⁶. Though possible, this process is unlikely as the sequential absorption is energetically allowed. (cp. Secs. 6.1 and 4.2.2).

In Sec. 6.1 it was noted that the pulse length of the FLASH radiation is on the order of ≈ 150 fs for this measurement. Considering that all excited states of the singly charged ion (Li^{+*}) reached here, are long-lived compared to this time-scale it is assumed that 3PDI proceeds sequentially. This implies that the electrons do not exchange energy, apart from the rare IE, during ionization. Even more importantly there will be hardly any post collision interaction (PCI) and thus the electron energies shown in Eqs. (6.5) and (6.4) are not changed by electron correlation.

As seen above the kinetic energies of the first emitted electron, dubbed e_1 from now

⁶The possible intermediate $\text{Li}^+(1s2p \ ^1P)$ -state, 62.2 eV above the ground-state is not in the FLASH energy spectrum

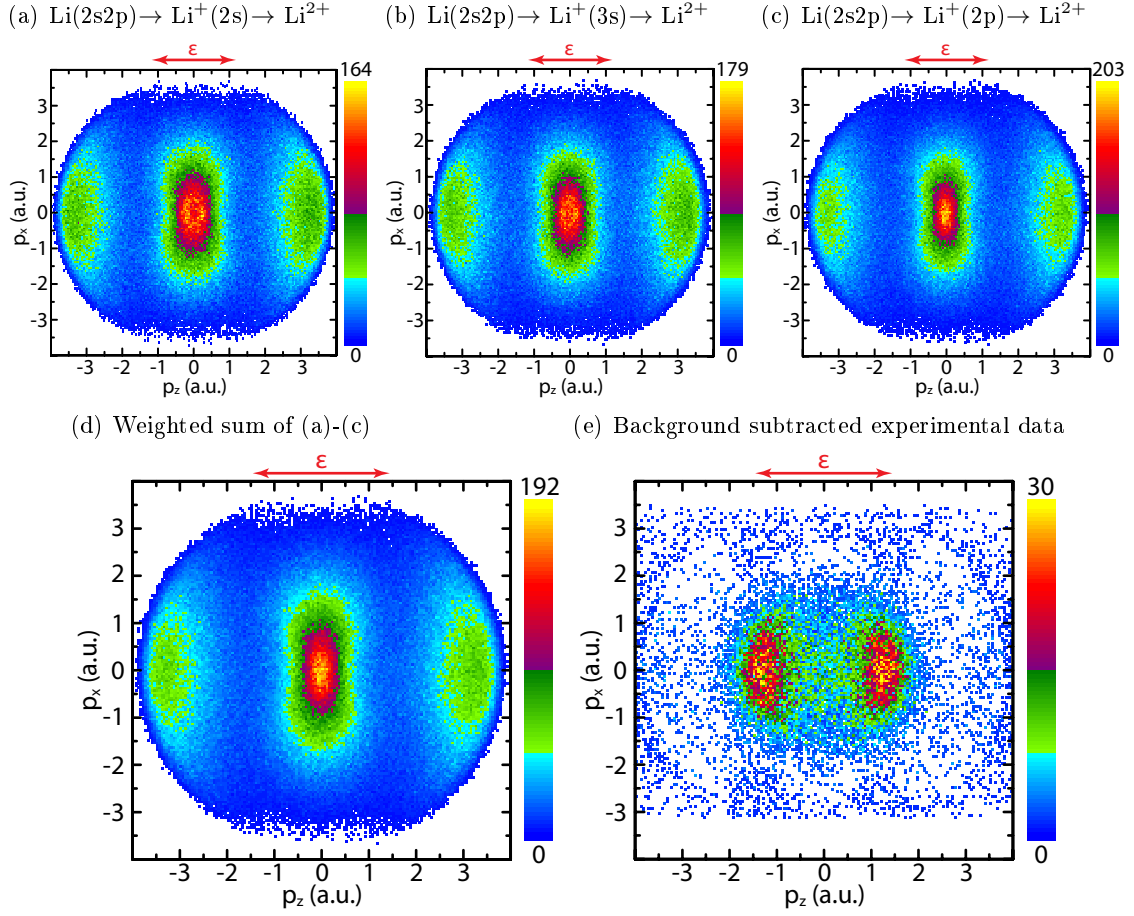


Figure 6.10: Results of the Monte-Carlo simulation as described in the text. In (a)-(c), the results of the individual reaction channels are shown according to Eqs. (6.4) (a) and (6.5)(c). Furthermore, the observed IE-channel of Eq. (6.4) is simulated in (b). Consequently, (d) illustrates the resulting momentum distribution, when (a) to (c) are weighted according to the relative ionization cross section of $\text{Li}(1s2s2p) \rightarrow \text{Li}^+(1s2s)$ and $\text{Li}(1s2s2p) \rightarrow \text{Li}^+(1s2p)$ and the obtained branching ratio between ionization and ionization excitation. Finally, (e) shows the results obtained when the scaled simulated is subtracted from the experimental distribution.

on and the electron ejected in the second step e_2 are very similar. At most they differ by 11.6 eV for the case of the intermediate 3S -state. If we postulate the emission of $e_{1,2}$ completely independent, this can result in recoil-ion momenta close to zero ($p_{\text{tot}} \approx 0$). In a simple picture the ion gets a kick in phase space from emission of e_1 , preferentially into direction of the laser polarization and ends up with a momentum closely resembling the ones obtained in single ionization⁷. Consequently, the ionization of e_2 gives another kick,

⁷Its not completely the same since in single ionization not all final states are detected.

again in direction of the laser polarization. Both momentum transfers can either add up or cancel each other leading either to very large (line at 3.5 a.u.) or very small final momenta of the ion. As a result, part of the 3PDI distribution overlaps with the distribution for two-photon absorption.

Nevertheless, the complete independence of both, the absorption and the electron emission, allows for the deduction of the final-state momentum distribution. With the known excess energies of the electrons (see Eqs. (6.5) and (6.4)), the known angular distribution from ionization of the $2p$ -electron (see Fig. 6.5) and assuming a pure p -wave angular distribution for ionization from the $2s$ -state the reaction can be simulated. Figure 6.10 shows the results of this simulation (a)-(c). Adding this simulated 3PDI contributions according to their respective cross sections (d) and scaling them to match the experimentally-observed high-energy 3PDI distribution leads to a “background free”, i.e., no three-photon contributions, final-state momentum distribution for the two-photon reaction as shown in Fig. 6.9(e).

The simulated data has been acquired by performing a *Monte Carlo* simulation of the reaction. This implied a simulation of each of the single ionization processes with the corresponding sequential removal of the second electron, over the full solid angle. As a result 3D-momentum vectors have been obtained for a total number of 5×10^5 events per reaction channel. Agreement with the experimental data was checked on SI of the $2p$ -electron. In order to subtract the simulated 3PDI data from the experimentally-measured recoil-ion momentum distributions, the simulated data has been treated likewise as the experimental data. In a first step the individual momentum components (p , p_x , p_y and p_z) have been calculated, from the "raw" momentum vectors. Subsequently, the data was integrated over p_y . Therefore, the results shown in Fig. 6.10(d) should closely match the partly hidden 3PDI distribution in Fig. 6.9. The remaining uncertainty in the simulation stems from the neglect of any populated states other than the $\text{Li}(1s2p)$ in the reaction channel, where e_1 originates from the $2s$ -shell.

In the experimental data the absolute number of 3PDI-events in the momentum interval $3.1 \text{ a.u.} \leq p \leq 4.0 \text{ a.u.}$ was retrieved through background subtraction⁸. Consequently, the simulated spectrum was scaled to match the number of counts from the experimental one in that same interval. Finally, the scaled simulated distribution was subtracted from the experimental data and Fig. 6.10(e) was gained.

It is found that the subtraction of the simulated spectra provides convincing results concerning large momenta, indicated by the almost complete absence of events outside the two-photon distribution. That the 3PDI distribution does not completely vanish is most likely owed to the low statistics of the experimental data for 3PDI. This strongly suggests

⁸In this case the TPDI distribution and noise.

the entirely independent emission of the two outgoing electrons for 3PDI. Thus, it is inferred that the same holds for the contribution of 3PDI for momenta smaller than 2.36 a.u., e.g. the part of the distribution that overlaps with the two-photon reaction. In the comparison of Fig. 6.9(a) with Fig. 6.10(e) no major changes in the in the cross section below $p = 2$ a.u. are observed. The only considerable quantitative difference is constituted by a slight reduction in the relative magnitude of the cross section in the momentum interval $0 \text{ a.u.} \leq p \leq 1 \text{ a.u.}$. With the 3PDI contribution the plateau reaches a magnitude of approximately 50 % of the peak value of the cross section, which is reduced to 40 % if 3PDI is subtracted. Nevertheless, the obtained results are important, when the experimental data is compared to theoretical calculations which solely consider the two-photon reaction. For the following qualitative discussion on the two-photon reaction however, the directly-measured momentum spectra are used, without inferring any assumptions.

Photo-Double ionization: In the following two-photon DI at 59.4 eV will be treated as PDI from the doubly excited state intermediate $\text{Li}^*(1s2s2p)$ state. Figure 6.9(a) shows that this reaction results in recoil ion momentum spectra strongly peaked along the laser polarization axis. The two main peaks are visible at final-state momenta around $p = \pm 1.30 \text{ a.u.}$ ⁹, just within the dashed black circle, tagging asymmetric energy sharing. Interestingly, there is no strong minimum inbetween the two peaks. Instead a plateau is visible. This is also not changed when subtracting the 3PDI simulation as seen in Fig. 6.10(e). Furthermore it is noted that an increased count-rate persists up to the maximum reachable energy, i.e. the solid black circle. Taking into consideration the PDI mechanisms discussed in Sec. 2.2.1, it is found that at an excess energy of roughly 40 eV above threshold, both the TS1 and SO process, as well as their interference, are expected to contribute to the total cross section (cp. Fig. 2.4). However, TS1 is assumed to dominate.

Hereafter, possible electron emission configurations leading to the observed cross section are discussed. The findings will be based on energy and momentum conservation, as well as, the selection rules for double electron escape presented in Sec. 2.5. Where possible the assignment to the respective PDI mechanisms will be given. As the selection rules strongly depend on the symmetry of the final state, it is instructive to study the reaction equations of the process. In analogy to Eq. (2.29), they read

$$\text{Li}(1s(2s2p \ ^1P) \ ^2P_{M=0}^o) + \gamma \longrightarrow \text{Li}^{2+}(1s \ ^2S^e) + 2e^- \ (^1S^e; \ ^1D^e) \quad (\textit{singlet}) \quad (6.7)$$

$$\text{Li}(1s(2s2p \ ^3P) \ ^2P_{M=0}^o) + \gamma \longrightarrow \text{Li}^{2+}(1s \ ^2S^e) + 2e^- \ (^3S^e; \ ^3D^e) \quad (\textit{triplet}), \quad (6.8)$$

⁹Note that this maximum is inferred from the 2D distribution. In the projection it will slightly shift towards lower momenta due to shape of the cross section.

where the initial photon absorption was omitted. As shown above, the major contribution to the total cross section is expected to originate from Eq. (6.8), as this state is more likely excited. As a consequence, the relative contribution of the singlet-states can be estimated from the mixing due to electrostatic interaction, which was found to be 4.7 % (cp. Sec. 6.2). The following discussion will always assume co-planar geometry, i.e. $\phi_1 = \phi_2 = 0$, which means that no out-of-plane momenta will be considered.

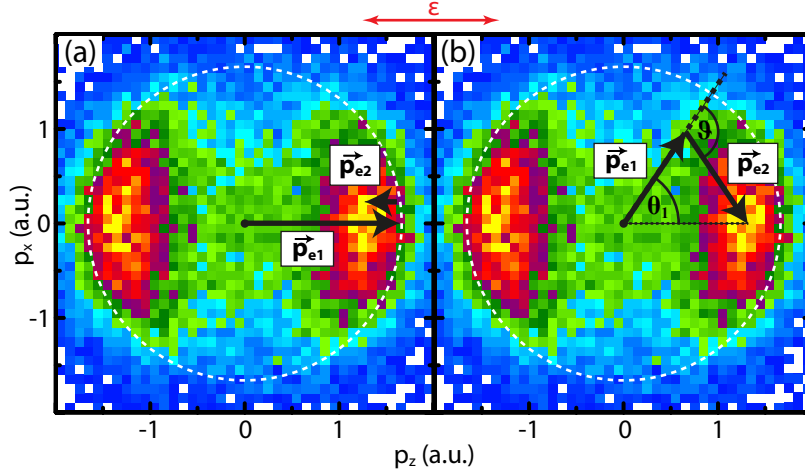


Figure 6.11: Possible electron emission patterns in PDI of $\text{Li}((1s2s2p))$. In (a) an electron configuration for asymmetric energy sharing is shown, while (b) illustrates a possible configuration for equal energy sharing. The arrows are to scale.

Figure 6.11 illustrates two conceivable geometries concerning energy sharing and mutual emission angles of the two electrons, which result in a final-state momentum of the recoil ion in the center of the main peaks. For better visibility only the region including the main features of PDI is displayed. In panel (a), the case of asymmetric energy sharing and back-to-back emission is displayed. From energy and momentum conservation the final state momenta required to explain the main peaks are found to be $p(e_1) = 1.63 \text{ a.u.}$ ¹⁰ and $p(e_2) = 0.34 \text{ a.u.}$. The back-to-back emission could be explained by electron repulsion in the continuum for both, the SO and the TS1 model. According to the selection rules this geometry is allowed for all encountered final states and hence is a very probable geometry to occur.

If only the SO model is considered, the line of argument is the following. From the relative cross section for photon absorption (cp. Sec. 6.2.1) it is known that most likely the 2s-electron will absorb the impacting photon. Consequently, its angular emission pattern will exhibit a dipolar-shape ($\beta_2 \approx 2$) along the laser polarization axis. Ejection of the

¹⁰The faster, i.e., more energetic, electron will always be denoted e_1 .

second electron stems from the projection of its wavefunction onto the new eigenstates of the system. Given that the occupied $2p$ -orbital is aligned along the laser polarization axis, also here a dipole-like emission pattern along ϵ is expected¹¹. In addition PCI would suppress parallel and favor back-to-back emission.

In contrast, Fig. 6.11(b) illustrates the equal energy sharing case. Here, the peak of the distribution is reached for the same opening angle for both electrons with respect to ϵ , i.e. $\theta = \theta_1 = -\theta_2 \approx 60^\circ$, which results in a relative emission angle of $\vartheta = \theta_1 - \theta_2 \approx 120^\circ$. However, this final-state configuration is unfavored for the triplet final states of the studied reaction. For the $^3S^e$ -state, equal energy sharing of the outgoing electrons is forbidden independent of the emission angle (selection rule **E** (cp. Sec. 2.5)). Moreover, for both encountered triplet two-electron continuum wavefunctions emission in the same hemisphere with the same opening angle with respect to the quantization axis (here ϵ) is rendered unfavored by selection rule **G**. As a result, this seems an unlikely geometry, since the major contribution to the cross section is expected to stem from the triplet-states.

Finally the plateau between the two main peaks, where the ion momentum is small. In order to not imprint any momentum on the recoiling ion, e.g. in the center of the distribution, the electrons have to leave the atom back-to-back with equal energy sharing. As a result, this excludes all triplet final-states as possible candidates for the plateau observed between the main structure. This originates from the Pauli exclusion principle for identical fermions or likewise selection rule **D**. In fact, all geometries close to $p_{\text{tot}} = 0$ are unfavored for triplet final states, due to selection rules **C** and **F**. Hence, it is found that the plateau is most likely caused by singlet final states. It has to be considered that the discussed figures are projections onto the p_x - p_z -plane, however, the plateau persists even if the projected p_y momenta are restricted to small values ($|p_y| < 0.1$ a.u.). A likely explanation is the higher cross section for DI in case of the singlet configuration (cp. Sec. 2.2.2), which compensates for the small relative abundance of only 4% in the initial state. A detailed discussion on this finding will be given in Sec. 6.4.

6.3 Comparison with Theoretical Predictions

The further interpretation of the obtained experimental data arises as a result of comparison with two different calculational approaches, performed by *Armstrong et al.* and *Kheifets*. In these calculations the time-dependent close-coupling (TDCC) and convergent close coupling methods (CCC) are employed, as described in Secs. 2.4.1 and 2.4.2, respectively. The specific details on how the lithium atom and the process of PDI is treated in

¹¹The slow electron in SO is only expected to show an isotropic angular distribution for initial s-states and if the m-sublevels are equally distributed.

the theoretical models are found in [CP03; Col09; CPR05; CP12] for the TDCC method and in [KFB09; Khe11; Khe10a; Khe10b] for the CCC method¹². Both theories omit the excitation process and thus calculate PDI from the $\text{Li}^*(1s2s2p\ ^2P_{M=0})$ -state. In both calculations the result for singlet and triplet two-electron continuum states have been calculated separately.

Figure 6.12 shows the experimental and theoretical results obtained for PDI from the

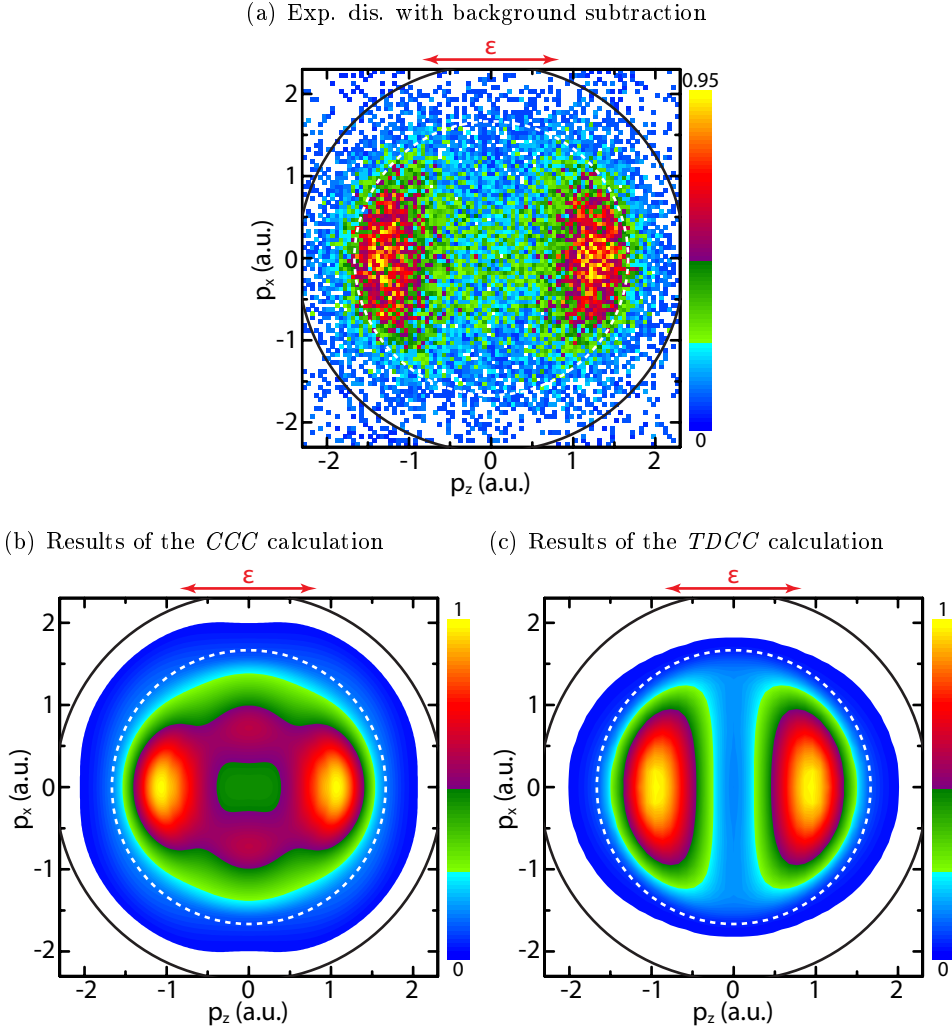


Figure 6.12: Comparison of the experimental Li^{2+} cross section (a) with calculations employing the *CCC* [KFB09] displayed in (b) and *TDCC* (c) [AC12] approach to solve the Schrödinger equation. The theoretical spectra are normalized to the interval $[0, 1]$ as is the experimental data. To account for outliers, at the given statistics, the color scale for the experimental distribution runs from 0 to 0.95. All datasets are integrated over p_y

¹²The first reference for both cases describes the calculation in detail.

$\text{Li}^*(1s2s2p\ ^2P_{M=0})$ -state at a photon energy of $E_\gamma = 59.4$ eV. The theoretical distributions comprise the deduced abundance of excited singlet and triplet states, respectively. That means the theoretical results for the singlet configuration have a weighting factor of approximately 4 % and the results for triplet final-states are weighted with 96 %¹³ (see Table 6.4 for the relative contributions). Both theories (Fig. 6.12(b) and (c)), show two main peaks oriented along the laser polarization axis ϵ in agreement with the experimental cross section. However in both calculations the peak is observed at smaller longitudinal momenta ($p_z(\text{TDCC}) = \pm 1$ a.u.; $p_z(\text{CCC}) = \pm 1.1$ a.u.) as compared to the experiment. ($p_z(\text{exp}) = \pm 1.2$ a.u.). While, the transverse (p_x -direction) extension of these peaks is comparable in experiment and the TDCC calculation, the main peaks observed in the CCC calculation show a considerably reduced transverse width.

Regarding the momentum distribution for small longitudinal momenta, all three cross sections exhibit different structures. As discussed above, in the experimental data the cross section displays a plateau in the region $-0.5 \text{ a.u.} \leq p_z \leq 0.5 \text{ a.u.}$. In contrast, the TDCC momentum pattern shows a pronounced minimum for longitudinal momenta smaller than 0.5 a.u., while in the CCC calculation peaks at p_x momenta of $\approx \pm 0.75$ a.u. appear for vanishing longitudinal momenta. Still, the CCC-calculation shows the same general trend as the experiment, as no strong minimum is observed amidst the main peaks.

In summary, it is noted that calculated cross sections do neither agree very well with the experimental momentum pattern nor with each other in the investigated case. To gain further insight and lift the discussion on a quantitative level projections of the cross section displayed in Fig. 6.12 on the laser polarization axis are studied in the following.

Figure 6.13 illustrates the projections of the respective cross sections onto the p_z , i.e. laser polarization, axis. All projections are peak normalized in order to allow for a discussion of the relative magnitude of the cross sections. In the experimental data an average of the highest lying datapoints was used for peak normalization to account for the outlier at $p_z = +1.2$ a.u.. The differences discussed, before also persist in the projection. If the TDCC result is compared to the experiment it is found that the peaks in the respective cross sections are 0.3 a.u. apart. Although the peaks are tighter spaced in the TDCC calculation, the minimum inbetween is more pronounced. It is reached for zero longitudinal momentum and the relative emission strength, i.e., the probability for that momentum in comparison to the peak value of the cross section, is at a 22 % level compared to 40 % in experiment. Since the TDCC cross section peaks at smaller values of p_z , it also decays faster for larger longitudinal momenta.

In the comparison of the CCC-result with the experimentally obtained data it is found

¹³The statistical weighting due to the larger phase-space available for the triplet-states is already included in the calculations.

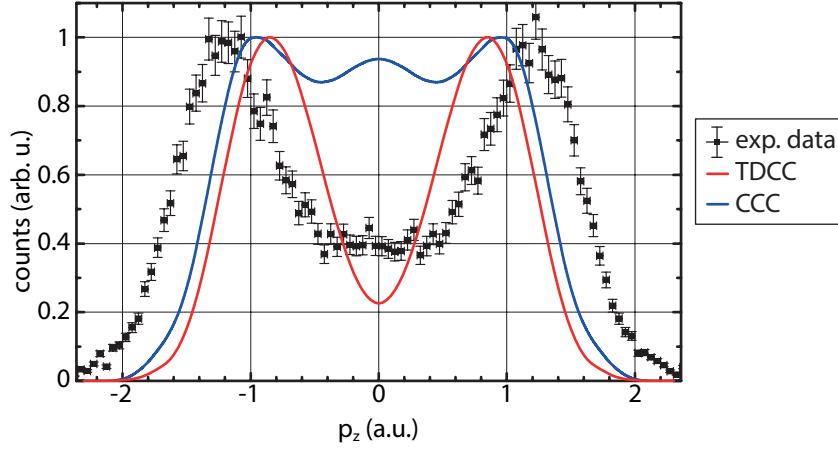


Figure 6.13: Projections of the theoretical and experimental distributions from Fig. 6.12 on ϵ . The black points are the experimental data with 3PDI-background subtraction, the red line shows the results of the TDCC calculation and the blue the one from the CCC. All data is peak normalized. Note, that for the exp. data an average of the highest lying data-points was used for peak normalization.

that theory obviously overestimates the probability for electron emission patterns resulting in small values of the longitudinal momenta. In fact, there is even a peak observed for $p_z = 0$, with a relative emission strength of over 90 %. Evidently, this peak originates from the maxima at $p_x = \pm 0.75$ a.u. (cp. 6.12(b)), which are not present in experiment. As before, the peaks for non-vanishing longitudinal momenta in the the momentum distribution gained by the CCC-method are in better agreement with experiment compared to the TDCC result.

Method	$\sigma_{\text{singlet}}^{2+} / \sigma_{\text{tot}}^{2+}$	$\sigma_{\text{triplet}}^{2+} / \sigma_{\text{tot}}^{2+}$
TDCC	0.57	0.43
CCC	0.83	0.17

Table 6.4: Relative contributions of the singlet and triplet final-states to the total ionization cross section according to the TDCC and CCC calculation. Note, that these values do only incorporate the pure statistical weighting between the singlet and triplet final-states and not any initial-state weighting.

The comparison of the two-dimensional momentum distributions, as well as, their projections on the laser polarization axis showed that there is considerable deviations between the theoretical and experimental findings. Moreover, it was demonstrated that there is not

only disagreement with the experiment but also in between the two theories. In particular for small longitudinal momenta, where the CCC approach overestimates the cross section and the TDCC approach underestimates it. From the experimental point of view the reason for the disagreement between the theories and experiment is difficult to determine. Even more so, as both theoretical approaches show excellent agreement for the case of helium (cp. Sec. 6.4). One reason, might be the different spin-coupling scheme employed for the CCC and TDCC calculation presented. The TDCC treats the excited lithium atom in the frozen core approximation, i.e., only the electrons in the L-shell are considered and the core with the 1s-electron is described by an effective potential [AC12]. In the CCC approach the spins of the 1s and 2p-electron in $\text{Li}^*(1s2s2p)$ are fixed to a singlet. As the 2p-electron originates from the 1s-shell through photon absorption ($\Delta S = 0$) this approach is reasonable.

Pure Singlet Calculations: As the excitation process in the first step of Eq. (6.2) almost exclusively populates the $\text{Li}(1s(2s2p\ ^3P)\ ^2P)$ -term, where the two outer electrons couple to a spin-triplet, and there is only little contribution of the $\text{Li}(1s(2s2p\ ^1P)\ ^2P)$ -term (cp. Sec.6.2), the theoretical distributions presented so far are clearly dominated by the triplet contribution to the final-state cross section. This holds even if the larger DI cross section for singlet spin configurations is considered (cp. Sec. 2.2.2). Taking into account the respective contributions assuming equally populated initial singlet and triplet states (Table 6.4), for the theoretical models a singlet contribution to the cross sections of 5.2 % for the TDCC and 16.9 % for CCC approach are derived, for the data presented in Fig. 6.12(b) and (c). Nevertheless, it is also instructive to study the pure singlet results for the calculations.

Figure 6.14(b) and (c) impressively illustrate the modified theoretical cross sections in case solely singlet final-states are considered. The major changes in the cross section in comparison with Fig. 6.12(b) and (c) originates from the complete absence of any selection rules for the reached singlet states (see Table 2.1). In addition the TS1 mechanism is stronger, for singlet-states. This is due to the symmetric wavefunctions for singlet-states, which allow the electrons to come close to each other in phase-space. In contrast, to triplet states, where the wave-function vanishes for $r_1 = r_2$.

Inspection of Fig. 6.14(a) to (c) surprisingly yields better agreement of the experimentally observed structures (a) with the pure singlet contributions of both calculations (b) and (c). In particular, the TDCC result for the singlet final state configuration (c) shows excellent qualitative agreement with the experimental data. Though, also the CCC calculation (d) is in better agreement with the experimental results than the total distribution (Fig. 6.12 (b)). Still, the calculations themselves, do obviously not agree with each other.

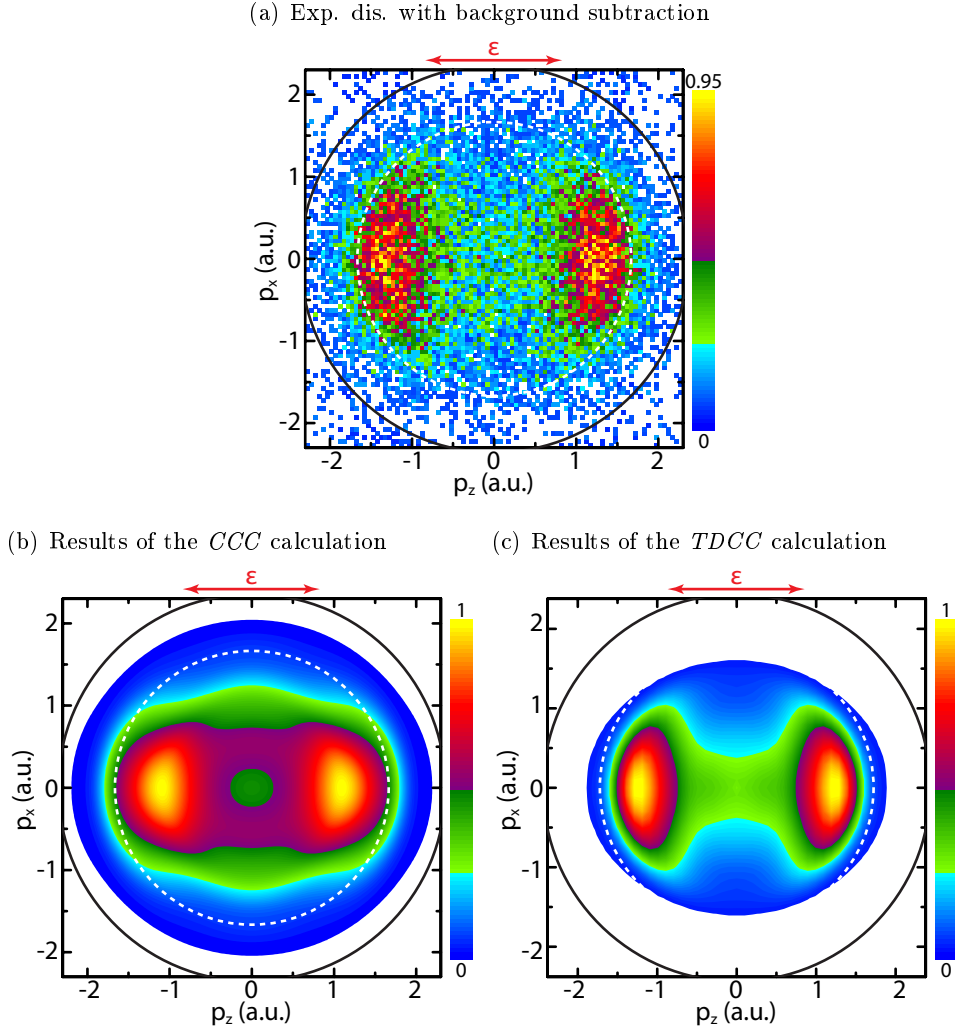


Figure 6.14: Same as Fig. 6.12, except that the theoretical results for a pure singlet state are shown.

For the CCC cross section, the peak pair at zero longitudinal momentum and transverse momenta of 0.75 a.u. has vanished and consequently the magnitude of the cross section for small momenta has decreased. However, it is still larger than experimentally observed. In case of the TDCC momentum pattern, the changes are even more pronounced. This is due to the low singlet contribution for the TDCC in Fig. 6.12(c) (see above). Here, the peak position of the main peaks is now at higher momenta and there is, like in experiment, a plateau between the peaks.

This qualitative finding is confirmed, when studying the projections of the singlet distributions in comparison with the experimental data (see Fig. 6.15). Apparently, an almost

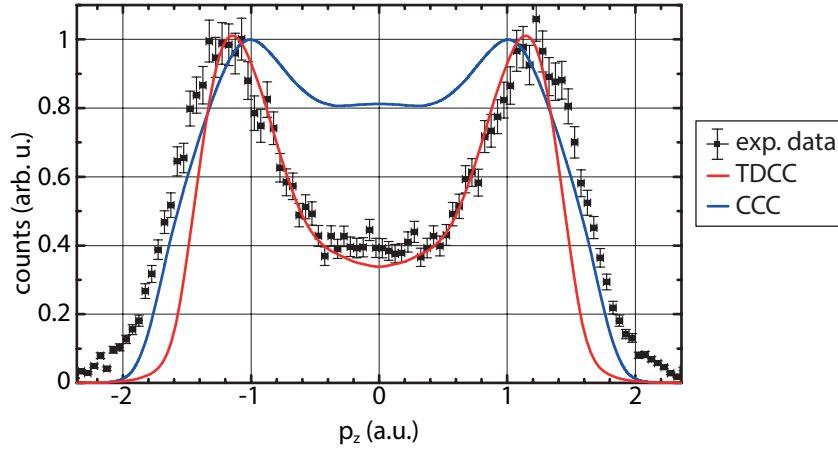


Figure 6.15: Same as Fig. 6.13 for the calculations only considering singlet final-states (Fig. 6.14(b),(c)).

perfect agreement of the TDCC-singlet calculation with the experimental results is observed up to longitudinal momenta of 1.3 a.u.. In case of the falling edges of the cross section, the CCC singlet calculation agrees very well with the experimental cross section, however the magnitude of the cross section for small p_z momenta is still overestimated by a factor of two. A discussion of these findings will be given in the next section, as the agreement of the pure singlet contribution is in marked contrast with the experimental determination of the excitation process (cp. Sec. 6.2).

6.4 Discussion

The presentation and description of the experimental data and, in particular, the comparison with theoretical work describing the DI reaction with the TDCC and CCC method showed pronounced differences in the experimental findings and the theoretical results. This is the case if the calculated singlet and triplet cross sections are weighted according to the excitation cross section and photon-flux present in experiment. If, in contrast, the pure singlet contributions of the calculations are considered, the agreement for the CCC-approach increases and for the TDCC method excellent agreement with experiment is observed. Nevertheless, the agreement between the calculations does not reach that level. In the following, the discussion will first focus on the comparison with the experiment before the differences between the calculations are studied.

Although, the excellent agreement of the TDCC singlet cross section suggests an almost complete absence of triplet-final states in experiment, this is highly unlikely. As of now, there is no experimental evidence for a drift in the wavelength of FLASH which would

lead to a strongly different population of the excited states compared to the one derived in Sec. 6.2. Therefore, it is concluded that mainly the triplet-configuration of the L-shell electrons is excited. As derived in Sec. 6.2, for the given wavelength distribution of FLASH, over 99 % of the excited state are in the $\text{Li}(1s(2s2p\ ^3P)\ ^2P_{M=0})$ -state.

The experimental data presented was taken within a few hours of beamtime at FLASH. During that time FLASH was running stable, which indicates the validity of the wavelength spectrum shown in Fig. 6.8. Moreover, several experimental runs have been conducted during that time with different filters employed (cp. Sec. 6.2) and no change in the cross section, as expected if the FLASH wavelength drifts towards the energy of the $\text{Li}(1s(2s2p\ ^1P)\ ^2P_{M=0})$ -term, has been observed. Indeed, the agreement of the individual datasets reached such a high level, that the experimental DI recoil-ion momentum distributions shown comprise several of the individual datasets taken, without altering the resolution of the momentum patterns.

However, for the TDCC cross section displayed in Fig. 6.15 agreement with experiment decreases with any mixing in of the calculated triplet cross section. In this scope, also spin-flips in the excited state due to spin-orbit interaction have to be considered. The time this process takes to induce a spin-flip is estimated by the energy difference of the respective states, which amounts to $\Delta E = 0.1$ meV which results in a time-scale on the order of picoseconds. Therefore, this process can be neglected.

As a result of this discussion, it is stated that the agreement between theory and experiment is not on a very high level for the reaction studied. This is evident from Figs. 6.12 and 6.13. The questions on the exact reasons for this remains open at the moment.

The difference between the theoretical calculations themselves is difficult to derive from an experimental point-of-view. One reason might be the distinct descriptions of the three-electron target state. As mentioned before in the TDCC the $1s$ -electron is in a way “omitted”, as the $\text{Li}^{2+}(1s)$ core is treated in the frozen core approximation¹⁴. In the CCC calculation this is different. Here, the full three electron target state is described and the spins of the $(1s2p)$ -electron pair in the $\text{Li}(1s2s2p)$ -target state is fixed to a singlet. This makes sense as the $2p$ -electron emerges from the $1s$ -shell through photon absorption. After photon absorption from the excited $\text{Li}(1s2s2p)$, the DI cross section is derived from the scattering of the liberated (photo-) electron on the Li^+ state, which is treated as a two-electron target [KFB09]. This finding is evidenced by the good mutual agreement between the two methods for the case of PDI from the excited $\text{He}(2s2p\ ^1P)$ -state, as illustrated in the Fig. 6.16. For a lithium target, the only difference compared to the He case, is the additional electron in the $1s$ -shell of lithium and the occurrence of both singlet and triplet

¹⁴This means that the $\text{Li}^{2+}(1s)$ -core is described by an effective potential.

final-states.

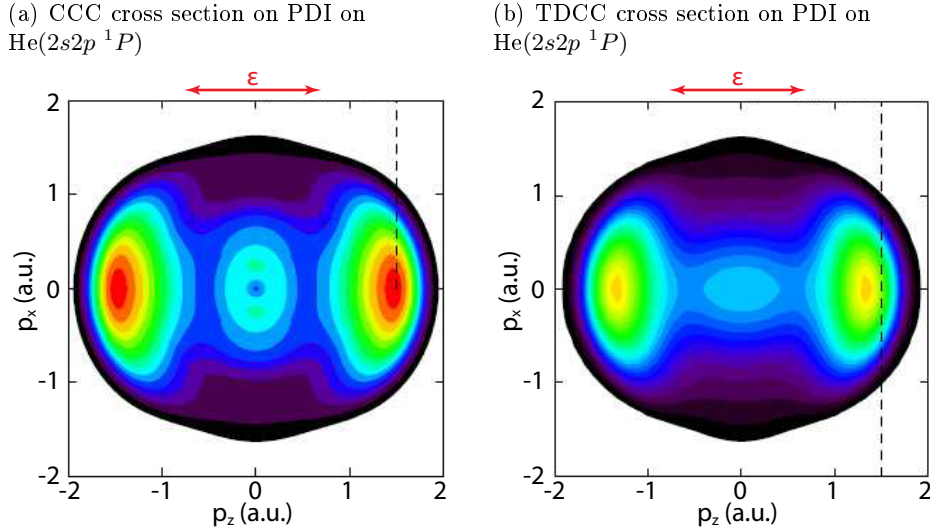


Figure 6.16: Calculated cross sections for PDI from the helium $\text{He}(2s2p\ ^1P)$ -state, as observed with the TDCC and CCC approach [Khe12]. Evidently, the CCC and TDCC approach are in good agreement for the "simple" helium target.

In conclusion differential cross section for two- and three-photon double ionization from the $\text{Li}(1s^22s)$ ground-state have been presented and compared to theoretical predictions of the reaction. It was found that the three-photon double ionization reaction is sequential in nature. After excitation to the $\text{Li}(1s2s2p)$ -state upon absorption of a first photon, two independent photon absorptions remove the $2s$ - and $2p$ -electron, respectively. The two-photon reaction was found to also proceed via the intermediate $\text{Li}(1s2s2p)$ -state and could therefore also be described in terms of photo-double ionization (PDI) from the excited state. As the discussion of the experimental results showed there is a certain singlet contribution to the DI cross section, despite the almost pure excitation to the $\text{Li}(1s(2s2p\ ^3P)\ ^2P)$ -term. This is attributed to the mixing of the $\text{Li}(1s(2s2p\ ^3P)\ ^2P)$ and $\text{Li}(1s(2s2p\ ^1P)\ ^2P)$ -terms and the larger DI cross section for singlet spin-configurations (cp. Sec. 2.2.2). Comparison, with theoretical calculations, clearly showed that multiple ionization of lithium offers additional challenges to the theoretical *ab initio* approaches, compared to the fundamental case of helium. As a possible reason for the discrepancies between experiment and theory the different spin-coupling schemes employed in both theories have been discussed. This might also be the reason why the TDCC-calculation for a pure singlet-coupling of the L-shell electrons and hence the wrong weighting of the spin-configurations present in experiment shows such excellent agreement with the experimental data. Either way there are open question on this reaction, which will be subject of further investigation.

7 Non-Sequential Two-Photon Double Ionization (NSDI) of Lithium

In photo-double ionization it is found that electron correlation is responsible for double ionization, as a single photon can not eject two independent electrons [BL91]. This situation changes when two photons are absorbed. Then, depending on the energy of the photons, double ionization may take place without any interaction between the outgoing electrons (compare Sec. 2.3). In that case the photo-electron energy spectrum exhibits two distinct peaks corresponding to the difference of the photon energy with the first and second ionization potential, respectively. If, however, the photon energy is chosen such that $\hbar\omega < \text{IP}_2^1$ and $2\hbar\omega > \text{IP}_1 + \text{IP}_2$, double ionization requires energy exchange between the ejected electrons. Therefore, the involved photons need to be absorbed in an interval of time shorter than the time an electron needs to leave the atom. Consequently, the observed electron energy spectrum will be modified. These two regimes dubbed *sequential* and *non-sequential* two-photon double ionization, attracted overwhelming interest in recent years, as the vast number of experimental and theoretical publications indicate (see for example [Kur10; Paz11; ANF12; Pal10; IK07] and references therein). The unique characteristic of the non-sequential process is given by the fact that here, both, the absorption of two-photons and the emission of two electrons occur simultaneously. Thus, it combines the regime of multiphoton absorption with the correlated motion of electrons while ejected from the atom and propagating in the continuum during double ionization.

Multiphoton reactions naturally arise for extremely high photon fluxes². A fundamental example for multiphoton absorption is given by the ionization of atoms and molecules by high intensity lasers in the infra-red. There, peak intensities on the order of $10^{14}\text{W}/\text{cm}^2$ combined with pulse lengths in the fs-regime are routinely achieved. Despite, the small photon energy of only $\approx 1.5\text{ eV}$, the tremendous photon fluxes allow for the ionization of such tightly bound atoms as argon and helium, by the simultaneous absorption of 11 and 17 photons, respectively. Although, non-sequential double ionization is also observed, it is of different nature than in the case presented. In the IR, the first electron gets ejected

¹IP₂ denotes the second ionization potential, i.e., the IP after removal of one electron.

²The number of photons per unit time and area.

through multiphoton absorption and is subsequently driven by the electric field of the laser radiation. Thereby it might eventually return to the parent ion and "knock" out a second electron in a field-assisted collision.

In contrast, a regime, where the absorption of only two photons provides sufficient energy to a ground state atom for the ejection of two electrons is only reached in the VUV. Due to the lack in suitable laser sources, it was not before 2005 that *Nabekawa et al.* could show the first experimental evidence for non-sequential two-photon double ionization (NSDI) in the intensity dependent ionization yield of He^{2+} . [Nab05]. Since then the progress in the development of high harmonic sources (HHG) and the advent of free electron lasers (FEL) sparked numerous experimental investigations in this new regime of light-matter interaction (see [Rud10] for an overview).

Pioneering differential experiments performed by *Rudenko et al.* on the NSDI of helium at $E_\gamma = 44$ eV close to the threshold energy for the reaction at 79 eV showed a preferential emission of both outgoing electrons in opposite hemispheres [Rud08]. Thus, indicating a strong correlation of the ejected electrons. This behavior was also reproduced by state-of-the-art theories [HMR08]. Further, experiment and theory agreed that in the sequential regime the energy sharing between the electrons is governed by $E_{e_1}/E_{e_2} = (E_\gamma - \text{IP}_1)/(E_\gamma - \text{IP}_2)$, i.e., the ratio in excess energy of two independently emitted electrons. This moved attention towards the boundary between the sequential and non-sequential process at $E_\gamma \rightarrow \text{IP}_2$, where several theories predicted the so-called *virtual sequential ionization* [Fou08; Hor07; HMR08]. In virtual sequential ionization the energy sharing between the electrons becomes more asymmetric, approaching those observed in sequential ionization which is still not allowed energetically. In a combined experimental and theoretical effort this process was finally confirmed for helium at $E_\gamma = 52$ eV [Kur10].

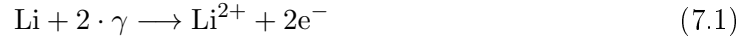
As this introduction showed, the subject to most of the experiments and, in particular, theories published on this topic so far was TPDI of helium, which serves as a prototype for NSDI of closed shell atoms. Lithium, which is studied in the present work can be viewed as a prototype for all open shell systems. In fact, it provides the most comprehensive target to study the electron dynamics in TPDI for electrons with strongly different binding energies. Consequently, this chapter will present the first results for the NSDI of lithium measured at a photon energy of 50 eV, far below the threshold for the sequential process ($\text{IP}_2 \approx 75$ eV), at the free electron laser in Hamburg (FLASH). The results obtained will be compared to calculations performed by *Armstrong et al.* solving the time-dependent Schrödinger equation (TDSE) by the TDCC approach (see also Sec. 2.4.2).

This chapter is organized as follows: In the next section the experimental conditions for which the results have been obtained will be elucidated. Thereafter, the non-sequential

single ionization from the K -shell of lithium is studied. This will allow for the deduction of further experimental facts, as for example the impact of space-charge on the momentum resolution. In Sec. 7.3 the obtained experimental momentum distributions will be presented and analyzed, before they are compared to theoretical predictions in the subsequent section. The chapter will conclude with a summary and discussion of the attained findings and a brief comparison to the case of He.

7.1 Experimental Framework

In the subsequent sections non-linear two-photon absorption by ground state lithium following the general reaction equation



is studied. In Secs. 2.3 and 4.2.2 it was shown that the yield of such processes crucially depends on the radiation intensity reached. In particular, in comparison with competing reactions such as the ionization by harmonic radiation, which only requires the absorption of a single photon or the ejection of the loosely bound valence electron from the neutral lithium atom. Therefore, it is important to have a profound knowledge on the experimental conditions in order to interpret the obtained results. For that reason the properties inherent to all results presented below will be summarized here. The discussion will be brief, where the respective effects have been studied previously.

The experiment was performed at the focused beamline 2 of FLASH (cp. Fig.5.23). The VUV-light, with a central wavelength of $25.1 \pm 1 \text{ nm}$ ($E_\gamma=49.6 \text{ eV}$)³, emerging from the beamline was focused by a toroidal mirror to a spot size of $25 \text{ }\mu\text{m}$. FLASH was operated at an effective repetition rate of 270 Hz, composed of 10 bunch trains. Each of the bunch-trains consisted of 27 micro-bunches, which were spaced in time by $5 \text{ }\mu\text{s}$. The laser pulse energy, in average $75 \text{ }\mu\text{J/pulse}$, was measured with a gas monitor detector permanently installed at the beamline. From the total charge of the electron bunch, here 0.4 nC , the pulse length can be estimated to be $\tau \approx 150 \text{ fs}$ [Sen12], with a coherence time of $\tau_{\text{coh.}} \approx 14 \text{ fs}$. Substituting these values into Eq. (4.19) an average peak intensity of

$$I_{\text{peak}} = 4.8 \times 10^{13} \approx 5 \times 10^{13} \text{ W/cm}^2 \quad (7.2)$$

³In the following we will refer to a photon energy of 50 eV.

Wavelength	Absorbed photons	E_γ (eV)	Cont. Li^+ (%)	Cont. Li^{2+} (%)
fundamental	2	50	97.2	96.5
3rd harmonic	1	150	2.8	3.5

Table 7.1: Contribution of the 3rd harmonic for single ionization and the expected contribution for DI. The cross sections for double ionization are taken from [Weh04]. From the obtained single ionization yield of two-photon absorption, the DI contribution is gained by assuming the same double-to single ionization ratio as for PDI at the given excess energy.

is obtained, for fully coherent radiation. As shown in Chap. 4 and in particular in Sec. 4.2.2, VUV-radiation emerging from free electron lasers is only partially coherent. Therefore, the actual peak intensity of the radiation can exceed the one derived in Eq. (7.2) considerably (for a discussion see Sec. 4.2.2). Equation (7.2) is thus a lower limit for the peak intensity present in the experiment.

During the experimental runs, high harmonic radiation has been suppressed by the use of aluminum filters (see also Chap. 6 for a more detailed discussion). The weakest filter used had a thickness of 200 nm, resulting in a suppression of radiation from the 2nd and 3rd harmonic by a factor of $> 5 \times 10^{-3}$. Taking into account, the intensity ratio between the fundamental and the harmonic radiation emerging from the undulator of the FLASH beamline that leads to an intensity ratio of

$$\frac{I_{\text{fund}}}{I_{\text{harmonic}}} \approx 10^6, \quad (7.3)$$

present in the experiment, indicating the negligibility of high harmonic radiation. These considerations are confirmed by experimental findings summarized in Table 7.1. The contributions of multiphoton single ionization (see next section) and single ionization of a K-shell electron by third harmonic photons have been extracted from the experimental distribution, by integrating over the respective final-state momenta. It is found that multiphoton ionization dominates the spectrum. From the single-to-double photo-ionization cross sections [Weh04] it is inferred that the same holds for double ionization. In particular, as single ionization in the K-shell and double ionization in the K- and L-shells both proceed via the absorption of two-photons for the chosen photon energy of 50 eV. Thus, both share the same intensity dependence and the relative contribution to the double and single ionization is the same, except for the respective cross sections.

Ion Yield Figure 7.1 shows the total number of detected ions for the intensity given by Eq. (7.2) and a detector bias voltage of $U_{\text{bias}} = -1500$ eV. For this setting a detection

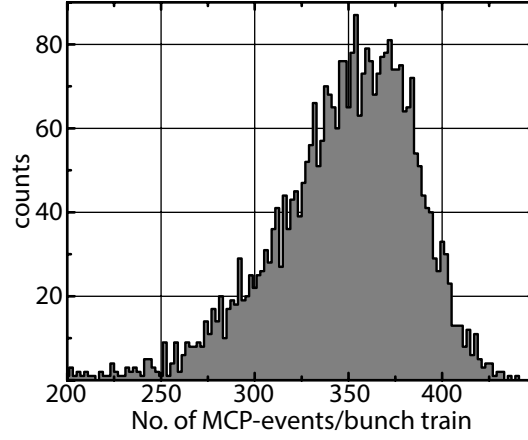
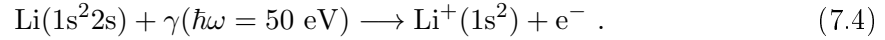


Figure 7.1: Illustration of the observed number of ions per pulse train for a MCP bias voltage of -1500 V. An average number of ≈ 370 ions are detected per pulse train. Here, each pulse train comprises 27 microbunches.

probability of ≈ 40 % for ground-state lithium ions is derived from Table 5.2. Therefore the major contribution to the distribution originates from the reaction



In order to estimate the total number of ions produced in a single FLASH laser pulse we will assume that this reaction is the only one to occur. Substituting the detection efficiency of the channel-plates $P_{\text{MCP}}^{\text{abs}} \approx 40$ % into Eq. (5.17) a total detection probability of $P_{\text{abs}}^{\text{Det}} \approx 24$ % is determined. From Fig. 7.1 the average total number of ions per bunch train (≈ 370) is deduced and taking into account the number of single laser pulses per train (27) a mean number of 13.6 ions/pulse is derived. To compensate for the effects of dead time on the MCP (compare Sec. 5.1.3), this number is increased by 10 %, resulting in a number of $\approx 15 \frac{1}{\text{pulse}}$ ions detected per pulse. As a result a total number of ions *created* per VUV-pulse of

$$N_{\text{Li}^+} \approx 62 \frac{1}{\text{pulse}} \quad (7.5)$$

is determined with Eq. (5.17). For such a count rate detector saturation would alter the experimental findings. Therefore, the scheme described in Sec. 5.1.4 has been used to only detect metastable, i.e., excited, and at least doubly charged ions. As shown before this leads to the detection of all doubly charged lithium ions and all triplet states of Li^+ . In case of singlet final-states only the $\text{Li}^+(1s2s \ ^1S)$ is observed. All other states decay to the ionic ground-state prior to impact on the detector. As no trace of the double ionization

reaction was observable for standard detector settings, the special detector settings were of crucial importance for the presented results.

7.2 Multiphoton Single Ionization

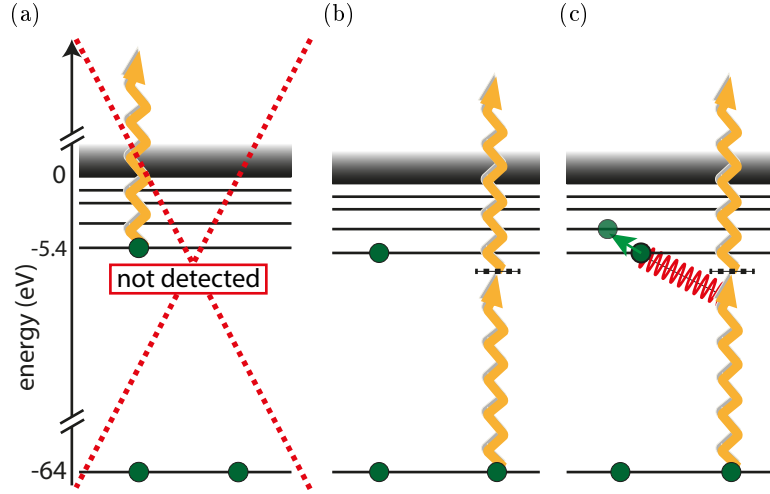


Figure 7.2: Schematic view on the single ionization pathways possible. In (a) ionization of the valence electron, which is not detected, is illustrated. In contrast (b) and (c) show single ionization from the K-shell, where (c) is the process of ionization plus excitation. The red jagged line indicates electron correlation.

Figure 7.2 illustrates the reaction channels leading to single ionization induced by the fundamental wavelength. The channel with the highest yield, displayed in (a), is ejection of the valence electron by single photon absorption. Due to the special detector settings it is hardly detected and therefore neglected. For K-shell single ionization (b), the simultaneous absorption of two-photon is required, since there is no electronic state with an energy close to 50 eV above the ground state in neutral lithium, which could serve as an intermediate resonance. In fact, the closest real state is the $\text{Li}^+(1s2s2p)$ -state with an energy of 58.9 eV above the ground-state. Thus, the lifetime of the excited virtual state can be estimated to around 400 as. Finally, (c) shows the same for the case of ionization plus excitation (IE). Here, the ejection of the primary K-shell electron triggers the excitation of the valence electron to higher lying states. Like for double ionization this can be mediated by the sudden change in the potential (shake-up) or a "hard" collision (knock-up). At an excess energy, for the given reaction, of only $E_{\text{exc}} \approx 34$ eV, knock-up is expected to dominate (compare Sec. 2.2.1). The reactions introduced in (b) and (c) comply with the following

equations

$$\text{Li}(1s^2 2s \ ^2S) + 2 \cdot \gamma \longrightarrow \text{Li}^+(1s 2s \ ^1,^3S) + e^- \ (32.9 \text{ eV } (^1S); 34.8 \text{ eV } (^3S)) , \quad (7.6)$$

$$\text{Li}(1s^2 2s \ ^2S) + 2 \cdot \gamma \longrightarrow \text{Li}^+(1s n s \ ^3S) + e^- \ (25.0 \text{ eV } (n = 3); 21.5 \text{ eV } (n = 4)). \quad (7.7)$$

The singlet configuration of the IE has been omitted as these final states decay to the ionic ground-state and are thus not detected.

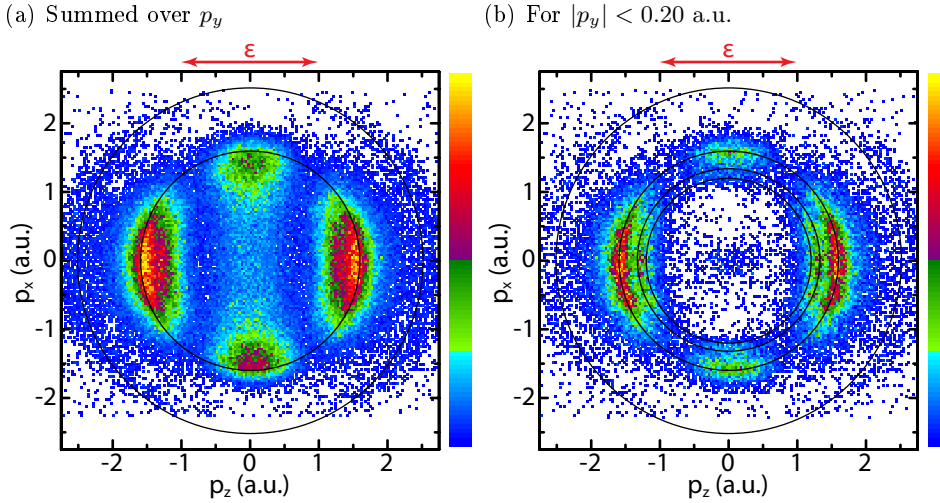


Figure 7.3: Li^+ recoil ion p_x - p_z momentum distributions where the third p_y momentum component was projected onto the p_x - p_z plane (a) and a cut for small out-of-plane momenta (b). From inside to outside the rings in (a) correspond to the expected momenta for two-photon absorption leaving the ion in the $\text{Li}^+(1s 2s)$ -state and ionization by 3rd harmonic radiation with the same final state. The additional rings in (b) mark the momentum reached when the final ionic state is either $\text{Li}^+(1s 3s)$ or $\text{Li}^+(1s 4s)$ (innermost ring).

The observed Li^+ momentum distributions, which corresponds to the photo-electron momentum distributions⁴, are shown in Fig. 7.3. The solid rings mark photo-electron momenta associated with specific excess energies, obtained in the various reaction channels. It is found that the final-state momentum pattern shows richer structures in comparison with the previous results for an intermediate resonance (see Fig. 6.9). In (a) a total number of two lines is observed. The strongest one (inner ring) is generated by pure two-photon ionization (Eq. (7.7)) and will be referred to as main line hereafter. The two minima per hemisphere and the pronounced maximum for emission perpendicular to the FLASH polarization ϵ indicate a dominant contribution of a d -partial wave in the final state for this

⁴As before momentum conservation dictates that the ion momentum must mirror the electron momentum in case of single ionization and vanishing projectile momentum.

reaction. Thus, evidencing two-photon absorption. For large momenta around 2.5 a.u. (outer ring), a weak contribution of ionization by 3rd harmonic radiation is visible. If the distribution is restricted to small out-of-plane momenta (Fig. 7.3(b)), i.e., $|p_y| < 0.2$ a.u., final states of other reaction channels are observable as well. For slightly smaller momenta as the main line, two additional lines appear. They are assigned to IE to the $\text{Li}^+(1s3s)$ -state for final-state momenta of $p \approx 1.35$ a.u. and to the $\text{Li}^+(1s4s)$ -state for momenta of $p \approx 1.27$ a.u.. Although, the latter distribution is hardly visible its occurrence persists through various spectra. All of the lines originating from non-linear two-photon absorption, exhibit similarly pronounced *d*-wave character (see also below). At the center of the diagram, i.e., for small total momenta, a peak is observed. Like for the single ionization at a photon energy of 59.4 eV, this stems from IE through the 3rd harmonic radiation, except that now $\text{Li}^+(2s2p)$ final states are populated.

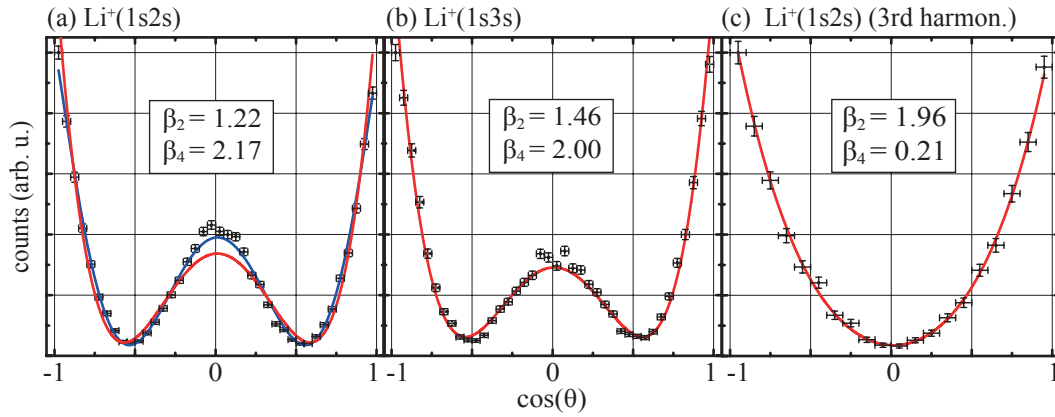


Figure 7.4: Photo-electron angular distributions (PADs) for the three most prominent final-state energies visible in Fig. 7.3. The red lines indicate fits with β_2 and β_4 according to Eq. (2.16). In (a) and (b) the lines emerging through two-photon absorption from the ground-state are displayed. The peak corresponding to emission perpendicular to the laser polarization at 0 evidences the strong *d*-wave characteristic. The blue line in (a) is a fit including β_6 , which is used for the simulations below (compare Sec. 7.3.1). In contrast (c) illustrates the angular distribution for ionization by 3rd harmonic radiation, which shows essentially a pure *p*-wave distribution.

Deeper insight into the partial-wave composition of the ejected electrons for the respective ionic final-states is gained by studying the photo-electron (ion) angular distributions (PAD), directly. Figure 7.4 shows the PAD of the main-line (a), the line associated to the excitation of the valence electron to the 3*s*-orbital (b) and ionization by 3rd harmonic radiation (c). The solid red lines in the figure are fits to the data-points with the parametrization of the cross section by Legendre-polynomials according to Eq. (2.16). As

evidently two-photons are absorbed the fits include the asymmetry parameters β_2 and β_4 . In (c), it is found that ionization through the 3rd harmonic results, as expected, essentially in a pure p -wave. There is a small contribution of β_4 , which can be attributed to background events. Furthermore the resulting fit-curve is almost unchanged when β_4 is forced to 0. In contrast, the PADs in (a) and (b), both exhibit a high-value of β_4 expressly underlining the coherent superposition of s and d waves in the final-state wavefunction. While the agreement of the fit with the $\text{Li}^+(1s3s)$ PAD is good, it is found that the $\text{Li}^+(1s2s)$ PAD can not be fully described by the Legendre-polynomials of second and fourth order, as it deviates from the distribution for perpendicular emission. Inclusion of β_6 (blue line) solves this issue, which can be accounted to dead times of the detector for electron emission along the laser polarization.

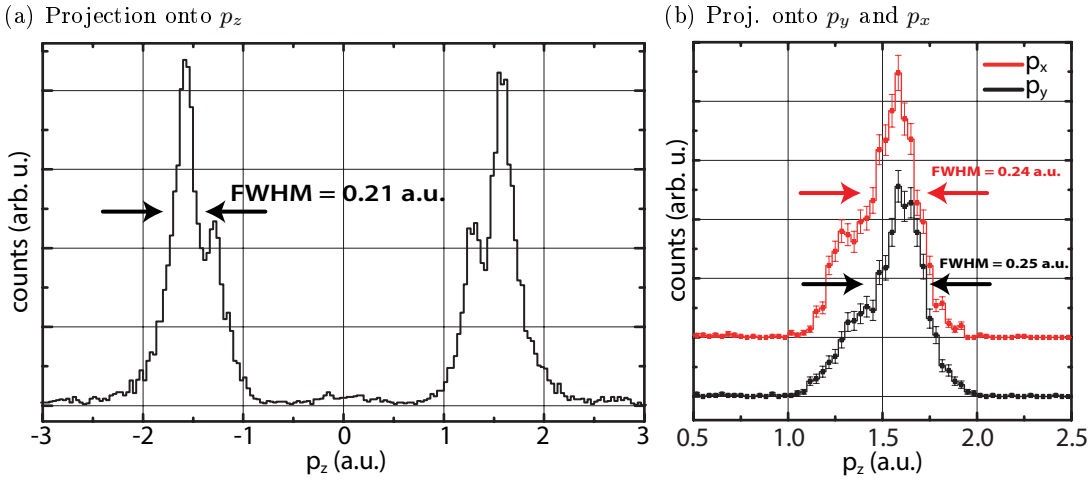


Figure 7.5: Projections on the individual momentum components. The momentum components not displayed in the individual plots are restricted to values below 0.2 a.u. .

Resolution and Space Charge Above, it was derived that an average number of approximately 60 ions was created in the interaction volume of the spectrometer for a single laser pulse emerging from FLASH. As it was shown in Sec. 6.1 and in [Kur11], such a number of charged particles can modify the observed momentum structures through space charge effects. Given that the final-state momenta are known (Eq. (2.1)) inspection of the momentum resolution and peak position in single ionization gives insight into the impact of space charge. Figure 7.5 shows projections on each of the individual momentum components, where the respective orthogonal momenta have been restricted to $|p_\perp| \leq 0.2$ a.u.. It is found that the resolution of all three momentum components is essentially the same. In general the resolution in TOF direction (p_z) is better than the ones in the detector plane.

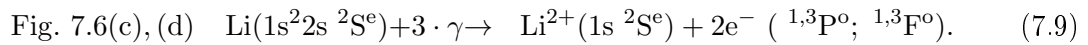
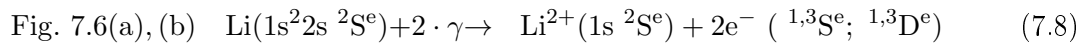
Therefore, it is concluded that the momentum uncertainty observed does not stem from the intrinsic resolution of the spectrometer. A fact, which is confirmed by the results presented in Sec. 6.1, where for a lower intensity a width of the peaks of $\Delta p_z(\text{FWHM}) = 0.14$ a.u. was determined, although the experiment was conducted at very similar settings.

The origin of the peak broadening apparent in the figure, is only partly due to space charge. The focus of the VUV-laser pulses is approximately a cylinder with a radius of $\omega_0 = 12.5 \mu\text{m}$ in the p_x - p_z -plane and a height corresponding to the Rayleigh length of ≈ 1 cm along the propagation direction of the light (p_y). Hence, the mean distance between the ions produced is much smaller in the focal plane of the VUV-radiation compared to the propagation direction of the light. As a result a broadening only due to space charge is expected to contribute mainly in p_x and p_z . For p_y we have to consider that the ion source volume is given by the spatial overlap of the photon trajectories with the atoms ballistically expanding after the magneto-optical trap is switched off. Consequently, the source volume is further extended in p_y direction which also leads to a degradation of the momentum resolution (cp. Sec. 5.1.2). It is thus found that the observed momentum resolution is a combined effect of space-charge and target extension.

Despite the broadening of the peaks no further effect, like the shift of the peaks in the momentum distribution reported in [Kur10] is observed. All observed final-state momenta comply with Eq. (2.1) and the laws of energy and momentum conservation. The only, additional effect is a slight asymmetry in the shape of the peak. It is, however, far less pronounced compared to the data presented in Fig. 6.6.

7.3 Non-Sequential Two- and Three-Photon Double Ionization

The subsequent discussion is centered around the experimental results on double ionization (DI) of lithium by photon absorption with the radiation properties given in Sec. 7.1. Evidently, the photon energy of 50 eV does not allow for DI by single photon absorption. More precisely, as no real intermediate state can be reached by this specific energy, DI demands for the "simultaneous", i.e., non-sequential, absorption of at least two photons. Consequently, the reactions investigated are given by the following equations:



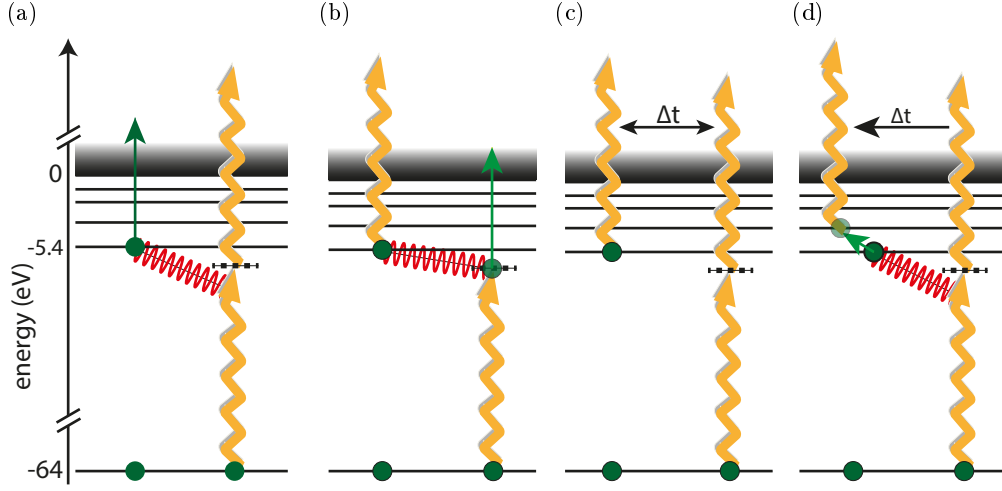


Figure 7.6: Illustration of the various pathways which lead to two- and three-photon double ionization. In (a) and (b) non-sequential two-photon reactions are shown. While, in (a) the K-shell electron absorbs both photons and undergoes a similar reaction as in PDI, in (b) each of the electrons absorbs one photon. In both cases DI is also enabled by electron correlation. Sequential three-photon reactions, with respect to the electron emission are illustrated in (c) and (d). In (c) the electrons are ejected completely independent, i.e., either the multi- or the single photon ionization can occur first. This changes in (d). Here, the excitation of the valence electron defines the sequence of events.

On the left hand side of the equation the corresponding panels from Fig. 7.6 are given. The first two equations describe DI by non-sequential absorption of two photons (NSDI), resulting in the simultaneous emission of both electrons. It is noted that the same partial waves as for the resonant case (Sec. 6.2) contribute to the final-state cross section. In contrast, Eq. (7.9) characterizes the process of sequential three-photon double ionization (SDI), which proceeds independently with regard to the ejection of the electrons. Independent of the sequence of double ionization, i.e., the chronological order of the removal of one K- and the L-shell electron, the emission of the valence electron to the continuum is a single photon process, while the removal of the inner shell electron requires the absorption of two-photons.

For NSDI there are two possible pathways to the double electron continuum displayed in Fig. 7.6(a) and (b). Panel (a) shows a channel, very similar to photo-double ionization (PDI). The K-shell electron absorbs both photons and on its way out of the atom it interacts with the second electron, thereby lifting it to the continuum. Despite the different angular momentum of the primary electron and the non-linearity in the intensity dependence, such a reaction can be explained in terms of the two-step-one (TS1) and shake-off

(SO) models.

In case (b) both, the K- and L-shell electrons individually absorb a photon. DI can occur only if considerable energy is transferred from the L-shell electron to the outgoing inner-shell electron which makes this reaction very unlikely.

Three photon double ionization (panels (c) and (d) in the figure) is expected to be sequential, with respect to the ejection of the two outgoing electrons. As the lifetime of the singly charged ion created in the first step will always exceed the duration of the FLASH laser pulses, the ejection of the second electron is most likely well separated in time. Therefore, independent electron emission is anticipated. The reaction channel shown in (c) leads to considerably different excess energies of the emitted electrons, depending on the temporal order of K- and L-shell ejection. In panel (d) a special case of (c) is illustrated, where the initial multiphoton K-shell ionization excites the remaining singly charged ion in the primary reaction.

Absorbed photons	$E_{\text{exc.}}^{\text{total}}$ (eV)	$p_{\text{max}}^{\text{ion}}(E_{e_1} \approx E_{\text{exc.}})$ (a.u.)	$p_{\text{max}}^{\text{ion}}(E_{e_1} = E_{e_2})$ (a.u.)
2	18.17	1.16	1.64
3	67.77	2.23	3.16

Table 7.2: Final-state momenta expected for certain energy sharings between the outgoing electrons for two- and three-photon absorption from ground-state lithium at a photon energy of 49.6 eV.

Figure 7.7(a) shows the obtained Li^{2+} recoil ion momentum distributions in the p_x - p_z -plane⁵ along with its projection on the longitudinal momentum axis p_z , which is parallel to the laser polarization ϵ . Like in Fig. 6.9 the rings in the figure correspond to final-state momenta from equal (solid) and extreme asymmetric energy sharing (dashed) for the two- (black) and three-photon (red) reaction. In the equal energy case parallel emission is assumed. Considering that the recoil ion momentum reflects the sum-momentum of the ejected electrons the equal energy, parallel emission case constitutes the maximum momentum which can be imprinted on the recoiling ion. The marked momenta are listed in Table 7.2.

Apparently, Fig. 7.7 demonstrates that both processes the NSDI and the SDI contribute to the cross section. Within the kinematical boundaries of the NSDI reaction a strong peak is observed at vanishing total momentum. Towards higher momenta an increased cross sections persists up to dashed black ring tagging the asymmetric energy sharing case for NSDI. For momenta solely attainable through the absorption of three photons peaks along

⁵As before the data is integrated over p_y .

the laser polarization (p_z) are observed just within the boundaries set by the kinematics of the process. While these are hardly visible in (a), panel (b) clearly evidences their existence. In the following the SDI process will be studied before the focus is moved to the NSDI channel.

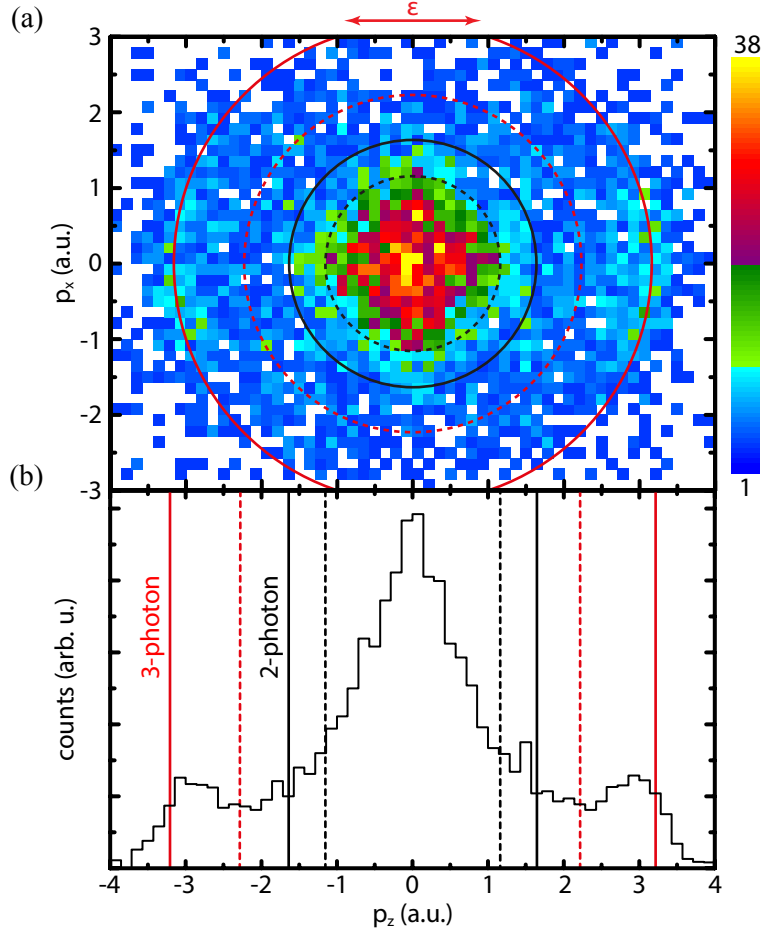
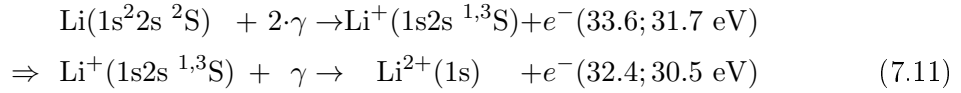
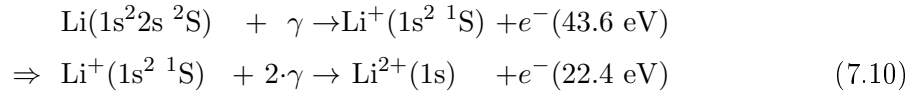


Figure 7.7: Li^{2+} momentum distribution for two- and three-photon double ionization. In (a) the momentum distribution as observed in the p_x - p_z -plane is shown. The data is integrated over p_y . In the lower panel (b) the projection of this data on the p_z -component is displayed. The dashed and solid lines mark the maximum achievable final-state momentum for extreme asymmetric energy sharing (dashed) and equal energy sharing (solid). Hereby, the black lines denote two-photon absorption, while the red-lines stand for three-photon absorption.

7.3.1 Three-Photon Sequential Double Ionization (SDI)

As discussed above, similar to the case of two-photon double ionization with an intermediate resonance (Sec. 6.2), also here a three-photon reaction-channel is observed in the Li^{2+} momentum distribution (Fig. 7.7). Its pathways are illustrated in Fig. 7.6(c) and its reaction equations read



assuming an independent ejection of the two electrons. Equations (7.10) and (7.11) show that while the initial removal of the inner shell electron leads to an almost equal energy sharing and thus also momentum partition of the escaping electrons, double ionization following emission of the valence electron results in an energy sharing of $E_{e1} \approx 2 \cdot E_{e2}$. Similar energy sharings are also obtained for the case of IE upon escape of the K-shell electron to the continuum (see Fig. 7.6(d)). This reaction follows largely Eq. (7.11) and leaves the singly charged lithium ion most likely in the $\text{Li}^+(1s3s)$ in the first step of ionization. The energy partition is $E_{e1} = 24.8 \text{ eV}$ and $E_{e2} = 43.0 \text{ eV}$.

To illustrate how this reflects in the recoil ion momentum distribution and in particular to investigate its potential impact on the interpretation of the NSDI reaction, *Monte Carlo* simulations of these reactions have been performed. The results are shown in Figure 7.8. The circles in the figure correspond to the highest possible momenta for two- (white) and three-photon reactions (black). In panel (a) the resulting Li^{2+} cross section for an initial K-shell ejection, incorporating the IE channel, is shown. It is found that the distributions exhibits three pronounced maxima for momenta of $\pm 3 \text{ a.u.}$ along the laser polarization and for vanishing momenta of the recoiling ion. The former are also observed in experiment, while the latter would be overlapped with the NSDI distribution. The appearance of these structures is naturally given by the predominant ejection of both electrons into the direction of the laser polarization. This happens either parallel (large momenta) or anti-parallel (vanishing momenta). Further, side maxima are observed at $p_z \approx \pm 1.25 \text{ a.u.}$, which originate both from perpendicular emission of the initial electron and IE in the initial step, where the energy sharing is less equal. The angular distribution of the primary K-shell electron is extracted from Fig. 7.4(a),(b) for both, pure single ionization and IE.

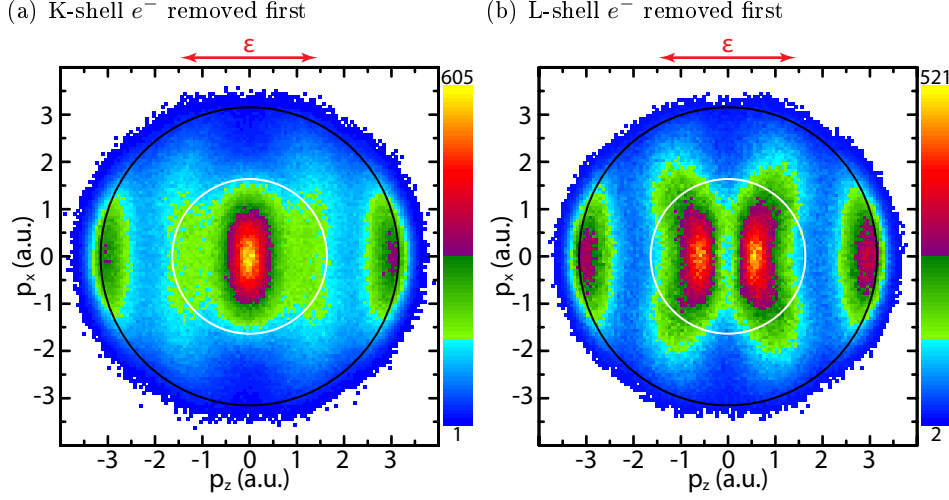


Figure 7.8: Simulations of the sequential removal of a K-shell and the valence electron by the absorption of three photons. Panel (a) shows the final state momenta obtained if the K-shell electron is removed first, while (b) depicts the distribution expected for the subsequent ejection of the valence and one of the K-shell electrons.

The second step, i.e., the ionization from $2s$ proceeds with $\beta_2 = 2$.

In contrast, panel (b) displays the cross section according to Eq. (7.10). The asymmetric energy sharing of the electrons yields two maxima in each hemisphere. They are observed at positions of $p_z = \pm 2.97$ a.u. and $p_z = \pm 0.60$ a.u.. In the first step the valence electron is emitted with an asymmetry parameter of $\beta_2 = 2$ for single photon ionization from an initial S -state, resulting in an ion momentum of 1.8 a.u., just in-between the two maxima. For the second step a PAD as observed in K-shell multiphoton single ionization was assumed, leading to the obtained momentum distribution.

Comparing Fig. 7.8(a) and (b), it is found that the SDI cross section will critically depend on the weighting of these two contributions. The large single ionization yield for standard ion detector settings (compare Sec. 7.1) indicates that emission of the L-shell electron is strongly dominant. Nevertheless, the temporal shape of laser-pulses emerging from FLASH (Sec. 4.2.1) does not allow for the deduction of the relative contributions of the two reaction channels. The multi-peaked structure of the radiation emerging from unseeded free electron lasers, as FLASH, results in different peak intensities reached from shot-to-shot. Therefore, it can not be concluded that the dominance of $\text{Li}^+(1s^2)$ in the single ionization yield implies a major contribution of this reaction as a precursor to three-photon double ionization. In addition the lack of generalized cross sections for the non-linear part of either reaction channel (compare to Eq. (2.17) and Sec. 4.2.2) prevents the calculation of

the relative yield through simulated FLASH laser pulses. These can be generated easily for example by the partial coherence model (see Sec. 4.2.3). As a consequence the distributions displayed in the figure have to be understood as guidelines in case that either of the two pathways is dominant.

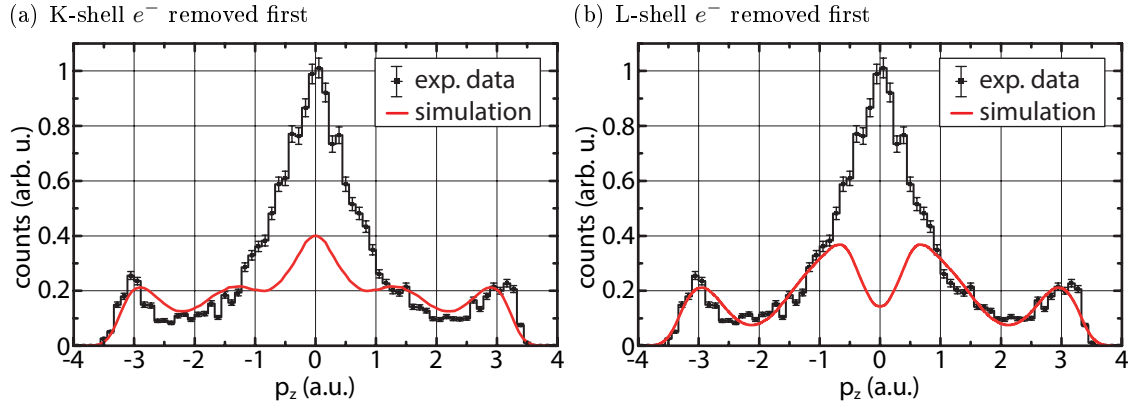


Figure 7.9: Projections on the longitudinal momentum axis (p_z) of the experimental data and the simulations shown in Fig. 7.8. The simulations have been scaled such that the integral number of counts in the peak at $p_z = \pm 3$ a.u. is the same in the experiment and the simulations.

The potential impact of three-photon double ionization on the NSDI distribution is illustrated in Fig. 7.9. It shows projections of the experimental and the simulated SDI reactions in comparison. The simulated data has been scaled to the total number of counts in the peak at large longitudinal momenta. As the simulations incorporate the width of the peaks observed in the experimental data, this procedure is justified. It is found that independent of the dominant channel of three-photon double ionization, these processes contribute considerably to the cross section at small final-state momenta, where NSDI is present.

Despite the strong peak for zero momentum in case of initial K-shell emission, the general shape of the cross section will stay qualitatively the same than before. The reason for this is that SDI from the K-shell exhibits a similar shape in the central region as two-photon double ionization. In contrast, if three-photon double ionization upon removal of the L-shell electron is dominant, it does mainly contribute in the wings of the NSDI cross section in longitudinal direction. Therefore, the cross section for NSDI would be reduced in magnitude there. These findings have to be considered when the non-sequential reaction is studied in the next section.

7.3.2 Non-Sequential Two-Photon Double Ionization (NSDI)

For final-state momenta within the kinematic boundaries of NSDI (solid black circle) in Fig. 7.7, the Li^{2+} momentum distribution, i.e., the cross section, shows a relatively smooth structure with a pronounced peak at $p_{\text{tot}} \approx 0$ a.u. . Towards higher momenta a slightly increased cross section on the p_x and p_z axis, which extends up to approximately $|p_x| = |p_z| = 1.2$ a.u. is observed. There are no additional peaks visible in the distribution. In fact, starting from vanishing recoil-ion momenta the cross section constantly decreases in all directions and exhibits a diamond shape. These findings indicate a strongly correlated motion of the ejected electrons. The absence of peaks along the laser polarization originates from considerable energy and angular momentum transfer between the electrons⁶. Therefore, the properties of the photons imprinted on the primary electron get "smeared out". In the following the two main features, the peak for vanishing recoil-ion momenta and the increased cross section along p_x and p_z will be elucidated.

The peak for zero total momentum corresponds to back-to-back emission of the two ejected electrons with equal energy sharing. This reveals a strong contribution of two-electron continuum wavefunctions, with singlet-spin coupling to the total cross section. In case of triplet final states this electron ejection pattern is forbidden by selection rule C (cp. Sec. 2.5). In addition, selection rules E and F show that for the triplet final-states of the observed reactions, many electron emission geometries leading to small recoil ion momenta, i.e., emission into opposite hemispheres with symmetric energy sharing, are forbidden (compare to Sec. 2.5). Thus, rendering small recoil ion momenta unfavored for the triplet case. Put another way, a major contribution of symmetric energy sharings to the cross section indicates the dominance of the TS1 mechanism, as it was shown in the discussion of the energy sharing for the TS1 and SO in Sec. 2.2.2. Taking into account that TS1 is far more effective for singlet spin-couplings, this provides another strong argument for a dominant contribution of singlet final-states to the cross section. The discussion will now move to non-vanishing recoil ion momenta. Only the reaction pathway considered in Fig. 7.6(a), constituting a similar reaction channel as in PDI, will be discussed. If the primary electron, e_1 , emerging from the K-shell interacts weakly with the secondary electron, e_2 , such that $E_{e_2} \ll E_{e_1}$, its angular emission pattern will mimic the one from IE. This is illustrated in Fig. 7.10(a), where the angular emission probability is constituted by the thin white line. Hence, it will be peaked along and perpendicular to the laser polarization axis. As a consequence of the small kinetic energy of e_2 , in combination with post collision interaction⁷, back-to-back emission of the electrons will be favored. The momentum is illustrated

⁶Otherwise, the momentum of the primary, i.e., the electron which absorbed sufficient photons to escape the atomic potential would manifest itself in a peak along ϵ .

⁷In other words electron repulsion.

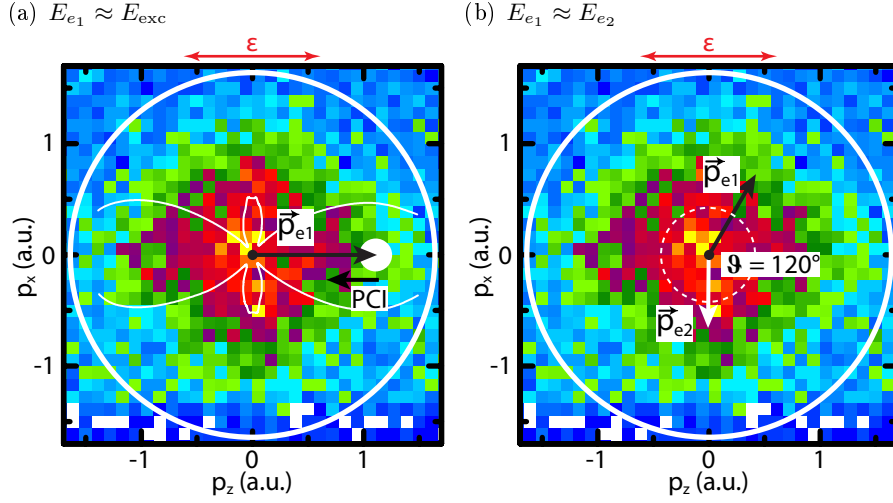


Figure 7.10: Illustration of possible energy sharings and emission angles leading to the observed momentum structures. Panel (a) illustrates the case of asymmetric energy sharing, where the white full circle corresponds to the momentum of the secondary electron. Through post-collision interaction (PCI) e_2 is forced to the opposite hemisphere than e_1 . In (b) the configuration for an energy sharing of $E_{e_1} \approx E_{e_2}$ and a relative emission angle of 120° is shown. The dashed circle marks the reachable momentum.

through the thick white circle. Ultimately, this leads to an increased count-rate along p_x and p_z and can be understood both, in terms of the SO and the TS1 process. Although, this final-state configuration is allowed for all spin couplings and partial waves, it would only result in count-rate close at the "edges" of the cross section. Considering an excess energy of less than 1 eV for e_2 , i.e., $p(e_1) > 1.12$ a.u. and $p(e_2) < 0.27$ a.u., and back-to-back emission a final-state momentum of $p(\text{Li}^{2+}) = 0.85$ a.u. is derived.

The remaining part of the cross section is understood by more symmetric energy sharings with large mutual emission angles. An illustration is given in Fig. 7.10(b) for a relative emission angle $\vartheta = 120^\circ$ and $E_{e_2} = E_{e_1}$. The resulting final state momentum is indicated by the dashed white circle. Since equal energy sharings demand a direct interaction of the electrons such configurations are mainly mediated by the TS1 mechanism.

In conclusion it was found that the experimentally observed cross section is constituted by both the SDI and the NSDI reaction. For NSDI the dominant contribution to the cross section is the TS1 mechanism with a singlet spin-configuration of the two electron wave-function in the continuum. This result is not changed by the possible overlap with the SDI channels, as neither of them would produce the strong peak at zero total momentum, which suggests the large contribution of TS1. Still, it was shown that the sequential processes

have to be considered in the interpretation of NSDI.

7.4 Comparison with Theory

In the following the experimental results will be compared to theoretical calculations by *Armstrong et al.* [AC12]. Like for the case of the intermediate resonance (see Chap. 6) the time-dependent close-coupling (TDCC) approach is applied to solve the time-dependent Schrödinger equation numerically on a grid. Details on the method can be found in [AC12; CPR04; CP06] and in Sec. 2.4.2. The calculations presented have been performed for two distinct laser-pulse profiles with a total length of 10 optical cycles, i.e., ≈ 840 attoseconds and a central frequency corresponding to a photon energy of 50 eV. A peak intensity of $I_p = 10^{15}$ W/cm² is reached for both profiles. While, one of the pulses comprises a \sin^2 intensity profile, the other is a flat-top trapezoidal pulse with ramp-on and off times of one optical cycle. The pulse profiles are illustrated in Fig. 7.11(c) and (e). Evidently, at the same peak intensity and pulse duration the flat-top pulse exhibits both a higher mean intensity and larger FWHM.

Figure 7.11 shows the direct comparison between the experimentally observed Li²⁺ cross section and the ones gained by solving the TDSE with the TDCC approach. Note, the different time-scales for the laser pulses used in the calculation ,panel (c) and (e), in comparison with the radiation emerging from FLASH (a). It is found that the general agreement between experiment and theory is excellent. In the central region, i.e., for momenta attainable by two-photon absorption (within the white circle), the calculated cross section exhibits a strong maximum for vanishing recoil ion momenta, as observed in the experimental data. Furthermore, the increased probability for Li²⁺ momenta oriented along and perpendicular to the laser polarization axis ϵ up to approximately 1 a.u. of momentum and hence the diamond shape of the cross section is reproduced for both pulses employed in theory. For the case of the \sin^2 -pulse (7.11 (d)), however, recoil ion momenta parallel to ϵ are more likely than those perpendicular to it. This behavior is reversed in experiment and for the flat-top pulse, which is therefore in better agreement with experiment. A minor deviation from the experimental findings is given by the overall width of the cross section for momenta smaller than 1.65 a.u. (white circle), which is slightly larger in experiment than in the calculations. This can be understood by taking into account both, the experimental uncertainty in the determination of the individual momentum components $\Delta p_{x,y,z}(\text{Li}^{2+}) = \sqrt{2} \cdot \Delta p_{x,y,z}(\text{Li}^+) \approx 0.35$ a.u. and the relatively coarse binning of the experimental data.

Inspection of the cross sections for momenta solely obtainable through absorption of three-photons (between the black and white circles in Fig. 7.11(b),(d) and (f)), demonstrates a

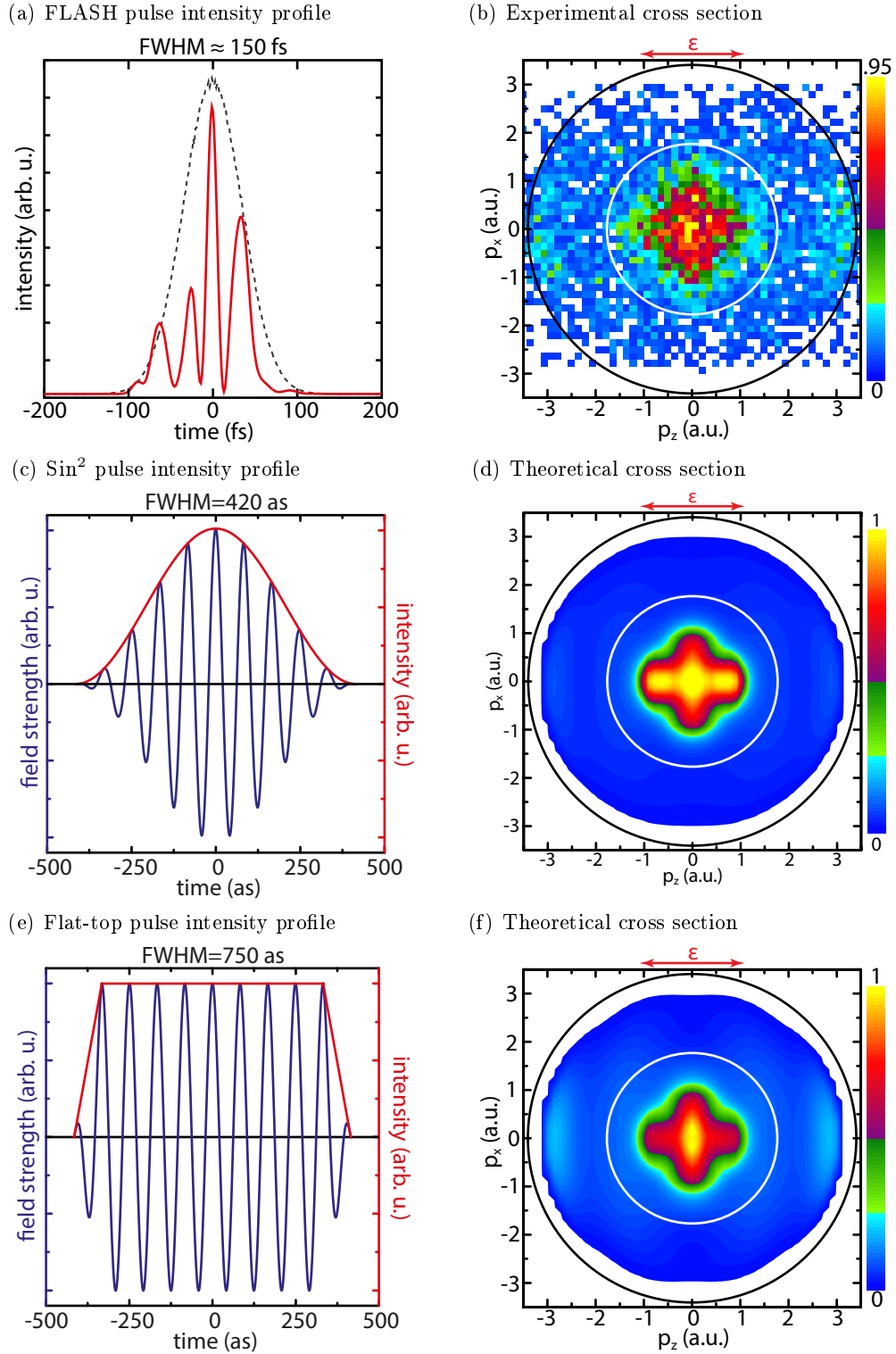


Figure 7.11: Experimental and theoretical distribution for two- and three-photon double ionization at a photon energy of 50 eV. For details see text.

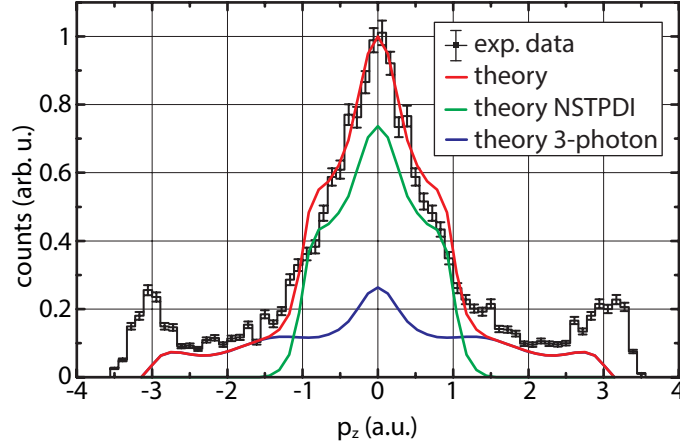
stronger relative contribution of SDI in the experimentally acquired cross section. While the difference is large in comparison with the calculation for the \sin^2 -pulse, it is almost neglectable for the trapezoidal laser pulse. One reason for this is the higher mean intensity for this pulse profile. Nevertheless, a shift of the peak position in theory towards smaller momenta of $p_z \approx \pm 2.8$ a.u. compared to 3 a.u. in experiment is observed for both laser-pulse profiles employed. In addition the cross section shown in Fig. 7.11(f) exhibits an increased count-rate in-between the central structure and the peaks at large momenta. As a matter of fact the experimental data (b) does not allow for the confirmation or neglectation of this effect which is hardly observed in (d).

In summary, the comparison of the theoretical and experimental Li^{2+} cross sections, yields the result that the calculations are in very good agreement with the experimental data. In particular, if a flat-top pulse is used to describe the radiation field. Still there are differences in the respective cross sections, especially for SDI. To elucidate this the projections of the data displayed in Fig. 7.11 on the laser-polarization axis will be studied.

Figure 7.12, shows the projections of both calculations and the experimental data on the longitudinal momentum axis p_z , i.e, parallel to the laser polarization axis. The experimental data (black) and the theoretical results (red) are peak normalized to allow for the investigation of the relative magnitudes of the theoretical and experimental cross section. The two- (green) and the three-photon (blue) contributions to the total TDCC cross section are scaled accordingly with the total theoretical cross section.

Inspection of Fig. 7.12(a) demonstrates that the agreement of theory and experiment is already good for the \sin^2 calculation. In particular, considering small longitudinal momenta in the final-state. For momenta smaller than 1 a.u., the only deviation consists in slight enhancement of the theoretical cross section between 0.5 and 1 a.u. compared to the observed one. Despite the good agreement within the kinematics of NSDI, for momenta where solely SDI contributes the obtained cross sections differ. Here, the theoretical distribution ranges below the experimental values starting from 1.2 a.u. of momentum. Furthermore, there is hardly any peak visible in the TDCC cross section for large longitudinal momenta. Thus, theory evidently underestimates the yield of SDI with respect to NSDI for the \sin^2 -laser pulse.

In contrast, in Fig. 7.12(b), where the experimental data is shown together with the TDCC-result for the trapezoidal pulse (see Fig. 7.11), almost perfect agreement between TDCC and experiment persists up to momenta of 2 a.u.. This is attributed to changes in SDI cross section of the TDCC calculation (blue), as the shape of the NSDI distribution stays constant at a quantitative level. Considering the relative magnitude of the NSDI cross section at the peak ($p_z = 0$) and the shoulder ($p_z \approx 0.8$) as a measure, shoulder-to-peak ratios of 0.6 are found in both Fig. 7.12 (a) and (b). There are two major changes in the SDI cross

(a) Projection of exp. and theo. cross section on p_z for the \sin^2 -pulse.

(b) Same as (a) but for trapezoidal pulse

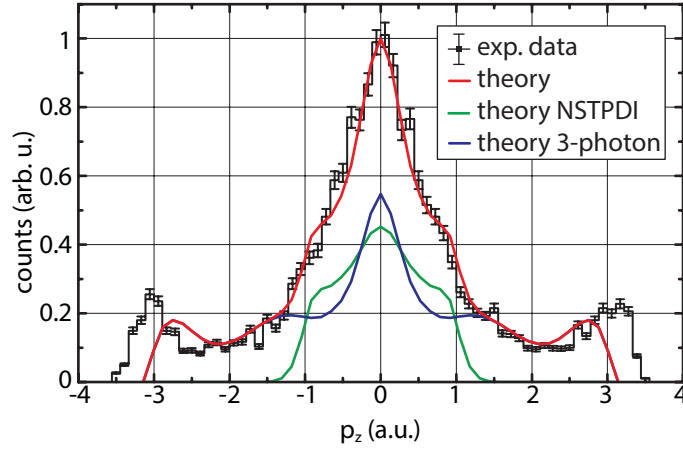


Figure 7.12: Peak normalized projections of the experimentally observed and the calculated cross sections on the longitudinal momentum axis. The black histogram shows the experimental data and the red line the TDCC results. The green and blue line mark the relative contribution of the two- and three-photon channels to the total theoretical result. The theoretical cross sections in (a) display the contribution of two- and three-photon reactions as observed with a \sin^2 pulse, whereas (b) shows the same for the trapezoidal pulse.

section. First, its relative strength in comparison to NSDI is increased. In fact, SDI even exceeds NSDI at vanishing momenta. Secondly, the cross section is more structured than in the case of the \sin^2 -pulse. Apart from the peak at vanishing momentum, strong peaks at $p_z \approx \pm 2.75$ a.u. and less pronounced peaks at $p_z \approx \pm 1.4$ a.u. are observed. Although, the theoretical distribution still peaks at smaller longitudinal momenta in comparison with

experiment.

The evident changes in the theoretical SDI cross section are assigned to the distinct temporal profiles of the respective laser pulses. The use of a trapezoidal pulse instead of \sin^2 one, both with the same peak intensity and overall pulse duration, brings about an increase of the mean intensity. In other words the photon flux is higher for the trapezoidal pulse. Therefore, SDI becomes more likely, as it constitutes effectively a three-photon reaction and will consequently scale with the intensity to the power of three. That explains the larger relative contribution of SDI for the trapezoidal pulse. The emergence of the peaks in the theoretical SDI cross section in Fig. 7.12 is, however, more subtle in nature. The second property of the laser-pulse that changes with its shape is the FWHM in time. This nearly doubles in case of the trapezoidal pulse compared to the 420 as for the \sin^2 -pulse. Thus, the mean time-delay between the ejection of the two electrons from the atom increases⁸. For that reason also the mean distance of the two-electrons in space will increase, resulting in a weaker Coulomb interaction between them. In a sense, the pulse length provides a measure for the impact of PCI on the final-state cross section.

Considering emission of both electrons into the same hemisphere, this is understood in the following way. The primary electron e_1 , i.e. the one emitted first, is repelled by the secondary one e_2 , which also screens the charge of the nucleus for e_1 . Therefore, e_1 is pushed and gains energy. In contrast e_2 , is slowed down by both e_1 and the higher effective charge of the parent ion. Hence, it loses energy. Ultimately, this leads to uneven energy sharings, i.e., smaller maximum momenta. In addition, as the time-delay $\Delta t_{e_1, e_2}$ and the relative emission angle are not fixed⁹, the amount of energy exchange is neither. This evidently smoothens the peak structures, which should be apparent for SDI (cp. Eqs. (7.11) and (7.10)). The finding that electron correlation in the final-state washes out the peaked structure of two-electron emission upon two-photon absorption was also found in [BL91], although in a slightly different context.

It is thus found that the experimental data and the theoretical predictions are in excellent agreement with each other. Within the kinematic boundaries of NSDI, given by the ionization potentials of lithium and the photon energy, the TDCC cross section reproduces the experimental one almost perfectly. In particular, for the flat-top trapezoidal pulse. The differences in the obtained cross sections, for the different pulse profiles, concerning the sequential channel of double ionization could be attributed to the distinct laser-pulse profiles in experiment and theory and will be thoroughly investigated in the next section. There, also the surprising result that theory agrees well with experiment, despite employ-

⁸With the assumption of an independent emission, i.e. , a purely sequential reaction.

⁹The ejections are independent.

ing a laser-pulse almost 2 orders of magnitude higher in intensity and nearly 2 orders of magnitude shorter in time will be discussed.

7.5 Discussion

In summary, it has been found that the non-sequential two-photon double ionization of lithium at a photon energy of 50 eV is strongly influenced by electron correlation, i.e., energy and angular momentum transfer between the outgoing electrons. The high probability for back-to-back emission with equal energies and thus vanishing recoil-ion momentum, clearly support this result. It persists even if the potential impact of the competing reaction constituted by the sequential removal of the two electrons through the absorption of three photons is taken into consideration. In addition, an increased count-rate for emission parallel and perpendicular to the laser polarization axis has been observed. As a consequence, the cross section exhibits a diamond shape. Comparison with theory yielded excellent agreement with the experimentally obtained cross section in case of NSDI, but also demonstrated differences for SDI. In particular, the sensitivity of the SDI cross section on the shape of the temporal laser-profile has been studied. Below these findings will be discussed.

Above it was pointed out that the theoretically employed pulse parameters differ significantly from the ones produced by the FLASH facility. While, FLASH laser pulses exhibit FWHMs on the order of 150 fs¹⁰ the pulses used in theory have lengths of 420 and 750 as with respect to their FWHM. Furthermore, the peak intensity used in theory was almost two orders of magnitude higher compared to experiment. As these differences have different impact on NSDI and SDI the respective reactions will be discussed separately.

In case of NSDI, the distributions obtained in experiment and also with both theoretically employed pulses show little overall differences. This is illustrated in Fig. 7.13, where the respective NSDI cross section of the \sin^2 and flat-top pulse are shown without the three photon contribution. The underlying reason for that is that the ejection of the two electrons to the continuum occurs simultaneously, i.e., on time-scales shorter than all laser-pulses employed [Fei09]. Therefore, the length of the pulse is irrelevant here, apart from the spectral width for very short pulses¹¹ $\tau \ll 100$ as. The negligibility of the far too high intensity in theory stems from the high frequency of the incident radiation. At $E_\gamma = 50$ eV the ponderomotive potential U_p introduced in Sec. 2.3 only amounts to 0.06 eV. If this is taken as a measure for the magnitude of the AC-stark shift [DK99a], the absence of any intermediate resonances is concluded. The virtual state populated by absorption of a photon

¹⁰At least for the presented measurements.

¹¹This is most likely the origin of the differences in Fig. 7.13

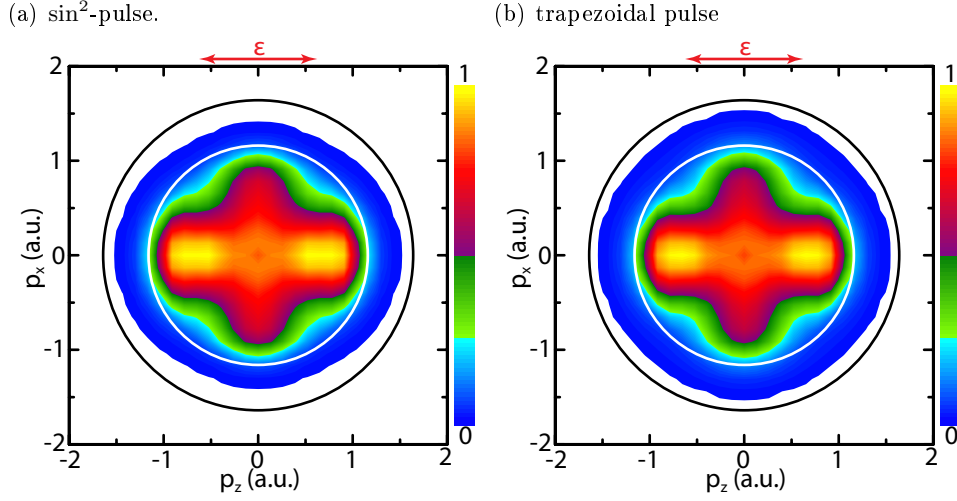


Figure 7.13: TDCC cross section for NSDI of lithium at $E_\gamma = 50$ eV for the 10 cycle \sin^2 -pulse (a) and the 10 cycle trapezoidal pulse (b). Evidently there are hardly any differences observed.

in the K-shell (cp. Fig. 7.6(a)) is approximately 10 eV below the closest real state. Higher order contributions, through absorption and emission of additional photons, resulting in two-photon absorption in the final-state, are explicitly excluded in the calculation. There, only two interactions of the atom with the light-field are allowed. Thus, possible higher order effects for the high intensity used in theory are suppressed. As a result, the intensity in the calculation can be scaled without changing the momentum pattern for NSDI considerably, as long as the impact of the electrical field of the laser radiation is small. This does of course only hold for the relative not for the total cross section.

For SDI the origin of the peaks for the trapezoidal pulse has been discussed above and was found to critically depend on the mean delay between the ejection of the primary and secondary electron, i.e. on their PCI. This in turn is dependent on the pulse length (FWHM) employed in theory. Purely theoretical studies [Fei09; Pal10], found a similar behavior for two-photon SDI of helium, by comparing results of TDCC calculations with different pulse length. While [Pal10] assigned this to the spectral broadening of the laser pulse for shorter FWHM, [Fei09] determined PCI as the origin of the disappearance of peaks associated with the excess energies of the respective ionization reactions. Here, the findings of [Fei09] are confirmed, as the spectral broadening should affect SDI and NSDI likewise. There are, however, hardly any changes observed in Fig. 7.13(a) and (b).

Figure 7.14 shows the comparison of the SDI contribution obtained with the trapezoidal pulse, with the ones gained by simulating the two pathways of SDI possible for $E_\gamma = 50$ eV.

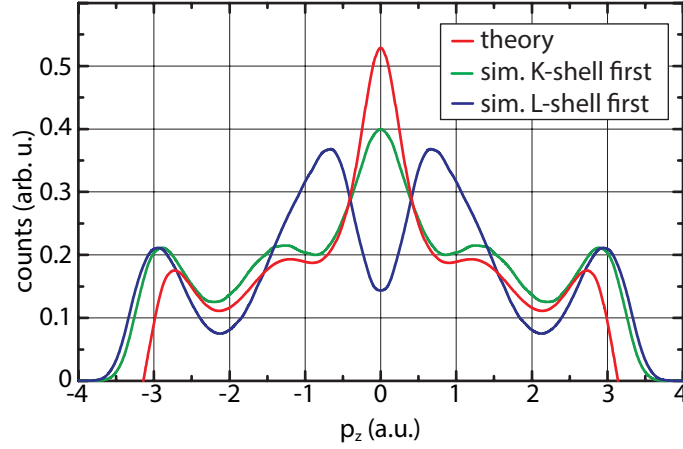


Figure 7.14: Projection of the theoretical SDI cross section (red) for the trapezoidal pulse together with the simulations of SDI proceeding via primary K-shell (green) and L-shell (blue) ejection. The scaling for the theoretical distribution follows the one from Fig. 7.12, while the scaling of the simulated cross section is given by the abundance of SDI in the experimental spectra (cf. Sec. 7.3.1.)

Evidently, the theoretical cross section shares distinct similarities with the simulation for primary emission of a K-shell electron. The good agreement of the overall theoretical cross section with the experimental data when the two-electrons are not emitted in the same direction, i.e. for momenta smaller than 2.5 a.u., suggests that this channel is also dominant in experiment. For the theoretical distribution¹² this is understood by the rapid rise and high peak value of the intensity. The non-linear dependence of the K-shell emission on intensity, makes this process more likely in this case. In the experiment the conditions are more complex. The multi-peaked structure of the FLASH laser-pulses (cf. Chap. 4) does not allow for such a clear identification instead the yield resulting from

$$\begin{aligned} \text{K shell : } Y &= \sigma_{01}^{(2)} \left(\frac{I}{\hbar\omega} \right)^2 \cdot \sigma_{12} \left(\frac{I}{\hbar\omega} \right) \\ \text{L shell : } Y &= \sigma_{01} \left(\frac{I}{\hbar\omega} \right) \cdot \sigma_{12}^{(2)} \left(\frac{I}{\hbar\omega} \right)^2 \end{aligned} \quad (7.12)$$

has to be calculated. Here, $\sigma_{k,l}^{(2)}$ denotes the generalized cross section for a 2-photon transition from charge-state k to charge-state l . As the generalized cross sections $\sigma_{01}^{(2)}$ and $\sigma_{12}^{(2)}$ are not available the calculation of the yields, with simulated FLASH-pulses (cp. Sec. 4.2.3) is, however, not possible presently. While the comparison with theory indicates, a dominant primary K-shell emission, the experimental single ionization yield (cp. Sec. 7.1) exhibits a

¹²The argument stays the same for the \sin^2 pulse.

leading contribution of L-shell emission. Therefore, no final conclusion on this part of the analysis can be given.

In order to classify the experimental and theoretical findings above it is instructive to draw the comparison between the two- and three-photon double ionization of lithium presented in the scope of this work and the even more fundamental case of helium. Not only because helium constitutes the most simple atomic species to study the influence of electron correlations and therefore attracted a lot of attention in recent years (see [Fei09; Pal10; Fou10; Rud10] and references therein) but also due to the excellent agreement obtained for experimental and theoretical cross sections [Kur10].

The direct comparison of the atomic structure of helium with lithium yields the insight that lithium constitutes a different regime of initial state correlation. Particularly, if the combined response of a K-shell and the L-shell electron upon the absorption of few-photons is probed. While, the initial state of helium exhibits a strong correlation of the two $1s$ electrons, the valence electron in lithium is far less correlated with the electrons in the closed $1s$ -shell. Moreover, lithium allows for both, singlet and triplet spin configurations in the final-state. For this reasons the final-state cross section and thereby the energy and angular momentum transfer of the two-electrons liberated to the continuum through photon impact is expected to exhibit distinct differences.

This manifests for example in the yield of the sequential and non-sequential channel of double ionization. For helium the dominance of either channel is usually¹³ defined by the photon energy. As long as it is below the second ionization potential of helium the non-sequential channel governs the final-state cross section. Above that photon energy SDI dominates. Since, no experimental evidence for a strong contribution of three-photon channels was found, the theoretical work also focused solely on two-photon reactions (see [Fou10; Fei09] and references therein). As the experimental and theoretical data above showed the clear distinction between the non-sequential and sequential regime by the energy of the incident radiation, vanishes in the case of lithium. Although, the photon energy for the presented data was chosen such that it ranged deep in the "non-sequential regime", a strong contribution from the competing sequential three-photon process was found. In fact, both reactions contributed equally to the final-state cross section.

In the non-sequential channel of TPDI of helium it was found that despite the strong correlation of the two outgoing electrons, the nodal plane for emission normal to the laser-polarization associated with an outgoing p -wave persists for both electrons. Therefore, it was concluded that each of the electrons absorbs a single photon, resulting in a dipole-

¹³This is only true if no ultra-short laser pulses $\tau < 100$ as or ultra-high intensities are used.

like emission pattern modified by PCI [Fei09]. In the recoil-ion distributions this results in peaks or slight enhancements of the cross section along the laser polarization (see for example [HRM10]). For lithium, not only an increased cross section along the laser polarization but also perpendicular to it was found (see Figs. 7.13 and 7.7). Hence, indicating the dominance of two-photon absorption in the K-shell (depicted in Fig. 7.6(a)) as the dominant channel of two-photon double ionization. Thereby, resembling the process of single photon double ionization, where DI can be viewed as a two-step process (cp. Sec. 2.2.1). In the first step the K-shell electron gets ionized by two-photon absorption. Subsequently, it scatters on the valence electron and liberates it to the continuum.

8 Conclusion and Outlook

This work is devoted to studies of the double-ionization (DI) dynamics of the simplest, many-electron open-shell atomic system lithium, upon absorption of two and three photons for two different photon energies in the vacuum ultra-violet (VUV). To achieve this goal three state-of-the-art experimental techniques have been combined. A magneto-optical trap provides an ultra-cold target sample of atomic lithium, with a temperature on the order of 500 μK . Its combination with a Reaction Microscope allows for the determination of the 3D-momentum vectors of, in principle, all charged particles emerging from an ionization reaction, with utmost resolution [Sch11]. In the present work the recoil-ion momentum distributions were measured. Finally, the unique capabilities of free-electron lasers, like FLASH (free-electron laser in Hamburg), with respect to the light-fields intensity, wavelength and peak brilliance, enables investigations of previously unobserved non-linear reactions in the VUV.

At a photon energy of $E_\gamma = 59.4 \text{ eV}$, DI proceeds via an intermediate resonance. Through a first photon absorption ground-state lithium is excited to the $\text{Li}(1s2s2p)$ -state. In a subsequent step the L-shell electrons are either removed by absorption of one (photo-double ionization) or two (sequential two-photon double-ionization) additional photons. It was demonstrated that in the latter reaction electron emission is independent and hence the two photon absorptions can be viewed as separate processes. In case of photo-double ionization from the excited lithium state, the differential Li^{2+} cross section was found to be strongly peaked along the linear polarization of the FLASH radiation, with a plateau extending between the two peaks, such that a dumbbell-like structure is observed. The PDI cross section was compared with two theoretical approaches solving the Schrödinger equation (SE), namely the convergent close-coupling (CCC) and the time-dependent close-coupling (TDCC) method. It was shown that the increased structural complexity of the lithium atom, in particular, in comparison with helium offers additional challenges to theoretical ab-initio methods to solve the SE. Specifically, the description of the excited three electron target configuration ($\text{Li}(1s2s2p)$) and the coupling of the individual spins were identified as a possible source of the observed deviations between both experiment and theory, as well as, the CCC and TDCC calculations. This finding is evidenced by the good

mutual agreement between the two theoretical methods for the case of PDI of the (2s2p) excited state of the simpler helium system.

For a photon energy of $E_\gamma = 50$ eV a different regime of light-matter interaction was probed. Here, double electron escape requires the simultaneous absorption of at least two photons. The analysis of the Li^{2+} cross section observed in experiment revealed a strong competition between the non-sequential two-photon double-ionization (NSDI) and the three-photon sequential double-ionization (SDI) channel¹. Furthermore, it was demonstrated that the NSDI cross section indicates a strongly correlated motion of the two escaping electrons. As a result of the experimental analysis, a simple picture of NSDI at $E_\gamma = 50$ eV in the case of lithium was suggested, where one of the K-shell electrons absorbs two photons² and subsequently liberates the second electron in an (e,2e)-like reaction in analogy to PDI.

In the comparison of the experimental cross section with theoretical predictions of NSDI, excellent agreement between the TDCC-calculation and the momentum pattern observed in experiment was found. This is despite the fact, that the calculations comprised an intensity exceeding the experimental one by two orders of magnitude and a pulse length two orders of magnitude shorter than for the laser-like radiation emerging from FLASH. In case of SDI, the agreement was not on such a high level. However, it was shown that this can be attributed to the stronger impact of post-collision interaction (PCI) for the short pulses employed in theory. As a consequence of these findings, the dependencies of the theoretically obtained cross section on both pulse-length and intensity have been discussed.

Concerning the experimental methodology the crucial importance of the special detector settings used (cp. Sec. 5.1.4), completely suppressing the detection of ground-state Li^+ was emphasized. Ultimately, only these settings allowed for the unambiguous determination of the Li^{2+} recoil-ion momentum cross section for the reactions discussed above. Moreover, the improvements on the experimental setup have been presented. Here, the decisive leap forward is the strongly reduced switching time (<1 ms) of the newly designed and implemented magnetic field coils generating the gradient field of the magneto-optical trap (cp. Sec. 5.2.2). As the complete absence of non-homogeneous magnetic fields is required for any coincidence detection of ions and electrons in a REMI, this will allow for kinematically complete experiments in the future.

¹Note, that also the sequential reaction comprises the simultaneous absorption of two photons. The term sequential refers to the electron emission.

²This expression is strictly speaking not valid, since photons are always absorbed by the whole system. It means that a single electron is imprinted with the properties of the incident photon(s).

Nevertheless, the possibility of kinematically complete experiments on multiphoton multiple ionization not only depends on the experimental setup employed, but also on the radiation properties of FLASH. During the measurements presented a pulse duration of at least 150 fs and a peak intensity of $5 \times 10^{15} \text{ W/cm}^2$ resulted in a huge background not only from ionization of rest gas atoms but also due to the competing single-ionization channels in the target. Hence, more than one event per laser pulse will be recorded, demanding for the assignment of the electrons to the parent ions through momentum conservation (cp. Sec. 5.1). This implies recording all charged particles emerging from such an reaction and thus already for double ionization a maximum detection efficiency of 4.3 % is derived (cp. Sec. 5.1.3).

Therefore, future studies on multiple ionization aiming at the coincident detection of ions and electrons would require shorter pulses in combination with higher intensities to increase the relative contribution of DI to the total ionization yield, as it was the case for the measurements performed in [Kur09]. In addition, a better knowledge of the radiation properties of the laser pulses emerging from FLASH would be desirable. Due to the stochastic nature of the self amplified spontaneous emission (SASE) process (cp. Chap. 4), the laser pulses exhibit considerable fluctuations on quantities like pulse duration, intensity and other important parameters. A current field of research aiming to ensure a higher stability in the properties of FLASH radiation is therefore constituted by the seeding of free electron lasers with high harmonic radiation [Sch10a].

In summary, it was shown that the investigation of multiple ionization of lithium provides important information on the ionization dynamics and the role of electron correlation for the case of open-shell systems. The understanding of these processes in particular for lithium is of special interest as it naturally constitutes the next step in complexity compared to the commonly studied "many-electron" atom helium. Here, the agreement between experimental and theoretical cross sections has, in general, reached a high level of agreement. As also shown in this work this is not always the case for lithium, which therefore provides the next testing ground for theory towards the ab-initio description of more complex atoms and even molecules.

As discussed above, the prospect of performing kinematically complete experiments on the multiple ionization of lithium is of high scientific interest. With the technical realization of fast-switching coils, which hardly induce any eddy currents in the rest of the setup, and successful coincidence measurements in a similar setup with similar switching times [Fis12], that goal is in reach. Obtaining fully-differential cross sections for the reactions

studied in this work could provide further insight into the role of electron correlation in ionization processes. In particular, for the measurement at a photon energy of $E_\gamma = 59.4$ eV it could shed further light on the question, why both theories and the experiment exhibit different cross sections. In the case of NSDI the recording of all final-state momenta would allow for an unambiguous determination of events emerging from two and three-photon ionization and hence test the theoretical model on a different level of precision.

A different but particularly interesting reaction to study is constituted by the sequential and non-sequential K-shell double-ionization of lithium. Here, the ionization dynamics right above and below the sequential threshold could be studied in a single experimental run. Close, to this threshold theories still deviate even for the simple case of helium and hence such a study would provide benchmark data for ab-initio calculations. The threshold for the non-sequential channel of this reaction is at a photon energy of $E_\gamma = 86.4$ eV. The energetic threshold for the sequential channel is at $E_\gamma = 108.4$ eV for $\text{Li}^{2+}(2s)$ final-states and at $E_\gamma = 106.1$ eV for $\text{Li}^{2+}(2p)$. Therefore, it is possible to laser-control this process by resonant excitation of the 2s-2p transition in ground-state lithium.

Appendix A: Atomic Units

Quantity	Formula	SI units
Mass	m_e	$9.10938 \cdot 10^{-31}$ kg
Charge	e	$1.60218 \cdot 10^{-19}$ C
Length	a_0	$5.29177 \cdot 10^{-11}$ m
Velocity	v_0	$2.18769 \cdot 10^6$ m s ⁻¹
Time	a_0/v_0	$2.41888 \cdot 10^{-17}$ s
Momentum	$m_e v_0$	$1.99285 \cdot 10^{-24}$ kg m s ⁻¹
Angular momentum	$\hbar = a_0 m_e v_0$	$1.05457 \cdot 10^{-34}$ kg m ² s ⁻¹
Frequency	$v_0/(2\pi a_0)$	$6.57969 \cdot 10^{15}$ Hz
Angular frequency	v_0/a_0	$4.13414 \cdot 10^{16}$ s ⁻¹
Energy	$e^2/(4\pi\epsilon_0 a_0^2)$	27.2116 eV
Electric field	$e/(4\pi\epsilon_0 a_0^2)$	$5.14221 \cdot 10^{11}$ V m ⁻¹
Magnetic field	$\hbar/(ea_0^2)$	$2.35052 \cdot 10^5$ T
Intensity	$1/2 c\epsilon_0(e/(4\pi\epsilon_0 a_0^2))^2$	$3.50953 \cdot 10^{16}$ W cm ⁻²

Quantity	Formula	SI units	Atomic units
Electron mass	m_e	$9.10938 \cdot 10^{-31}$ kg	1
Elementary charge	e	$1.60218 \cdot 10^{-19}$ C	1
Planck constant	\hbar	$1.05457 \cdot 10^{-34}$ kg m ² s ⁻¹	1
Proton mass	m_p	$1.67262 \cdot 10^{-27}$ kg	1836.15
Atomic mass unit	$\text{amu} = \frac{1}{12}m(^{12}\text{C})$	$1.66054 \cdot 10^{-27}$ kg	1822.89
Velocity of light	c	$2.99792 \cdot 10^8$ m s ⁻¹	137.04
Influence constant	ϵ_0	$8.85419 \cdot 10^{-12}$ A s V ⁻¹ m ⁻¹	$1/(4\pi)$
Induction constant	$\mu_0 = 1/(c^2\epsilon_0)$	$e\pi \cdot 10^{-7}$ V s A ⁻¹ m ⁻¹	$4\pi/137.04^2$

Appendix B: Properties of Lithium

Property	Symbol	Value [Ref.]
Atomic Number	Z	3
Nucleons	$Z+N$	7
Natural Abundance	η	92.4 % [WAB83]
Atomic Mass	m	7.016 004 amu [Ems95] $1.165035 \cdot 10^{-26}$ kg
Nuclear Spin	I	$3/2$
1st Ionization Potential	IP_{Li}	5.3917 eV [Nis]
2nd Ionization Potential	IP_{Li^+}	75.640 eV [Nis]
3rd Ionization Potential	$IP_{Li^{2+}}$	122.454 eV [Nis]
Wavelength Vacuum D2($2^2S_{1/2}-2^2P_{1/2}$)	λ_{vac}	670.9767 nm [San95]
Wavelength Vacuum D1($2^2S_{1/2}-2^2P_{3/2}$)	λ_{vac}	670.9616 nm [San95]
Lifetime 2^2P	τ	27.10 ns [MAH96]
Natural Linewidth 2^2P	γ	$36.90 \cdot 10^6$ s $^{-1}$ 5.873 MHz
Saturation Intensity D2	I_s	2.54 mW/cm 2
Hyperfine Structure Constant $2^2S_{1/2}$	a_{HFS}	401.76 MHz [Wal03]
Hyperfine Structure Constant $2^2P_{3/2}$	a_{HFS}	-3.05 MHz [OAO75]

Table 8.1: Basic properties of 7Li .

Appendix C: Filter transmissions

During the measurements at the free electron laser in Hamburg (FLASH) various filters have been employed to reduce the relative contributions of either the fundamental wavelengths or higher harmonics radiation. In the following the respective filter transmissions will be displayed for the wavelengths of interest.

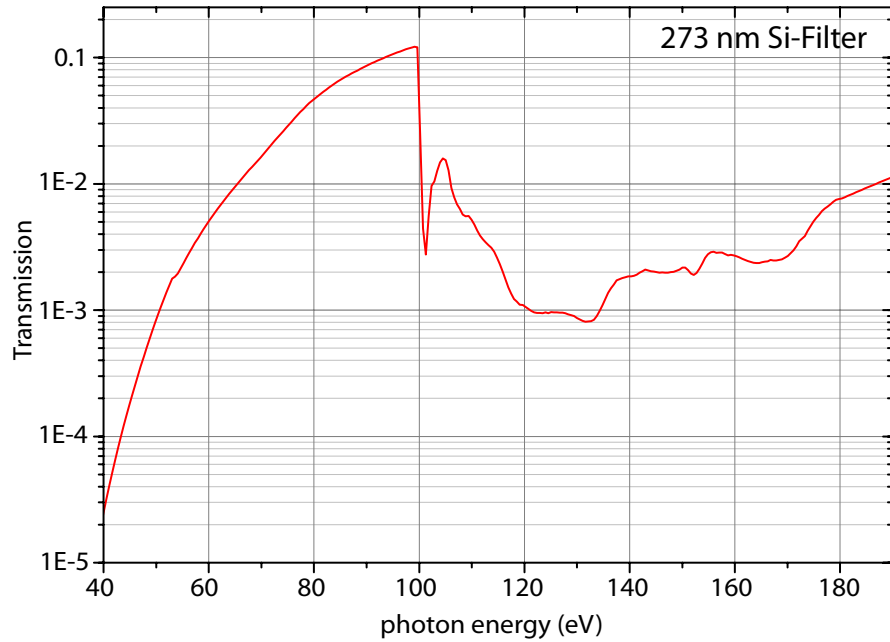


Figure 8.1: Transmission of the 273 nm thick silicon filter

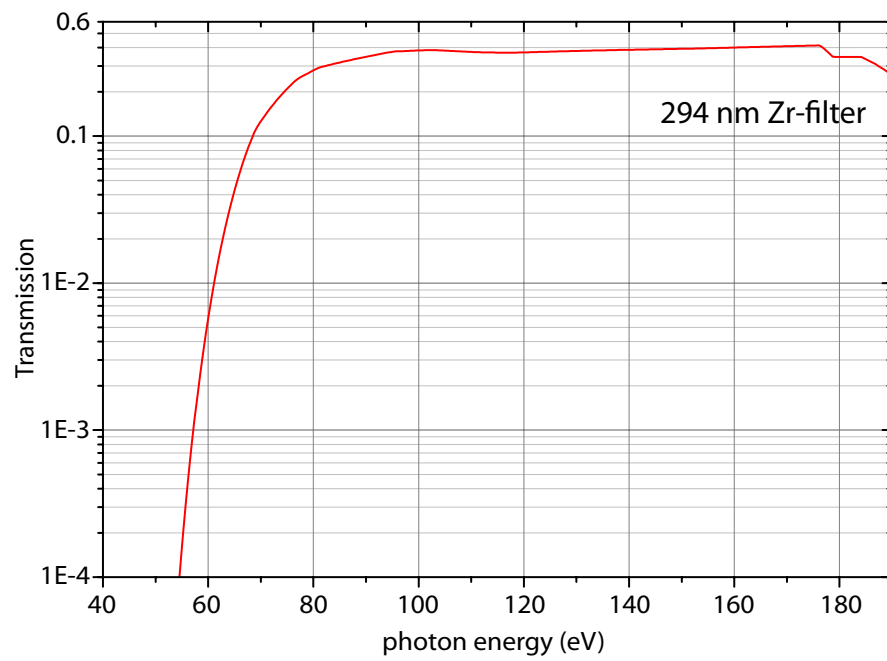


Figure 8.2: Transmission of the 294 nm thick zirconium filter

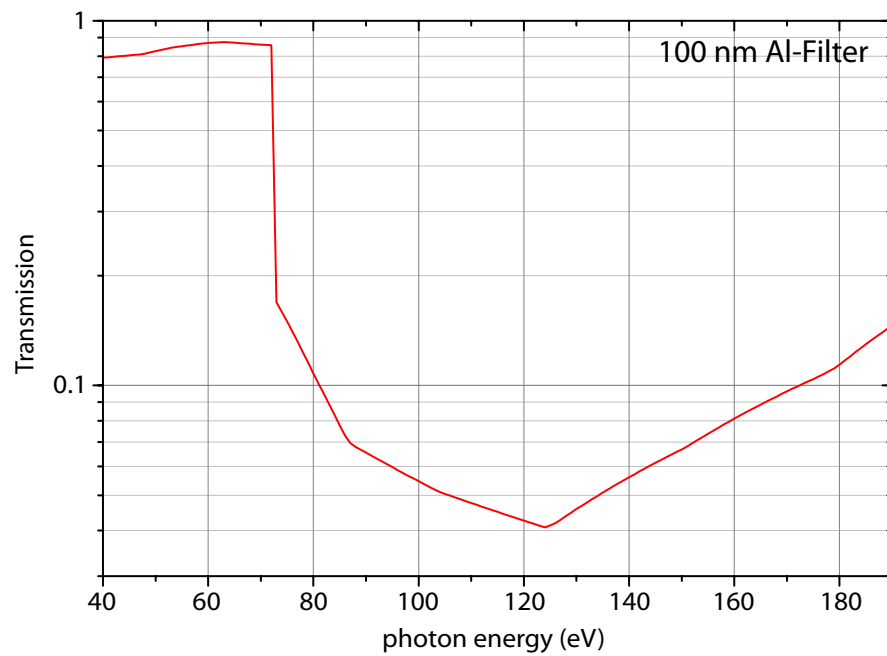


Figure 8.3: Transmission of the 100 nm thick aluminum filter

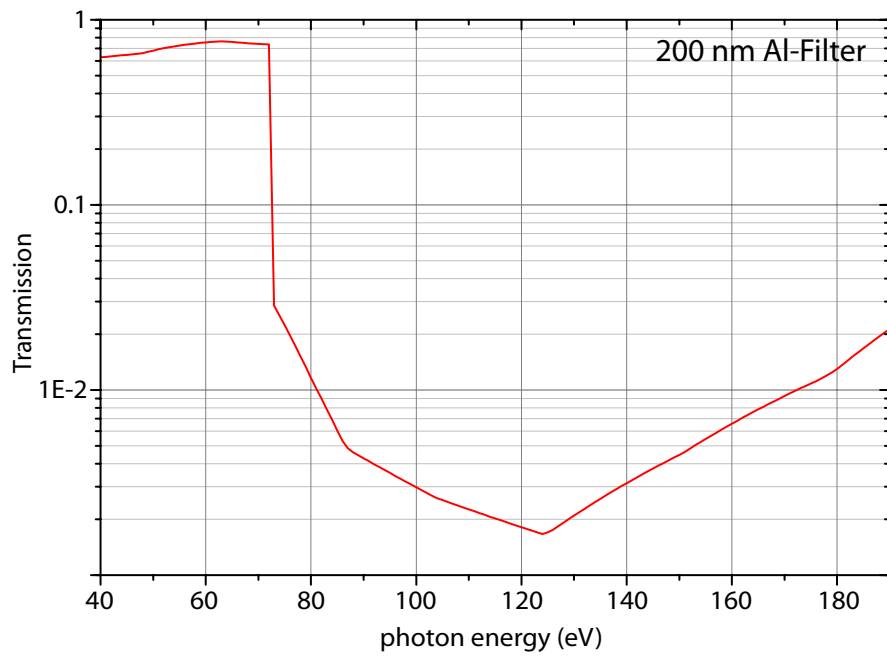


Figure 8.4: Transmission of the 200 nm thick aluminum filter

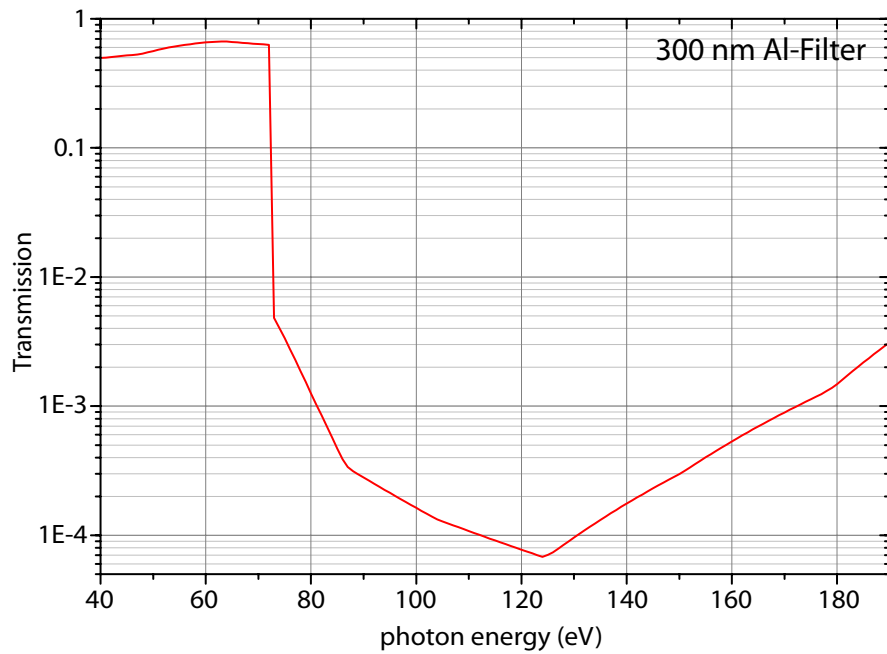


Figure 8.5: Transmission of the 300 nm thick aluminum filter

Appendix D: Dominant Decay Channels of singly excited ${}^7\text{Li}^+$

In the measurements for two-photon resonance enhanced double ionization and non-sequential two-photon double ionization the detectors (see Sec. 5.1.4) have been operated in a regime which allowed only for the detection of either excited singly charged or doubly charged atomic lithium. Therefore, the dominant decay channels of the various excited states of Li^+ have to be known.

To gain a thorough understanding of the processes investigated and the spectra recorded

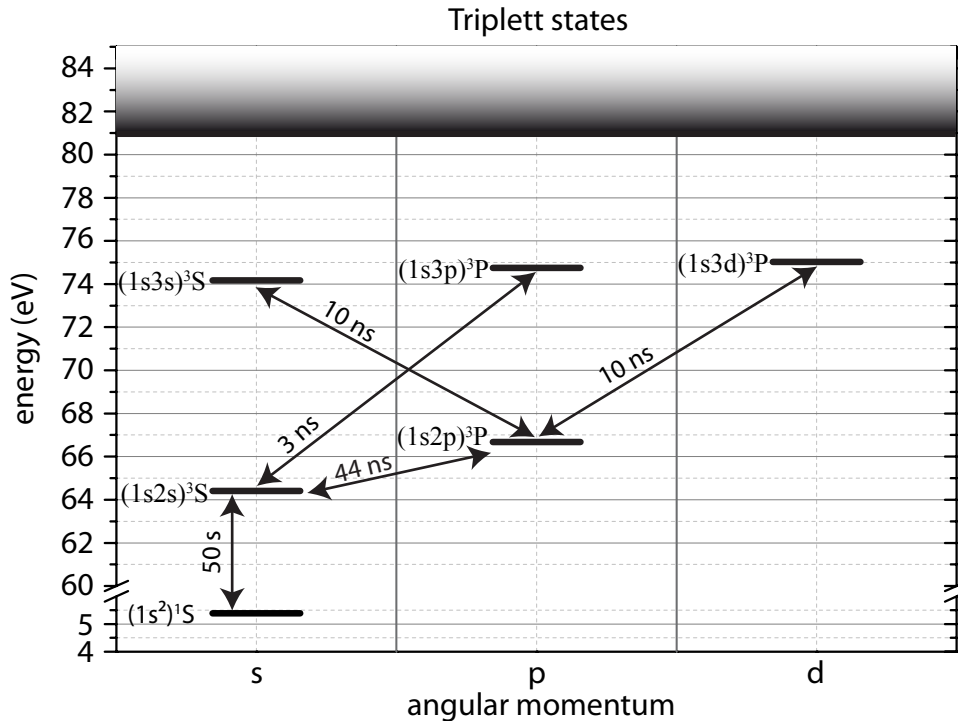


Figure 8.6: Dominant decay channels of the triplet states of the singly-charged lithium ion.

it is important to identify the final-states which are recorded by the detection system. In Sec. 5.1.4 it has been shown that only particles, whose internal energy exceeds the

work function of the channel plate by a factor of 2 are able to create secondary electrons and thus are detected. In the case of lithium this implies that the ionic ground-state, i.e. $\text{Li}^+(1s^2)$ -state, will not be detected. Given that the TOF, for the spectrometer settings used, amounts to approximately $50 \mu\text{s}$, the final states which do not decay to the ionic ground state in this time have to be determined.

Figure 8.6 illustrates the decay channels for the case that the remaining electrons of the lithium ion couple to a triplet state. According to Pauli's principle the decay to the ${}^7\text{Li}(1s^2)$ -state would require a spin-flip for all triplet states. This in turn leads to the accumulation of atoms in the $(1s2s)^3S$ -state. The $(1s2s)^3S \rightarrow (1s^2)^1S$ transition does not only imply a spin-flip, but is also dipole forbidden. The lifetime of this metastable state amounts to approximately 50s . Hence, for ionization plus excitation into triplet-states all final-states are detected. Furthermore, since all states excited in the ionization reaction have gathered in the same state by the time they arrive at the detector, they are all detected with equal probabilities.

Regarding, ionization plus excitation with singlet final states a more diverse situation

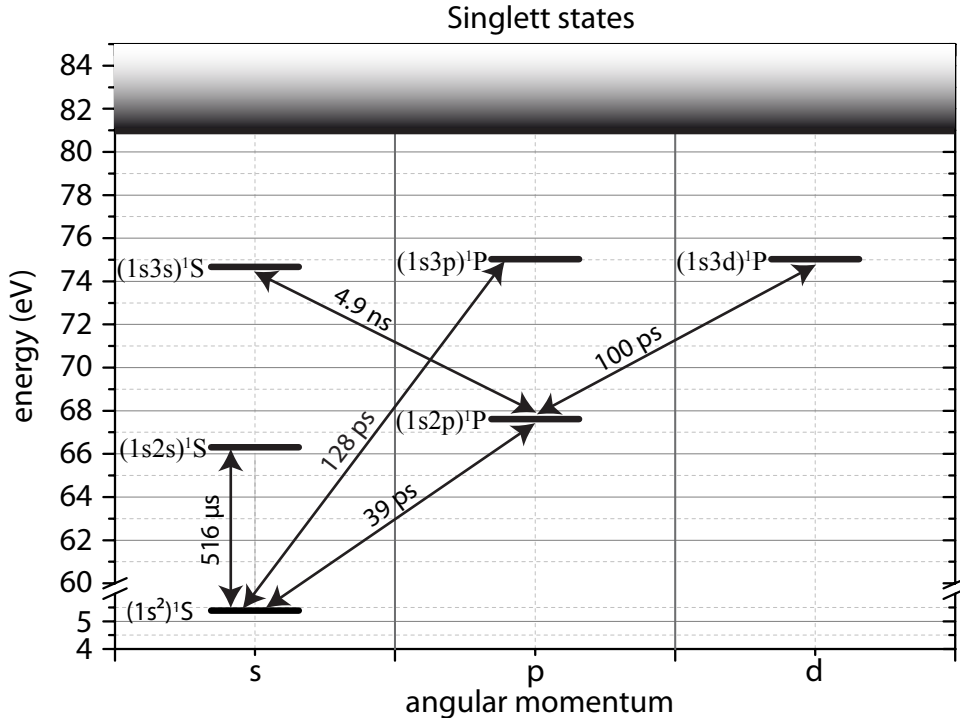


Figure 8.7: Dominant decay channels of the singlet states of the singly charged lithium ion.

is encountered. The direct decay to the ground-state does not require a spin-flip, which

results in a fast decay off all but one final states to the $(1s^2)^1S$ state. The exception is given by the $(1s2s)^1S$ -state. Like for the corresponding triplet state its decay is forbidden in dipole approximation and is therefore only allowed via a quadrupole transition. With a lifetime of $516\mu s$, the largest fraction of atoms excited to this state will arrive at the detector before decaying. The detection probability should be resembling the one of the triplet state, as first the states energy is almost the same and second the same Auger decay channels exist.

Bibliography

- [AC12] G. S. J. Armstrong and J. Colgan: “Angular distributions for two-photon double ionization of lithium”. In: *Physical Review A* 86.2 (2012), p. 023407.
- [Ack07] W. Ackermann et al.: “Operation of a free-electron laser from the extreme ultraviolet to the water window”. In: *Nature Photonics* 1.6 (2007), pp. 336–342.
- [AH05] L. Avaldi and A. Huetz: “Photodouble ionization and the dynamics of electron pairs in the continuum”. In: *Journal of Physics B: Atomic, Molecular and Optical Physics* 38.9 (2005), S861.
- [And95] M. H. Anderson et al.: “Observation of Bose-Einstein Condensation in a Dilute Atomic Vapor”. In: *Science* 269 (1995), p. 198.
- [ANF12] S. Askeland, R. Nepstad, and M. Førre: “Two-photon double ionization of helium by attosecond laser pulses: Evidence of highly correlated electron motion”. In: *Physical Review A* 85.3 (2012), p. 035404.
- [AW] F. Aumayr and H. Winter: “Potential Electron Emission from Metal and Insulator Surfaces”. In: *Slow Heavy-Particle Induced Electron Emission from Solid Surfaces*. Vol. 225. Springer-Verlag Berlin Heidelberg, pp. 79–112.
- [Ayv02] V. Ayvazyan et al.: “Generation of GW Radiation Pulses from a VUV Free-Electron Laser Operating in the Femtosecond Regime”. In: *Physical Review Letters* 88.10 (2002), p. 104802.
- [Bar79] R. A. Baragiola et al.: “Ion-induced electron emission from clean metals”. In: *Surface Science* 90.2 (1979), pp. 240–255.
- [BDM05] A. Becker, R. Dörner, and R. Moshhammer: “Multiple fragmentation of atoms in femtosecond laser pulses”. In: *Journal of Physics B: Atomic, Molecular and Optical Physics* 38.9 (2005), S753–S772.
- [BF96] I. Bray and D. V. Fursa: “Convergent Close-Coupling Method: A "Complete Scattering Theory"?” In: *Physical Review Letters* 76.15 (1996), p. 2674.
- [BKA04] P. Bolognesi, G. C. King, and L. Avaldi: “Photo-double-ionization of atoms”. In: *Radiation Physics and Chemistry* 70.1–3 (2004), pp. 207–236.

- [BL91] H. Bachau and P. Lambropoulos: “Theory of the photoelectron spectrum in double ionization through two-photon absorption from $\text{He}(2s^2)$ ”. In: *Physical Review A* 44.1 (1991), R9.
- [Blo35] F. Bloch: “Double Electron Transitions in X-Ray Spectra”. In: *Physical Review* 48.3 (1935), pp. 187–192.
- [BLZ67] C. N. Burrous, A. J. Lieber, and V. T. Zaviantseff: “Detection Efficiency of a Continuous Channel Electron Multiplier for Positive Ions”. In: *Review of Scientific Instruments* 38.10 (1967), pp. 1477–1481.
- [Bou00] B. Boudaïffa et al.: “Resonant Formation of DNA Strand Breaks by Low-Energy (3 to 20 eV) Electrons”. In: *Science* 287.5458 (2000), pp. 1658–1660.
- [BPN84] R. Bonifacio, C. Pellegrini, and L.M. Narducci: “Collective instabilities and high-gain regime in a free electron laser”. In: *Optics Communications* 50.6 (1984), pp. 373–378.
- [Bra02] I. Bray et al.: “Electrons and photons colliding with atoms: development and application of the convergent close-coupling method”. In: *Journal of Physics B: Atomic, Molecular and Optical Physics* 35.15 (2002), R117–R146.
- [Bre03] R. Bredy et al.: “MOTRIMS as a generalized probe of AMO processes”. In: *Nuclear Instruments and Methods in Physics Research Section B: Beam Interactions with Materials and Atoms* 205 (2003), pp. 191–195.
- [Bro01] I. N. Bronstein et al.: *Taschenbuch der Mathematik*. 5th ed. Verlag Harri Deutsch, Frankfurt a.M., 2001.
- [BS92] I. Bray and A. T. Stelbovics: “Convergent close-coupling calculations of electron-hydrogen scattering”. In: *Physical Review A* 46.11 (1992), pp. 6995–7011.
- [BSS02] R. Barrios, P. Skurski, and J. Simons: “Mechanism for Damage to DNA by Low-Energy Electrons”. In: *The Journal of Physical Chemistry B* 106.33 (2002), pp. 7991–7994.
- [Car67] Th. A. Carlson: “Double Electron Ejection Resulting from Photo-Ionization in the Outermost Shell of He, Ne, and Ar, and Its Relationship to Electron Correlation”. In: *Physical Review* 156.1 (1967), pp. 142–149.
- [Cha06] H. N. Chapman et al.: “Femtosecond diffractive imaging with a soft-X-ray free-electron laser”. In: *Nature Physics* 2.12 (2006), pp. 839–843.
- [Cha11] H. N. Chapman et al.: “Femtosecond X-ray protein nanocrystallography”. In: *Nature* 470.7332 (2011), pp. 73–77.

-
- [Chu97] K. Chung: “Photoionization of lithium below the $\text{Li}^+ 1s2s^3$ threshold”. In: *Physical Review A* 56.5 (1997), R3330–R3333.
- [Chu85] S. Chu et al.: “Three-Dimensional Viscous Confinement and Cooling of Atoms by Resonance Radiation Pressure”. In: *Physical Review Letters* 55.1 (1985), pp. 48–51.
- [Chu86] Steven Chu et al.: “Experimental Observation of Optically Trapped Atoms”. In: *Physical Review Letters* 57.3 (1986), pp. 314–317.
- [Col01] J. Colgan et al.: “Total integral and ejected-energy differential cross sections for the electron-impact ionization of lithium”. In: *Physical Review A* 63 (2001), p. 062709.
- [Col09] J. Colgan et al.: “Total cross sections for the double photoionization of Li from the ground and excited states”. In: *Physical Review A* 80.6 (2009), p. 063414.
- [CP03] J. Colgan and M. S. Pindzola: “Total and differential cross-section calculations for the double photoionization of the helium $1s2s^{1,3}$ states”. In: *Physical Review A* 67.1 (2003), p. 012711.
- [CP06] J. Colgan and M. S. Pindzola: “Energy differential cross sections for the triple photoionization of lithium”. In: *Journal of Physics B: Atomic, Molecular and Optical Physics* 39 (2006), pp. 1879–1887.
- [CP12] J. Colgan and M. S. Pindzola: “Angular Distributions for the Complete Photofragmentation of the Li Atom”. In: *Physical Review Letters* 108.5 (2012), p. 053001.
- [CPR04] J. Colgan, M. S. Pindzola, and F. Robicheaux: “Lattice Calculations of the Photoionization of Li”. In: *Physical Review Letters* 93 (2004), p. 053201.
- [CPR05] J. Colgan, M. S. Pindzola, and F. Robicheaux: “Double and triple photoionization of Li”. In: *Physical Review A* 72 (2005), p. 022727.
- [Dav95] K. B. Davis et al.: “Bose-Einstein Condensation in a Gas of Sodium Atoms”. In: *Physical Review Letters* 75.22 (1995), pp. 3969–3973.
- [Dem04] W. Demtröder: *Experimentalphysik 2: Elektrizität und Optik*. Springer-Verlag, 2004.
- [DK00] N. Delone and V. Krainov: *Multiphoton processes in atoms*. 2nd ed. Springer-Verlag, 2000.
- [DK99a] N. Delone and V. Krainov: “AC Stark shift of atomic energy levels”. In: *Physics-Uspekhi* 42 (1999), pp. 669–687.

- [DK99b] N. B. Delone and V. P. Krainov: *Multiphoton Processes in Atoms*. Springer-Verlag, 1999.
- [Don02] E. A. Donley et al.: “Atom-molecule coherence in a Bose-Einstein condensate”. In: *Nature* 417 (2002), p. 529.
- [Dor11] C. Dornes: “3D-focusing Spectrometer for a Reaction Microscope”. Diploma thesis. Universität Heidelberg / Max-Planck-Institut für Kernphysik, 2011.
- [Dor02] A. Dorn et al.: “Double ionization of helium by electron impact in the impulsive regime”. In: *Physical Review A* 65.3 (2002), p. 032709.
- [Dör00] R. Dörner et al.: “Cold Target Recoil Ion Momentum Spectroscopy: A ‘momentum microscope’ to view Atomic Collision Dynamics”. In: *Physics Reports* 330 (2000), pp. 95–192.
- [Dör98] R. Dörner et al.: “Photo-double-ionization of He: Fully differential and absolute electronic and ionic momentum distributions”. In: *Physical Review A* 57.2 (1998), pp. 1074–1090.
- [Dür07] M. Dürr et al.: “(e,3e) on Helium at Low Impact Energy: The Strongly Correlated Three-Electron Continuum”. In: *Physical Review Letters* 98 (2007), p. 193201.
- [Düs06] S. Düsterer et al.: “Spectroscopic characterization of vacuum ultraviolet free electron laser pulses”. In: *Optics Letters* 31.11 (2006), pp. 1750–1752.
- [Ela09] J. H. D. Eland: *Dynamics of double photoionization in molecules and atoms*. Vol. 141. John Wiley & Sons, Inc., 2009.
- [Eli76] L. R. Elias et al.: “Observation of Stimulated Emission of Radiation by Relativistic Electrons in a Spatially Periodic Transverse Magnetic Field”. In: *Physical Review Letters* 36.13 (1976), p. 717.
- [Emm10] P. Emma et al.: “First lasing and operation of an ångstrom-wavelength free-electron laser”. In: *Nature Photonics* 4.9 (2010), pp. 641–647.
- [Ems95] J. Emsley: *The Elements*. Oxford Chemistry Guides. New York: Oxford. Univ. Press, 1995.
- [EP97] A. T. J. B. Eppink and D. H. Parker: “Velocity map imaging of ions and electrons using electrostatic lenses: Application in photoelectron and photofragment ion imaging of molecular oxygen”. In: *Review of Scientific Instruments* 68.9 (1997), pp. 3477–3484.

-
- [Erg06] Th. Ergler: “Zeitaufgelöste Untersuchungen zur Fragmentationsdynamik von H₂ (D₂) in ultra-kurzen Laserpulsen”. PhD thesis. Universität Heidelberg / Max-Planck-Institut f. Kernphysik Heidelberg, 2006.
- [FAH05] J. Feldhaus, J. Arthur, and J. B. Hastings: “X-ray free-electron lasers”. In: *Journal of Physics B: Atomic, Molecular and Optical Physics* 38.9 (2005), S799–S819.
- [Fai86] F. H. M. Faisal: *Theory of Multiphoton Processes*. Plenum Press New York, 1986.
- [Far30] P. T. Farnsworth: *Electron Multiplier*. 1930.
- [Fei08] J. Feist et al.: “Nonsequential two-photon double ionization of helium”. In: *Physical Review A* 77.4 (2008), p. 043420.
- [Fei09] J. Feist et al.: “Probing Electron Correlation via Attosecond XUV Pulses in the Two-Photon Double Ionization of Helium”. In: *Physical Review Letters* 103.6 (2009), p. 063002.
- [Fel10] J. Feldhaus: “FLASH – the first soft x-ray free electron laser (FEL) user facility”. In: *Journal of Physics B: Atomic, Molecular and Optical Physics* 43.19 (2010), p. 194002.
- [Fis03] D. Fischer: “Mehr-Teilchen-Dynamik in der Einfach- und Doppelionisation von Helium durch geladene Projektile”. PhD thesis. Universität Heidelberg / Max-Planck-Institut f. Kernphysik Heidelberg, 2003.
- [Fis04] M. Fischer et al.: “New Limits on the Drift of Fundamental Constants from Laboratory Measurements”. In: *Physical Review Letters* 92 (2004), p. 230802.
- [Fis12] D. Fischer et al.: “Ion-lithium collision dynamics studied with an in-ring MOTReMi”. In: *arXiv:1204.6173* (2012).
- [Fle01] X. Flechard et al.: “Kinematically Complete Charge Exchange Experiment in the $Cs^+ + Rb$ Collision System Using a MOT Target”. In: *Physical Review Letters* 87.12 (2001), p. 123203.
- [Foo05] C. J. Foot: *Atomic Physics*. Oxford: Oxford University Press, 2005.
- [Fou08] L. Foucar: “Auslese von Delaylinedetektoren mit Hilfe von Transientenrekordern”. PhD thesis. Johann Wolfgang Goethe-Universität, Frankfurt a.M., 2008.
- [Fou06] E. Fomouo et al.: “Theory of multiphoton single and double ionization of two-electron atomic systems driven by short-wavelength electric fields: An ab initio treatment”. In: *Physical Review A* 74 (2006), p. 063409.

- [Fou08] E. Fomouuo et al.: “Evidence for highly correlated electron dynamics in two-photon double ionization of helium”. In: *Journal of Physics B: Atomic, Molecular and Optical Physics* 41.5 (2008), p. 051001.
- [Fou10] E. Fomouuo et al.: “Time-dependent analysis of the mechanism for two-photon double escape in helium: from very long to attosecond time scales”. In: *Journal of Physics B: Atomic, Molecular and Optical Physics* 43.9 (2010), p. 091001.
- [Fra02] G. W. Fraser: “The ion detection efficiency of microchannel plates (MCPs)”. In: *International Journal of Mass Spectrometry* 215.1-3 (2002), pp. 13–30.
- [Fri98] H. Friedrich: *Theoretical Atomic Physics*. Springer-Verlag, 1998.
- [Frü11] Ulrike Frühling: “Light-field streaking for FELs”. In: *Journal of Physics B: Atomic, Molecular and Optical Physics* 44.24 (2011), p. 243001.
- [Geh03] M. E. Gehm: “Preparation of an optically-trapped degenerate Fermi gas of ^6Li : Finding the route to degeneracy”. PhD thesis. Duke University, 2003.
- [Gen] *Genesis program package*. <http://pbpl.physics.ucla.edu/reiche>. 2013.
- [GM31] M. Göppert-Mayer: “Über Elementarakte mit zwei Quantensprüngen”. In: *Annalen der Physik* 401 (1931), pp. 273–294.
- [Gre02] M. Greiner et al.: “Quantum phase transition from a superfluid to a Mott insulator in a gas of ultracold atoms”. In: *Nature* 415 (2002), pp. 39–44.
- [GW62] G. W. Goodrich and W. C. Wiley: “Continuous Channel Electron Multiplier”. In: *Review of Scientific Instruments* 33.7 (1962), pp. 761–762.
- [HCP08] I. V. Hertel and Schulz C-P: *Atome, Moleküle und optische Physik*. Springer, 2008.
- [HG50] V. Hughes and L. Grabner: “The Radiofrequency Spectrum of Rb^{85}F and Rb^{87}F by the Electric Resonance Method”. In: *Physical Review* 79.2 (1950), p. 314.
- [HK07] Z. Huang and k.-J. Kim: “Review of x-ray free-electron laser theory”. In: *Physical Review Special Topics - Accelerators and Beams* 10.3 (2007), p. 034801.
- [HM08] M. Harvey and A. J. Murray: “Cold Atom Trap with Zero Residual Magnetic Field: The ac Magneto-Optical Trap”. In: *Physical Review Letters* 101.17 (2008), p. 173201.
- [HMG98] H. W. van der Hart, K. W. Meyer, and C. H. Greene: “Double photoionization and ionization excitation of the metastable helium S states”. In: *Physical Review A* 57.5 (1998), pp. 3641–3645.

-
- [HMR08] D. A. Horner, C. W. McCurdy, and T. N. Rescigno: “Triple differential cross sections and nuclear recoil in two-photon double ionization of helium”. In: *Physical Review A* 78.4 (2008), p. 043416.
- [Hor07] D. A. Horner et al.: “Two-photon double ionization of helium above and below the threshold for sequential ionization”. In: *Physical Review A* 76.3 (2007), p. 030701.
- [HRM10] D. A. Horner, T. N. Rescigno, and C. W. McCurdy: “Nuclear recoil cross sections from time-dependent studies of two-photon double ionization of helium”. In: *Physical Review A* 81.2 (2010), p. 023410.
- [HS75] T. W. Hänsch and A. L. Schawlow: “Cooling of gases by laser radiation”. In: *Optics Communications* 13 (1975), p. 68.
- [IK07] I. A. Ivanov and A. S. Kheifets: “Two-photon double ionization of helium in the region of photon energies 42–50eV”. In: *Physical Review A* 75.3 (2007), p. 033411.
- [Jag02] O. Jagutzki et al.: “Multiple Hit Readout of a Microchannel Plate Detector With a Three-Layer Delay-Line Anode”. In: *IEEE Transactions on Nuclear Science* 49.5 (2002), pp. 2477–2483.
- [Jen05] U. D. Jentschura et al.: “Precise Calculation of Transition Frequencies of Hydrogen and Deuterium Based on a Least-Squares Analysis”. In: *Physical Review Letters* 95.16, 163003 (2005), p. 163003.
- [Jia10a] Y. H. Jiang et al.: “Temporal coherence effects in multiple ionization of N₂ via XUV pump-probe autocorrelation”. In: *Physical Review A* 82.4 (2010), p. 041403.
- [Jia10b] Y. H. Jiang et al.: “Ultrafast Extreme Ultraviolet Induced Isomerization of Acetylene Cations”. In: *Physical Review Letters* 105.26 (2010), p. 263002.
- [Joc03] S. Jochim et al.: “Bose-Einstein Condensation of Molecules”. In: *Science* 302.5653 (2003), pp. 2101–2103.
- [Kas89] M. A. Kasevich et al.: “RF-spectroscopy in an Atomic Fountain”. In: *Physical Review Letters* 63 (1989), pp. 612–616.
- [KB96] A. S. Kheifets and I. Bray: “Calculation of double photoionization of helium using the convergent close-coupling method”. In: *Physical Review A* 54.2 (1996), R995–R997.
- [Kel65] L. V. Keldysh: “Ionization in the field of a strong electromagnetic wave”. In: *Soviet Physics JETP* 20 (1965), p. 1307.

- [KFB09] A. S. Kheifets, D. V. Fursa, and I. Bray: “Two-electron photoionization of ground-state lithium”. In: *Physical Review A* 80.6 (2009), p. 063413.
- [Khe01] A. S. Kheifets: “On different mechanisms of the two-electron atomic photoionization”. In: *Journal of Physics B: Atomic, Molecular and Optical Physics* 34.8 (2001), pp. L247–L252.
- [Khe12] A. Kheifets. private communication. 2012.
- [Khe10a] A. S. Kheifets et al.: “Differential cross sections of double photoionization of lithium”. In: *Physical Review A* 82.2 (2010), p. 023403.
- [Khe10b] A. S. Kheifets et al.: “Spin effects in double photoionization of lithium”. In: *Physical Review A* 81.2 (2010), p. 023418.
- [Khe11] A. S. Kheifets et al.: “Interference effects in L-shell atomic double photoionization”. In: *Journal of Physics B: Atomic, Molecular and Optical Physics* 44 (2011), p. 011002.
- [KI09] F. Krausz and M. Ivanov: “Attosecond physics”. In: *Reviews of Modern Physics* 81.1 (2009), p. 163.
- [Kin77] B. M. Kincaid: “A short-period helical wiggler as an improved source of synchrotron radiation”. In: *Journal of Applied Physics* 48.7 (1977), p. 2684.
- [KM96] C. Kurtsiefer and J. Mlynek: “A 2-dimensional detector with high spatial and temporal resolution for metastable rare gas atoms”. In: *Applied Physics B: Lasers and Optics* 64.1 (1996), pp. 85–90.
- [Kna05] A. Knapp et al.: “Photo double ionization of helium 100 eV and 450 eV above threshold: I. Linearly polarized light”. In: *Journal of Physics B: Atomic, Molecular and Optical Physics* 38.6 (2005), pp. 615–633.
- [Kno05] S. Knoop et al.: “Single ionization and electron capture in $\text{He}^{2+} + \text{Na}$ collisions”. In: *Journal of Physics B: Atomic, Molecular and Optical Physics*. 38 (2005), pp. 1987–1998.
- [Kra10] F. Krasniqi et al.: “Imaging molecules from within: Ultrafast angström-scale structure determination of molecules via photoelectron holography using free-electron lasers”. In: *Physical Review A* 81.3 (2010), p. 033411.
- [Kra96] B. Krassig et al.: “State dependence of angular correlation patterns in double photoionization”. In: *Journal of Physics B: Atomic, Molecular and Optical Physics* 29.18 (1996), pp. 4255–4265.

-
- [Kre05] M. Krems et al.: “Channel electron multiplier and channelplate efficiencies for detecting positive ions”. In: *Review of Scientific Instruments* 76.9 (2005), pp. 093305–093305–7.
- [Kur11] M. Kurka: “Zwei-Photonen-Doppelionisation von Helium und D2-Molekülen am Freie-Elektronen-Laser in Hamburg”. PhD Thesis. Universität Heidelberg / Max-Planck-Institut für Kernphysik, Heidelberg, 2011.
- [Kur09] M. Kurka et al.: “Two-photon double ionization of Ne by free-electron laser radiation: a kinematically complete experiment”. In: *Journal of Physics B: Atomic, Molecular and Optical Physics* 42.14 (2009), p. 141002.
- [Kur10] M. Kurka et al.: “Differential cross sections for non-sequential double ionization of He by 52 eV photons from the Free Electron Laser in Hamburg, FLASH”. In: *New Journal of Physics* 12.7 (2010), p. 073035.
- [Lam76] P. Lambropoulos: “Topics on Multiphoton Processes in Atoms”. In: ed. by D.R. Bates and B. Bederson. Vol. 12. *Advances in Atomic and Molecular Physics*. Academic Press, 1976, pp. 87–164.
- [Lec75] C. Lecompte et al.: “Laser temporal-coherence effects on multiphoton ionization processes”. In: *Physical Review A* 11.3 (1975), pp. 1009–1015.
- [Leo94] W. R. Leo: *Techniques for Nuclear and Particle Physics Experiments*. Springer-Verlag, 1994.
- [Lin05] A. M. Lindenberg et al.: “Atomic-Scale Visualization of Inertial Dynamics”. In: *Science* 308.5720 (2005), pp. 392–395.
- [LMZ98] P. Lambropoulos, P. Maragakis, and J. Zhang: “Two-electron atoms in strong fields”. In: *Physics Reports* 305.5 (1998), pp. 203–293.
- [LSW92] K. Lindquist, M. Stephens, and C. Wieman: “Experimental and theoretical study of the vapor-cell Zeeman optical trap”. In: *Physical Review A* 46.7 (1992), pp. 4082–4090.
- [Mad71] J. M. J. Madey: “Stimulated Emission of Bremsstrahlung in a Periodic Magnetic Field”. In: *Journal of Applied Physics* 42.5 (1971), p. 1906.
- [MAH96] W. I. McAlexander, E. R. I. Abraham, and R. G. Hulet: “Radiative lifetime of the $2P$ state of lithium”. In: *Physical Review A* 54.1 (1996), R5–R8.
- [MB95] F. Maulbetsch and J. S. Briggs: “Selection rules for transitions to two-electron continuum states”. In: *Journal of Physics B: Atomic, Molecular and Optical Physics* 28.4 (1995), pp. 551–564.

- [Mer95] V. Mergel et al.: “State Selective Scattering Angle Dependent Capture Cross Sections Measured by Cold Target Recoil Ion Momentum Spectroscopy”. In: *Physical Review Letters* 74.12 (1995), pp. 2200–2203.
- [Mit08] R. Mitzner et al.: “Spatio-temporal coherence of free electron laser pulses in the soft x-ray regime”. In: *Optics Express* 16.24 (2008), p. 19909.
- [Mos94] R. Moshhammer et al.: “Low-Energy Electrons and Their Dynamical Correlation with Recoil Ions for Single Ionization of Helium by Fast, Heavy-Ion Impact”. In: *Physical Review Letters* 73.25 (1994), pp. 3371–3374.
- [Mos96] R. Moshhammer et al.: “A 4π recoil-ion electron momentum analyzer: a high-resolution “microscope” for the investigation of the dynamics of atomic, molecular and nuclear reactions”. In: *Nuclear Instruments and Methods in Physics Research Section B: Beam Interactions with Materials and Atoms* 108.4 (1996), p. 425.
- [MS99] H. J. Metcalf and P. van der Straten: *Laser Cooling and Trapping*. Springer-Verlag, 1999.
- [Mun01] S. R. Muniz et al.: “Measurements of capture velocity in a magneto-optical trap for a broad range of light intensities”. In: *Physical Review A* 65.1 (2001), p. 015402.
- [Nab05] Y. Nabekawa et al.: “Production of Doubly Charged Helium Ions by Two-Photon Absorption of an Intense Sub-10-fs Soft X-Ray Pulse at 42 eV Photon Energy”. In: *Physical Review Letters* 94.4 (2005), p. 043001.
- [Ngu04] H. Nguyen et al.: “Recoil ion momentum spectroscopy using magneto-optically trapped atoms”. In: *Review of Scientific Instruments* 75.8 (2004), pp. 2638–2647.
- [Ngu11] J. Nguyen et al.: “Direct observation of ultrafast-electron-transfer reactions unravels high effectiveness of reductive DNA damage”. In: *Proceedings of the National Academy of Sciences* 108.29 (2011), pp. 11778–11783.
- [Nis] *NIST Atomic Spectra Database*. 2012.
- [NL01] L. A. A. Nikolopoulos and P. Lambropoulos: “Multichannel theory of two-photon single and double ionization of helium”. In: *Journal of Physics B: Atomic, Molecular and Optical Physics* 34.4 (2001), p. 545.
- [OAO75] H. Orth, H. Ackermann, and E. W. Otten: “Fine and Hyperfine Structure of the 2^2P Term of ^7Li ; Determination of the Nuclear Quadrupole Moment”. In: *Zeitschrift für Physik A* 273 (1975), pp. 221–232.

-
- [Osc60] P. K. Oschepkov et al. In: *Pribory. Tekh. Eksper.* 4 (1960), p. 89.
- [Pal10] A. Palacios et al.: “Two-photon double ionization of the helium atom by ultra-short pulses”. In: *Journal of Physics B: Atomic, Molecular and Optical Physics* 43.19 (2010), p. 194003.
- [Paz11] R. Pazourek et al.: “Universal features in sequential and nonsequential two-photon double ionization of helium”. In: *Physical Review A* 83.5 (2011), p. 053418.
- [PB01] Th. Pattard and J. Burgdörfer: “Half-collision model for multiple ionization by photon impact”. In: *Physical Review A* 64.4 (2001), p. 042720.
- [PBM06] A. Palacios, H. Bachau, and F. Martin: “Enhancement and Control of H₂ Dissociative Ionization by Femtosecond VUV Laser Pulses”. In: *Physical Review Letters* 96.14 (2006), p. 143001.
- [Pel88] C. Pellegrini: “Progress toward a soft X-ray FEL”. In: *Nuclear Instruments and Methods in Physics Research Section A: Accelerators, Spectrometers, Detectors and Associated Equipment* 272.12 (1988), pp. 364–367.
- [Pfe10] Th. Pfeifer et al.: “Partial-coherence method to model experimental free-electron laser pulse statistics”. In: *Optics Letters* 35.20 (2010), pp. 3441–3443.
- [PK61] E. S. Parilis and L. M. Kishinevskii: “The Theory of Ion-Electron Emission”. In: *Soviet Physics-Solid State* 3.4 (1961), pp. 885–891.
- [PM82] W. D. Phillips and H. Metcalf: “Laser Deceleration of an Atomic Beam”. In: *Physical Review Letters* 48.9 (1982), pp. 596–599.
- [PS03] C. Pellegrini and J. Stöhr: “X-ray free-electron lasers - principles, properties and applications”. In: *Nuclear Instruments and Methods in Physics Research Section A: Accelerators, Spectrometers, Detectors and Associated Equipment* 500.1–3 (2003), pp. 33–40.
- [Raa87] E. L. Raab et al.: “Trapping of Neutral Sodium Atoms with Radiation Pressure”. In: *Physical Review Letters* 59.23 (1987), pp. 2631–2634.
- [Res99] T. N. Rescigno et al.: “Collisional Breakup in a Quantum System of Three Charged Particles”. In: *Science* 286.5449 (1999), pp. 2474–2479.
- [Ric09] M. Richter et al.: “Extreme Ultraviolet Laser Excites Atomic Giant Resonance”. In: *Physical Review Letters* 102.16 (2009), p. 163002.
- [Rol11] S. Roling et al.: “Temporal and spatial coherence properties of free-electron-laser pulses in the extreme ultraviolet regime”. In: *Physical Review Special Topics - Accelerators and Beams* 14.8 (2011), p. 080701.

- [Rud04] A. Rudenko et al.: “Resonant structures in the low-energy electron continuum for single ionization of atoms in the tunnelling regime”. In: *Journal of Physics B: Atomic, Molecular and Optical Physics* 37.24 (2004), pp. L407–L413.
- [Rud08] A. Rudenko et al.: “Recoil-Ion Momentum Distributions for Two-Photon Double Ionization of He and Ne by 44 eV Free-Electron Laser Radiation”. In: *Physical Review Letters* 101.7 (2008), p. 073003.
- [Rud10] A. Rudenko et al.: “Exploring few-photon, few-electron reactions at FLASH: from ion yield and momentum measurements to time-resolved and kinematically complete experiments”. In: *Journal of Physics B: Atomic, Molecular and Optical Physics* 43.19 (2010), p. 194004.
- [Sam90] J. A. R. Samson: “Proportionality of electron-impact ionization to double photoionization”. In: *Physical Review Letters* 65.23 (1990), pp. 2861–2864.
- [San95] C. J. Sansonetti et al.: “Measurements of the resonance lines of ^6Li and ^7Li by Doppler-free frequency-modulation spectroscopy”. In: *Physical Review A* 52.4 (1995), pp. 2682–2688.
- [Sch08] M. Schuricke: “Multiphoton Ionization of Lithium”. Diploma thesis. Universität Heidelberg / Max-Planck-Institut f. Kernphysik Heidelberg, 2008.
- [Sch10a] J. R. Schneider: “FLASH - from accelerator test facility to the first single-pass soft x-ray free-electron laser”. In: *Journal of Physics B: Atomic, Molecular and Optical Physics* 43.19 (2010), p. 194001.
- [Sch10b] S. Schreiber: “Soft and Hard X-ray SASE Free Electron Lasers”. In: *Reviews of Accelerator Science and Technology* 03.01 (2010), p. 93.
- [Sch98] W. Schmitt: “Kinematisch vollständige Experimente zur Einfachionisation von Helium durch hochenergetische Schwerionen”. PhD thesis. Johann-Wolfgang-Goethe-Universität, Frankfurt a.M., 1998.
- [Sch11] M. Schuricke et al.: “Strong-field ionization of lithium”. In: *Physical Review A* 83.2 (2011), p. 023413.
- [Sco88] G. Scoles, ed.: *Atomic and Molecular Beam Methods*. Vol. I. New York: Oxford University Press, 1988.
- [SCR02] T. Schneider, P. L. Chocian, and J.-M. Rost: “Separation and Identification of Dominant Mechanisms in Double Photoionization”. In: *Physical Review Letters* 89.7 (2002), p. 073002.

-
- [Scu06] S. W. J. Scully et al.: “Doubly excited resonances in the photoionization spectrum of Li^+ : experiment and theory”. In: *Journal of Physics B: Atomic, Molecular and Optical Physics* 39.18 (2006), pp. 3957–3968.
- [SDR08] P. Schmüser, M. Dohlus, and J. Rossbach: *Ultraviolet and Soft X-Ray Free-Electron Lasers*. Springer-Verlag, 2008.
- [Sei11] M. M. Seibert et al.: “Single mimivirus particles intercepted and imaged with an X-ray laser”. In: *Nature* 470.7332 (2011), pp. 78–81.
- [Sen09] A. Senftleben: “Kinematically complete study on electron impact ionisation of aligned hydrogen molecules”. PhD thesis. Universität Heidelberg / Max-Planck-Institut f. Kernphysik Heidelberg, 2009.
- [Sen12] A. Senftleben et al.: “Characterization of Extreme Ultra-Violet Free-Electron Laser Pulses by Autocorrelation”. In: *Multiphoton Processes and Attosecond Physics*. Ed. by K. Yamanouchi and K. Midorikawa. Vol. 125. Springer Proceedings in Physics. 10.1007/978-3-642-28948-4_11. Springer-Verlag, 2012, pp. 61–68.
- [Shi08] T. Shintake et al.: “A compact free-electron laser for generating coherent radiation in the extreme ultraviolet region”. In: *Nature Photonics* 2.9 (2008), pp. 555–559.
- [Sin08] A. Singer et al.: “Transverse-Coherence Properties of the Free-Electron-Laser FLASH at DESY”. In: *Physical Review Letters* 101.25 (2008), p. 254801.
- [Sor07] A. A. Sorokin et al.: “X-ray-laser interaction with matter and the role of multiphoton ionization: Free-electron-laser studies on neon and helium”. In: *Physical Review A* 75.5 (2007), p. 051402.
- [Spi05] F. Spiegelhalder: “Setting up a Lithium Magneto-Optical Trap as a Target for a Reaction Microscope”. Diploma thesis. Universität Heidelberg / Max-Planck-Institut für Kernphysik, 2005.
- [SR03] Tobias Schneider and Jan-Michael Rost: “Double photoionization of two-electron atoms based on the explicit separation of dominant ionization mechanisms”. In: *Physical Review A* 67.6 (2003), p. 062704.
- [SSY06] E.L. Saldin, E.A. Schneidmiller, and M.V. Yurkov: “Statistical properties of the radiation from VUV FEL at DESY operating at 30 nm wavelength in the femtosecond regime”. In: *Nuclear Instruments and Methods in Physics Research Section A: Accelerators, Spectrometers, Detectors and Associated Equipment* 562.1 (2006), pp. 472–486.
- [ST07] B. E. A. Saleh and M. C. Teich: *Photonics*. Wiley-Interscience, 2007.

- [Ste07] J. Steinmann: “Multiphoton Ionization Of Laser Cooled Lithium”. PhD thesis. Universität Heidelberg / Max-Planck-Institut f. Kernphysik Heidelberg, 2007.
- [Ste05] A. T. Stelbovics et al.: “Electron-impact ionization of helium for equal-energy-sharing kinematics”. In: *Physical Review A* 71.5 (2005), p. 052716.
- [Str10] L. Strüder et al.: “Large-format, high-speed, X-ray pnCCDs combined with electron and ion imaging spectrometers in a multipurpose chamber for experiments at 4th generation light sources”. In: *Nuclear Instruments and Methods in Physics Research Section A: Accelerators, Spectrometers, Detectors and Associated Equipment* 614.3 (2010), pp. 483–496.
- [Tow95] C. G. Townsend et al.: “Phase-space density in the magneto-optical trap”. In: *Physical Review A* 52.2 (1995), pp. 1423–1440.
- [Ull03] J. Ullrich et al.: “Recoil-ion and electron momentum spectroscopy: reaction-microscopes”. In: *Reports on Progress in Physics* 66 (2003), p. 1463.
- [Ull97] J. Ullrich et al.: “Recoil-ion momentum spectroscopy”. In: *J. Phys. B* 30 (1997), pp. 2917–2974.
- [VD65] G. S. Voronov and N. B. Delone: “Ionization of the xenon atom by the electric field of ruby laser emission”. In: *JETP Letters* 1.2 (1965), p. 66.
- [VH01] G. Verbockhaven and J. E. Hansen: “Energies and autoionization widths in the lithium iso-electronic sequence”. In: *Journal of Physics B: Atomic, Molecular and Optical Physics* 34.12 (2001), pp. 2337–2361.
- [WAB83] R. C. Weat, M. J. Astle, and W. H. Beyer, eds.: *CRC Handbook of Chemistry and Physics*. 64th edition. Boca Raton: CRC Press, 1983.
- [Wal03] J. Walls et al.: “Measurement of isotope shifts, fine and hyperfine structure splittings of the lithium D lines”. In: *European Physical Journal D* 22 (2003), pp. 159–162.
- [Wal94] B. Walker et al.: “Precision Measurement of Strong Field Double Ionization of Helium”. In: *Physical Review Letters* 73.9 (1994), pp. 1227–1230.
- [Wan53] G. H. Wannier: “The Threshold Law for Single Ionization of Atoms or Ions by Electrons”. In: *Physical Review* 90.5 (1953), pp. 817–825.
- [Way93] D. Waymel et al.: “Measurements of angular correlations between two photo-electrons in the 1 P 0 symmetry”. In: *Journal of Physics B: Atomic, Molecular and Optical Physics* 26.6 (1993), pp. L123–L128.
- [web13] FLASH webpage: www.flash.desy.de. 2013.

-
- [Weh10] R. Wehlitz: *Simultaneous Emission of Multiple Electrons from Atoms and Molecules Using Synchrotron Radiation*. Vol. 58. 2010.
- [Weh04] R. Wehlitz et al.: “Double-to-single photoionization ratio of lithium at medium energies”. In: *Physical Review A* 69.6 (2004), p. 062709.
- [WH00] S. Wolf and H. Helm: “Ion-recoil momentum spectroscopy in a laser-cooled atomic sample”. In: *Physical Review A* 62.4 (2000), p. 043408.
- [Wiz79] J. L. Wiza: “Microchannel Plate Detectors”. In: *Nuclear Instruments and Methods in Physics* 162 (1979), pp. 60–1.
- [WJL08] R. Wehlitz, P. N. Juranić, and D. V. Lukić: “Double photoionization of magnesium from threshold to 54eV photon energy”. In: *Physical Review A* 78.3 (2008), p. 033428.
- [WM55] W. C. Wiley and I. H. McLaren: “Time-of-Flight Mass Spectrometer with Improved Resolution”. In: *Review of Scientific Instruments* 26.12 (1955), pp. 1150–1157.
- [YMR10] F. L. Yip, C. W. McCurdy, and T. N. Rescigno: “Double photoionization of excited lithium and beryllium”. In: *Physical Review A* 81.6 (2010), p. 063419.
- [Zhu10] G. Zhu: “Photofragmentation of Lithium Atoms Studied with MOTReMP”. PhD thesis. Johann Wolfgang Goethe-Universität, Frankfurt a.M., 2010.
- [Zhu09] G. Zhu et al.: “Controlling Two-Electron Threshold Dynamics in Double Photoionization of Lithium by Initial-State Preparation”. In: *Physical Review Letters* 103.10 (2009), p. 103008.
- [Åbe70] T. Åberg: “Asymptotic Double-Photoexcitation Cross Sections of the Helium Atom”. In: *Physical Review A* 2.5 (1970), pp. 1726–1729.